Physics Reports 847 (2020) 1–102

Contents lists available at ScienceDirect

Physics Reports

journal homepage: www.elsevier.com/locate/physrep

On virus growth and form

Roya Zandi [a,*], Bogdan Dragnea [b], Alex Travesset [c], Rudolf Podgornik [d,e]

[a] Department of Physics and Astronomy, University of California, Riverside, CA 92521, USA
[b] Department of Chemistry, Indiana University, Bloomington, IN 47405, USA
[c] Department of Physics and Astronomy, Iowa State University and Ames Lab, Ames, IA 50011, USA
[d] School of Physical Sciences and Kavli Institute for Theoretical Sciences, University of Chinese Academy of Sciences, Beijing 100049, China
[e] CAS Key Laboratory of Soft Matter Physics, Institute of Physics, Chinese Academy of Sciences (CAS), Beijing 100190, China

ARTICLE INFO

Article history:
Received 13 May 2019
Received in revised form 11 December 2019
Accepted 30 December 2019
Available online 15 January 2020
Editor: H. Orland

ABSTRACT

We review approaches aimed at deciphering the physical mechanisms responsible for viral structure and assembly. We discuss the basic principles of condensed matter physics, macroscopic electrostatics and elastomechanics as they apply to nanosized two-dimensional biomolecular shells with spherical topology and icosahedral symmetry, as well as their proper extension to nonspherical structures pertinent to retroviruses. We examine the relation between the virus structure, the physical interactions that are driving their (self)assembly and the thermodynamics of transition from an isotropic protein solution to the assembled shell state, and discuss the driving forces for large-scale structural reorganizations characterizing maturation processes in the already assembled nano-shells. We furthermore review physical models corresponding to the condensed states of confined genome-carrying biopolymers in viral nano-shells during virus self-assembly and host-cell infection processes, and show how the combination of discrete and continuum coarse grained mechanics, commonly used in the fundamental physical description of viruses, together with the pertinent description of generic long-range electrostatic and specific short-range interactions give insight into the details of structural order and mechanical properties of viruses and elucidates their role in nano-container and nano-machine functions.

Contents

* Corresponding author.
E-mail address: royaz@ucr.edu (R. Zandi).

https://doi.org/10.1016/j.physrep.2019.12.005
0370-1573/

1. Introduction

1.1. Biological shape: A diagram of forces

A hundred years ago, D'Arcy Thompson eloquently formulated his interpretation of biological shape as a *diagram of forces*, in the sense that shape is revealing of the physical forces that have acted upon its formation [1]. The goal of this review can then be discerned in the spirit of his visionary work as bringing together some of the recent advances in *physical virology*, aiming at understanding virus growth and form in the context of the physical interactions that are driving their (self)assembly.

Considering the sweeping view of Thompson's pioneering work on the general theory of morphogenesis, it may appear that the focus has narrowed considerably. However, viruses are associated with every form of life [2], and it has been noted that they harbor a diversity which, in terms of genome organization and replication strategies, exceeds that of the three domains of life taken together [3]. Despite such diversity, broad general features do exist; they have allowed for virus classification according to their physical as well as biological properties. For instance, large groups of viruses share general structural characteristics such as symmetry, shape, and size of the protein shell, as well as the nature of genome packing and ordering within the viral proteinaceous shell together with the pertinent interactions, or furthermore exhibit similar replication and proliferation strategies (pathways for formation of mRNA) [4].

Seeking a unifying perspective on the physical driving forces behind virus growth and form is therefore a justified endeavor and has proven to be ripe with insights into the details of the physical mechanisms at work in the context of virus structures and functions.

1.2. A confluence of scales

Viruses are a diverse group of replicating (macro)molecular protein–nucleic acid complexes, devoid of their own metabolism, and obligated to their host for essential functions [5]. Viruses have evolved features on a level of refinement that continues to surpass synthetic self-assembled nanomaterials, such as stoichiometric control and re-configurability. These innate characteristics are desirable and potentially critical for many future technologies such as sustainable energy harvesting [6–8], high latency information storage [9,10], and nanomedicine [11,12]. Particularly active research in the latter area is currently focused on therapeutic delivery [13] and imaging applications [14–16].

Virus organization has provided inspiration for a range of unique bio-enabled self-assembling systems and innovative material concepts such as bio-inspired photosynthetic systems with efficient energy and electron transfer [17], novel photonic and plasmonic structures using a design derived from virus self-assembly [18], or all the way to higher order complex coupled catalysts [19,20]. In this context, virus phenomena and properties concerning assembly, stability, and transformation of viruses, which are of a purely physical origin and thus transferrable to an artificial system, are certainly of major interest.

Viruses are *quintessential nano-objects* with very rich physical phenomenology the study of which includes fundamental nanoscale long- and short-range interactions, details of polymer behavior in confined and constrained systems, kinetics and thermodynamics of self-assembly of a quasi two-dimensional system, co-operative effects in co-assembly of nucleic acids and proteins, and striking geometrical and topological properties of capsids requiring detailed discrete mathematics and/or differential geometry descriptions.

The treatment of generalized physical forces driving virus growth and form is particularly challenging because of the span of the spatio-temporal scales and strengths of constitutive interactions which characterize virus assembly. Specifically, at the spatial scale inhabited by most viruses, there is a confluence of characteristic energies associated with a variety of interactions including electrostatic, thermal, mechanical, etc. [21]. These interactions, by virtue of their very different magnitudes at other spatial scales, are generally treated within separated fields of physical sciences. However, at nanoscale, as Quake and Phillips pointed out [22], mechanical, electrostatic, and thermal interactions, and even some biologically-important chemical bond interactions *may have comparable magnitudes*. There is then a substantial cross-talk between different degrees of freedom that – at any other scale – could be safely neglected, but not at the scales inhabited by viruses. Thus, the aim of this review is also to introduce a holistic picture of the *physical virology* that illustrates the complex interplay between thermodynamic driving forces, mechanical stresses, and long-range electrostatic interactions driving the virus assembly.

The general geometrical principles in the construction of virus shells (capsids) as polyhedral cages are discussed in Section 2. Symmetry enforced geometrical selection rules provide the basis for the classification of spherical viruses and allow the formulation of the simplest general phenomenological theory of virus self-assembly. Several types of experiments aiming at measuring the mechanical properties of viruses are discussed in Section 3. A detailed theoretical perspective of the interplay between symmetry, topological defects, and mechanical properties is provided in Section 4. The virus shell contains, protects, transports, and presents the genome for replication in response to environmental cues. Packaging of the genome inside a capsid is required in order to form a functional virus through highly orchestrated processes encompassing a bewildering variety of strategies among different viruses, nevertheless displaying a universality based on the prominence of electrostatic interactions, additionally implying different consequences in the case of DNA and/or RNA viruses. Fundamentals of genome packaging in viruses are discussed in Section 5, with important differences in the ordering of encapsidated DNA as compared to the co-assembled RNA. We conclude in Section 6 with an overview of kinetic experiments in virus assembly which have contributed to the realization that, in viruses, accuracy in molecular assembly does not have to come at the cost of speed.

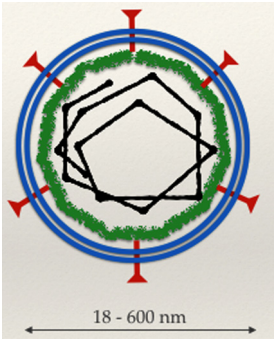

Fig. 1. Generic schematic representation of the main components of an isometric virus (black: genomic cargo, green: protein capsid, blue: lipid layer), red: glycoproteins playing a role in target recognition. The size span is from tens to hundreds of nm.

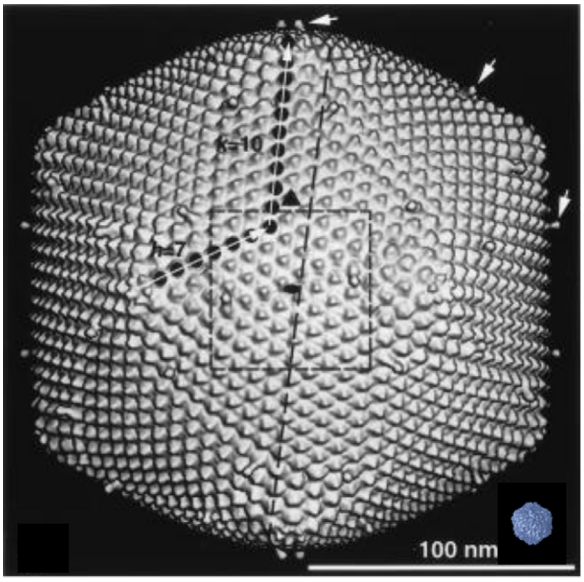

Fig. 2. Size span of icosahedral virus shells illustrated by a comparison between single particle reconstruction images of one of the largest (PpV01) and one of the smallest (porcine circovirus) viruses.
Source: With permission from Refs. [26] and [25].

2. Virus form

Virus particles come in many sizes and shapes and vary enormously in the number and nature of the protein molecules from which they are built. The particular size and shape of a capsid is found to depend on many physical variables such as pH, ionic strength, multivalent cations, viral genome, concentration of proteins, etc.

Fig. 1 presents a sketch of the general major components encountered in viruses. Their mutual arrangement is not always the one depicted here, but most of the time, from inside out, we distinguish: the nucleic acid genome (black), the capsid shell (green), and in the case of enveloped viruses also a lipid membrane envelope (blue) studded with proteins (red) for host recognition and entry. Non-enveloped viruses are constituted solely of a cargo mainly formed of nucleic acid genome, and a shell. This is the case for most icosahedral, single-stranded (ss) RNA viruses [4].

A group apart among viruses illustrates a unique paradigm in molecular assembly. These are viruses that protect, transport, and deliver their genome with the help of a cage called the capsid, constructed as a symmetric protein tiling of a closed surface, which encapsulates nucleic acid(s) and enzymes. Stringent constraints related to genomic economy, as first realized by Crick and Watson [23], often lead to a construction strategy employing many copies of identical subunits. Building block identity necessarily favors symmetry and the highest volume-to-surface ratio regular polyhedron is the icosahedron. Interestingly, icosahedral symmetry is pervading among isometric viruses [24], from the smallest, 17 nm diameter, circovirus [25], to the 220 nm diameter PpV01, a marine algal virus and a veritable Behemoth by comparison [26], Fig. 2.

The general classification rules for spherical viruses have been identified in their seminal contribution by Caspar and Klug [27], who singled out the most basic virus assembly principles, stemming from the molecular interactions between the capsid protein subunits, as well as introduced the proper quantitative triangulation number measure for the virus size, fully compatible with their symmetry. Their vision thus gave a common framework for the variability of size as well as universality of symmetry of the viral shape.

2.1. The Caspar-Klug construction

In 1956 Crick and Watson [23] argued that capsids of (small) viruses, with relatively short genomes, have to be composed of a large number of identical protein subunits arranged either in helical motifs or in the shapes of regular polyhedra. Multiple redundancy of protein subunits in viral shells, *i.e.*, the fact that they are present in multiple copies, is evolutionally favored since it implies that the genome only has to encode for a small number of distinct genes, which keeps its length, and therefore the size and energy cost of the virus assembly, manageably small.

Following this seminal work, Caspar and Klug [27] elaborated its basic ideas further and argued that the regular polyhedra should have *icosahedral symmetry* since an icosahedron has the largest volume-to-surface ratio of all the regular polyhedra. They noted that, while all small viruses appear to be regular, not all regular viruses are small, and proposed an *Aufbau Prinzip* [28] for viral assembly, that provides for maintaining the same symmetry at vastly different sizes. The main assumption behind the Caspar–Klug model is the tendency of systems composed of interacting subunits to form the maximum number of the most stable bonds between them. Consequently, in a planar 2D hexagonal sheet with the assumption of isotropic interactions between subunits, each site has six nearest neighbors and the close-packed identical capsid protein subunits are placed at positions compatible with protein asymmetry. Folding this planar 2D lattice into a closed surface, topologically equivalent to a sphere, then leads directly to its mapping onto an icosahedron surface by cutting exactly 12 60° sectors from the initial 2D sheet and stitching the remaining 2D mesh together, while preserving exactly the bonding pattern of all the protein subunits in the lattice, Figs. 3 and 4. This stitching process generates 12 fivefold vertices from the original hexagonal lattice, characterized by five as opposed to the original six nearest neighbors.

This geometric construction then leads to an icosahedral shell composed of exactly 60 subunits, 5 per each five-fold vertex, distributed in completely *equivalent positions* by symmetry and preserving the bonding pattern of the 2D hexagonal lattice. As many simple viruses are composed of a much larger number of subunits, Caspar and Klug devised an extension of their model by introducing the notion of *quasi-equivalence*. This would be accomplished again by cutting out triangular sections that would not preserve the sixfold symmetry of the lattice, Figs. 3 and 4, but stitching then the remaining 2D mesh together in this case would preserve the bonding pattern of the protein subunits in the 2D lattice only approximately. The sites of protein subunits in the icosahedral structure would be in this case only *quasi equivalent*, since they would not preserve the symmetry of the original 2D lattice, but would in this way allow for the shell to be composed of more than 60 subunits, enabling the construction of virus shells of any size.

This procedure implies a variable number of hexamers connecting the 12 fivefold vertices quantified by the path along the unit vectors $\mathbf{a}_{1,2}$ of the 2D lattice that leads from one vertex to a neighboring one. When this path can be quantified by the hexagonal lattice unit vectors $\mathbf{a}_1$ and $\mathbf{a}_2$, as $h\mathbf{a}_1 + k\mathbf{a}_2$, with h, k non-negative integers, then the total number of protein subunits in the quasi-equivalent positions would be 60 T, where

$$T = h^2 + k^2 + hk. \tag{1}$$

Here, T is referred to as the *triangulation number* of the virus and h, k measure the number of steps in the direction of the two unit vectors of the hexagonal lattice that connect one five-fold symmetric site to another: to get from one five-fold symmetric site to another, one has to move over h six-fold symmetric sites along a row of nearest neighbor bonds on the hexagonal lattice, then turn 60° and move another k six-fold symmetric steps, see Fig. 3. This definition furthermore implies a strict *selection rule* $T = 1, 3, 4, 7\ldots$ with 60, 180, 240, and 420 . . ., capsid protein units, respectively.

If the icosahedron has a higher triangulation number – even if all proteins are chemically identical – some will be in an environment of 5 neighbors (5-fold vertex area: *pentons*) and others will be in a 6 neighbors environment (*hexons*). Hence the positioning of each protein is not equivalent to all the other ones, but by necessity only *quasi-equivalent*. The triangulation number thus measures the number of quasi-equivalent positions in the viral capsid. Viruses with different triangulation numbers thus differ in the number of proteins as well as the size, as shown in Fig. 5.

A generalization based on the Caspar–Klug construction was proposed for non-isometric virus capsids, e.g. the bacteriophage T4 and the human immunodeficiency virus (HIV), by Nguyen, Bruinsma and Gelbart [31]. The folding template for the construction of a spherocylinder is shown in Fig. 6. In addition to (h, k), two more integers are needed for the construction of a spherocylindrical shell. The shape of a spherocylinder is then determined by two pairs of basis vectors (a_1, a_2) and (b_1, b_2) and two pairs of integers (h, k) and (n, m) such that $A = n(ha_1 + ka_2)$ and $B = m(hb_1 + kb_2)$. This method can be used to construct conical structures too, but since there are different numbers of pentagons on each cap of the shell, the procedure of construction of the shell is necessarily more complex. Fig. 7 illustrates the construction of a conical shell with an inhomogeneous distribution of pentagons: 5 in the smaller cap and 7 in the larger cap of a cone, see [31]. The total number of capsomers of a spherocylinder can be determined as $N = 10mn(h^2 + k^2 + hk) + 2$, while in the case of a cone it is $N = 10(2m^2n^2)(h^2 + k^2 + hk) + 2$.

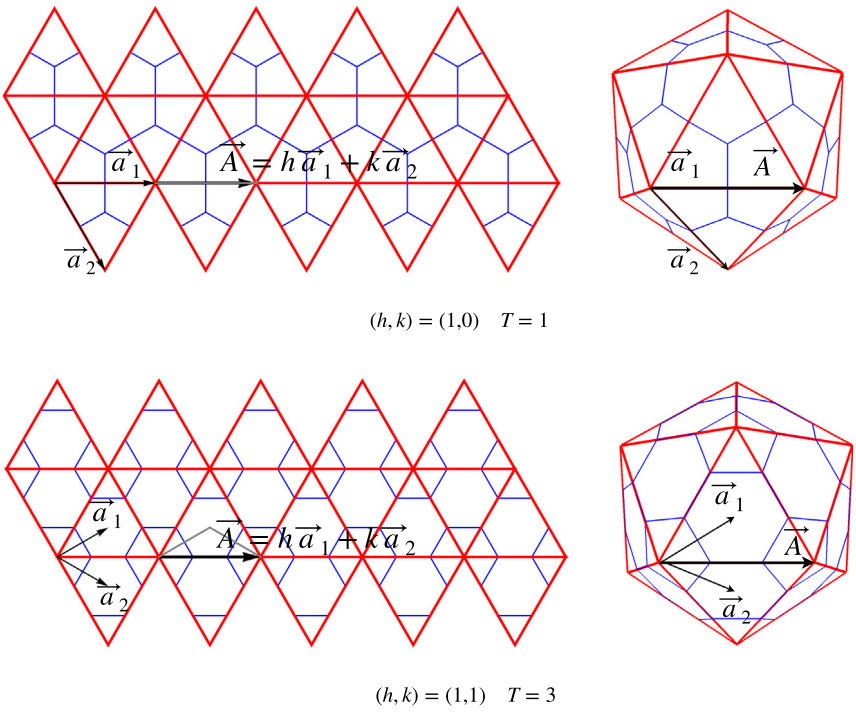

Fig. 3. Caspar–Klug model of mapping of a planar 2D hexagonal sheet onto an icosahedron surface. The structures correspond to $T = 1$ and $T = 3$.

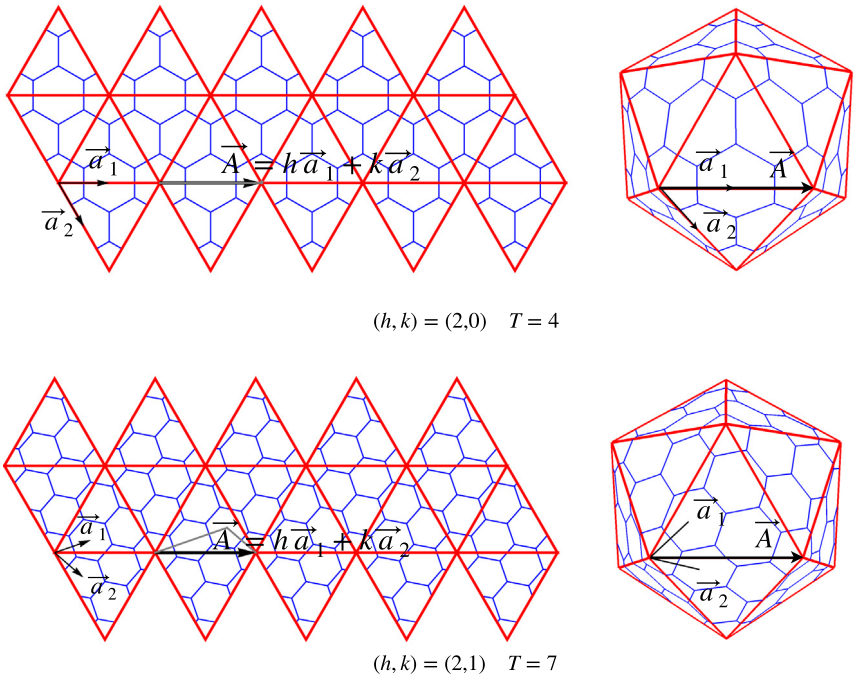

Fig. 4. Caspar–Klug structures for $T = 4$ and $T = 7$.
Source: Adapted from Ref. [29].

Though many virus types can be described *via* the Caspar–Klug geometric construction or its generalized versions, not all isometric viruses conform to the principles of quasi-equivalence. In order to put the classification and structural principles of viral design onto a broader basis, Lorman and Rochal [32–34] devised a more comprehensive approach based

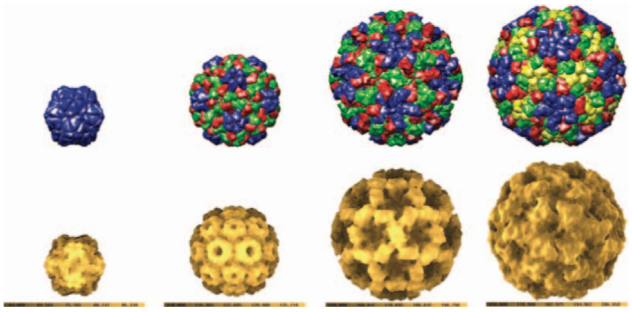

Fig. 5. Examples of viruses characterized by different triangulation numbers (left to right): $T = 1$ (satellite tobacco mosaic virus), $T = 3$ (Cowpea Chlorotic Mottle Virus (CCMV)), $T = 3$ (Norwalk virus) and $T = 4$ (Nudaurelia capensis ω virus). The figure shows a 5 Å-resolution rendering of the subunit coordinates (above) and a radial rendering view of the virus particle (below). The images were obtained with the viper particle explorer software (VIPER) at http://viperdb.scripps.edu/.
Source: Adapted from Ref. [30].

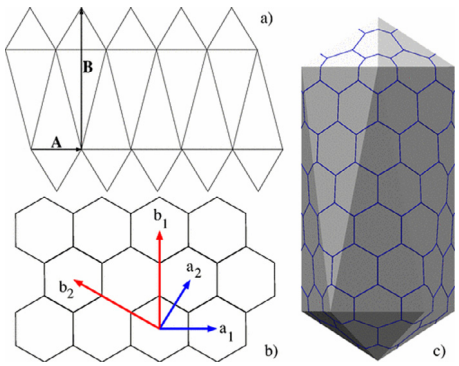

Fig. 6. Construction of a spherocylindrical capsid. (a) Folding template for a spherocylinder. (b) The basis vectors are illustrated: $A = n(ha_1 + ka_2)$ and $B = m(hb_1 + kb_2)$ with (h, k) and (n, m) any two pairs of non-negative integers as long as $m > n$. If $m = n$, the spherocylinder reduces to an icosahedron. (c) A spherocylinder structure with $n = 2$, $m = 0$, and $h = 3$, $k = 0$.
Source: With permission from Refs. [31].

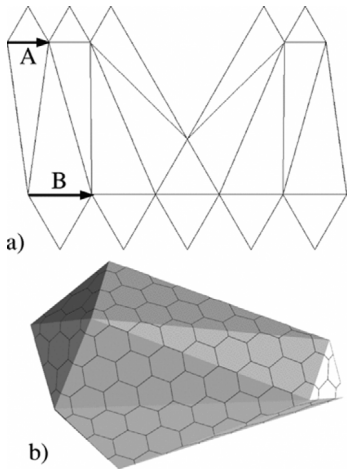

Fig. 7. Construction of a conical shell. (a) Folding template of a cone. The two lattice vectors $A = n(ha_1 + ka_2)$ and $B = m(hb_1 + kb_2)$ are parallel, with (h, k) and (m, n) any two pairs of non-negative integers with $m > n$. (b) A cone with $h = 1$, $k = 0$, $m = 3$, and $n = 2$.
Source: With permission from Refs. [31].

on the fundamental notion that "protein subunits and the nucleic acid chain spontaneously come together to form a simple virus particle because this is their lowest energy state" [35], *i.e.*, the virus structure is a result of (free) energy minimization. In this approach the Caspar–Klug geometric construction appears as one of the possible energetically favorable symmetry

states, while several other ones, known to exist in the virus zoo but not being amenable to the straightforward Caspar–Klug construction, have obtained in this generalized framework a definitive rationale for their existence.

In another recent generalization of the Caspar–Klug construction, Twarock and Luque [36] argue that this theory is just a special case of a more general crystallographic design principle for icosahedral and octahedral capsid architectures, derivable from the Archimedean lattices and their duals. This particular generalization aims to elucidate the structural principles for different capsids with either the same number of structural proteins, or with a combination of minor and major capsid proteins as *e.g.* in the case of non-quasi-equivalent architectures in the HK97 lineage.

2.2. Phenomenological (Landau) theory of virus self-assembly and its generalizations

Caspar and Klug already proposed that virus "self-assembly is a process akin to crystallization and is governed by the laws of statistical mechanics" [24], implying that a theory similar to the general Landau phenomenological theory of crystallization should be applicable also to the self-assembly of capsids. It could furthermore provide accurate and clear predictions close to the crystallization point based solely on a small number of phenomenological parameters [37]. Of course a phenomenological theory cannot deal with molecular details that should be covered by specific molecular models. Since the shape of small viruses with icosahedral symmetry is close to spherical, one could treat the viral self-assembly as a problem of crystallization on a spherical surface with protein angular distribution on the capsid given by the maxima in the corresponding *coarse grained density distribution*, consistent with the symmetry requirements. This coarse grained protein density distribution could *grosso modo* describe the packing of protein centers of mass or even the packing of whole groups of proteins on the capsid surface but not the finer details at the amino acid or even at the atomic resolution level, as revealed by the structural probes such as cryo-microscopy or x-ray diffraction [38].

In the Landau phenomenological theory the protein density distribution function is assumed to be quantifiable by an *order parameter* describing the crystallization, $\rho = \rho_0 + \rho(\Omega)$, where ρ_0 is an isotropic density of proteins in the parent solution and $\rho(\Omega)$, with $\Omega = (\theta, \phi)$ the angular coordinates, is the critical system of self-assembly density waves describing the deviations from the uniform solution density. The critical part of ρ can be written as a series in spherical harmonics $Y_{\ell,m}(\theta, \phi)$, with the general form

$$\rho(\Omega) \longrightarrow \rho_\ell(\theta, \phi) = \sum_{m=-\ell}^{m=\ell} A_{\ell,m}\, Y_{\ell,m}(\theta, \phi), \tag{2}$$

and is given within the standard Landau theory by an irreducible representation of the rotational symmetry group, corresponding to a single (critical) term $\rho_\ell(\theta, \phi)$, *i.e.*, by omitting the summation over the index ℓ. The associated free energy then follows as a function of the *rotationally invariant* combinations of amplitudes $A_{\ell m}$ of the spherical harmonics. The latter are solutions of the angular part of the Laplace equation with eigenvalue $-\ell(\ell + 1)$ and can be written in a canonical form as

$$Y_{\ell,m}(\theta, \phi) = \sqrt{\frac{2\ell + 1}{4\pi} \frac{(\ell - m)!}{(\ell + m)!}}\, P_\ell^m(\cos\theta)\, e^{im\phi},$$

where $P_l^m(x)$ are the associated Legendre polynomials [39]. Notably, the above expansion of ρ does not in general exhibit an icosahedral symmetry. Only special combinations of the spherical harmonics, referred to as the *icosahedral spherical harmonics*, exhibit this symmetry.

The icosahedral spherical harmonics can be introduced only for particular even or odd values of ℓ. The even values follow the selection rule $\ell = 6i + 10j$, where i, j are integers, corresponding to the sequence $\ell = 6, 10, 12, 16 \ldots$, while the odd values are constrained by the selection rule $\ell = 15 + 6i + 10j$, so that the sequence becomes $\ell = 15, 21, 25, 27 \ldots$ [33]. The difference between the two ℓ sequences is shown in Fig. 8 for the case of $\ell = 10$ and $\ell = 21$. The two sequences are connected with the fact that an icosahedron has 6 5-fold axes, 10 3-fold axes, and 15 2-fold axes. The lowest even value is thus $\ell = 6$, while the lowest odd value would be $\ell = 15$. In addition, odd icosahedral harmonics change sign under inversion, and can be thought of as representing two different density distributions, corresponding to two different, D and L, *chiral isomers*.

While the odd and even icosahedral spherical harmonic sequences are both *a priori* possible, they are not equivalent. The proteinaceous shell is composed of asymmetric chiral proteins, and as a consequence should not exhibit spatial inversion and mirror planes, *i.e.*, it can only contain rotational symmetry. The chiral nature of capsid proteins would then effectively constrain the ℓ expansion to odd icosahedral spherical harmonics only [32,33], thus ensuring that the ordered, assembled phase is also chiral.

If the viral self-assembly is similar to crystallization [27], the self-assembled state of capsid proteins in a simple virus particle would then correspond to the lowest free energy state [40,41]. The form of the free energy close to a crystallization transition of an unconstrained system has been analyzed by Landau [37], while the corresponding modifications in the case of constrained crystallization on a spherical surface have been put forth by Lorman and Rochal [32]. In the latter case, close to the self-assembly point the Landau free energy can be approximated by a power series of the critical system of density waves, $\rho(\Omega)$, as

$$\mathcal{F}_L[\rho] = \mathcal{F}_0 + \oint_S d\Omega \left(\tfrac{1}{2} A(T, c)\rho^2 + \tfrac{1}{3} B(T, c)\rho^3 + \tfrac{1}{4} C(T, c)\rho^4 + \cdots \right). \tag{3}$$

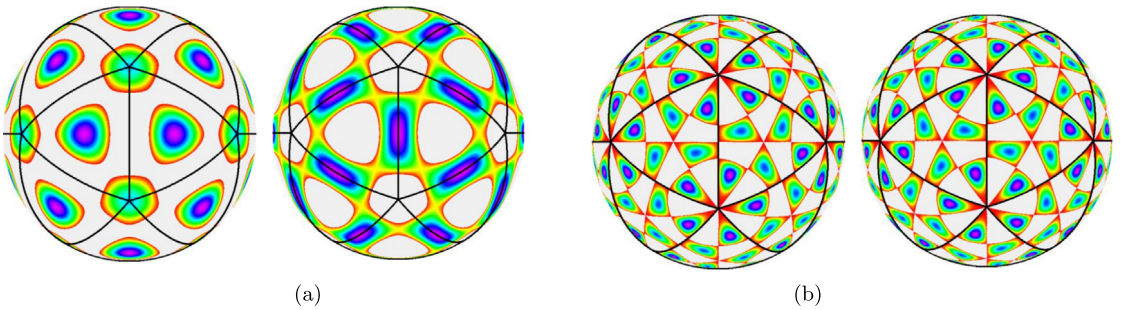

Fig. 8. Critical density waves $\rho(\Omega)$ across a sphere for $\ell = 10$ (a) and $\ell = 21$ (b) icosahedral spherical harmonic expansion, explicitly showing the icosahedral symmetry. Pairs in (a) and (b) show positive (left) and negative (right) values of $\rho(\Omega)$, i.e., describing the deviations from the mean solution protein density. The odd ℓ density distribution does not contain spatial inversion and mirror planes, and shows two chiral isomers. Graphics courtesy of S. Rochal.

The thermodynamic equilibrium is hence obtained by minimizing $\mathcal{F}_L[\rho]$ w.r.t. $\rho(\Omega)$. After integrating over the spherical surface and performing the expansion over spherical harmonics, Eq. (2), the free energy should contain only powers of $A_{\ell,m}$ consistent with icosahedral symmetry that are rotationally invariant. Furthermore, according to the precepts of the Landau theory, the series should contain only a single ℓ term, an irreducible representation of the rotational symmetry group, corresponding to the spherical harmonic mode that describes the protein density of a fully assembled, *i.e.*, "crystallized" capsid, thus

$$\begin{aligned}\mathcal{F}_L[A_{\ell,m}] = \mathcal{F}_0 &+ \tfrac{1}{2}A(T,c)\sum_{m_1,m_2=-l}^{+l} A_{\ell,m_1}A_{\ell,m_2}\delta\,(m_1+m_2)\\ &+ \left[\tfrac{1}{3}B(T,c)\sum_{m_1,m_2,m_3}(\ldots)A_{\ell,m_1}A_{\ell,m_2}A_{\ell,m_3}\delta\,(m_1+m_2+m_3)\right]\\ &+ \tfrac{1}{4}C(T,c)\sum_{m_1,m_2,m_3,m_4}(\ldots)A_{\ell,m_1}A_{\ell,m_2}A_{\ell,m_3}A_{\ell,m_4}\delta\,(m_1+m_2+m_3+m_4)+\cdots\end{aligned} \tag{4}$$

where $A(T,c), B(T,c)$ and $C(T,c)$ are temperature and composition dependent phenomenological coefficients of the Landau theory. The dots stand for numerical weight coefficients required by the rotational symmetry, omitted for the purpose of a clear general line of argumentation. The third term in the above equation is in square brackets, since it would additionally vanish for any odd ℓ, due to the absence of spatial inversion and mirror planes as in the case of a capsid composed of chiral protein subunits.

The essence of the above general picture of capsid protein "crystallization" can be glimpsed from two simple cases, corresponding to the lowest values provided by the two selection rules, *i.e.*, $\ell = 6$ and $\ell = 15$ (see above). Assume first that the self-assembly units are achiral, so the lowest value admissible by the selection rule would be $\ell = 6$, leading to

$$\rho_6(\theta,\phi) = \sum_{m=-6}^{+6} A_{6,m}\; Y_{6,m}(\theta,\phi) \longrightarrow Q_6 Y_h(6), \tag{5}$$

with Q_6 the *order parameter amplitude* and the *icosahedral spherical harmonic* of the form

$$Y_h(6) = Y_{6,0}(\theta,\phi) + \sqrt{\tfrac{7}{11}}Y_{6,5}(\theta,\phi) - \sqrt{\tfrac{7}{11}}Y_{6,-5}(\theta,\phi), \tag{6}$$

a linear combination of $Y_{6,m}$ invariant under icosahedral point group with an even symmetry under inversion ($\mathbf{r} \longrightarrow -\mathbf{r}$), *i.e.*, it transforms as a scalar. In general, icosahedral spherical harmonics of order ℓ are given by a linear combination of spherical harmonics containing only those m that exhibit all the rotational symmetries of an icosahedron and there exist systematic construction algorithms that yield the appropriate coefficients in the linear expansion, which have been extensively tabulated [42]. For this case the Landau free energy, Eq. (4), yields

$$\mathcal{F}_L = \mathcal{F}_0 + \tfrac{1}{2}A(T,c)Q_6^2 + \tfrac{1}{3}B(T,c)Q_6^3 + \tfrac{1}{4}C(T,c)Q_6^4 + \cdots \tag{7}$$

and minimizing it w.r.t. the order parameter amplitude Q_6 results in

$$Q_6\left(A(T,c) + B(T,c)Q_6 + C(T,c)Q_6^2\right) = 0. \tag{8}$$

Since the third order term in the free energy is non-zero, this implies a first order transition, characterized by a finite jump of the amplitude from $Q_6 = 0$ to a finite value, as well as the existence of intermediate and/or precursor assembly states.

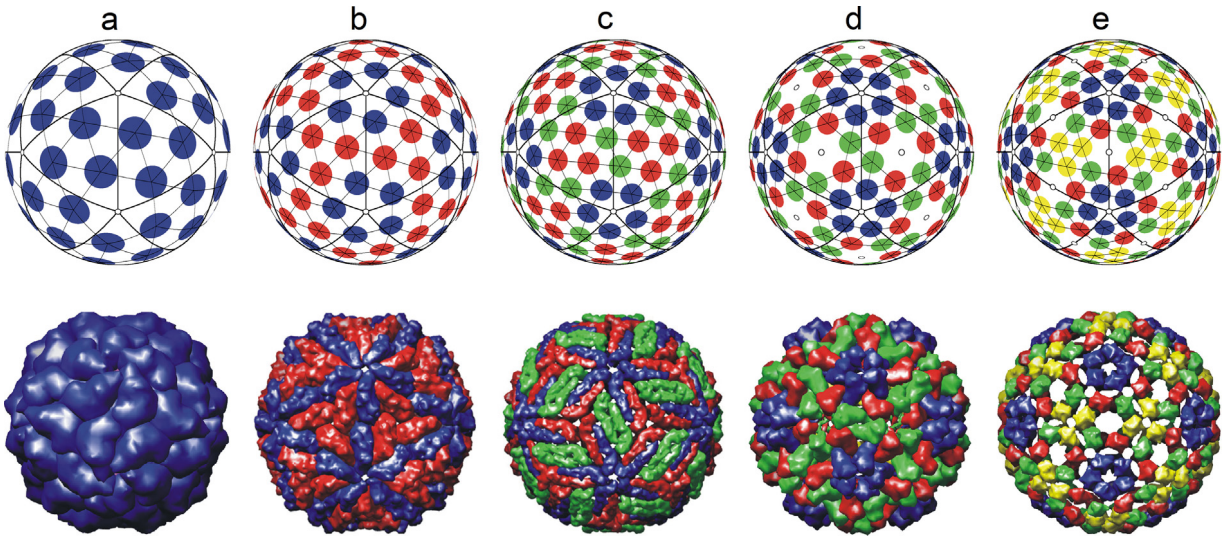

Fig. 9. Association between the nonequivalent maxima of the lowest odd ℓ icosahedral density wave distributions with the corresponding protein positions (colored disks). The upper sequence shows the lowest ℓ chiral spherical lattices that do or do not belong to the Caspar–Klug lattices: (a) $\ell = 15, T = 1$ (CK), (b) $\ell = 21, T = 2$ (non-CK), (c) $\ell = 25, T = 3$ (non-CK), (d) $\ell = 27, T = 3$ (CK) and (e) $\ell = 31, T = 4$ (CK). The corresponding experimental capsid structures are shown in the lower sequence: (a) Satellite Tobacco Mosaic virus (composed of 60 proteins); (b) L-A virus (120 proteins); (c) Dengue virus (180 proteins); (d) Chlorosome Vigna virus (180 proteins); (e) Sindbis virus (240 proteins). Protein centers of mass are located approximately in the occupied nodes of the spherical lattices.
Source: Adapted from Ref. [34].

This is consistent with experiments on cowpea chlorotic mottle virus (CCMV) assembly that implicate the existence of precursor states with capsid protein bound to the RNA molecule, followed by intermediate assembly states that then lead to full capsid formation and shedding of excess protein [43]. The first order transition self-assembly mechanism gains additional support from the thermal dissociation studies of CCMV virions and loaded capsids Monte-Carlo simulation studies [44], as well as from Brownian dynamics simulation of icosahedral capsid assembly around a flexible polymer exhibiting nucleation of a capsid "embryo", followed by growth and finally full assembly [45].

In the case of $\ell = 15$, the self-assembly units are assumed to be chiral and the Landau free energy, Eq. (4), does not contain a third order invariant. The critical density wave then decomposes into

$$\rho_{15}(\theta,\phi) = \sum_{m=-15}^{+15} A_{15,m}\, Y_{15,m}(\theta,\phi) \longrightarrow Q_{15} Y_h(15). \tag{9}$$

Again, Q_{15} is the order parameter amplitude and in this case $Y_h(15)$ has an odd symmetry under inversion ($\mathbf{r} \longrightarrow -\mathbf{r}$), *i.e.*, it transforms as a pseudo-scalar and can be obtained as

$$\begin{aligned} Y_h(15) = {} & \tfrac{3003}{625} Y_{15,-15}(\theta,\phi) - \tfrac{33\sqrt{15834}}{625} Y_{15,-10}(\theta,\phi) - \tfrac{3\sqrt{667667}}{125\sqrt{5}} Y_{15,-5}(\theta,\phi) \\ & - \tfrac{3\sqrt{667667}}{125\sqrt{5}} Y_{15,5}(\theta,\phi) + \tfrac{33\sqrt{15834}}{625} Y_{15,10}(\theta,\phi) + \tfrac{3003}{625} Y_{15,15}(\theta,\phi). \end{aligned} \tag{10}$$

The coefficients in this expansion are obtained either by various direct construction algorithms to generate symmetry adapted spherical harmonics for the icosahedral point group, based on the standard projection operator technique involving the use of Wigner rotation matrices, or from existing tabulated values [46].

The relationship between the density wave description in the phenomenological theory of viral shell assembly and the Caspar–Klug theory is presented for $\ell = 15, 21, 25, 27, 31$, see Fig. 9. For $\ell = 21$ there are 2 nonequivalent maxima and it definitely cannot be a Caspar–Klug structure. The $\ell = 25$ structure with 3 nonequivalent maxima superficially looks like a Caspar–Klug structure, corresponding to $(h, k) = (1, 1)$, but on closer inspection shows no hexagonal arrangements of protein positions and thus cannot be associated with any Caspar–Klug structure, *even if* the number of protein positions satisfies the $(h, k) = (1, 1)$ Caspar–Klug selection rules.

Chiral handedness has the symmetry properties of a pseudo-scalar and can consequently assume only two values. It behaves as a scalar in all symmetry transformations, except under inversion where it changes sign. This means that to each odd ℓ correspond two chiral isomers (left and right chirality). The free energy Eq. (4) and the minimization condition now does not contain the third order term since ℓ is odd and therefore exhibits a particularly simple form

$$\mathcal{F}_L = \mathcal{F}_0 + \tfrac{1}{2} A(T,c) Q_{15}^2 + \tfrac{1}{4} C(T,c) Q_{15}^4 + \cdots \quad \text{with} \quad Q_{15}\Big(A(T,c) + C(T,c) Q_{15}^2\Big) = 0. \tag{11}$$

This form of the free energy, restricted to fourth and lower order density terms, now first of all implies a second order, continuous transition from $Q_{15} = 0$ state, which precludes the formation of intermediate and/or precursor assembly states observed in experiments (see above). However, the first order phase transition for odd harmonic ordered phases with nucleation and hysteresis could be obtained straightforwardly, if the Lorman–Rochal theory would be generalized by including sixth and higher order density terms. In addition, stability analysis shows that odd icosahedral harmonic equilibrium solutions including $\ell = 15$ are unstable, corresponding to a saddle-point and not to a minimum, while lowest lying even icosahedral harmonic equilibrium solutions including $\ell = 6$ are stable [47]. Finally, one needs to add here that the construction of critical density waves is based solely on their symmetry and irreducibility, not being associated with the nature of the self-assembly transition itself.

It thus seems that in the Landau theory of virus self-assembly [32] the achiral states describe the icosahedral symmetry better than the chiral ones, which is at odds with the observed properties of capsid protein subunits and assembled virus structures. These discrepancies led to further generalizations of the theory by Bruinsma and coworkers [47,48], who proposed several modifications to make the theory capable of describing the observed properties of viral assembly while preserving its basic features. First of all one needs to jettison the assumption of an *a priori* choice of ℓ in writing down the Landau free energy. Its proper value should actually be the result of minimization of a more general Landau–Brazovskii theory [49], applied to a spherical surface, that properly takes into account the inherent length-scales in the problem, so that the lowest-energy modes correspond to a specific value of the ℓ harmonic [47]. An interesting feature of such Landau–Brazovskii theory is that there is nothing to prevent considering not only the pure states but also the composite states, with a superposition of two or more pure neighboring ℓ states. For instance, the mixed "15 + 16" combination is stable and the transition into the composite stable icosahedral state becomes a continuous (or a weakly first-order) phase transition with a broken chiral symmetry and an achiral isotropic state. To encompass also the fact that the isotropic state already contains chiral (protein) components, additional chiral terms need to be added to the Landau–Brazovskii theory, making non-icosahedral even ℓ states develop an admixture of secondary icosahedral states and thus becoming possible candidates for the icosahedral ordering [48]. On the other hand, the "15 + 16" mixed state which exhibited a broken chiral symmetry on the Landau–Brazovskii level ceases to be problematic, since with proper choice of the coupling constant the two chiral isomers exhibit different energies and the chiral coupling breaks the symmetry between them, while in addition also making the parent phase, i.e., the isotropic solution of protein components, chiral.

While the picture of possible self-assembly scenarios of virus structures that could be provided by the Landau theory promised manageable simplicity, eventually it leads to further generalization of the original Landau-based approach [47,48], actually making more molecular level approaches highly desirable.

The phenomenological theory of capsid self-assembly based on the generalized Landau or Landau–Brazovskii theory of constrained crystallization can provide at least in principle a general account of the symmetry, packing geometry and feasibility of different assembly scenarios but it cannot describe fully the molecular details which can only be addressed in theories with molecular resolution. Furthermore, once the symmetry and packing geometry are established, a continuum elasticity theory can address the mechanical properties of viral shells, the nature and distribution of capsid protein packing defects, as well as the effects of external mechanical loads and the induced deformations and instabilities. In the following, we review several types of nanomechanical experiments and the new perspectives they have opened in physical virology.

3. Nanomechanical experiments

3.1. Mechanochemistry and virus function

Virus particles are composed of interacting (macro)molecules such as nucleic acids, residing in a bathing ionic solution with its own molecular composition. They therefore possess many-body properties, which are often size-dependent such as internal (osmotic) pressure due to nucleic acid confinement and ionic distribution across the capsid interface, as well as mesoscopic elastic energy of their shells. These properties are important for developing a mechanistic understanding of virus behavior, but not easy to infer directly from molecular characteristics and structure alone. Moreover, constitutive intermolecular interactions engendering collective responses are often sensitive to changes in the chemical environment, as well as thermal fluctuations ubiquitous at mesoscopic scale. Consequently, studying mechanochemical properties in detail benefits from single particle approaches able to address mechanical response in a controlled chemical environment.

The power of mechanical measurements in single virus experiments was first convincingly illustrated by the *optical tweezers approach* to studies of the double-stranded (ds) DNA packaging through tailed phages [50]. The ability to mechanically pull on the DNA being spooled by the packaging motor and quantify the forces involved has led to the discovery of the most powerful molecular motor known to date. Those experiments also revealed the sequence of regimes in the genome translocation process. *In singulo* data corroborated ensemble averaging measurements of other related mechanical variables such as the osmotic pressure that inhibits DNA ejection [51], allowed for an estimate of the internal osmotic pressure, and suggested the broad mechanistic features of the early infection whereby phages utilize this stored energy of an *osmotic coil* to initiate the injection of their genomes in the bacterium cytoplasm [52,53]. Recent models aimed at predicting the forces and pressures exerted by the genome on the capsid, which include contributions from electrostatic repulsion and bending energy [54–57] are reviewed here in Section 5. Therefore, mechanical experimental and modeling works have contributed decisively to the current mechanistic view of the Hershey and Chase experiment [58] which famously demonstrated that phages do not enter bacteria in ways similar to virus entry in eukaryotic cells (see below) [59].

The magnitude of internal osmotic pressures resulting from DNA packaging raised the question of how a procapsid, which is spontaneously pre-assembled by weak interactions, could withstand such stresses. In the majority of cases, the answer is maturation, *i.e.* a series of irreversible processes responsible for, among other things, significant changes in the mechanical properties of the virus shell [60–62]. Specifically, some bacteriophages such as HK97 and P22 pre-stress their shells [63,64]. That this is the case has become known from nanoindentation experiments by atomic force microscopy (AFM). Pre-stress has been long utilized by engineers to increase the stiffness of built structures, from bicycle wheels to bridges. The relatively recent realization that pre-stress is present in virus shells as well, illustrates the point that a complete description of biological function in viruses would benefit from including a many-body perspective in addition to the more wide-spread, molecular one. The elastic theory of continuous media (see Section 4) provides such a perspective. However, since most biological materials are viscoelastic, *i.e.*, have a time-dependent strain–stress relationship, there is the question of the validity domain of an elastic description of viruses and virus shells. Moreover, due to the discrete nature and small size, in a biological setting stochastic fluctuations could be the dominant mechanism by which viruses advance along the pathways of their life cycle, with the values of ensemble average properties occupying a secondary role. A reverberation of this is that the inherent structural fluctuations computed for several types of viral capsids are predisposed to assist or favour functionally-oriented conformational changes [65,66]. These current uncertainties are setting the stage for further research approaches.

Tailed bacteriophages are far from being the only viruses for which mechanical properties vary significantly between different life stages. A case in point is the human immunodeficiency virus (HIV), which assembles at the plasma membrane of a cell into an immature non-infectious particle and, during budding and separating from the host cell, undergoes a global structural and compositional transformation, and becomes an infectious particle [67]. Mature and immature HIV particles have very different stiffnesses (stress/strain ratio) [68]. These differences have been connected to the ability of HIV to translocate across the plasma membrane at entry [69]. There is therefore indication for instances in which, non-local, mechanical properties regulate crucial processes in virus infection.

In other cases, the link between mechanical properties and biological function is more convoluted. For the human adenovirus, subtle local chemical transformations within the structural part of the capsid can produce significant changes in its mechanical properties. Thus, Van Rosmalen et al. have shown that a single-point mutation in one of the minor cement proteins doubles the human adenovirus capsid mechanical strength [70]. Notably, this mutation did not affect the cement protein's ability to fulfill its multiple roles along the virus life-cycle; the mutant was still infectious and a correlation between virus mechanics and infectivity has not been established in this case. However, it is clear that individual, small perturbations may reinforce each other — a collective response characteristic, and what appears to be a tolerably small local chemical perturbation by single protein standards, may result in a significant change of the macroscopic, mechanical properties.

We infer from these examples that virus shell mechanics is a sensitive function of capsid chemistry, which is expected considering the capsids ability to respond strongly to a variety of chemical cues for performing various functions. As a result, being able to characterize virus mechanochemistry and understanding its biological role, and its determinants, could potentially lead to novel biomimetic delivery vectors and new classes of antivirals.

3.2. Contact mechanics

Contact mechanics designates the balancing act between external adhesive forces resulting from interfacial interactions with cellular organelles and the elastic restoring force within the virus shell. An instance where mechanical compliance to external stresses is likely to take a central role is, for example, when the resulting strain may be a factor promoting switching between states [71]. A detailed mechanistic view of the large-scale virus transformations triggered by mechanical contact may lead to previously unexplored pathways toward delivery vectors that emulate virus characteristics honed by evolution. However, so far, it is not clear for instance whether such a viromimetic carrier should be *elastic* – soft or stiff – for efficient entry, or if it should be *plastic*.

It is instructive to follow a generic virus' pathway from the extracellular space to the replication site and determine the stages where such strains are likely to occur. The first physical barrier that viruses must overcome to gain entry into a host cell is the plasma membrane. The most frequent entry mechanism is by *endocytosis* — a set of processes whereby a membrane invagination closes around a virus, which is followed by engulfment of the virus-carrying vesicle into the intracellular space [72].

Endocytosis is often receptor mediated, *i.e.* ligands immobilized on the virus surface bind selectively and multivalently to cellular receptors at the plasma membrane such as sialic acids, integrins, or cell adhesion molecules from the immunoglobulin family, see Fig. 10. This ensures specificity of host targeting as well as other benefits (evading immune surveillance, directed transport) [72]. The current view is that a particle initially binds to a patch of bound receptors, thus anchoring the particle to the membrane. At this point, a signaling pathway may be triggered to enroll cellular processes such as *clathrin and caveolin scaffolding* which will assist with the progress of inclusion. Enrolling the cellular machinery is helpful because the work required to create a membrane vesicle is similar to $\sim 300\ k_BT$ [73] whereas the ligands may be expressed sparsely on the virus surface, with ligand–receptor binding providing less than $\sim 10\ k_BT$ per bond. How much of the membrane deformation energy is provided by multivalent ligand–receptor interactions and how much of the curvature is ensured by clathrin (or caveolin) is currently unclear. While the clathrin triskelion is believed to possess an

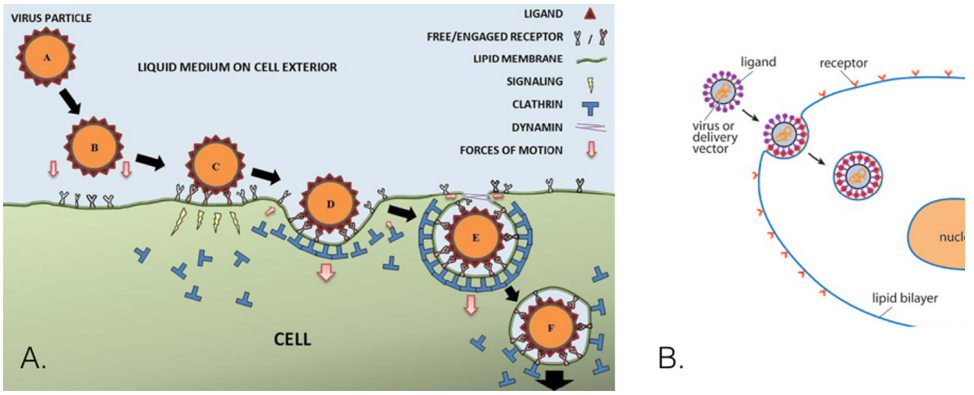

Fig. 10. Receptor-mediated endocytosis. A. Stages of clathrin-assisted pathway in which membrane curvature is assisted by clathrin assembly. (from Ref. [72]). B. Clathrin/caveolin-independent pathway in which membrane curvature is driven by receptor–ligand binding (from Ref. [75]).

intrinsic curvature [74], see discussion in Eqs. (40) and (147), that curvature cannot match that of all viruses which enter by endocytosis. Thus, it is reasonable to expect the existence of external stress in several entry mechanisms.

A few enveloped viruses, *i.e.* viruses that have their capsids sheathed in a lipid/glycoprotein layer, enter the cell by fusing their envelope with the plasma membrane after binding multivalently to its glycosphingolipids without help from clathrin or caveolin [76]. In this case, multivalent ligand–receptor binding appears to be the main driving force for curving the cell membrane around the particle. Thus, the entire cost in elastic energy of bending the membrane is covered by the virion. It has been suggested that free receptors on the plasma membrane diffuse toward the edge of the initial binding patch where they progressively bind virus-immobilized ligands, bringing more of the membrane into contact with the particle until the entire particle is surrounded by the plasma membrane [77]. Whether viruses act as mechanically non-compliant or compliant particles during this process remains unknown. In any case, the elastic energy required to bend plasma membrane is not negligible compared to the free energy change for assembly of a simple icosahedral virus, which is of the order of $\sim$ 1000 k_BT, see discussion on mechanical properties. Currently available cryo-electron micrographs illustrating plasma membrane translocation stages for large, enveloped viruses indicate a full spectrum of possibilities: on a case by case, one could notice contact deformation, local deformation, or no observable deformation of the virus during endocytosis, Fig. 11. Note, however, that cryo-electron micrographs are snapshots frozen in time and, and as we shall see, the mechanical compliance of viruses could be stochastic and different from the properties of bulk materials over the time scales relevant to translocation [78].

In addition, receptor binding is frequently the trigger of conformational changes in the virion itself (see *e.g.* Refs. [80,81]). The same can be said about other instances of virus-membrane interaction e.g. when, in late endosomes, capsid destabilization is triggered by pH and by interactions at the endosomal interface, which facilitate genome presentation. Viruses have to cross not only plasma and intracellular membranes, but also narrow conduits between plant cells called plasmodesmata, Fig. 12, and the nuclear pore complex as, for instance, in the case of the adeno-associated virus, which usurps cellular transport pathways through the nuclear pore complex [82,83].

While it is not clear whether mechanical compliance at contact is part of a general entry strategy, models suggest that kinetics of entry should be different between the compliant and non-compliant particle scenarios [84]. It is therefore of interest to inquire to what degree mechanical compliance is one of the evolutionary optimized virus features. However, measuring deformation, especially for small viruses ($\lesssim$ 100 nm), during translocation remains a considerable challenge. For instance, a uniaxial compression of only 2 nm of a typical icosahedral $T = 3$ virus such as CCMV, would correspond to a change in the free energy of about 14.5 kcal/mol an effective elastic constant of 0.22 N/m was assumed [85]. This small deformation is challenging to measure with current methods if/when it happens, especially in a cell. Yet, the elastic energy associated with it is several times higher than the pair-wise shell protein association energies of 3–8 kcal/mol [86]. Thus, with multivalent virus-membrane interactions at entry and elastic energy required to bend the membrane of the order of 100 kcal/mol, it seems reasonable to hypothesize that viruses undergo strain during translocation. Despite the challenge in measuring its magnitude and effects *in vivo*, the *in vitro* studies mainly by atomic force microscopy (AFM) have suggested several productive ways to explore the mechanochemical processes occurring during virus binding to a surface. We review few examples in the following.

3.3. Atomic force microscopy and force spectroscopy approaches to virus mechanochemistry

As alluded to before, tackling problems in the virus contact mechanics category has the added challenge that macroscopic, ensemble averaged properties are likely to loose some of their relevance at nanoscale and over the finite time scales associated with virus translocation (ms to tens of seconds). Specifically, in discussing the mechanics of

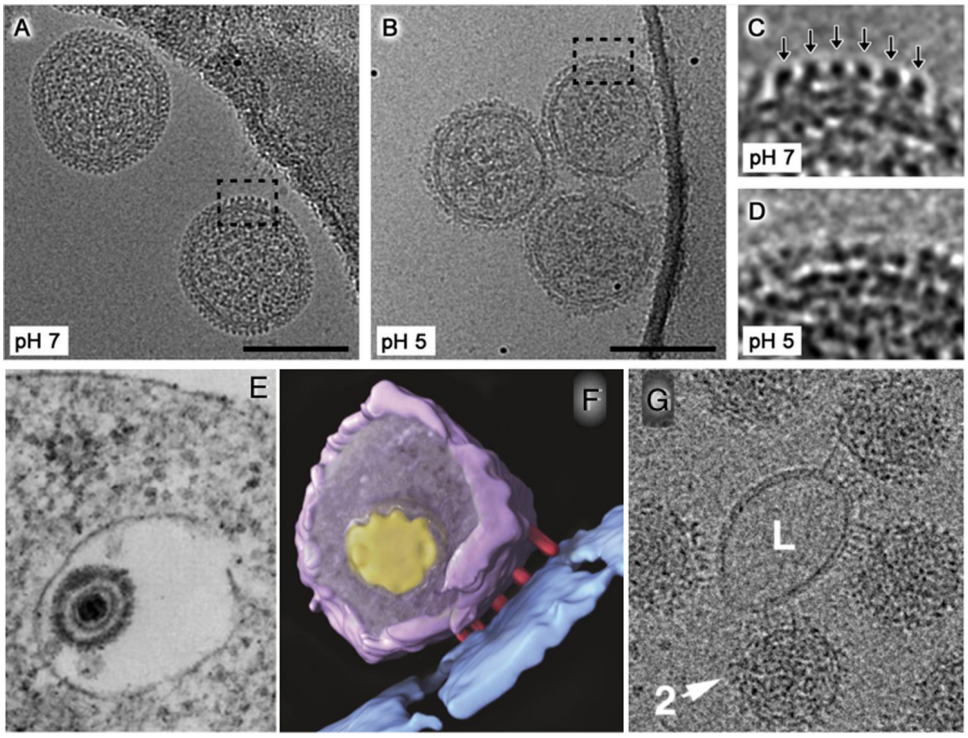

Fig. 11. Different types of morphological changes occur in a few enveloped viruses interacting with the plasma membrane. (A and B) Representative cryo-electron micrographs of the pH-dependent fusion of the Tula virus. Scale bar, 100 nm. (C and D) Close-ups of the areas indicated in panels A and B with the regular lattice of envelope glycoprotein spikes indicated with arrows in panel C. No regular lattice is visible in the virions incubated at pH 5 (A-D from Ref. [79]). (E) Herpes simplex virus undergoing receptor-mediated endocytosis (from Ref. [72]). (F) Cryo-electron tomographic image of a human immunodeficiency virus type I bound at the plasma membrane. (G) Sindbis virus bound to a liposome mimic of the plasma membrane (from Ref. [80]).

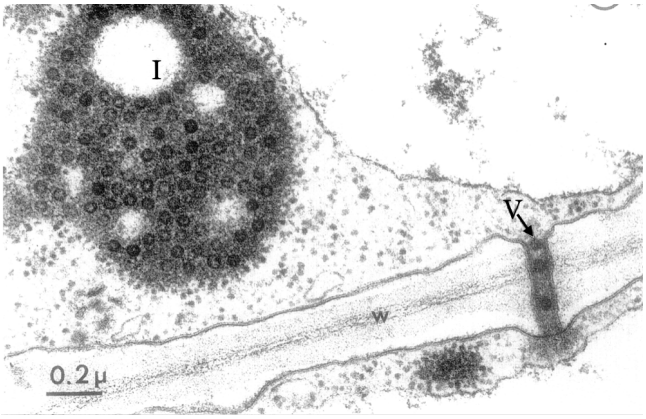

Fig. 12. Transmission electron micrograph of a section through a leaf cell infected with the dahlia mosaic virus (∼ 35 nm dark disks) showing a linear arrangement of virions squeezing through a plasmodesma to reach an uninfected cell. The large electron dense mass (I) is a cytoplasmic inclusion containing numerous virions. V: virion; w: cell wall.
Source: From Ref. [82].

an elastic body one assumes that deformation is reversible. In reality, this is possible only if the deformation occurs with infinitesimal speed so that thermodynamic equilibrium can be assumed at every instant [87], see also Section 4. When internal relaxation processes are present and occur at various speeds, the mechanical response to stress becomes time-dependent. In particular, virus mechanical transformations are expected to be accompanied by dissipative, solvent viscosity effects. Moreover, it was found that relaxation times in proteins are not simply proportional to solvent viscosity,

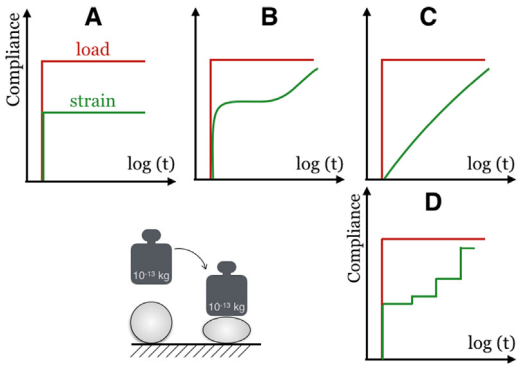

Fig. 13. A–C: Different types of time-dependence in the mechanical behavior of materials as revealed by creep experiments: A. elastic; B. viscoelastic; C. liquid; D. typical response of a non-enveloped icosahedral virus particle in the same type of experiment.

as one may expect if the solvent were the only source of friction [88]. Based upon these observations we would expect a time dependence in the mechanical response of viruses. When can we ignore it and when should we not?

Fig. 13A–C illustrates different types of time-dependent behavior observed by loading the material and recording the magnitude of deformation in time. Such a time-course measurement of the ratio between strain and stress, or compliance, is called a creep experiment [89]. In which of the material categories of Fig. 13A–C does a single virus fit? Recent AFM-assisted creep experiments by Hernando-Pérez et al. suggest that the mechanical response under compression of individual small icosahedral viruses *does not fit*, in general, in any of the categories listed for bulk materials [90], Fig. 13D. Averaging the response in Fig. 13D among many virus particles may lead to something similar to the viscoelastic material in Fig. 13B (or to the elastic material in Fig. 13A, if the experimental time scale is sufficiently short), but such average responses may not necessarily describe the dynamic behavior of a single virus under stress, and thus the relevant virus–host biomechanics.

There is already a wealth of experimental results available documenting the mechanical behavior of viruses. Its main body consists of atomic force microscopy nanoindentation experiments [91–94]. These have been complemented by a variety of computational work, with approaches ranging from continuum elastic and viscoelastic models to all-atom simulations [65,95–102], which are described in Section 4. It is useful here to give a brief description of the generic AFM nanoindentation experiment, as it represents a basis for further comparisons with other types of approaches that will be discussed here.

AFM is a surface scanning imaging technique capable of operating at physiological conditions (liquid, room temperature) with nanometer spatial resolution [103]. During AFM imaging, a sharp probe (tip) is brought close to the sample surface, down to the point where repulsive probe–surface interactions start to generate a response in a nanomechanical strain sensor. The probe–sample distance is maintained constant (usually $\sim$ 1–10 nm) by feeding the response of the strain-sensing element into a piezo actuator that regulates the probe position relative to the sample. Raster-scanning the probe while recording piezoactuator motion normal to the surface generates a topographic image of the sample. The rapid decay of intermolecular forces with distance is responsible for the very high spatial resolution in the direction of the applied force. Typical force sensitivity in liquid is a few tens of pN [103].

In recent years, faster speeds, overall miniaturization of the optomechanical assembly and probes, as well as advanced probe/sample modeling have increased the appeal of AFM probing of a variety of biological materials, ranging from tissues to viruses [104–106]. In terms of imaging, AFM has several distinct advantages in the study of biological samples: First, it is a true *in singulo* method. Averaging of the type used in cryo-electron microscopy (cryo-EM) is not required in order to reach usable signal-to-noise ratio, making this methodology in particular useful in the studies of pleiomorphic viruses or viruses that are asymmetric. A case in point is the investigation of the giant mimivirus in which AFM [107] was used in conjunction with serial degradation by lysozyme and bromelain [108]. This 750 nm diameter virus would have been too large to embed in a thin layer of vitreous ice, as required for high resolution cryo-em. Second, AFM allows real-time observations of phenomena with spatial resolution nearing single oligomeric complexes in response to chemical or physical stimuli, provided dynamics are slower than $\sim$ 1 min. Examples of unique capabilities in this sense include the visualization of the shedding of specific capsomers during disassembly [107], and of the time course healing of packing defects in a virus shell [109].

Because AFM relies on force detection, it represents a natural choice for mechanical measurements. The most widespread approach so far in the study of virus mechanics is nanoindentation [91,110], whereby, after having identified the location of a virus immobilized on the substrate, the probe is brought above the center of the virus. The probe then descends on the virus until a prescribed maximum force is attained, after which the tip is retracted. At each step on the tip–surface approach trajectory, the force on the AFM cantilever, which serves as the strain sensor, and the piezoactuator displacement are recorded. Since the elastic constant of the cantilever is known or easy to find, virus indentation can be inferred at each step, Fig. 14.

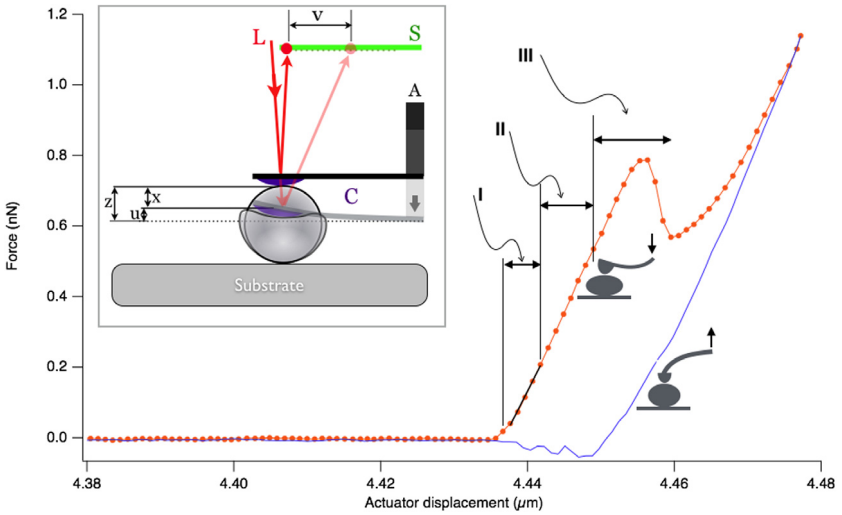

Fig. 14. Inset: Cartoon of an AFM nanoindentation experiment; A = actuator, C = cantilevered probe, L = laser, z = vertical actuator displacement and x = actual indentation. A typical force–displacement curve from a single BMV particle adsorbed on graphite in liquid [90]. The red curve corresponds to compression and the purple one to retraction. The black vertical lines represent approximate limits of the different mechanical regimes (values from the coarse-grained simulations of the corresponding virus, by Krishnamani et al. [111]).

Fig. 14 presents a typical force–displacement dependence obtained from a single BMV particle adsorbed on mica, in low ionic strength buffer at pH 5, where this virus particle is most stable. At the first sight, there is qualitative resemblance between curves calculated using nonlinear continuum elasticity finite element approaches [112] but also, and perhaps in greater measure, with homogeneous uniaxial compression stress–strain curves computed for viscoplastic polymer shells [113]. Multi-scale coarse-grained modeling of CCMV capsids, aimed at capturing response to a broad stress range, identified three mechanical regimes along the compression curve [111]. These regimes are approximately depicted in Fig. 14: Starting at low stress, the first regime corresponds to an elastic response. The second regime is transitional, where localized plastic events occur in the molecular network but the shell maintains long-range connectivity and thus the ability to partially recover after compression. The third regime corresponds to extended plastic events leading to global failure. In this regime, the particle abruptly yields to compression and does not recover.

Phenomenological parameters such as the effective elastic constant (regime I) and the yield force can be thus obtained, which enables comparisons of global mechanical properties for different virus states. A lot of information can be extracted by studying the effects on the capsid elasticity and strength [114,115] of coat protein mutations, of the nucleic acid–protein interactions [116,117], of chemical cues [118,119], of maturation [69,120] and of comparisons of wild-type virions and empty viral capsids [114],

At "low" stress, the response is linear (see Section 4.5.4 about how elasticity theory gives the shape of deformations as a function of stress). What exactly is "low" depends on the species, the time it takes to do the experiment, and the chemical environment: For CCMV at low pH, according to the computational analysis of Krishnamani et al. the elastic region ends before compressing the particle via purely repulsive walls by $\lesssim 3$ nm ($\sim$ 10% of the diameter). This is significantly less than the apparent linear portion of the representative force–displacement curve in Fig. 14, where the linear regime extends up to $\sim$ 20% of the diameter. In Section 4.5.4 we describe the nuances in applying linear elasticity to the experiments, but a question remains whether viruses belong to a broader class of materials that exhibit an apparent linear stress–strain relationship, and yet undergo microscopic plastic events. This type of behavior has been observed in soft materials with nanoscale heterogeneity. Thus, in amorphous polymeric glasses, local plastic events at extremely small strains have been observed well below the yielding point, in a regime where deformation is traditionally described as elastic [121]. Such materials are characterized by significant dynamic heterogeneity, *i.e.* the temporal dynamic range of fluctuations is broad, extending several orders of magnitude the molecular relaxation time, a feature that might be reasonably expected from proteinaceous shells, as well. In support of the idea that such stochastic plastic local events may occur in viruses, even at very small stresses, we note the "fatigue" experiments carried out on different viruses by repeatedly compressing the virus at peak forces of only $\sim$ 100 pN [107,122]. The fatigue treatment results in a time-dependent stress–strain relationship and ultimately, to irreversible transformations [93], and even disassembly [123]. It follows that a virus kept under mechanical stress an extended period of time may show changes in its mechanical properties. Since typical loading rates in AFM nanoindentation, *i.e.*, the velocity by which the piezoactuator approaches the prescribed compression force, are of the order of 0.1–10 μm/s [124], the time it takes for probing the virus in AFM nanoindentation is $\approx$ 0.3–30 ms. As these times are likely shorter than the duration of stresses associated with translocation processes in cells, Hernando-Pérez et al. carried out a single virus creep experiment in which they could observe the mechanical response to a constant

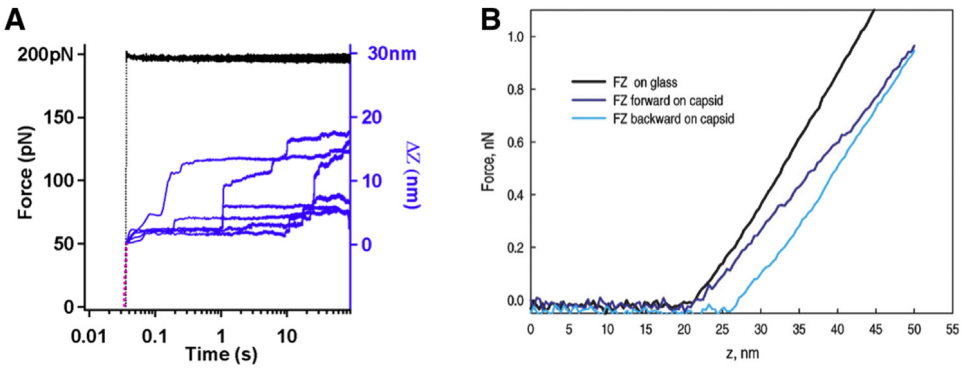

Fig. 15. A. Creep experiments on empty BMV capsids. Load: 200 pN. ΔZ is the change in probe position normal to the surface required to maintain the load constant. Black: force loading vs time. Pink: the initial, rapid loading period (from Ref. [90]). B. Conventional ramp-loading experiment done on a similar capsid (from CCMV) showing the force required to push the AFM probe contacting the particle a certain vertical distance (z). Despite the apparent linearity of the force–displacement, there is hysteresis indicative of a non-equilibrium process (from Ref. [85]).

load over extended times, up to a few tens of seconds, and compared the behavior of empty BMV capsids with that of wild-type BMV particles, Fig. 15 [90].

Both samples showed creep manifesting as a time-course sequence of discrete drops in particle height. An analysis of these drops (steps) led to the following main findings:

- Intermittency of deformation was observed in both types of particles (with and without the RNA). Therefore intermittency is a feature of the capsid, and likely due to the discrete nature of its structural subunits.
- Creep was not observed in wild-type virions at any point for loading forces below 250 ± 50 pN. However, no such load threshold was observed for empty capsids. If it exists, it was below the detection limit. The difference between RNA-loaded and empty BMV capsids highlights the possible involvement of the nucleic acid cargo in shaping the assembly interface. Interestingly, on the same lines, Michel et al. have found that empty capsids present visible hysteresis at nanoindentation while wild-type virions do not, Fig. 15B, [85].
- The onset of creep is marked by a discrete event, manifested by a $\sim$ 2.5 nm step, presumably by the creation of a certain type of virus shell lattice defect.

Such transitions from elastic to plastic deformation are not captured by the conventional linear *continuous* description, and require considerations of irreversibility, with the inclusion of topological defects such as dislocations, described in detail in Section 4. Based upon qualitative similarities between the statistics of steps in the virus creep experiments [90] and those previously observed on microscopic crystals [125] and in simulations of deformation of curved colloidal crystal shells [126], a hypothetical model was constructed for the virus creep experiments. The idea is that stress–strain curves exhibit abrupt jumps as a result of dislocation activity [127]. Nucleation of dislocations can happen even at small loads. in this scenario, the interactions between intrinsic disclinations (pentamers) and the newly created dislocations may hold a role in defect dynamics. However, determining whether this is the case will require further research.

It is worth noting that the elastic properties of virus shells could in principle be obtained from inelastic (Brillouin) light scattering. This would have the advantage of very small amplitudes of deformation (and true reversibility). However, attempts at identifying localized virus particle modes in the Brillouin spectra from microcrystals of the satellite tobacco mosaic virus have not been successful [128]. A more recent effort on the lines of elastic properties measurements via vibrational spectroscopy suggested that it may be possible to achieve resonant dipolar coupling of microwaves with confined acoustic vibrations in a rod-shaped virus [129].

3.3.1. Contact mechanics of icosahedral viruses on a rigid surface

The role of intrinsic defects (pentamers) in the mechanics of deformation may extend beyond the above dynamic effects, see Section 4. Thus, Zeng et al. have determined that, on both mica and highly-oriented pyrolitic graphite (HOPG) surfaces, BMV particles will adsorb preferentially with a three-fold axis down, Fig. 16 [130]. As the two surfaces have distinct chemical properties (one is polar, the other one non-polar), the authors surmised that the bias in orientation could be the result of a physical property, potentially the difference in local compliance between pentamers and hexamers. A potential explanation comes from the elasticity theory, which predicts that the larger the Foppl–von Kármán (FvK) number (see Section 4.4.4), the greater the stiffness measured along a five-fold symmetry axis (on a pentamer) with respect to that measured along a three-fold symmetry axis (on hexamers) [131,132]. The estimated FvK number for CCMV, which is very similar with BMV, is 900. This value is believed to be high enough to observe stiffening around pentamers [131]. Thus, upon adsorption, the soft areas (hexamers) comply with the flat surface to maximize adhesion and the virus sits on a tripod formed by stiff pentameric vertices. Orientation bias at adsorption was also observed in P22 bacteriophage capsids on chemically-modified glass surfaces, although in that case its origin is believed to have a chemical nature [133].

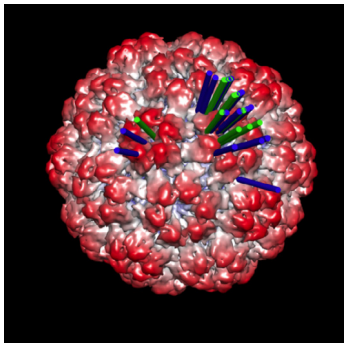

Fig. 16. BMV model with distribution of observed directions normal to the substrate surface relative to the virus, at adsorption. Data from high resolution AFM maps. The colored lines mapped onto the model are the normals to the substrate. Each normal line corresponds to a particle. (HOPG substrate: green; mica substrate: blue). The lines bunch around the 3-fold symmetry axis of the shell.
Source: From Ref [130].

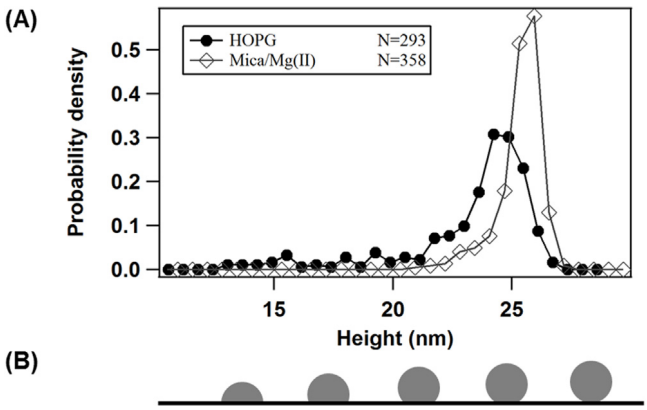

Fig. 17. A. Height histograms of BMV particles adsorbed on mica and HOPG, in liquid. B. Pictorial explanation of the observed height distribution.

Surface bias of virus orientation at adsorption helps to create a more homogeneous virus population when mechanically probing the balancing act between adhesion upon contact, which tends to increase contact area, and the elastic deformation of a shell, which resists it, as it involves a significant cost (see Eq. (142) and the discussion thereafter.) Shape transformations result of contact mechanics have been studied extensively in relation with the adhesion of vesicles [134]. Much less is known about shape transformations of polyhedral protein shells. Specifically, little is known about how the balance between potential pre-stresses, cohesive forces, and adhesive forces is attained. The likely reason for this is the general assumption that strain from adhesive forces is negligible. At the first sight, this is a reasonable perspective: viruses are smaller, with shells that are less fluid, and somewhat thicker than the membranes of lipid vesicles. We have seen, however, that even small strains are likely to trigger defect-mediated plastic events. Could it be that despite initial stiffness, deformation could occur slowly in time, through a cascade of microscopic plastic events?

To determine whether non-specific virus adsorption to a non-compliant substrate can be detected in the form of a virus shape transformation, Zeng et al. have examined the height of BMV particles adsorbed from solution on atomically-flat surfaces (mica and highly-oriented pyrolitic graphite (HOPG)) [130]. In the case of a dominating orientation, a narrow distribution of maximum heights was expected. However, measurement of maximum virus particle heights on HOPG and mica showed height histograms peaking at values 3–4 nm below the nominal 28.4 nm for BMV, on both substrates. In addition, the height histograms were asymmetric, with the more extended tail containing the lower heights. Height distribution peak position and peak width depended on the substrate, which suggested a chemical effect that could not come from anything but adhesion, Fig. 17. Thus, the effect of adhesion forces on the shape of a surface-adsorbed virus can be observed in the height histograms.

The exact shape of the surface-distorted polyhedral protein cage is unknown, at this point, although the main ingredients for such calculation are discussed in Section 4.4. A simplified analysis based on the Helfrich model [135], that is, the extrinsic curvature in Eq. (36) only, without elastic terms has been attempted [130]. This heuristic model provides an estimate for the interfacial energy of adhesion ($\sim 0.1\ k_BT/nm^2$), and the radius of the contact area (~ 5 nm). From these estimates, the excess elastic energy resulting from adhesion is $\approx 30\ k_BT$.

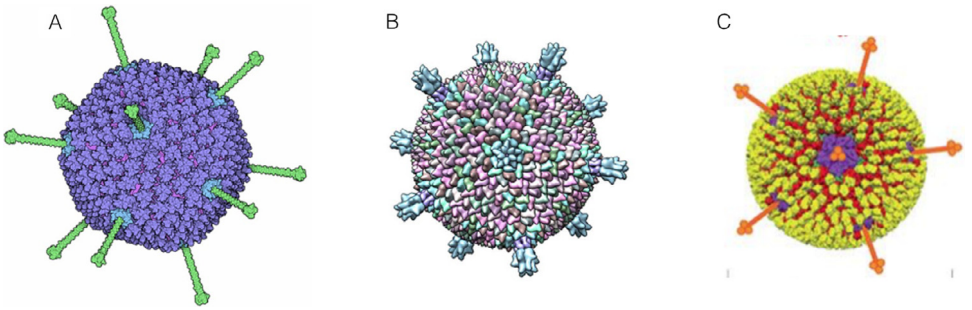

Fig. 18. Examples of viruses expressing ligands for cellular targeting at the icosahedral vertices: A. Adenovirus [137]; B. Sulfolobus turreted icosahedral virus I [136]; C. Mammalian orthoreovirus [138].

Returning to the question of whether the threshold of plasticity might be already reached at non-specific adsorption, we note that the estimate for the excess elastic energy from adhesion is safely below that of the elastic energy corresponding to the maximum indentation allowable in the elastic regime($\approx 200\ k_BT$), estimated by Krishnamani et al. for CCMV [111]. However, one should keep in mind that this conclusion might switch if: (a) the balance between cohesive and adhesive forces changes, and (b) if a more realistic model were adopted. Unfortunately, up to now we know of no molecular dynamics or multi-scale coarse-grained simulation approaches that have tackled the problem of contact mechanics for viruses.

In regard to the difference in mechanical compliance between hexamers and pentamers it is interesting to note that the virions of the Sulfolobus turreted icosahedral virus 1 [136], the adenovirus [137], and the orthoreovirus [138], and a few others, all express their ligands for cell surface receptor binding, solely at the icosahedron vertices (5-fold symmetry axes), Fig. 18. Is this a coincidence, or is the specific stiffness/flexibility afforded by this particular location somehow advantageous for binding [139]?

We conclude this subsection with a note on the difference between stiffness and thermodynamic stability as sometimes one is considered a proxy for the other. This may be acceptable in some cases (when stiffness is the result of increased bonding) but incorrect in others. For instance, the *Salmonella typhimurium* bacteriophage P22 assembles into a $T = 7$ empty pro-capsid first. Viral DNA is subsequently packaged using a motor. Maturation is triggered by DNA packaging so that the mature capsid becomes capable to resist the increased internal pressure as discussed. The maturation transformation from procapsid to mature capsid can be recapitulated *in vitro*, by gentle heating (65 °C for 10 min). However, extended heating (75 °C, 20 min) induces selective release of subunits from the 5-fold icosahedral vertices (pentons) to produce another capsid form, which has a 10 nm hole at each of the 12 5-fold vertices (Fig. 19A), [19,140]. Therefore, the sites of maximum stiffness resulting from stress imposed by the curvature are also the sites of higher chemical potential (minimum thermodynamic stability).

An intriguing case is that of the immature capsid of the human immunodeficiency virus type 1 (HIV 1), Fig. 19B–C. HIV 1 assembles its shell at the plasma membrane from a poly-protein called Gag. The shell packages nucleic acid (RNA) and other cargo proteins and buds in an enveloped form into the extracellular space [141], where the virus matures to an infectious form by proteolytic cleavage and reassembly of the Gag domains and RNA. The HIV 1 immature particle has a rather unique organization: its shell shows extended regions of hexagonal symmetry, separated by voids (multiply-connected vacancies) and/or possibly, disordered areas of lower density [142,143].

One also distinguishes a larger gap, usually facing the cytoplasm [144], Fig. 19B. However, other smaller voids seem to have been incorporated earlier during assembly, Fig. 19C. Although there are fluctuations in size and position, from the hexagonal tiling directions one finds that the smaller voids are roughly placed at locations where pentameric disclinations would be expected in a complete, icosahedral particle. Is the incompleteness of the HIV 1 immature shell a result of the segregation of defects to intrinsic disclination sites as the shell grows?

The large gap on the cytoplasmic side has been explained as a result of the scission before shell completion by the endosomal sorting complexes required for transport (ESCRT) machinery of the cell [141]. This hypothesis is supported by the observation that, when the scission is inhibited, no large gap is observed. A complementary hypothesis based upon the intrinsic curvature of Gag is that an elastic strain barrier develops against membrane diffusion of Gag towards the growing shell, since the neck that forms between the plasma membrane and the bud has negative curvature, while Gag is assumed to have positive curvature [145]. The latter hypothesis can explain why the assembly slows down after a fraction of the Gag shell has been assembled, thus clarifying why the large gap area is not completely random (it fluctuates about an average of 30% of the particle area). Nevertheless, while hypotheses based on ESCRT assisted scission and intrinsic curvature effects explain the location and size of the large gap, they do not explain the presence of the small vacancies in areas opposite to the cytoplasmic side gap, which assemble early. These minor gaps and the conspicuous absence of isolated pentagonal disclinations are more likely to be the result of how crystallization happens on a sphere. Thus, in colloids, the phenomenon occurs by the formation of a single crystalline domain, which forces mobile defects, such

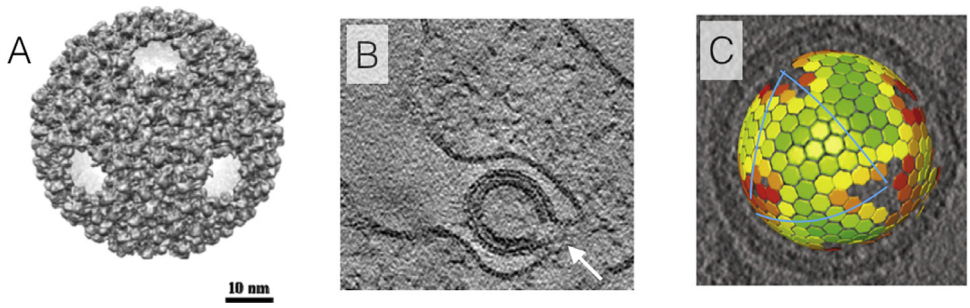

Fig. 19. A. The P22 capsid looses its pentameric capsomers (pentons) after exposure to high temperature [19]. B. A slice through a cryo-electron tomogram showing HIV 1 budding at the plasma membrane (from Ref. [144]). The arrow points to a large gap in the virion shell, facing the cytoplasmic space. C. Gag protein tiling in an immature HIV particle superimposed onto a section through the tomographic reconstruction of the corresponding virus (from Ref. [143]). Hexagons represent Gag hexamers (cross-sections at a fixed radius close to the particle surface) and the colors encode for the confidence level for each subunit location and orientation (green: high). Here, the large void pointing towards the cytoplasm is on the far side of the particle with respect to the viewer. Only the smaller voids, which presumably have been incorporated early on during assembly are visible. The blue lines are a guide to the eye; they are parallel to hexamer rows which at angles corresponding to an icosahedral tiling of the sphere.

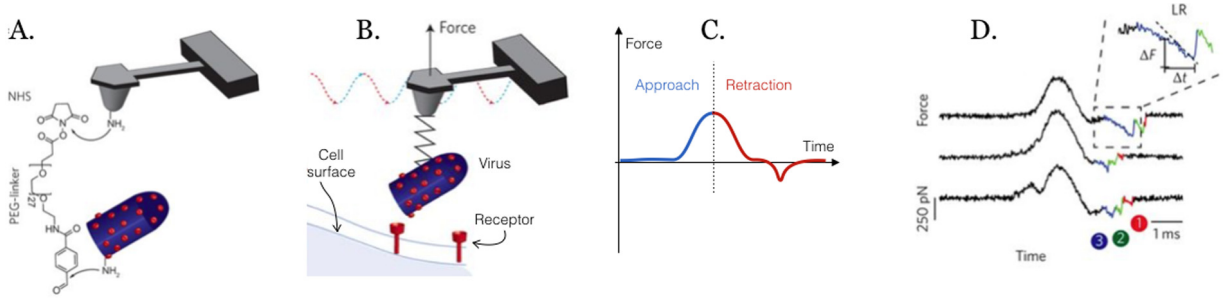

Fig. 20. Single-virus nanomechanical probing of initial stages of virus entry. A. A virion is covalently attached to the tip by a single, long, flexible linker. B. The virion is allowed to probe the cell surface intermittently. Occasionally, glycoproteins on the virus shell (red dots) encounter cellular receptors (red cup-shaped features) and bind to them. C. The approach and retraction curve is acquired at each pixel. Negative forces correspond to adhesion, positive to repulsion. D. Representative experimental force–time curves. Multiple rupture events, colored in blue, green and red indicate simultaneous interactions between the virus and cell surface.
Source: Adapted from Refs. [150,151].

as dislocations into 12 and v, acancisiesolated areas at locations roughly distributed the same as the disclinations of icosahedral packings [146,147].

The above examples illustrate how ideas originating in multibody mechanics can inform virus behavior in different instances of virus–host interactions. A final example of nanomechanics explorations aimed at deciphering cellular entry is described in the following.

3.3.2. Nanomechanical probing of receptor-mediated virus-cell membrane interactions

As introduced above, viruses often initiate adhesive interactions with the surface of a cell via specific, sequential, cooperative multivalent binding of virus surface glycoproteins to cell receptors [148–150]. The event may trigger then one of the several possible cellular signaling pathways for virus entry. To unveil the sequence of events leading to host cell recognition and entry, a different type of AFM experiment than the ones discussed above has been performed. In these nanomechanical experiments, the virus is attached to the tip via a long, flexible linker, Fig. 20A. and intermittently placed on the cell membrane while slowly scanning over the cell surface, Fig. 20B. Retraction force–displacement curves are collected at each step. When cognate receptors are present on the cell surface, retraction curves display sudden jumps corresponding to individual molecular unbinding events, Fig. 20C. For each unbinding event, the loading rate (LR) is determined using the slope on the force–time curve, for the duration corresponding to the adhesion event, Fig. 20D.

Reaction rate models [152–154] are then used to quantitatively interpret the force vs loading rate data, in both the limiting kinetic and equilibrium regimes [150]. Extracting absolute rates and dissociation constants allowed the formulation of new mechanistic hypotheses for virus entry. For instance, the surprisingly weak binding affinity in the millimolar range could be reconciled with the high entry efficiency if one assumes multivalent binding is a frequent event. Multiple, weak bonds is a strategy that ensures selectivity in many examples of biological association processes. Multivalency of receptor binding prior entry is supported by direct experimental observations [150].

In concluding this section, we note that nanomechanical experiments deliver a broad spectrum of data, some of which have set virus processes in a new light. Methods able to bridge intracellular and *in vitro* work have yet to be developed. Having access to dynamics is of essence as fluctuations over the biological time scales are important. Theories that capture correctly the spectrum of fluctuations need to be developed. The new perspectives have to be communicated in accessible form to and further pervade the broader biological community.

Experiments such as those discussed above reveal the fundamental necessity of developing a thorough theoretical understanding of the mechanical properties of viral shells. This is a challenging task, as the theory of elasticity needs to be extended to curved spaces to include the presence of defects (disclinations), with a subtle interplay of topology and geometry. There has been a remarkable progress in this area, with important results whose relevance goes beyond the physics of viruses, as we will discuss in detail in the next section.

4. Mechanics of virus shells

The simplicity of virus structures with icosahedral symmetry classified by the T numbers, see Eq. (1) and Figs. 3 and 4, reflects a fundamental connection between the elasticity theory [87] and the theory of defects [155,156] built upon topology and differential geometry [157]. In this section, we review the basic concepts to make these connections explicit. The theory provides selection rules that explain some of the characteristics of virus structure. The theoretical framework presented extends far beyond viruses and allows an understanding of many other effects that are observed in related systems.

It is therefore the purpose of this section to provide a review of the theory of elasticity including examples that go beyond viruses, with the purpose of inspiring new approaches and developments that may, eventually, find their way into the field. Furthermore, a review of these systems shows many relations that reflect *universal* properties of elastic shells.

The structures of isometric virus shells are examples of geometric frustration [158]. They illustrate a situation in which the geometry prevents a system from attaining the ground state consistent with the intrinsic order (2d crystalline). This reflects in the presence of defects and stress buildup, which distributes non-uniformly across the capsid [159] upon assembly. This stress may lead to successful assembly [160] and in the global and local mechanical compliance of the virus shell. In turn, the latter is likely to be a critical factor in various required interactions between the virus shell and cellular organelles (e.g. plasma and endosomal membranes, pores). Furthermore, interpretations of the rich data from uniaxial virus compression experiments that rely on elastic models have enjoyed widespread popularity and provide an often satisfactory phenomenological pathway towards comparing the mechanical properties of different viruses or of viruses in different states [64,91,93,161]

Therefore this section will wander beyond the scope of virus to provide a more general overview. We will also review some general results on the elasticity of planar and curved surfaces and differential geometry, as they underlay the methods necessary to understand the mechanics of virus shells.

4.1. Summary of 2D planar elasticity

The theory of elasticity studies how solids deform when subjected to external constraints. Given the focus of this review, we will start by summarizing the most important aspects in flat 2D systems. For a more detailed description we refer to the classical book by Landau and Lifshitz [87] and other more recent references [155,156]. We will consider a 2D solid consisting of M generic particles at positions $\vec{r}_i$ with $1 \leq i \leq M$. At this point, the nature of the particles is irrelevant; they may be atoms, molecules, proteins, etc. We then parameterize their (center of mass) positions as

$$\mathbf{r}_i(\mathbf{R}_i) = \mathbf{R}_i + \mathbf{u}_i(\mathbf{R}_i)\,, \tag{12}$$

where $\mathbf{R}_i$ are the coordinates of a 2D triangular lattice. The notation $\mathbf{u}_i(\mathbf{R}_i)$ serves to emphasize that the displacement u_i is different at each point. We interpret the coordinates $\mathbf{R}_i$ as defining the positions of the particles before a deformation takes place, the *reference space*, while $\mathbf{r}_i$ are the coordinates after the deformation, the *actual space*. In flat systems both reference and actual space are planes. Note that if $\mathbf{u}_i = 0$ then we assume that the actual space positions are a perfect 2D lattice, such as the triangular one shown in Fig. 21.

The strain tensor is then defined as

$$u_{lk} = \frac{1}{2}\left(\frac{\partial u_l}{\partial x_k} + \frac{\partial u_k}{\partial x_l} + \frac{\partial u_s}{\partial x_l}\frac{\partial u_s}{\partial x_k}\right), \tag{13}$$

and a finite displacement from a triangular lattice, see Fig. 21, has an energetic cost given by

$$F_T(\vec{u}) = F_T(u_{ij}) = F_0 + \int d^2\mathbf{x}\left(\frac{\lambda}{2}u_{ll}^2 + \mu u_{ij}^2\right) \equiv F_0 + F_E(u_{ij}) \tag{14}$$

where the discrete points defining the positions $\vec{R}_i$ in reference space have been approximated by a continuous integral, and we used a summation convention where all the repeated indices are summed over. Note that rigid translations and rotations do not cost any energy, and this is why the elastic energy is a function of the strain tensor only [87]. The reference energy F_0 is often ignored, but it has some physical meaning, as we will soon discuss. A fundamental and powerful property of the above elastic energy is that all the dependence on microscopic details such as the nature of the particles, interaction potentials, etc. are entirely parametrized by the λ and μ constants, known as the Lamé coefficients.

Other elastic constants that frequently appear in the literature and that will be extensively used in this review are:

$$\begin{array}{lll} B = \lambda + \mu & & \text{Bulk Modulus} \\ Y = \frac{4B\mu}{B+\mu} & = \frac{4(\mu+\lambda)\mu}{\lambda+2\mu} & \text{Young Modulus} \\ \nu = \frac{B-\mu}{B+\mu} & = \frac{\lambda}{\lambda+2\mu} & \text{Poisson ratio} \end{array}$$

see Ref. [156] for many properties of these constants.

The other fundamental quantity in elasticity theory is the stress tensor $\sigma_{ij}(\mathbf{x})$. If $\vec{n}$ (n_j $j = 1,2$) represents a unit normal vector to a surface, then

$$F_i(\mathbf{x}) = \sigma_{ij}(\mathbf{x}) n_j \tag{15}$$

represents the actual force per unit area at point $\mathbf{x}$ along the direction defined by $\vec{n}$. The stress is a function of the strain defined by

$$\sigma_{ij}(\mathbf{x}) = \left.\frac{\delta F(u_{ij})}{\delta u_{ij}(\mathbf{x})}\right|_T = \lambda u_{ll}(\mathbf{x})\delta_{ij} + 2\mu u_{ij}(\mathbf{x}) \ , \tag{16}$$

where the derivative is taken at constant temperature T. Alternatively, the strain can be considered as a function of the stress by inverting Eq. (16). The result is

$$u_{ij}(\mathbf{x}) = -\frac{\nu}{Y}\sigma_{ll}(\mathbf{x})\delta_{ij} + \frac{1+\nu}{Y}\sigma_{ij}(\mathbf{x}) \ . \tag{17}$$

It becomes clear that u_{ij} and σ_{ij} are conjugate variables in the thermodynamic sense, just like volume and pressure among many others.

The condition that the solid is at equilibrium implies a minimum of the free energy. Eq. (14) then gives

$$\delta F_E = \int d^2\mathbf{x}\sigma_{ij}\delta u_{ij} \ . \tag{18}$$

In 2D, a general symmetric tensor has three independent components. However, from Eq. (13), the $u_{\alpha\beta}$ is entirely determined by the displacement, see Eq. (12), a 2 dimensional vector, and therefore, Eq. (18) does not imply $\sigma_{\alpha\beta} = 0$ as not all variations of u_{ij} are independent.

So far, the equations presented involve no approximations. We will now consider *linear elasticity theory* and ignore the quadratic terms in the strain Eq. (13), then Eq. (18) becomes,

$$\delta F_E = \int d^2\mathbf{x}\sigma_{ij}\partial_i\delta u_j, \tag{19}$$

which, using integration by parts and divergence theorem, leads to the equation

$$\partial_i\sigma_{ij} = 0 \qquad \text{and} \quad \sigma_{ij}u_j\big|_{\partial\mathcal{B}} = 0 \ , \tag{20}$$

where $\partial\mathcal{B}$ denotes the boundary of the system. For simplicity, we will ignore boundaries for the time being, but we will discuss them further later on as they play a very important role, particularly during virus self-assembly. The elastic equation may be solved by introducing the Airy function χ (and making use of the totally antisymmetric tensor $\epsilon_{ik} = 0$ if $i = k$, $\epsilon_{12} = 1$)

$$\sigma_{ij} = \epsilon_{ik}\epsilon_{jl}\partial_k\partial_l\chi(\mathbf{r}) \ , \tag{21}$$

which automatically satisfies Eq. (20). Then Eq. (17) becomes,

$$u_{ij} = -\frac{\nu}{Y}\nabla^2\chi(\mathbf{x})\delta_{ij} + \frac{1+\nu}{Y}\epsilon_{ik}\epsilon_{jl}\partial_k\partial_l\chi(\mathbf{r}) \ . \tag{22}$$

The condition that the displacement is single valued implies that there are no "sources or sinks" of strain [155]

$$\epsilon_{ik}\epsilon_{jl}\partial_k\partial_l u_{ij} = 0 \rightarrow \nabla^2\nabla^2\chi(\mathbf{x}) = \Delta^2\chi(\mathbf{r}) = 0 \ , \tag{23}$$

must apply, which is known as the bi-harmonic equation. Using Eqs. (21) and (22) we find

$$\begin{aligned} \frac{\lambda}{2}u_{ii}^2 + \mu u_{ik}^2 &= \frac{1}{2}\sigma_{ij}u_{ij} \\ &= \frac{1}{2}\epsilon_{ik}\epsilon_{jl}\partial_k\partial_l\chi(\mathbf{r})u_{ij} \\ &= \frac{1}{2Y}(\Delta\chi)^2 + \frac{1+\nu}{2Y}\partial_i\left(\partial_i\partial_j\chi\,\partial_j\chi - \partial_i\chi\,\Delta\chi\right) \\ &= \frac{1}{2Y}(\Delta\chi)^2 + \frac{1+\nu}{2Y}\epsilon_{ik}\epsilon_{jl}\partial_i\partial_j(\partial_k\chi\,\partial_l\chi), \end{aligned} \tag{24}$$

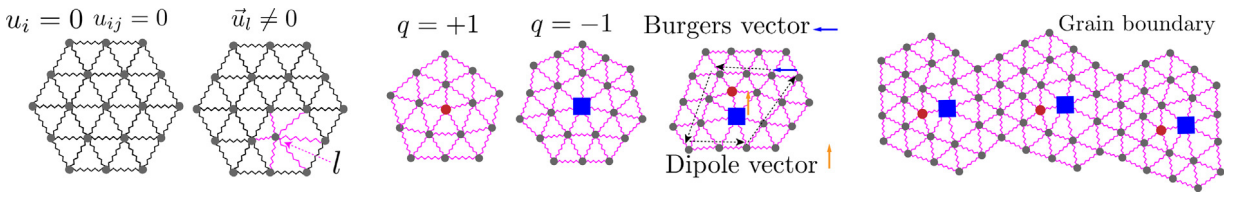

Fig. 21. The "perfect" triangular lattice. A non-zero displacement at one point in the triangular lattice ($\vec{u}_\ell \neq 0$). A pentamer ($q = +1$ disclination). A heptamer ($q = -1$ disclination). A pentamer–heptamer pair (dislocation with Burgers vector $\vec{b}$ or dipole $\vec{d}$) and a low angle grain boundary, where dislocations are clearly separated.

and the elastic energy Eq. (14) becomes

$$F_E(u_{ij}) = F_E(\chi) = \frac{1}{2Y}\int d^2\mathbf{x}(\Delta\chi)^2 + \frac{1+\nu}{2Y}\int d^2\mathbf{x}\epsilon_{ik}\epsilon_{jl}\partial_i\partial_j(\partial_k\chi\,\partial_l\chi) = \frac{1}{2Y}\int d^2\mathbf{x}(\Delta\chi)^2 + \text{boundary terms}\ . \tag{25}$$

The second term is a total derivative, and therefore only contributes if there is a boundary.

In order to apply the elasticity theory, the formalism needs to incorporate the role of defects and to be generalized to a curved actual space. Further, it is important to understand how accurate the linear approximation is and how to obtain the Lamé coefficients λ and μ from the underlying microscopic interactions. This is the purpose of the following two subsections.

4.2. Intrinsic defects and low symmetry order

A perfect triangular lattice, like the one in Fig. 21 has zero elastic energy. A non-zero displacement will certainly deform the lattice and generate some strains, but as shown in Fig. 21, each particle will still remain connected to the same nearest neighbors. Cases where the number of nearest neighbors are different than six are known as *disclinations*. The disclination charge is defined as

$$q = 6 - \text{coordination}\ . \tag{26}$$

A pentamer (coordination 5) is a $q = +1$ disclination, while a heptamer (coordination 7) is a $q = -1$ disclination. More general disclinations of charges $q = 2, 3, -2, -3$ are also relevant and appear in some situations, see Fig. 23.

The construction of a $q = +1$ disclination proceeds as described in Fig. 22. A $q = -1$ is analogous except that instead of removing a $\frac{\pi}{3}$ wedge, the disclination is built by adding an additional $\frac{\pi}{3}$ wedge to an excised edge radial from the core, the so-called *Volterra construction* [162]. A dislocation is built by adding an additional row of particles, and, as shown in Fig. 21, may be regarded as a bound disclination pair of opposite charges. A dislocation is characterized by a Burgers $\vec{b}$ vector, whose direction is perpendicular to the dipole moment $\vec{d}$, defined as the vector joining the five-seven pair. There are additional topological defects of interest [156,163] besides disclinations and dislocations, such as vacancies, interstitials, etc. [155], but they will not be further elaborated in this review.

The equation defining the Airy-function Eq. (21) is not modified by the presence of defects and Eq. (22) also remains the same. However, the displacements are singular at the disclination cores. The bond angle θ, see Fig. 22, which measures the orientation of a given bond between two particles, has the explicit form [156]

$$\theta(\mathbf{x}) = \frac{1}{2}\epsilon_{ij}\partial_i u_j(\mathbf{x})\ . \tag{27}$$

As illustrated in Fig. 22, the bond angle along any circuit $\mathcal{D}$ that encloses the disclination turns by $q\frac{\pi}{3}$ and therefore it implies

$$\oint_{\mathcal{D}} d\theta(\mathbf{x}) = \frac{\pi}{3}q\ . \tag{28}$$

This last condition together with Eq. (27) and the definition of the Airy function Eq. (21) leads to the bi-harmonic Eq. (23), which is modified according to [155]

$$\frac{1}{Y}\Delta^2\chi(\mathbf{x}) = \frac{\pi}{3}\sum_i q_i\delta(\mathbf{x}-\mathbf{x}_i)\ , \tag{29}$$

where $\mathbf{x}_i$ $i = 1\ldots M$ parameterize the positions of all the different disclinations and q_i their charges.

Disclinations are the "building blocks" for all topological defects in triangular lattices. Hence, the bi-harmonic Eq. (29) could be used as our final equation to describe defects. However, in most applications, tightly bound disclinations of

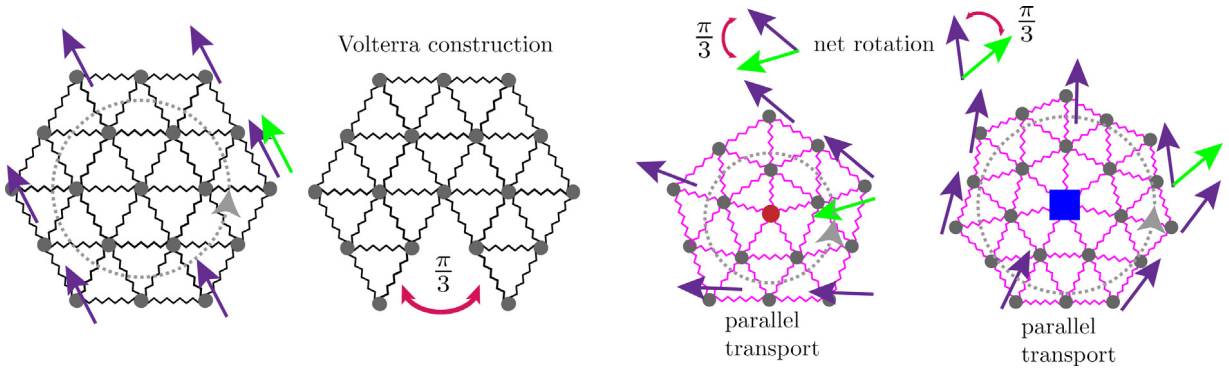

Fig. 22. Construction of a disclination of charge $q = +1$: Starting with a perfect triangular lattice, a wedge of angle $\frac{\pi}{3}$ is excised and the resulting wedges joined. Once joined, strains become inevitable. The bond angle θ Eq. (27) rotates by $\pm\frac{\pi}{3}$ around a disclination $q = \pm 1$.

opposite charges are more conveniently regarded as independent "dipoles", so called *dislocations*. As it is clear from Fig. 9, there are no dislocations present in virus capsides, a point to which we return further below. Due to the absence of dislocation in viruses, we only focus on disclination defects in this review. Taylor Expanding the δ-functions in terms of the disclination separation d^i_k and dropping the higher order terms, the bi-harmonic equation becomes

$$\frac{1}{Y}\Delta^2\chi(\mathbf{x}) = \frac{\pi}{3}\sum_i q_i\delta(\mathbf{x}-\mathbf{x}_i) + \frac{\pi}{3}\sum_i d^i_k\partial_k\delta(\mathbf{x}-\mathbf{x}_i)\ , \tag{30}$$

For a disk with finite radius, R (see Fig. 22), the solution of the Airy function for a disclination of charge q at the center of this disk gives [164,165]

$$\chi(\rho) = \frac{Yq}{24}r^2\left[\log(\rho/R) - \frac{1}{2} + \frac{12}{Yq}\Pi\right]\ , \tag{31}$$

where cylindrical coordinates are used and the boundary condition is such that $\sigma_{\rho\rho}(\rho = R) = \Pi$, and hence, Π is the applied external (surface) pressure at the boundary. The elastic energy Eq. (25) then becomes

$$F_E(R,\Pi) = \frac{Y\pi}{288}q^2R^2 + \frac{\pi}{8B}\Pi^2R^2\ . \tag{32}$$

where B is the Bulk modulus. Even if the external surface pressure is zero ($\Pi = 0$) the energy grows quadratically with the radius (or linearly with the surface area). Looking at the problem from a geometric perspective, this is expected: We are trying to tile a disk with equilateral triangles. However, five triangles meeting at the disclination core, if truly equilateral they would add to 300 degrees instead of 360, and therefore each triangle has to take some distortion so that the energy grows with the number of triangles.

Analytical results beyond linear elasticity are possible in some cases but generally, they are very difficult to obtain. It becomes imperative to resort to numerical methods. One that has proven to be very efficient considers M particles at positions $\vec{r}_i$. Nearest neighbors are connected by a harmonic potential $V(\vec{r}_i,\vec{r}_j)$ implying an elastic energy [164]

$$F_D = \sum_{\langle i,j\rangle} V(\vec{r}_i,\vec{r}_j) = \frac{\epsilon}{2}\sum_{\langle i,j\rangle}\left(|\vec{r}_i-\vec{r}_j| - a\right)^2 \tag{33}$$

where a is the lattice constant of the ideal triangular lattice and the sum runs over all possible nearest neighbors. For large M, the discrete equation is equivalent to the elastic free energy Eq. (14) with elastic constants $\lambda = \mu = \frac{\sqrt{3}}{4}\epsilon$ [164], implying, furthermore, $Y = 2\epsilon/\sqrt{3}$ and $\nu = 1/3$. It is in principle possible to include more general elastic constants, see Ref. [165], which lead to important consequences [166], but this will not be pursued for this review.

The advantage of the model defined by Eq. (33) is that it can be solved (numerically) without approximations, thus allowing to investigate the limits of linear elasticity theory. It has also played a very important role in numerical studies of virus shells. Applications of Eq. (33) to an isolated disclination [166] gives

$$\lim_{R\to\infty}\frac{F_D}{YA} = 0.0035 \approx \frac{1}{288} = 0.0040\ , \tag{34}$$

where A is the area occupied by the crystal. This result shows that linear elasticity incurs in some (very small) error compared with the exact result.

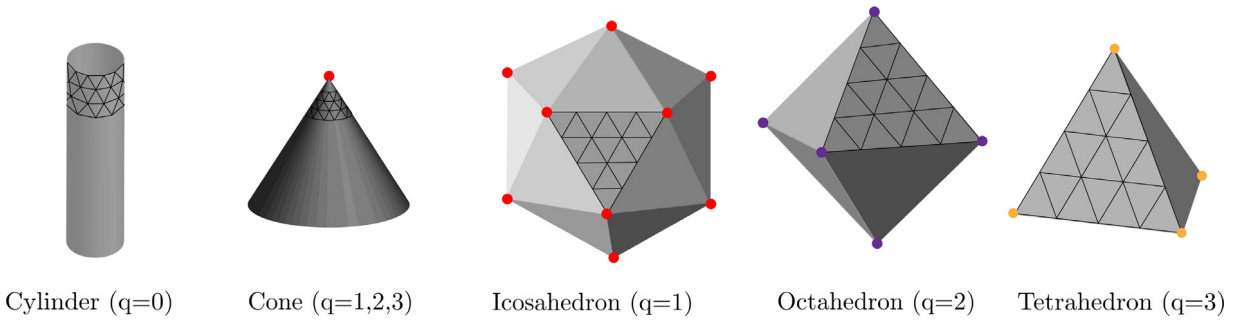

Fig. 23. Different lattices with zero elastic energy and disclinations of different charge. Here q is the disclination charge as defined in Eq. (26).

Table 1
N_v, N_e, N_f are the number of vertices, edges and faces of the triangulation. The numbers n, m are arbitrary integers. For the cone $q = 1, 2, 3$. The quantity a is the lattice constant. The Geometric parameters are: Cylinder (Radius R and height L), cone (aperture angle α), platonic solids (Radius R of the circumscribed sphere), that is the sphere that touches all vertices. Note that the $q = 1$ icosahedradelta triangulation coincides with the $h = 0$ (at any k magic number), Eq. (1).

Geometries from Fig. 23						
Geometry	Parameters	N_v	N_e	N_f	H (Extr)	$\bar{K}$ (Gaussian)
Cylinder	$a = \frac{R}{2\pi n} \quad L = m\frac{\sqrt{3}}{2}a$	$n(m+1)$	$3\ nm + n$	$2mn$	$\frac{1}{R}$	0
Cone	$\sin(\alpha) = 1 - q/6$	$1 + (6-q)n(n+1)/2$	$(6-q)(3n^2+n)/2$	$(6-q)n^2$	$\frac{\cot(\alpha)}{\rho}$	$2\pi(1-\sin(\alpha))$
Icosahedron	$a = \frac{R}{n\sin(\frac{2\pi}{5})}$	$10n^2+2$	$30n^2$	$20n^2$		$\frac{\pi}{3}$
Octahedron	$a = \frac{\sqrt{2}R}{n}$	$4n^2+2$	$12n^2$	$8n^2$		$\frac{\pi}{2}$
Tetrahedron	$a = \frac{\sqrt{8}R}{\sqrt{3}n}$	$2n^2+2$	$6n^2$	$4n^2$		π

4.3. 2D elasticity in curved space

4.3.1. General considerations

Virus capsids divide space into an interior and an exterior, and as shown in Figs. 2 and 7 adopt different shapes such as spherical (with some degree of faceting) and/or cylindrical. Therefore, application of elasticity requires its generalization into curved geometries. The mathematical formulation of elasticity in curved space is considerably involved, so before dwelling into its precise formulation, it is valuable to provide an intuitive understanding of its basic tenants.

A very important result, which is implicit in all our previous discussions in elasticity theory is the following observation

$$\text{Zero elastic energy} \Leftrightarrow \text{Tiling with equilateral triangles} \tag{35}$$

This is illustrated in Fig. 21, where a perfect triangular lattice has zero displacement and therefore zero elastic (free)energy. It is also obvious from the model Eq. (33), if all nearest neighbors are separated by the lattice constant a, the elastic energy becomes identically zero.

In view of the equivalence defined by the observation following from Eq. (35), we now analyze the curved geometries described in Fig. 23, *i.e.* cylinder, cone, icosahedron, octahedron and tetrahedron; all can be tiled with equilateral triangles under the conditions described in Table 1. Not only the lattice constant and the geometric parameters of the surface have to satisfy certain conditions ensuring that they are commensurate with the available area, but equilateral triangulations are only possible for certain "magic" numbers of vertices N_v, as well as edges connecting nearest neighbors N_e and triangles N_f.

Fig. 23 shows that the free energy may need additional terms besides Eq. (14) (or its discrete version, Eq. (33)). This is because the energy of all five geometries described in Fig. 23 cannot all be equal to a perfect triangular lattice on a plane, which numerical calculations show that it has the lowest energy [167]. The simplest term breaking this degeneracy is

$$F_{extr} \equiv \frac{\kappa_D}{2}\int d^2\mathbf{x} H^2(\mathbf{x}) \ , \tag{36}$$

where κ_D is the bending rigidity and $H(\mathbf{x})$ is the *extrinsic curvature*. In the absence of elastic terms, this defines the Helfrich model [135]. The mean curvature, equal to the average of the two inverse principal radii of curvature, is then properly defined as half of the extrinsic curvature. Some authors use mean curvature to imply the extrinsic curvature as defined here. We will use the term extrinsic curvature in order to avoid any ambiguity, specially with the mathematical literature. A plane has $H(\mathbf{x}) = 0$ and therefore minimizes this term, while for all other surfaces in Fig. 23 $F_{extr} > 0$ and hence, the

degeneracy is lifted. Besides the plane, there are many other surfaces that satisfy $H(\mathbf{x}) = 0$, they are known as minimal surfaces [168,169] and play an important role in many physical problems [169]. So far, minimal surfaces have not found relevant applications in virus systems and therefore will not be discussed further.

There are more consequences to Fig. 23: As discussed previously, see Eq. (32), the energy of a single isolated disclination is prohibitively large in flat space: It grows with the radius square. Yet, for the icosahedral, octahedral or tetrahedral lattices, the total elastic energy is exactly zero. One way to reconcile these two considerations is to postulate that the free energy Eq. (14) in curved geometries is

$$F_E = \mathcal{F}_E(s(\mathbf{x}) - K(\mathbf{x})) \,, \tag{37}$$

where $s(\mathbf{x})$ is the disclination density, $K(\mathbf{x})$ is the Gaussian curvature and $\mathcal{F}_E(0) = 0$. In other words, the defect density screens the Gaussian curvature. The minimum energy is achieved when both $s(\mathbf{x}) - K(\mathbf{x}) = 0$ and $H(\mathbf{x}) = 0$ and gives a planar triangular lattice as the only solution that satisfies these two equations. Those solutions where $s(\mathbf{x}) = K(\mathbf{x})$ are known to satisfy the perfect screening condition [170–172] and may be achieved for an infinite number of particles on any finite geometry [173] at the cost of adding an infinite number of dislocations. Even before properly defining the extrinsic and Gaussian curvatures, which are discussed in the Appendix see Fig. 78, we will first provide an intuitive description for the five cases shown in Fig. 23.

The Gaussian curvature is entirely located at the "cusps" of the polyhedra, marked by small, colored spheres in Fig. 23. This follows from Fig. 78 as everywhere else there is at least one curvature radius $r_1 = \frac{1}{\kappa_1}$ that is identically zero. Therefore, the Gaussian curvature consists of a discrete sum of δ-functions:

$$K(\mathbf{x}) = \bar{K} \sum_{i=1}^{N_G} \delta(\mathbf{x} - \mathbf{x}_i) \,, \tag{38}$$

where $N_G = 12, 8, 4$ for icosahedron, octahedron and tetrahedron respectively, and $\{\mathbf{x}_i\}_{i=1\ldots N_G}$ the positions of the "cusps", with $\bar{K}$ given in Table 1. The defect density is given by

$$s(\mathbf{x}) = \frac{\pi}{3} \sum_{i=1}^{N_G} q_i \delta(\mathbf{x} - \mathbf{x}_i) \,. \tag{39}$$

Note that by construction all the vertices with coordination different from six are located at the "cusps", the same points where the Gaussian curvature is non-zero. Thus, for all the geometries in Fig. 23, the perfect screening condition $s(\mathbf{x}) = K(\mathbf{x})$ is satisfied and the elastic energy is identically zero, $\mathcal{F}_E(0) = 0$.

The discussion so far has made the assumption that whatever is the nature of the particles described, they can be represented as point particles. If the particles can be approximated as spheres, all the previous considerations immediately apply, but this is not always the case. There are many possible particle shapes to consider, but one that is relevant for this review, in connection with scaffolding proteins, see Fig. 36, are particles with conical shapes. In that case, the extrinsic curvature is replaced by a term

$$F_{extr} \equiv \frac{\kappa_D}{2} \int d^2\mathbf{x} (H(\mathbf{x}) - H_0)^2 \,, \tag{40}$$

where H_0 is the spontaneous curvature and it may be either positive or negative. The elastic energy Eq. (37) remains unchanged; the zero energy solution consists of particles forming a perfect triangular lattice on an infinite cylinders of radius $R_c = \frac{1}{H_0}$ such as the one shown in Fig. 23. Note that the form of Eq. (40) can be immediately recast as a sum of a quadratic term in extrinsic curvature, a linear term including spontaneous curvature , and an additional surface pressure term, see the discussion after Eq. (43). Implicit in our discussion in the following section is the role of differential geometry and topology. Because these concepts are scattered through different sources and textbooks, we therefore present a survey of differential geometry and topology in the Appendix, so that the review is entirely self contained.

4.3.2. Covariant formulation

We have provided an intuitive theory of elasticity in curved spaces before. We now apply the differential geometry and the surface topology methods (discussed in the Appendix) to introduce a rigorous formulation of the theory. We start with the extrinsic curvature term Eq. (36) and adopt the following expression

$$F_{extr} \equiv \frac{\kappa_D}{2} \int d^2\mathbf{x} \sqrt{g} (H(\mathbf{x}))^2 \,, \tag{41}$$

where this term only differs from the one in Eq. (36) by the presence of the $\sqrt{g}$, see Eq. (189). This term is necessary as it ensures that F_{ext} is reparameterization invariant, that is, does not depend on the particular choice of the coordinates used to describe the system. The units of the bending rigidity are $[\kappa_D]$ = Energy and therefore, on purely dimensional ground, the typical contribution to the free energy will grow at most logarithmically with a characteristic length of the system R, $F_{extr} \sim \kappa_D \log(R/a)$, with a the lattice constant. Another term that can be considered is

$$F_{intr} \equiv \bar{\kappa_D} \int d^2\mathbf{x} \sqrt{g} K(\mathbf{x}) = 4\pi \bar{\kappa}_D \chi_E \tag{42}$$

where $\bar{\kappa}_D$ is the Gaussian bending rigidity and has the same dimensions as the bending rigidity. The last expression follows from the Gauss–Bonet theorem, see Appendix Eq. (199). If the surface has a boundary Eq. (42) reduces to a boundary term. This contribution is difficult to isolate in actual experiments, but it may be theoretically important in some situations. Other local possible contributions vanish for $R \to \infty$ and the two terms Eqs. (41) and (42) are the only two necessary to describe the system in the continuum limit. In connection with the elasticity theory defined by Eq. (14), the analysis of the elastic constants gives the scaling $[\mu, \lambda, Y] = \text{Energy} \times \text{Length}^{-2}$ so that $F_E \propto YR^2$, which grows much more rapidly than the logarithmic growth of the extrinsic term, as already apparent from the analysis of a single disclination on a disk Eq. (32). There is an additional geometric term that is potentially relevant:

$$F_{surf} = \sigma \int d^2\mathbf{x}\sqrt{g}(\mathbf{x}) \,, \tag{43}$$

where σ is the surface tension, which has units of $[\sigma] = \text{Energy} \times \text{Length}^{-2}$ and hence should contribute as $F_{surf} \propto \sigma R^2$, thus competing with the elastic energy if present.

A covariant formulation for the elastic free energy Eq. (14) is not straight-forward. Let us consider first a covariant formulation of the planar case. In differential geometry language, Eq. (12) defines a diffeomorphism [157] between reference and actual space. Distances in actual space are measured according to the metric:

$$ds = d\vec{r} \cdot d\vec{r} \equiv g_{ij}(\mathbf{R}) dR^i dR^j = \left(\delta_{ij} + u_{ij}\right) dR^i dR^j \,, \tag{44}$$

thus showing that the strain tensor introduced in Eq. (13) is basically the non-trivial part of the actual space metric and it can be written in an aesthetically pleasing form [174], $u_{\alpha\beta} = g_{\alpha\beta} - \bar{g}_{\alpha\beta}$. The metric defined in reference space is given by $\bar{g}_{ij} \equiv \delta_{ij}$, which immediately leads to a possible covariant generalization of Eq. (14) given by

$$F_E(g_{ij}) = \int d^2\mathbf{x}\sqrt{\bar{g}} \left(\frac{\lambda}{2} (\bar{g}^{\alpha\beta} u_{\alpha\beta})^2 + \mu u_{\alpha\beta} \bar{g}^{\alpha\delta} \bar{g}^{\beta\gamma} u_{\beta\gamma} \right) \,. \tag{45}$$

We notice however, that each metric tensor has three independent degrees of freedom, but the strain tensor should only have two, the two displacements. Indeed, there is a further constrain, and that is, that the geometry is planar, which amounts to the constraint on the Gaussian curvature to be exactly zero. Therefore, the elastic equations follow from

$$\delta F_E(g_{ij}) = 0 \quad \text{with constraint } K(g_{ij}) = 0 \,, \tag{46}$$

that is, the elastic equations consist in finding, among all flat metrics, the one that minimizes Eq. (45). The above free energy can immediately be generalized to curved space and the minimization Eq. (46) reads now

$$\delta F_E(g_{ij}) = 0 \quad \text{with constraint } K(g_{ij}) = K_r(\mathbf{R}) \,, \tag{47}$$

where $K_r(\mathbf{R})$ is now the Gaussian curvature of the given surface. The change in going from Eqs. (46) to (47) may look very innocent; nevertheless, it has profound consequences. It reveals the very important result that in a curved geometry (with non-zero Gaussian curvature), the strain cannot vanish. This leads to the Geometric Frustration (GF) theorem:

In curved space there is geometric frustration, implying that the stress is necessarily present and cannot vanish.

This follows because if the stress vanishes, the same is true for the strain $u_{\alpha\beta} = g_{\alpha\beta} - \bar{g}_{\alpha\beta}$, and therefore there is a choice of coordinates for which $g_{ij} = \bar{g}_{ij}$ but this is in contradiction with the fact that $K = 0$ for the reference metric $\bar{g}_{ij}$ while $K = K_r(\mathbf{R}) \neq 0$ for the actual metric g_{ij}. In other words, geometric frustration arises because the two metrics are incompatible, i.e. have different Gaussian curvatures.

At this point, we need to be a bit more precise about the reference and actual coordinates and metrics. We will denote as $\mathbf{x}$ the actual coordinates and as $\bar{\mathbf{x}}$ the reference coordinates, see Fig. 24. Hereon, we will refer with an overline to reference frame quantities. The application

$$\mathbf{x} = \mathcal{F}(\bar{\mathbf{x}}) \,, \tag{48}$$

is a mapping of the reference into the actual domain, see Fig. 24. It physically represents how the particles in the reference domain $\bar{\mathcal{B}}$, which consists of a perfect triangular lattice that may include defects but has zero elastic energy, see Fig. 23, map into the actual domain $\mathcal{B}$. This perfect triangular lattice is in some situations, such as when the defect density contains additional dislocations, not possible to visualize in flat 3 dimensional space, but in what follows we will leave these more abstract conceptual issues aside.

Another possible generalization for Eq. (14) consists of

$$F_E(\bar{g}_{ij}) = \int d^2\mathbf{x}\sqrt{g} \left(\frac{\lambda}{2} (g^{\alpha\beta} u_{\alpha\beta})^2 + \mu u_{\alpha\beta} g^{\alpha\delta} g^{\beta\gamma} u_{\beta\gamma} \right) \,, \tag{49}$$

where now the reference metric $\bar{g}_{\alpha\beta}$ is unknown while $g_{\alpha\beta}$ is the metric of the corresponding surface, which is known. Although both forms of the free energy, Eqs. (45) and (49), agree within linear order elasticity, their results may differ when computed at higher orders, an issue that we will not address further here as we will consistently use Eq. (49) hereon. The additional equation for $\bar{g}_{\alpha\beta}$ is

$$\bar{K}(\bar{g}_{ij}) = s(\mathbf{x}) \,, \tag{50}$$

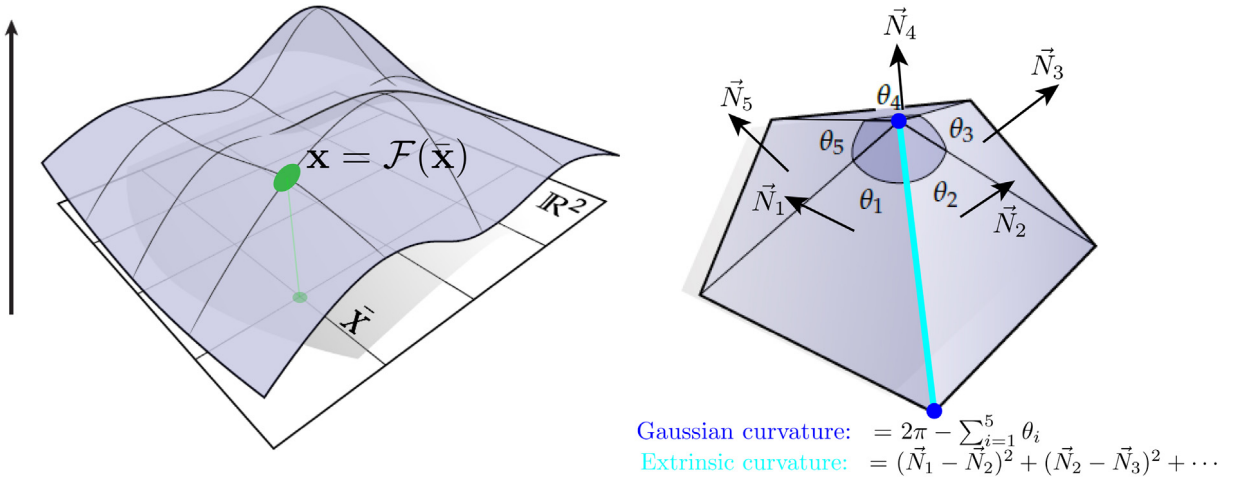

Fig. 24. Illustration of the mapping Eq. (48) and the definitions of the discrete Gaussian (Eq. (71)), which is localized at the vertices, and Extrinsic Curvature (Eq. (70)), which is localized along the edges. figure adapted from http://www.cs.cmu.edu/kmcrane/Projects/DDG/ and has been used under a Creative Commons Attribution-NonCommercial-NoDerivs 3.0 Unported License (courtesy of Keenan Crane).

that is, the curvature of the reference metric is the same as the defect density, which if the defect density is not zero, results in curvature at some points, see Fig. 23.

The goal of the calculation is thus to compute the reference metric $\bar{g}_{\alpha\beta}$ and then obtain $\mathcal{F}$ as the solution to the problem, namely, the positions and strains in actual space and the resulting elastic free energy. It is convenient to define [175]

$$A^{\alpha\beta\gamma\delta} = \frac{Y}{1-\nu_P^2}\left(\nu_P g^{\alpha\beta}g^{\gamma\delta} + (1-\nu_P)g^{\alpha\gamma}g^{\beta\delta}\right) \tag{51}$$

$$A_{\alpha\beta\gamma\delta} = \frac{1}{Y}\left((1+\nu_P)g_{\alpha\gamma}g_{\beta\delta} - \nu_P g_{\alpha\beta}g_{\gamma\delta}\right) ,$$

in such a way that $A^{\alpha\beta\gamma\delta}A_{\gamma\delta\alpha'\beta'} = g^{\alpha}_{\alpha'}g^{\beta}_{\beta'} = \delta^{\alpha}_{\alpha'}\delta^{\beta}_{\beta'}$. Then a covariant free energy is defined so that it reduces to the standard elastic energy for an isotropic medium, that is

$$\frac{\lambda}{2}(g^{\alpha\beta}u_{\alpha\beta})^2 + \mu u_{\alpha\beta}g^{\alpha\delta}g^{\beta\gamma}u_{\beta\gamma} = A^{\alpha\beta\gamma\delta}u_{\alpha\beta}u_{\gamma\delta}, \tag{52}$$

while the stress tensor is given by

$$\sigma^{\alpha\beta} = \frac{1}{\sqrt{g}}\frac{\delta F}{\delta u_{\alpha\beta}} = A^{\alpha\beta\gamma\delta}u_{\gamma\delta} . \tag{53}$$

Before continuing, it is important to recap the main aspects of the covariant formalism in a more concrete setting. The actual metric $g_{\alpha\beta}(\mathbf{x})$ is known and corresponds to the metric of the curved surface. For example, for a symmetric spherical cap, it would be

$$g_{\alpha\beta}(\mathbf{x})dx^{\alpha}dx^{\beta} = dr^2 + R^2\sin^2(r/R)d\psi^2 , \tag{54}$$

where r is the radial distance from the center of the cap and ψ the azimuthal angle. The reference metric $\bar{g}_{\alpha\beta}(\bar{\mathbf{x}})$ is also known, and, in the absence of disclinations corresponds to a disk, such that

$$\bar{g}_{\alpha\beta}(\bar{\mathbf{x}})d\bar{x}^{\alpha}d\bar{x}^{\beta} = d\rho^2 + \rho^2 d\phi^2 , \tag{55}$$

where ρ is the polar distance and ϕ the corresponding angle. What is not known is the mapping Eq. (48)

$$\bar{\mathbf{x}} = \mathcal{F}^{-1}(\mathbf{x}) \rightarrow (\rho,\phi) = (\mathcal{F}_1(r,\psi), \mathcal{F}_2(r,\psi)) , \tag{56}$$

which substituted in Eq. (55) gives $\bar{g}_{\alpha,\beta}(\mathbf{x}) = \bar{g}_{\alpha,\beta}(r,\psi)$. No matter what the actual form of $\mathcal{F}$ is, it will always be such that the Gaussian curvature satisfies

$$\bar{K}(\mathbf{x}) - K(\mathbf{x}) = 0 - \frac{1}{R^2} \neq 0 \tag{57}$$

implying that the strains will be non-zero and also that the free energy Eq. (49) will be non-zero. This incompatibility of the reference and actual metric is the origin of the geometric frustration, as discussed in deriving the GF theorem.

The equilibrium equations are derived by considering an infinitesimal transformation $\mathcal{F} = 1 + \xi$, so that $\delta\bar{g}_{\alpha\beta} = \bar{\nabla}_\alpha\xi_\beta + \bar{\nabla}_\beta\xi_\alpha$ and obviously $\delta g_{\alpha\beta} = 0$, yielding the equilibrium condition

$$\delta F = \frac{1}{2}\int_{\mathcal{B}} d^2\mathbf{x}\sqrt{g}\sigma^{\alpha\beta}\delta\bar{g}_{\alpha\beta} = \int_{\mathcal{B}} d^2\mathbf{x}\left[\frac{\partial}{\partial x_\alpha}\left(\sqrt{g}\sigma^{\alpha\beta}\xi_\beta\right) - \sqrt{\bar{g}}\,\bar{\nabla}_\alpha\left(\left(\frac{g}{\bar{g}}\right)^{1/2}\sigma^{\alpha\beta}\right)\xi_\beta\right] \tag{58}$$

The first term is a total derivative, and it can be converted to an integral along the boundary, allowing to include line tension and other external conditions, see Ref. [166]. From the definition of the covariant derivative, see Eq. (191), the equations determining equilibrium can be reduced to

$$\nabla_\alpha\sigma^{\alpha\beta} + \left(\bar{\Gamma}^\beta_{\alpha\gamma} - \Gamma^\beta_{\alpha\gamma}\right)\sigma^{\alpha\gamma} = 0\ . \tag{59}$$

This equation was derived first in Refs. [174,176]. If there are boundaries present, an additional condition is needed, for example $\sigma^{\alpha\beta} = 0$ at the boundary. Eq. (59) shows that for the stress tensor, thus defined, in general

$$\nabla_\alpha\sigma^{\alpha\beta} \neq 0 \tag{60}$$

contrary to what a naive generalization from flat (actual) space might have suggested.

A general solution to Eq. (59), first reported in Ref. [175], is given by the *Ansatz*

$$\sigma^{\alpha\beta} = \frac{1}{\sqrt{g}}\frac{1}{\sqrt{\bar{g}}}\epsilon^{\alpha\rho}\epsilon^{\beta\gamma}\bar{\nabla}_\rho\bar{\nabla}_\gamma\chi\ , \tag{61}$$

where $\epsilon^{12} = 1$, thus providing an exact and covariant generalization for the Airy function χ, already introduced in Eq. (21). The proof that Eq. (61) provides a general solution of the equilibrium equations in terms of the Airy function can be found in Ref. [166].

The Gaussian curvature $\bar{K}$ is then given by the expression

$$\bar{K}(\mathbf{x}) = \frac{\pi}{3}\sum_{i=1}^{M}\frac{q_i}{\sqrt{g}}\delta(\mathbf{x} - \mathbf{x}_i) \tag{62}$$

describing "quanta" of curvature which are the disclinations. If we consider dislocations as independent quantities defined by Burgers vector $\mathbf{b}$, then they appear as "quanta" of geometrical torsion [157] defined by

$$\bar{T}_\alpha(\mathbf{x}) = \sum_{i=1}^{M}\frac{b^i_\alpha}{\sqrt{g}}\delta(\mathbf{x} - \mathbf{x}_i)\ . \tag{63}$$

See Refs. [166,173] for an extensive discussion. The free energy Eq. (49) can be written in the form

$$\begin{aligned} F &= \frac{1}{2}\int_{\mathcal{B}}\sigma^{\alpha\beta}A_{\alpha\beta\rho\sigma}\sigma^{\rho\sigma}dVol_g \\ &= \int_{\mathcal{B}}\frac{g}{\bar{g}}\left((1+\nu_p)g^{\alpha\rho}g^{\beta\sigma} - \nu_p g^{\alpha\beta}g^{\rho\sigma}\right)\bar{\nabla}_\alpha\bar{\nabla}_\beta\chi\bar{\nabla}_\rho\bar{\nabla}_\sigma\chi\, dVol_g\ . \end{aligned} \tag{64}$$

Up to this point, all formulas are exact. We recall that the GF theorem described above remains true, since a number of discrete curvatures cannot be made equal to the Gaussian Curvature of the surface as it is continuous. It leaves open, however, the possibility of approximating the continuous curvature with a finite sum of defects that becomes increasingly large as the lattice constant is smaller (infinite N limit), which has shown to satisfy the perfect screening condition, see Refs. [173,177].

The above approach provides a covariant formalism for elasticity in curved space. The screening condition Eq. (37), however, does not become explicit. Intuitively, from Fig. 23, it should be possible to write the free energy Eq. (64) as a functional depending only of $s - K$, but this, has not been proved so far. This screening result maybe obtained by making additional assumptions, such as, for example, linear elasticity theory. In that case, an elaborate calculations [175] shows

$$\frac{1}{Y}\left(\Delta^2\chi^{(I)} + 2K\Delta\chi^{(I)} + (1+\nu_p)g^{\mu\lambda}\nabla_\mu K\nabla_\lambda\chi^{(I)}\right) = s(\mathbf{x}) - K(\mathbf{x})\ ,$$

which has the expected form $\chi \equiv \mathcal{F}(s-K)$ in agreement with the assumption of Eq. (37). In these situations, including the very important case of the sphere, where the curvature is constant, we have

$$\frac{1}{Y}(\Delta + K)\Delta\chi^{(I)} = s(\mathbf{x}) - K(\mathbf{x})\ . \tag{65}$$

In general, $\Delta \gg K$. For example, for a sphere the eigenvalues of the Laplacian are $l(l+1)$, hence $l(l+1)/R^2 \gg 1/R^2$ [178]. Thus, with a presumably small error, we can make the further simplification

$$\frac{1}{Y}\Delta^2\chi^{(I)} = s(\mathbf{x}) - K(\mathbf{x})\ , \tag{66}$$

which is the simplest as well as the most commonly used form. The stress tensor within this level of approximation is

$$\sigma^{\alpha\beta} = g^{\alpha\beta}\Delta\chi^{(l)} - g^{\alpha\mu}g^{\beta\nu}\nabla_\mu\nabla_\nu\chi^{(l)} \,, \tag{67}$$

and the free energy may be expressed in the screening form Eq. (37)

$$F_E = \frac{Y}{2}\int d^2\mathbf{x}\sqrt{g}(x)d^2\mathbf{y}\sqrt{g}(y)\,(s(\mathbf{x}) - K(\mathbf{x}))\,\frac{1}{\Delta^2}\bigg|_{x,y}(s(\mathbf{y}) - K(\mathbf{y}))\,, \tag{68}$$

which has been extensively used in many studies [167,170,178–183]. A detailed analysis of the validity for the different approximations can be found in Ref. [166]. A recent detailed analysis of the elasticity in spherical caps is provided in Ref. [184]. The formulas describing the continuum formalism, have the important merit of relating elasticity theory to concepts in geometry, but they are, indeed quite complex. Fortunately, it is possible to formulate the problem within a simpler, discrete formalism.

4.3.3. Lattice (discrete) formulation

The discretization proceeds by first considering a triangulation $\mathcal{T}_S$, with approximately equilateral triangles whose ideal length is a. The elastic free energy has already been defined in Eq. (33), and it is already covariant, so does not require any further modification. In regard to the extrinsic curvature term, Eq. (36), we make use of Eq. (197) to obtain the identity

$$\int d^2\mathbf{x}\sqrt{g}H^2(\mathbf{x}) = \int d^2\mathbf{x}\sqrt{g}g^{\alpha\beta}\partial_\alpha\vec{N}\cdot\partial_\beta\vec{N} + 2\int d^2\sqrt{g}K(\mathbf{x})\,. \tag{69}$$

Using the discretization

$$\int d^2\mathbf{x}\sqrt{g}g^{\alpha\beta}\partial_\alpha\vec{N}\cdot\partial_\beta\vec{N} \equiv \sum_{\langle k,l\rangle}(\vec{N}_k - \vec{N}_l)^2 \tag{70}$$

where $\vec{N}$ is the normal to the corresponding triangle and the sum runs over nearest neighbor triangles and is defined along the edges, see Fig. 24. As for the Gaussian curvature, the discretization follows Regge calculus [185], first introduced to provide a lattice version for General Relativity, which gives

$$\int d^2\mathbf{x}\sqrt{g(\mathbf{x})}K(\mathbf{x}) = \sum_i \delta_i, \tag{71}$$

where δ_i is the quantity

$$\delta_i = 2\pi - \sum_{\mathrm{T}\in i}\Phi_i \tag{72}$$

where Φ_i is the angle of the triangle meeting at i (see Fig. 24) and corresponds to the curvature residing at the vertices, a point already noticed further above. It has been shown in Ref. [185] that $\sum_i \delta_i = 2\pi\,\chi_E$, so the model satisfies the Gauss–Bonnet theorem Eq. (199) exactly for any triangulation and not just in the thermodynamic limit.

Collecting all the terms, the lattice formulation becomes

$$\begin{aligned} F &= \frac{\epsilon}{2}\sum_{\langle i,j\rangle}\left(|\vec{r}_i - \vec{r}_j| - a\right)^2 + \frac{\kappa_D}{2}\sum_{\langle k,l\rangle}(\vec{N}_k - \vec{N}_l)^2 + (\bar{\kappa_D} + \kappa_D)\sum_i \delta_i \\ &= F_E + F_{intr} + F_G \,, \end{aligned} \tag{73}$$

Here F_{intr} labels the contribution from extrinsic geometry and $\bar{\kappa_D}$ is the Gaussian bending rigidity. There is also, the possible addition of a surface tension term, see Eq. (43). Numerically at least, this discrete model is much simpler to solve than its continuum counterpart. One might wonder, given its complexity, whether it is really worth to develop the continuum model. Our response to this question is obviously positive; the continuum model allows us to connect the elasticity in curved spaces with geometric invariants such as Gaussian curvature, metric properties, etc. In particular, it is not obvious at all how the perfect screening condition and other asymptotic properties of elasticity in curved spaces may follow from Eq. (73) with full generality. Further generalizations of the discrete model to include spontaneous curvature, etc. is necessary to describe viruses, and will be discussed later in the context of the elasticity of viral shells.

4.4. Elasticity and defects at play: Sphere as an example

The theory of elasticity in curved geometries has found applications in many areas of physics, see, for example, Refs. [170,183,186–189]. It would be the subject of a different report to review them all. Instead, we will provide a detailed discussion of the elasticity of curved crystals on the sphere, which will serve to illustrate concrete examples of the formalism previously introduced. Some of these results explain many experimental observations in viruses, and as we will see, they also help to understand why certain effects, routinely observed in other systems are not present for viruses. We will also include some related cases, relevant for the subject of this review, that go beyond the sphere.

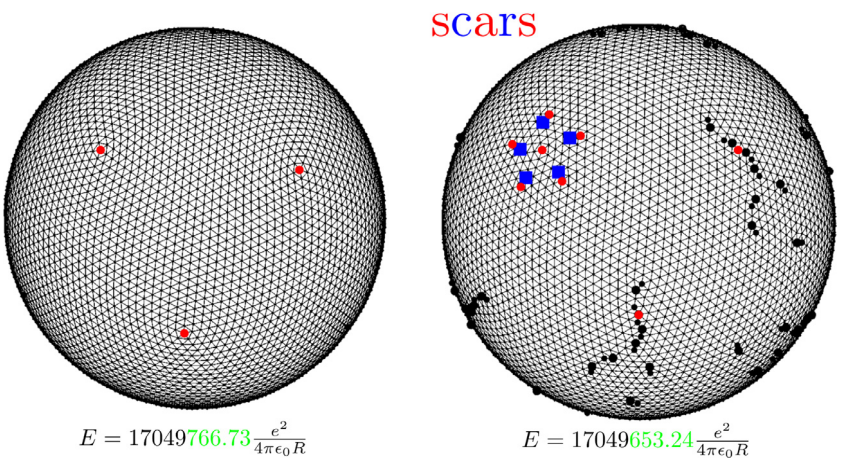

Fig. 25. Minimization by Pérez-Garrido, Dodgson and Moore [179], showing that configurations with additional dislocations, see Fig. 22, have lower energy than the icosadeltahedral configuration ($M = 5882$). Values of the energy for each configuration are quoted. There are 12 scars on the right figure, where only three are completely visible.

4.4.1. The thomson and related problems from numerical minimizations

In 1904, J.J. Thomson [190] posed the question of finding the ground state of M equally charged particles constrained to be on a sphere, interacting through the Coulomb interaction. With the discovery of the atom, the interest on the Thomson problem faded until L.L. Whyte in 1952 [191] revived it as a relevant mathematical question, which is not devoid of important cases such as tesselations of the sphere, having important applications in areas such as astronomy, coding and others. In 1986, simulated annealing was applied to the Thomson problem [192], thus initiating a number of numerical studies that continue to this day. We briefly summarize some of the most relevant results. Erber and Hockney [193], analyzed the local minima, and found that for number of particles between $70 \leq M \leq 110$, the number of (local) minima n_0 grows exponentially, as

$$n_O(M) = 0.382 \exp(0.0497M) \ . \tag{74}$$

Other studies, see Refs. [194–197] developed sophisticated algorithms to obtain optimal configurations for relatively small number of particles (< 130). A remarkable result was obtained by Pérez-Garrido et al. as it was shown [179] the presence of a finite number of dislocations radially distributed from the twelve disclinations in the ground state for systems containing $M = 2132(T = 213)$, $4002(T = 400)$ and $5882(T = 588)$ particles, which later were dubbed "scars" [186], see Fig. 25. Subsequent numerical studies confirmed the presence of scars for large (of a few thousands or more) number of particles [198]. The question therefore became what was the critical value M_c, such that for $M > M_c$ scars appear. Numerical minimizations [199,200] obtained for $M_c < 550$, finally showed

$$M_c \approx 410 \ , \tag{75}$$

as discussed in Ref. [201]. Given the exponentially growth presented in Eq. (74), it may appear that the absolute minima may only be reached after a random walk crossing a faster than exponentially large number of activation barriers. If this were the case, achieving the global minima(equilibrium) would be hopeless.

Quite interestingly, there is a considerable structure in local minima as visualized by *disconnectivity graphs* (DG) [202–204]. Here is how a DG is constructed: First, all the local minima and transition states (local maximum with exactly one unstable (negative eigenvalue)) are enumerated. The local minima are spread along the x-axis and at a position in the y-axis corresponding to their energy. The y-axis is split into a number of discrete energy thresholds illustrated by the dashed lines in Fig. 26a and b: A minimum is connected to another minimum if the corresponding transition state that connects these two minima has the energy value below the nearest threshold. If the transition state has higher energy than the threshold then these two minima are not connected, see Fig. 26a, c for examples.

In Ref. [205], the DG for the Thomson problem for $M = 132, 135, 138, 141, 144, 147, 150$ have been calculated. They correspond to a Palm tree, see Fig. 26a consisting of local minima with small activation barriers that conform to an exponential large number of local minima (Eq. (74)) arranged as a "funneled landscape", with a unique global icosadeltahedra-like minima. The one dimensional plot in Fig. 26 may suggest that the number of transition states is equal to the number of local minima, but in fact, there are usually many more transition states (roughly M times more) than local minima, so that each minima is connected to more than two other minima, see Fig. 26. Quite interestingly, the study by Mehta et al. [205] established that the minima conform to a small world network, see Fig. 26b, where the global minima is a "hub" such that it is accessible by hoping over a small (around 6) transition states. Thus, any process (or

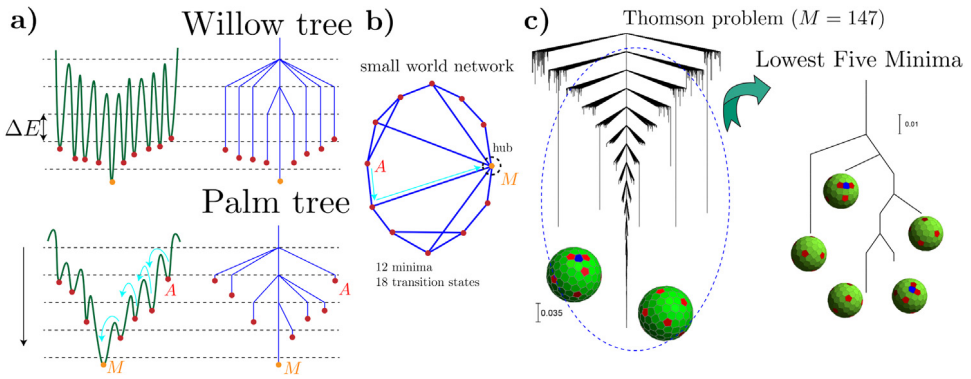

Fig. 26. (a) Two different cases of disconnectivity graphs: The Willow tree has large activation barriers while the palm tree represents a funneled landscape with small nucleation barriers [203]. (b) Example of a small world network: Each minimum is a vertex and each link represents a transition state connecting any two minima: The global minima is a hub and any local minimum is connected through at most 4 transition states. (c) Disconnectivity graph for the Thomson problem $M = 137$ [205]. (Last figure is a courtesy of David Wales.)

algorithm) that allows jumping over transition states, will quickly reach the global minima, and in this way, it overcomes the exponential growth Eq. (74).

Studies of the DG of the Thomson problem for $M > M_c$ seem beyond current computational capabilities, but it seems obvious that when additional defects appear, see Fig. 25, the single funneled landscape in Fig. 26 will no longer apply and instead, many funneled complex landscapes and the breaking of the small world network property will occur, thus hampering the ability of the system to find the global minima. It is appealing to speculate that the small world network property would make self-assembly very unlikely and relate it to the absence of virus capsids containing dislocations.

Other problems consisting in distributing many points on a sphere are also of great interest, such as, for example:

- *Tammes Problem*: Maximize the smallest distance among M-points on the sphere, which in physical terms consists in optimizing the packing fraction.
- *Fekete Points*: Is the name given to the Thomson problem in the Mathematics literature. Often, instead of the Coulomb interaction a more general potential of the form $1/r^s$ is used.
- *Equal Area partition:* partitioning of the sphere into M equal-area parts with small diameters.
- *Spherical Designs: Construction of uniformly distributed points on the sphere.*

While the solutions known to the above problem [206,207], that is, the positions of the particles differ, their main properties follow the same trends as the Thomson problem with the ground state showing scars [126,180,208–211] with a M_c value consistent with Eq. (75) and funneled landscapes.

Other generalizations of the Thomson problem include characterizing the minimum for connected (polymer-like) charged particles on the sphere, which has direct relevance for understanding the packing of genetic material onto the inner surface of capsid [212].

Elasticity theory provides a very powerful framework, thus connecting general mathematical problems to the mechanical properties of virus shells.

4.4.2. Continuum elasticity theory and spherical crystals: Universality

We will consider now the application of the continuum theory of elasticity to the Thomson (and related) problems. This will illustrate the relevance of the continuum theory to the conceptual framework and properly contextualize numerical work. It will also emphasize many universal (independent of the molecular details) predictions obtained from elasticity theory. This universality allows us to use simple potentials to investigate the physics of viruses, as the properties remain valid even if the interactions among individual components (the proteins) are unknown.

The starting point is the elastic free energy Eq. (68) describing disclination interactions, which requires the calculation of the inverse of the bi-Laplacian on a sphere.

$$\frac{1}{4\pi}\chi(\theta^a,\phi^a;\theta^b,\phi^b) = \frac{1}{\Delta^2} = R^2\sum_{l=1}^{\infty}\sum_{m=-l}^{l}\frac{Y_m^l(\theta^a,\phi^a)Y_m^{l*}(\theta^b,\phi^b)}{l^2(l+1)^2}\,, \tag{76}$$

where $Y_m^l(\theta,\phi)$ are the spherical harmonics and (θ,ϕ) are the spherical coordinates. The $l = 0$ term does not appear in the sum as a consequence of the topological relation Eq. (201), which if not satisfied, the above sum becomes infinite as $l(l+1) = 0 \times 1 = 0$. As shown in Ref. [178], Eq. (76) is equivalent to

$$\chi(\theta^a,\phi^a;\theta^b,\phi^b) = R^2\left(1 + \int_0^{\frac{1-\cos\beta}{2}} dz\,\frac{\ln z}{1-z}\right)\,. \tag{77}$$

where β is the geodesic arc connecting (θ^a, ϕ^a) and (θ^b, ϕ^b) on the sphere, and is given by

$$\cos\beta = \cos\theta^a \cos\theta^b + \sin\theta^a \sin\theta^b \cos(\phi^a - \phi^b) \ . \tag{78}$$

Thus, the final expression for the elastic energy of a spherical crystal with N disclinations follows from Eqs. (68) and (76)

$$F_E = \frac{\pi Y}{72} R^2 \sum_{i=1}^{N}\sum_{j=1}^{N} q_i q_j \chi(\theta^i, \phi^i; \theta^j, \phi^j) + N\, E_{core} \ , \tag{79}$$

where we included the core energy (E_{core}). Thus, given a number of N disclinations (satisfying Eq. (201)), the above expression gives the elastic energy.

Expanding the δ function in the disclination density in terms of spherical harmonics one obtains

$$\begin{aligned} s(\mathbf{x}) &= \frac{\pi}{3\sqrt{g}} \sum_{i=1}^{N} q_i \delta(\mathbf{x}, \mathbf{x}_i) \\ &= K(\mathbf{x}) + \frac{\pi}{3R^2} \sum_{l=1}^{\infty} \sum_{m=-l}^{l} Y_m^l(\theta, \phi) \sum_{i=1}^{N} q_i Y_m^{l*}(\theta_i, \phi_i), \end{aligned} \tag{80}$$

This last identity makes it clear that if we were to identify N disclinations located in positions $(\theta_i, \phi_i)_{1\le i\le N}$ such that

$$\sum_{i=1}^{N} q_i Y_m^l(\theta_i, \phi_i) = 0 \ , \tag{81}$$

for all l, m, then the perfect screening condition $s(\mathbf{x}) - K(\mathbf{x}) = 0$ would be satisfied and the geometric frustration would be completely removed. Of course, this is impossible for a finite number of defects N, in agreement with the GF theorem, but can be achieved for $N \to \infty$ [173].

Eq. (79) provides the basis for analyzing the numerical simulations of the Thomson and related problems: It successfully predicts the scar configurations observed in simulations with $M_c \approx 305$, see Eq. (75) and many other results. The study of defect arrangements for large number of particles is fascinating, but not central to the physics of viruses. Instead, we focus on configurations with exactly 12 $q = +1$ disclinations. In that case, Eq. (79) is given by

$$F_E^{12} \equiv C(i_1, \ldots, i_{12}) \cdot \frac{\pi Y}{72} R^2 + 12\, E_{core} \ , \tag{82}$$

where $i_1 \ldots$ parameterizes the positions of the 12 $q = +1$ disclinations. This equation generalizes Eq. (34) to include the sphere curvature and the interaction among disclinations. In Ref. [178] it is shown that the minimum elastic energy occurs when the defects sit at the vertices of an icosahedron $\mathcal{I}$, with energy

$$F_E^{\mathcal{I}} \equiv C_{\mathcal{I}} \cdot \frac{\pi Y}{72} R^2 + 12\, E_{core} = 0.604 \cdot \frac{\pi Y}{72} R^2 + 12\, E_{core} \ , \tag{83}$$

which serves to quantify the amount of geometric frustration, see GF theorem, present in an icosadeltahedral lattice (that is, one defined by the T-numbers). Note that the $C_{\mathcal{I}}$ is a *universal* constant, that is, independent of the potential or the nature of the particles. This type of universal predictions as well as general relations, such as the screening condition Eq. (80) makes the continuum approach very valuable. Because these predictions are universal, we can use any particle potential to describe the interactions. For example a simple repulsive potential such as the ones described by

$$V(r) = \frac{e^2}{r^\gamma} \quad 0 < \gamma < 2 \ . \tag{84}$$

Using Ewald summations, it is possible to calculate the total energy of a "perfect" triangular lattice, the constant F_0 (Eq. (14)) and Y the Young modulus [180]

$$\begin{aligned} Y &= 4\eta(\gamma) \frac{e^2}{A_C^{1+\gamma/2}} \ , \\ \frac{F_0}{Me^2} &= \theta(\gamma) \left(\frac{4\pi}{A_C}\right)^{\gamma/2} + \frac{\pi}{A_C R^{\gamma-2}} \rho(\gamma) \ , \end{aligned} \tag{85}$$

where $\eta(\gamma)$, $\theta(\gamma)$ and $\rho(\gamma)$ are potential-dependent coefficients, whose precise value is given in Ref. [167] (Table 2) and A_C is the area per particle, which for M particles on the sphere is $A_C = 4\pi R^2/M$. Introducing the Young modulus Y into Eq. (82) gives

$$F_E^{12} = \frac{4\eta(\gamma)}{(4\pi)^{1+\gamma/2}} \frac{\pi}{72} C(i_1 \ldots i_{12}) M^{1+\gamma/2} \frac{e^2}{R^\gamma} + 12 E_c \ . \tag{86}$$

Table 2
Comparison between the analytical Eq. (88) and numerical Eq. (89) for the coefficient $a_1(\gamma)$. More extensive cases are discussed in Ref. [167].

γ	$a_1(\gamma)$	(n,n)	$(n,0)$
1.5	1.51473	1.51454(2)	1.51445(2)
1.25	1.22617	1.22599(7)	1.22589(7)
1.0	1.10494	1.10482(3)	1.10464(3)
0.75	1.04940	1.04921(6)	1.04910(6)
0.5	1.02392	1.02390(4)	1.02372(4)

Thus, the calculation using the simple potential Eq. (84) consists of a zero point energy (Eq. (85)), which has been previously defined in Eq. (14)), and another contribution from the twelve disclinations Eq. (83) or Eq. (82). If we assume that those are all contributions to the energy, then we can write

$$F_T = \left(\frac{M^2}{2^{\gamma-1}(2-\gamma)} + \left[\frac{\theta(\gamma)}{(4\pi)^{\gamma/2}} + \frac{4\eta(\gamma)}{(4\pi)^{1+\gamma/2}} \frac{\pi}{72} C(i_1, \ldots, i_{12}) \right] M^{1+\gamma/2} + \mathcal{O}(M^{\gamma/2}) \right) \frac{e^2}{R^\gamma} , \tag{87}$$

which shows that the energy can be expressed for the large M expansion of the form:

$$F_T = \frac{e^2}{2R^\gamma} \left[a_0(\gamma) M^2 - a_1(\gamma) M^{1+\frac{\gamma}{2}} + a_2(\gamma) M^{\frac{\gamma}{2}} + \cdots \right] , \tag{88}$$

where $a_0(\gamma) = 2^{1-\gamma}/(2-\gamma)$ and the subleading coefficients $a_i(\gamma)$ depend explicitly on the potential and on the positions and number of disclinations. The first (non-extensive) term is proportional to M^2 and is usually canceled by a uniform background charge for a Wigner crystals of electrons in jellium models [184].

The expansion Eq. (88) gives an analytic expression for the first two coefficients $a_0(\gamma)$, $a_1(\gamma)$. Given that $a_0(\gamma)$ does not depend on the position of the defects, the $a_1(\gamma)$ coefficient maybe numerically obtained by explicitly constructing the (n, m) icosadeltahedral lattices with particles interacting with the potential Eq. (84) and computing the limit

$$a_1^{(n,m)}(\gamma) = \lim_{M\to\infty} \frac{2R^\gamma E_G/e^2 - a_0(\gamma) M^2}{M^{1+\gamma/2}} . \tag{89}$$

The results, shown in Table 2 show an agreement of 4–5 significant digits. This is remarkable, specially given that two terms, which should contribute at this order, see Eq. (66), have been ignored. For all values of γ, it is true that

$$a_1(\gamma) > a_1^{(n,n)}(\gamma) > a_1^{(n,0)}(\gamma) . \tag{90}$$

We should emphasize that the coefficient $a_1(\gamma)$ is computed by using $C^{\mathcal{I}}$, defined in Eq. (83), thus providing a very stringent test of the universality.

We finally note that Eq. (90) strongly suggests that Eq. (88) for the a_1-coefficient is missing at least one term, which is positive and sensitive to different icosadeltahedral lattices. This term does not come from the extrinsic curvature Eq. (41) and other terms previously considered, as those contribute to $a_2(\gamma)$, as discussed in Ref. [167]. In virus shells, the explicit form of the potential among components, needed to calculate the elastic constants, is very difficult to calculate. Still, whatever is the form of that potential, its net effect is to provide a value for Eq. (85), which shows that the icosahedral symmetry of the 12 disclinations, the icosadeltahedral lattices, in the (global minimum) equilibrium follow as an unambiguous and universal prediction of continuum elasticity. There are many more universal predictions, like the growth of the elastic energy as R^2 and many others discussed further below. Finally, although its contribution is clearly small, the clarification of the missing term implied by Eq. (90) might be necessary for a complete understanding of the mechanics of virus capsids.

4.4.3. Spherical crystals with boundaries

It is instructive to consider a crystal of radius R_m (see Fig. 27) constrained on a sphere with radius R. This problem illustrates the role of boundaries in curved space elasticity as it adds the possibility to submit the crystal to a tensile or compressible force (σ_b) at the boundary [172,213,214]. The main qualitative aspects of this problem are summarized in Fig. 27(b, f, g), which shows the different situations that may occur, namely:

- E_{core} small: if $R_m/R \ll 1$, the spherical cap is "neutral" (net disclination charge is $= 0$, Fig. 27b), while for $R_m/R \sim 1$ it is "charged"(net disclination charge is > 0, Fig. 27f), so there is a critical value $R_c/R \equiv r_c$ where the system has a transition. If $a/R_m \gg 1$ additional m-scars will also be developed to relieve the excess geometric frustration.
- E_{core} large (Fig. 27g): Disclinations are forbidden: the crystal consists of defect free ribbon domains.

Neutral finite length grain boundaries are sometimes referred to as "pleats" [170]. Furthermore, the precise meaning of a large or small core energy has not yet been clarified. Let us note that a defect free spherical cap of radius R_m will have

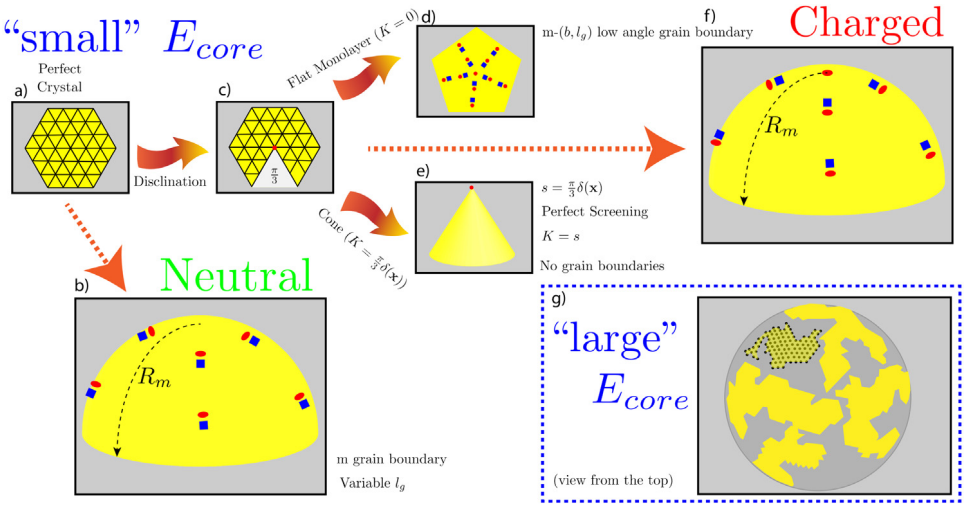

Fig. 27. Illustration of the generation of scars: (a, c) Volterra construction of a disclination from a triangular lattice; (d) if the crystal is constrained to a plane, and m-(b, l_g) grain boundary (Burger's vector b, with dislocations separated by l_g lattice constants, screens the curvature eliminating the R^2 growth in the free energy Eq. (32)). (e) If, the plane is allowed to buckle, a cone forms, see Fig. 23. (f) A scar is a compromise between these two limits (d and e), where the grain boundary develops a variable spacing. (b) Another possibility is a neutral defect structure, with grain boundaries compensating for the curvature. (g) If E_{core} is large, then defects become forbidden and the crystal breaks down into flat ribbons free of any disclinations.

an elastic energy [213]

$$F_E = \frac{\pi}{364} Y R^2 \left(\frac{R_m}{R}\right)^6 \propto R_m^6 \,. \tag{91}$$

If defects are allowed (core energy small), then the cost of this term is avoided by generating disclinations before the domain becomes too large and the hefty R_m^6 cost takes place. If defects are forbidden (large E_{core}), then this R_m^6 is avoided by branching into ribbons, where the width w is small, so that these ribbons are basically cylinder patches, see Fig. 23. The elastic energy of a ribbon, approximated as a rectangle of width w and length $l_R \gg w$ is [146]:

$$F_E = \frac{9}{5120} Y R^2 \left(\frac{w}{R}\right)^5 \frac{l_R}{R} \,, \tag{92}$$

which is indeed small. The ribbon occurs at a much larger line tension cost due to the boundaries, but, without the possibility of generating defects, it is still much more favorable than the R_m^6 growth implied by Eq. (91).

The elucidation of the neutral to charged transition has important implications for virus self-assembly [214]. A geometric approach to this problem is described in Fig. 27. Following Ref. [177], one considers an isosceles triangle whose edges have length ρ on the sphere (the method is easily generalized to any other curved geometry). The length of the third edge $l(\rho)$, then is

$$H(\rho) = l(\rho) - \rho = \pm n_l a \tag{93}$$

where a is the lattice constant, n_l is an integer, and $\alpha = \frac{\pi}{6-q}$ in Fig. 28a). This is the geometric implementation of the principle for the best possible tiling with equilateral triangles, which gives the lowest elastic energy, Eq. (35).

In Fig. 28b the function $H(\rho)/R$ is shown for a spherical cap and for a plane, where the function is linear. Also in Fig. 28 the elastic free energy Eq. (33) is shown. The value for r_c is obtained by imposing that the perfect screening condition is satisfied on the spherical crystal as a whole

$$\int d^2\mathbf{x} s(\mathbf{x}) = \int d^2\mathbf{x} K(\mathbf{x}) \to \frac{\pi}{3} = 2\pi(1-\cos(r_c)) \,, \tag{94}$$

or $r_c = \arccos(5/6) = 0.59$. The geometric approach embodied by Eq. (93) is general and makes use of the discrete free energy Eq. (33). The same problem has also been discussed within continuum elasticity [172,214]. A common approach consists in solving Eq. (66), namely

$$\frac{1}{Y}\Delta^2 \chi^{II} = s(\mathbf{x}) - K(\mathbf{x}) \,, \tag{95}$$

where the Laplacian Δ is that of flat space(compare with Eq. (66)) with boundary conditions. This is an expansion in low curvature, which becomes asymptotically exact for $R_m/R \ll 1$, see Ref. [164]. Analytical expressions for the Airy function

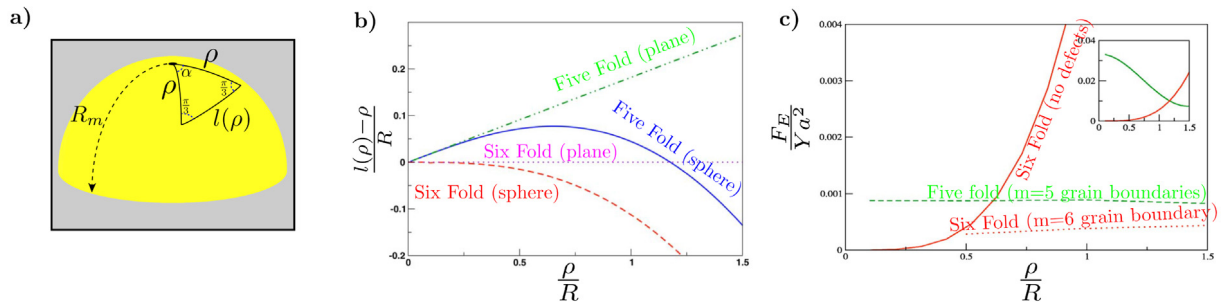

Fig. 28. Spherical cap: (a) Description of the calculation implied by Eq. (93). (b) The function $l(\rho)$ and the energy of the wedge. (c) Energy corresponding to $R_m/a = 50$, see Ref. [177]. The region where the single disclination becomes favorable to the neutral configuration is expanded in the inset.

within the small curvature expansion, with and without disclinations, are available in Ref. [214]. The more challenging case of a spherical cap with an off-centered disclination has been solved by Grason [215].

It should be noted, that the actual value r_c where a "charged" over a "neutral" domain is preferred depends on how r_c is precisely defined. If one considers a neutral domain where defects enter through the boundary, a recent calculation predicts $r_c \sim 0.66$ [160], in (approximate) agreement with our previous estimates. Comparing a neutral domain with one with a disclination at the center, gives $r_c \sim 0.81$ [184,215]. These results have important implications for the dynamics of viruses and will be described further in this review. As mentioned before, no virus with scars (dislocations) have been found; larger viruses adopt conical, see Fig. 27 or cylindrical shapes, see Fig. 38, thus avoiding the presence of dislocations.

4.4.4. Dynamic geometry: von Kármán equations

All the cases discussed so far have considered a frozen geometry, but there are many important effects that occur when the geometry itself is dynamical and allowed to fluctuate. Obviously, the problem becomes more involved, as the order (of the crystal) influences the geometry and vice versa, Thus adding additional degrees of freedom to the problem. Fluctuations in geometry may occur due to thermal effects or mechanical instabilities. The former is the subject of crystalline membranes, see Ref. [216], which are not central to the physics of viruses. In this review, we will focus on the latter. We first derive the general equations. For definiteness, we recall the free energy of the system, which is the sum of Eq. (49), Eq. (41), and Eq. (42):

$$F = F_E(\bar{g}_{ij}) + F_{extr} + F_{intr} \ . \tag{96}$$

We should note that these equations show *gauge invariance* as they remain invariant under global reparametrizations. We will therefore consider the Monge gauge, which parameterizes the surface as $\vec{r}(\mathbf{x}) = (x, y, \zeta(x, y))$ with the actual metric given by

$$g_{ij} = \begin{bmatrix} 1 + (\partial_x \zeta)^2 & \partial_x \zeta \, \partial_y \zeta \\ \partial_x \zeta \, \partial_y \zeta & 1 + (\partial_y \zeta)^2 \end{bmatrix} \tag{97}$$

The reference metric is $\bar{g}_{ij} d\bar{x}^i \bar{x}^j = \delta_{ij} d\bar{x}^i \bar{x}^j$, which is under the transformation $\bar{\mathbf{x}} = \mathbf{x} - \mathbf{u}(\mathbf{x})$ with the negative sign as a consequence of Eq. (12), equivalent to considering the Lagrangian elasticity, see Ref. [156]. Then, the reference metric is

$$\bar{g}_{ij} \approx \delta_{ij} - \frac{1}{2}(\partial_i u_j + \partial_j u_i) = \delta_{ij} - u_{ij} \ , \tag{98}$$

and the actual metric is approximated as

$$g_{ij} \approx \delta_{ij} + \delta_{ij} \partial_i \zeta \, \partial_j \zeta \ , \tag{99}$$

where both metrics are expressed in terms of the $\mathbf{x}$ coordinates. It is very important to notice that with our choice of reference metric Eq. (98), the curvature condition is automatically satisfied (as the curvature is the same as the metric δ_{ij}). defining

$$w_{ij} \equiv g_{ij} - \bar{g}_{ij} = u_{ij} + \partial_i \zeta \, \partial_j \zeta \ , \tag{100}$$

the free energy Eq. (45), including the approximation of small displacements $\partial_j u_i \ll 1$ as assumed in Eq. (102) reads (the expected elastic term)

$$F_E = \int d^2\mathbf{x} \left(\mu w_{ij}^2 + \frac{\lambda}{2} (w_{ii})^2 \right) \tag{101}$$

The extrinsic curvature has a simple form in the Monge gauge, namely

$$H = \delta_{ij}\partial_i\left(\frac{\partial_j\zeta}{(1+\delta_{ij}\partial_i\zeta\,\partial_j\zeta)^{1/2}}\right)\,, \tag{102}$$

and the metric determinant g is

$$g = (1+\delta_{ij}\partial_i\zeta\,\partial_j\zeta)\,, \tag{103}$$

which immediately leads to

$$\begin{aligned} F_{extr} &= \frac{\kappa_D}{2}\int d^2\mathbf{x}\sqrt{g}H^2 = \frac{\kappa_D}{2}\int d^2\mathbf{x}\sqrt{1+\delta_{ij}\partial_i\zeta\,\partial_j\zeta}\left(\partial_i\frac{\partial_i h}{(1+\delta_{ij}\partial_i\zeta\,\partial_j\zeta)^{1/2}}\right)^2 \\ &\approx \frac{\kappa_D}{2}\int d^2\mathbf{x}(\Delta\zeta)^2+\cdots\,, \end{aligned} \tag{104}$$

where $\Delta=\delta_{ij}\partial_i\partial_j$ is the flat Laplacian. Within the Monge gauge, the Gaussian curvature is

$$K = \frac{\partial_x^2\zeta\,\partial_y^2\zeta-(\partial_x\partial_y\zeta)^2}{(1+\partial_i\zeta\,\partial_i\zeta)^2} = \frac{1}{\sqrt{g}}\epsilon_{ij}\partial_i\Omega_j \tag{105}$$

where Ω_i has a complicated expression that will not be needed here, but it serves to illustrate that the term $\int d^2\mathbf{x}\sqrt{g}K$ is a total derivative (a topological term), as expected from the Gauss–Bonnet theorem, see Eq. (199).

Minimizing over ζ (geometry) and u_{ij} (order), the von Kármán (vK) equations, describing both defects and fluctuations of geometry, follow (where the rhs comes from the elastic free energy)

$$\kappa_D\Delta^2\zeta = [\chi,\zeta] \tag{106}$$

$$\frac{1}{Y}\Delta^2\chi = -\frac{1}{2}[\zeta,\zeta]\equiv -K \tag{107}$$

where $[a,b]=\epsilon_{\alpha\beta}\epsilon_{\mu\nu}\partial_\alpha\partial_\mu a\partial_\beta\partial_\nu b$, and the stress tensor is $\sigma_{\alpha\beta}=\epsilon_{\alpha\mu}\epsilon_{\beta\nu}\partial_\mu\partial_\nu\chi$. The covariant form of the $[a,b]$ symbol is

$$[a,b]=\frac{1}{g}\epsilon^{\alpha\beta}\epsilon^{\mu\nu}\nabla_\alpha\nabla_\mu a\nabla_\beta\nabla_\nu b\,, \tag{108}$$

which is necessary to write the vK equations in arbitrary coordinates (as done for shells with boundaries further below). Note that Eqs. (106) and (107) involve the geometry as a dynamical variable, different from our previous discussions where the geometry was fixed.

The vK equations are highly non-linear and, in general very difficult to solve. There are approaches, such as Ref. [217], that facilitate numerical solutions. It is convenient to define the Foppl–von Kármán (FvK) number γ [164,218] as

$$\gamma \equiv YL^2/\kappa_D$$

where L is a characteristic length of the problem. In order to properly visualize the importance of the FvK number, we will briefly discuss the case of a wedge of angle α and length L [218–220], see Fig. 30, for large values of γ, which as we further illustrate below, see Fig. 29, has important implications for the elasticity of virus capsids. If y are the coordinates perpendicular and x are along the wedge, let us define the quantities [218]

$$\begin{array}{llll} \bar\chi=\frac{\chi}{\kappa_D} & \bar\zeta=\frac{\zeta}{L} & \bar x=\frac{x}{L} & \bar y=\frac{y}{L} \\ \tilde\chi=\gamma^{-\delta/2}\bar\chi & \tilde\zeta=\gamma^{-\beta/2}\bar\zeta & \tilde x=\gamma^0\bar x & \tilde y=\gamma^{-\beta/2}\bar y \end{array}\,. \tag{109}$$

The first row defines dimensionless quantities, while the second defines the anomalous dimensions β,δ for length and energy, respectively. Note that the exponent for $\bar x$ is zero, as the coordinate along the wedge should scale with the distance and cannot develop anomalous dimensions. The extrinsic energy satisfies

$$\begin{aligned} F_e &\propto 1/Y\int dxdy(\Delta\chi)^2\propto\kappa_D\gamma^{\delta-1}\gamma^{\beta/2}(1/\gamma^{2\beta}+1) \\ F_{intr} &\propto \kappa_D\int dxdy(\Delta\zeta)^2\propto\kappa_D\gamma^{3\beta/2}(1/\gamma^{2\beta}+1) \end{aligned} \tag{110}$$

If both terms are of the same order, then it follows the scaling relation

$$\delta-\beta=1\,. \tag{111}$$

The value of the exponents β,δ maybe obtained from the vK equations rescaled according to Eq. (109). They are

$$\Delta^2\bar\zeta = [\bar\chi,\bar\zeta] \tag{112}$$

$$\Delta^2\bar\chi = -\frac{\gamma}{2}[\bar\zeta,\bar\zeta] \tag{113}$$

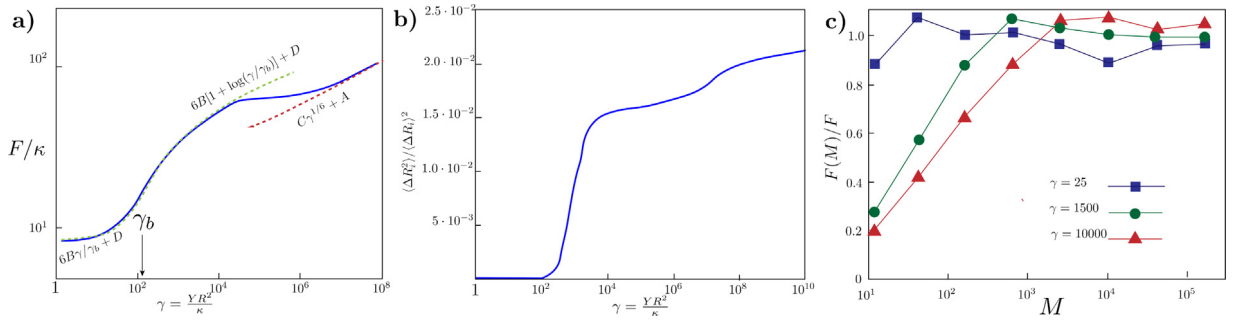

Fig. 29. (a) Free energy of the shell, the green dotted line is Eq. (126) while the red dotted line is Eq. (128), adapted from Ref. [221]. (b) Asymmetry of the shell quantified from Eq. (129), adapted from Ref. [221]. (c) Investigation of finite size effects measured from Eq. (132), adapted from Ref. [96].

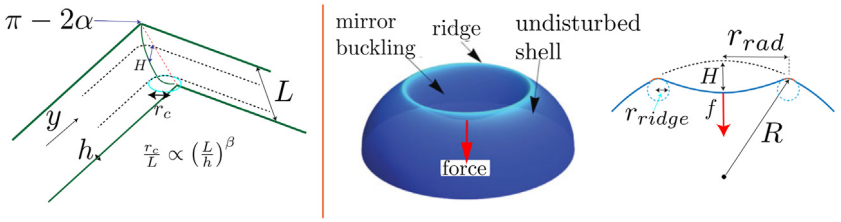

Fig. 30. Buckling of a simple ridge and the physical interpretation of the exponent β. Visualization of the solution to the Pogorelov problem, where an external force creates a ridge of curvature radius r_{ridge}. Also illustrated are the variables of the problem. Middle figure courtesy of D. Vella, see also Ref. [222].

Upon rewriting the quantities, we have

$$\gamma^{\beta/2}\left[\frac{\partial^4\tilde{\zeta}}{\partial\tilde{x}^4}+\gamma^{-\beta}\frac{\partial^4\tilde{\zeta}}{\partial\tilde{x}^2\partial\tilde{y}^2}+\gamma^{-2\beta}\frac{\partial^4\tilde{\zeta}}{\partial\tilde{y}^4}\right]=\gamma^{(\delta-\beta)/2}[\tilde{\chi},\tilde{\zeta}] \tag{114}$$

$$\gamma^{\delta/2-1}\left[\frac{\partial^4\tilde{\chi}}{\partial\tilde{x}^4}+\gamma^{-\beta}\frac{\partial^4\tilde{\chi}}{\partial\tilde{x}^2\partial\tilde{y}^2}+\gamma^{-2\beta}\frac{\partial^4\tilde{\chi}}{\partial\tilde{y}^4}\right]=-\frac{1}{2}[\tilde{\zeta},\tilde{\zeta}] \tag{115}$$

From equation the coefficients of both sides of the first equation one obtains the relation $\delta = -2\beta$, which substituted in the second provides

$$\beta = -1/3 \quad , \quad \delta = 2/3\,. \tag{116}$$

Further inspection rules out other solutions to Eqs. (114) and (115). Note that the scaling relation Eq. (111) is obviously satisfied. Thus, we reach the important conclusion that the energies scale as

$$\frac{F}{\kappa_D} \propto \gamma^{-\beta/2} = \gamma^{1/6} \quad \gamma \gg 1\,. \tag{117}$$

A more detailed calculation [218,220] gives

$$\frac{F}{\kappa_D} = 1.2\alpha^{7/3}\gamma^{1/6} \quad \gamma \gg 1\,. \tag{118}$$

The exponent β determines the radius of curvature r_c of the ridge according to

$$\frac{r_c}{L} \propto L^{\beta} = L^{-1/3}\,, \tag{119}$$

see Fig. 30. The above results are what is needed to describe the mechanics of viruses, which we discuss next. Interesting applications in other problems are described in the review by Witten [223].

4.5. Continuum theory of viral shells: Buckling and external forces

4.5.1. Magnitude of elastic constants

For M particles interacting with a given potential, such as $1/r^{\gamma}$ see Eq. (84), the elastic constants Eq. (85) are given by an energy $\mathcal{E}$ introduced by the potential divided by a lattice constant a square, $Y \sim \mathcal{E}/a^2$. The same calculations also

imply $\kappa_D \sim \mathcal{E}$. With these parameters, we find $\gamma \propto \mathcal{E}R^2/(\mathcal{E}a^2) \propto (R/a)^2 \gg 1$. Similar conclusions are reached if one (incorrectly) considers the elastic constants consisting of a three dimensional isotropic solid with Young Modulus Y_{3d} and Poisson ratio ν making a very thin capsid of width $h \ll R$. In that case [87], the 2D elastic constants are

$$\begin{aligned} Y &= hY_{3d} \\ \kappa_D &= \frac{h^3}{12(1-\nu^2)}Y_{3d} \\ \bar{\kappa_D} &= -\frac{h^3}{12(1+\nu)}Y_{3d}\ . \end{aligned} \tag{120}$$

where $\bar{\kappa_D}$ is the Gaussian bending rigidity. With these elastic constants, the FvK number of an object with dimension R is

$$\gamma = \frac{YR^2}{\kappa_D} = 12(1-\nu^2)\frac{R^2}{h^2} \equiv k_\nu^4 \frac{R^2}{h^2}, \tag{121}$$

with the last equation defines k_ν. Note that if Y, κ_D are known, an effective thickness maybe defined by $h = \gamma^{-1/2}R/k_\nu^2$.

From the above analysis one may be lead to the inescapable conclusion that the limit of large γ, described by the anomalous dimensions Eq. (116) is the only one that needs to be considered. However, this is not always the case, for at least two reasons: First, the description of the asymptotic limit defined by Eq. (116) not only requires $\gamma \gg 1$, but the more restrictive condition $\gamma \gg 10^6$ [218]. Second, and more relevant, in many problems such as colloidosomes [186], the value of κ_D is not determined by the interaction potential between particles, but rather, by the interaction between the particles and the interface (an oil-water interface). Therefore, if the particles are confined to an interface, the value of κ_D maybe tuned so that the FvK parameter takes any arbitrarily small value.

As they apply to viruses, typical values of γ are of 10^3 [221], much below the limit $\gamma \gg 10^6$, which would require T numbers of the order of 10^5. Furthermore, in many situations, there is the effect of scaffolding proteins, which provides a mechanism to tune the value of κ_D independently of the elastic constants.

4.5.2. Shells with boundaries: buckling transition

Fig. 27 defines a Buckling Transition (BT), where a $q = +1$ disclination buckles out of the plane leading to a crystal that satisfies the perfect screening condition and therefore has zero elastic energy. This defines the buckling transition for zero bending rigidity $\kappa_D = 0$, that is, for $\gamma \to \infty$. At finite FvK numbers, the actual geometry of the buckled disclination is not a cone, as this shape has very large bending energy.

The determination of shapes and energies for a buckled disclination for finite FvK was addressed in Ref. [164], where a disk of radius R with a disclination or a dislocation at its center was considered, see Fig. 22, showing that a buckling transition occurs for sufficiently large crystals

$$R > R_b \equiv c\left(\frac{3\kappa_D}{\pi Y}\right)^{1/2} \tag{122}$$

where $c = 13(q = +1), 14.2(q = -1)$. Here R_b is a critical buckling radius, such that only if the crystal size R is larger than R_b buckling will occur. Note that $R_b = 0$ if $\kappa_D = 0$, so buckling will always occur in the absence of bending rigidity, as expected from our previous intuition, see Fig. 23. The free energy of the buckled disclination is

$$F \equiv F_E + F_{extr} = B\kappa_D \log(R/R_b) + F_{in}(Y, \kappa_D) = \frac{\hat{c}}{2}\kappa_D \log(\gamma/\gamma_b) + F_{in}(Y, \kappa_D)\ , \tag{123}$$

where $B = 1.159(q = +1), 2.276(q = -1)$, and $F_{in}(Y, \kappa_D) = F_E(R_b, \Pi = 0)$, with $F_E(R, \Pi)$ the free energy of a flat disclination Eq. (32). Note that the large growth with R^2 in Eq. (32) is now replaced by a much more modest logarithm, as the Gaussian curvature is almost concentrated at the tip, where it is screened by the disclination. Similar results are available for dislocations, see Ref. [164], as well as grain boundaries [224].

Based on the scaling relations Eq. (117), the logarithmic regime defined by Eq. (123) cannot hold for sufficiently large γ. Therefore, there must exist a $\gamma_c \gg \gamma_b$, such that

$$F \approx \kappa_D\left(\tilde{C}\gamma^{1/6} + \tilde{A}\right) \quad \text{for } \gamma \gg \gamma_c. \tag{124}$$

In this case, the shape of the buckled disclination approaches that of an icosahedral, octahedral or tetrahedral vertex, see Fig. 23, with the energy concentrated or "focused" [223] along the edges.

4.5.3. Complete shells

A complete shell includes twelve $q = 1$ disclinations as the only defects, which follows from the topological condition Eq. (201). At sufficiently small FvK and for a large enough number of particles $M > M_C \approx 400$, scars emerge, see Figs. 25 and 27. Here, we concentrate on the relevant case for virus shells, in which the number of particles $M < M_c$ is small and thus no scars are present.

The free energy consists of the three extensible discussed contributions

$$F = F_E + F_{extr} + F_{intr} \ , \tag{125}$$

where F_E is given in Eq. (49), F_{extr} in Eq. (41) and F_{intr} in Eq. (42). The lattice version Eq. (73), is equivalent to the continuum. In Fig. 29A the free energy, computed with the lattice version, is shown as a function of the FvP parameter. From Eq. (123), for not too large values of γ one expects

$$F = \begin{cases} 6B\kappa_D\gamma/\gamma_b + D & \text{for } \gamma < \gamma_b \\ 6B\kappa_D[1+\log(\gamma/\gamma_b)] + D & \text{for } \gamma > \gamma_b \end{cases} \tag{126}$$

The extrinsic curvature is $H = 2/R$ for a sphere, so the D term results from Eqs. (41) and (42), giving $D = 4\pi(2 + \frac{\bar{k}}{\kappa_D})$, since

$$\int d\mathbf{x}\sqrt{g}H^2 = 4\int \sin(\theta)d\theta d\phi = 16\pi \quad \text{and} \quad \int d\mathbf{x}\sqrt{g} = 4\pi \ . \tag{127}$$

For large values of γ, the expectation, see Eq. (124), is

$$F = \kappa_D\left(C\gamma^{1/6} + A\right) \ , \tag{128}$$

with $C = 30\tilde{C}$ and $A = 30\tilde{A}$ as there are 30 ridges. Thus, there is a buckling transition at $\gamma \approx \gamma_b = 130$, and another transition towards the asymptotic rigid regime at $\gamma_c \approx 10^5$.

It is also of interest to investigate the asymmetry of the overall shell, defined as

$$\langle \Delta R_i^2\rangle / \langle \Delta R_i\rangle^2 = \frac{1}{M}\sum_{j=1}^{M}\frac{(R_j - \langle R\rangle)^2}{\langle R\rangle^2} \ , \tag{129}$$

which as shown in Fig. 29B illustrates the buckling transition for $\gamma \approx \gamma_b$.

The previous results are obtained for zero spontaneous curvature $H_0 = 0$, see Eq. (40). The generalization for non-zero spontaneous curvature adds a new dimensionless order parameter

$$\alpha \equiv \frac{2\theta_0 A^{1/2}}{\sqrt{3}a} \tag{130}$$

where A is the area of the shell, and θ_0 defines the spontaneous angle of curvature, defined in the discrete extrinsic curvature energy Eq. (147). It is related to the spontaneous curvature by

$$H_0^2 a^2 = \frac{12\sin^2(\theta_0/2)}{1 + 3\sin^2(\theta_0/2)} \ . \tag{131}$$

As discussed in Ref. [225], for increasing α the shell transition from spheres to cylinders and for increasing γ, the cylinders facet into polyhedra, similarly as discussed for spheres.

Virus shells are typically small, so it is of interest to investigate how fast the limit $M \to \infty$ is approached. This was addressed in Refs. [96,226], see Fig. 29C, where the ratio

$$F(M)/F(M \to \infty) \equiv F(M)/F \ , \tag{132}$$

measuring the free energy computed with a finite number of particles M relative to the thermodynamic limit is shown. For small values of γ the convergence to the thermodynamic limit is very fast; for example, for $\gamma = 25$ $M = 12$ (icosahedron), already converges, while for large values of $\gamma \sim \mathcal{O}(1000)$ the convergence does not occur until $M = 10^3$. Overall, Fig. 29C illustrates that the mechanical response of a small system (at large values of γ) may differ significantly from the one predicted by continuum models, see also the discussion in Ref. [226], which represent the thermodynamic limit. We should mention other interesting studies where defects are dynamically generated [227] or the shell consists of several particle species [188,228].

4.5.4. Shells under external loads

In the previous examples, we discussed the spontaneous buckling that would occur in an experiment where a disclination is inserted into an otherwise perfect planar lattice. Buckling may also be obtained as the result of imposing external tension [87] or a uniform external (osmotic) pressure [229]. A particular important case for viruses consists of the buckling that occurs following indentation, by, for example, a metallic tip. In its simplest formulation, the problem consists in characterizing the mechanical properties of a shell subjected to the action of a perpendicular force, known as the Pogorelov problem [87], which can be given a partial analytical solution. Even though the Pogorelov problem may be excessively simple for rigorous quantitative descriptions of mechanical properties, we will derive the general equations that include the necessary terms for a more rigorous description. In this way, the solution of the Pogorelov problem provides a practical example illustrating how to use these equations and hopefully will motivate future developments.

Our starting point are the vK equations Eqs. (106) and (107), which we write for an axisymmetric solution including an external force as

$$\begin{aligned}\kappa_D \Delta^2 \zeta &= \frac{1}{r}\frac{d}{dr}\left(\frac{d\chi}{dr}\frac{d\zeta}{dr}\right) - \frac{f}{2\pi r}\delta(r)\\ \frac{1}{Y}\Delta^2\chi &= -\frac{1}{2r}\frac{d}{dr}\left[\left(\frac{d\zeta}{dr}\right)^2\right],\end{aligned} \tag{133}$$

where $\Delta = \frac{1}{r}\frac{d}{dr}\left(r\frac{d}{dr}\right)$. Note that one can also include a pressure term on the equation, see Refs. [230,231]. The case of including a disclination has already been discussed in this review, see Ref. [164]. To our knowledge, the case of both a force and a disclination has yet to be solved. It is convenient to express the vertical displacement relative to the unperturbed spherical shell and define a derivative of the Airy function as a new variable

$$\zeta(r) = -\frac{r^2}{2R} + w(r) \quad \psi(r) = \frac{d\chi(r)}{dr}\,. \tag{134}$$

with these definitions, the vK Eq. (133) becomes

$$\begin{aligned}\kappa_D\Delta^2 w + \frac{1}{Rr}\frac{d(r\psi)}{dr} - \frac{1}{r}\frac{d}{dr}\left(\psi\frac{dw}{dr}\right) &= -\frac{f}{2\pi r}\delta(r)\\ \frac{r}{Y}\frac{d}{dr}\left[\frac{1}{r}\frac{d(r\psi)}{dr}\right] &= \frac{r}{R}\frac{dw}{dr} - \frac{1}{2}\left(\frac{dw}{dr}\right)^2 - \frac{r^2}{2R^2},\end{aligned} \tag{135}$$

and the stresses are $\sigma^{rr} = \psi/r$ and $\sigma^{\phi\phi} = \psi'$. From here onwards, we will follow the beautiful paper by Gomez et al. [222], and we refer there for further technical details or the derivation of many results.

A common situation in borrowing results for thin plates or shells from elasticity theory is that rather than using the FvK number the relevant results are expressed in terms of the shell thickness h. Given values of ν, R and γ a thickness h is defined by Eq. (121). The following dimensionless quantities

$$\rho = \frac{r}{(hR)^{1/2}} \quad , \quad W = \frac{w}{h} \quad , \Psi = \frac{\psi}{Yh} \quad , \quad \mathcal{F} = \frac{fR}{\kappa_D k_\nu^4}\,, \tag{136}$$

are introduced, so that the vK equations become

$$\begin{aligned}\frac{1}{k_\nu^4}\Delta^2 W + \frac{1}{\rho}\frac{d(\rho W)}{d\rho} - \frac{1}{\rho}\frac{d}{d\rho}\left(\Psi\frac{dW}{d\rho}\right) &= -\frac{\mathcal{F}}{2\pi}\frac{\delta(\rho)}{\rho}\\ \rho\frac{d}{d\rho}\left(\frac{1}{\rho}\frac{d(\rho\Phi)}{d\rho}\right) &= \rho\frac{dW}{d\rho} - \frac{1}{2}\left(\frac{dW}{d\rho}\right)^2 - \frac{h}{R}\rho^2 \quad .\end{aligned} \tag{137}$$

At leading order in $h/R \sim 1/\gamma^{1/2} \ll 1$ the last term maybe dropped, which is the physical statement that the stresses created as a consequence of the applied force $\mathcal{F}$ are much larger than the ones already present in the undisturbed shell, see the GF theorem. These equations must be supplemented with the boundary conditions

$$\begin{aligned}W(0) &= -\frac{H}{h} \equiv -\Delta\\ W'(0) &= 0\\ \lim_{\rho\to 0}[\rho\Psi'(\rho) - \nu\Psi(\rho)] &= 0\\ W(\infty) = W'(\infty) &= \Psi(\infty) = 0\,.\end{aligned} \tag{138}$$

Here $H = \Delta h$ is the depth at which the spherical shell is poked. The first equation is obvious from Fig. 30 as it expressed that the depth is, indeed H. The second states that the height is a minimum at the point of force application, the third is the statement that the displacement at the origin is zero (by symmetry) and the last equations state that sufficiently away from the application, the stresses are negligible. Since the force f and the depth $H = \Delta h$ are conjugate to each other, there is an equation of state $\mathcal{F}(\Delta)$ relating them. Eqs. (137) and (138) set up the full problem of indentation of a spherical shell. The full solution [222], see Fig. 30, establishes that:

- The elastic Energy is concentrated on a ridge of curvature radius

$$r_{ridge} = \sqrt{Rh}. \tag{139}$$

.

- The ridge is located at a radius

$$r_{rad} = \sqrt{R^2 - (R-H)^2} = \sqrt{HR} \gg r_{ridge}. \tag{140}$$

from the application of the force.

- The shape for $r \leq r_{rad}$ is given by an inverted spherical cap of radius R (mirror symmetry).
- The equation of state for $\Delta > 1$, is given by

$$\mathcal{F} = (1.67) 2\pi k_\nu^{-3} \Delta^{1/2} \equiv c_{exact} \Delta^{1/2} \ . \tag{141}$$

For the sake of historical comparison, the result by Pogorelov is $c_{pogo} = \frac{3\pi j_0}{12^{3/4}(1-\nu^2)}$, with $j_0 = 1.15092$. Note that the dependence on the Poisson ratio ν is different for c_{pogo} and c_{exact}.

It is possible to derive the above formulas by scaling arguments, similar to those used in Eq. (118) and discussions around it, see [87], but they require a discussion that is beyond the scope of this review. In full dimensional form, the equation of state is

$$\frac{H}{h} = \frac{f^2 R^2}{c_{exact}^2 \kappa_D^2 k_\nu^4} \ , \tag{142}$$

which shows that the dependence between H and f is not linear. This expression is equivalent to the one quoted in the book by Landau and Lifshitz [87]. Integration of Eq. (142) gives the free energy as

$$F = \kappa_D k_\nu^2 c_{exact} \frac{H^{3/2}}{R h^{1/2}} \ , \tag{143}$$

as quoted in [87].

For small forces, defined by $\Delta \ll 1$, there is a linear regime [231]

$$\mathcal{F} = \hat{k}_0 \Delta = \frac{8}{k_\nu^2} \Delta \ , \tag{144}$$

a result previously derived in Ref. [232]. with the deformation of the shell confined to a circle of radius $r = \sqrt{hR}/k_\nu \sim \sqrt{hR} = r_{ridge}$ around the indentation force. Also, for very large values $\Delta \gtrsim 12$, there is a secondary buckling transition where the full axisymmetric rotational symmetry breaks down into a more reduced p-fold ($p = 3, 4, \ldots$) symmetry [233,234], see Ref. [217] for a recent approach.

Applied to the case of virus shells, Eq. (142) has several limitations: (a) The shell is not spherical, but rather, icosahedral like, specially for large FvK parameters where the formula holds. Thus, the assumed shape is inconsistent with the actual shape. (b) The indentation force is exerted by a tip with finite thickness rather than a point force. (c) The response of the shell will depend on the location of the tip relative to the disclinations. Eq. (141) is the starting point to incorporate all these many effects.

The mechanical properties of a shell have been extensively investigated by numerical methods. First of all, If the equation of state is described by a power law it may be written as

$$\frac{H}{R} = \mathcal{F}(f/\sqrt{\kappa_D Y}) \ , \tag{145}$$

with the same $\mathcal{F}$ as in Eq. (141) (or the linear regime for small forces). Numerical solutions reported in Refs. [96,235] do show an approximate agreement with Eq. (145) for $\frac{H}{R} \lesssim 0.3$, although the data is more consistent with a linear regime.

A related problem is the mechanical response of a virus capsid under and an external pressure, which has been numerically investigated by Siber [226], showing that the Buckling transition is unaffected by small enough pressures, thus occurring at $\gamma \approx \gamma_b$ at any external pressure $P \lesssim 0.3Y/R_v$, where R_v is the radius of the shell at $\gamma \to 0$. To our knowledge, analytical solutions for this problem have not been developed.

4.6. Equilibrium structure of small protein shells (discrete model)

In previous sections we showed that, based on continuum elasticity theory, the minimum energy structures assume configurations with icosahedral symmetry (or cylindrical-like structures). However, many protein cages like clathrins, ferritins, and carboxysomes [236], assemble spontaneously to form other types of symmetric shells. Indeed the *in vitro* self-assembly studies of viral shells reveal in addition to icosahedral symmetry, structures with octahedral or cubic symmetries also form [237]. A complete account of the location of the defects in these structures and their symmetry as a function of their physical properties is not, at present, completely understood.

To study the factors that contribute to the symmetry or location of pentamers in the small protein cages, Panahandeh et al. [236] performed a series of MC simulations using equilateral triangular building blocks, along the lines of Eq. (33). Equilateral triangles provide a universal description of the building blocks of protein shells: They can form a hexagonal sheet in the flat space and assemble into pentagons or disclinations, which is necessary in the curved space. To obtain the equilibrium structures of protein nanoshells, Panahandeh et al. calculated the total energy of a triangular network involving both the stretching and bending energies. A triangular mesh defines a reference metric where all triangle edges have the same distance b_0, and an actual metric in which this distance, after deformation is given by b_i^a, the length of the ath edge in the ith subunit. Then, in this notation, the discrete model of Eq. (33) is

$$E_s = \sum_i \sum_{a=1}^{3} \frac{k_s}{2} (b_i^a - b_0)^2 \tag{146}$$

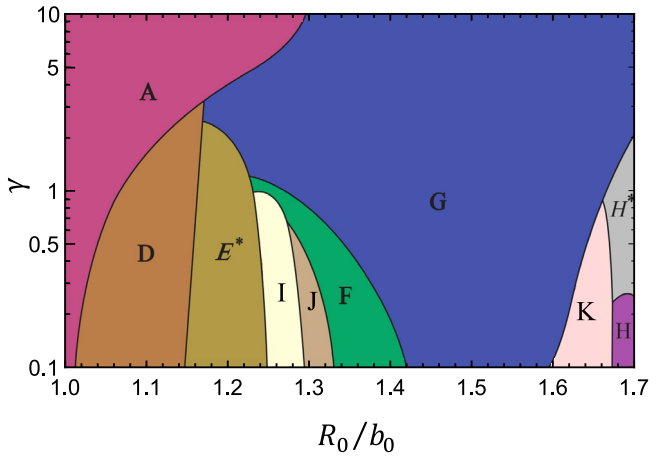

Fig. 31. Phase diagram of the equilibrium structures of different protein cages for various values of γ and R_0/b. Each shaded area is related to a single structure. The regions $A-K$ correspond to shells with $n_s = 20,\ 28,\ 36,\ 50,\ 60,\ 80,\ 40,\ 44$ and 76 subunits. The symmetry of each structure is illustrated in Fig. 32. For H and H^* structures $n_s = 80$.
Source: Adapted from [236].

The stretching energy involves with the deformation of triangles from the equilateral shapes. The bending energy can be derived from Eqs. (69) and (70), and can be written as

$$E_b = \sum_{\langle ij \rangle} k_b(1 - \cos(\theta_{ij} - \theta_0)) \tag{147}$$

with $\langle ij \rangle$ the index pairs of adjacent triangles, k_b the torsional spring constant, and θ_0 the preferred dihedral angle between two adjacent subunits, the discrete version of Eq. (40). The angle θ_0 corresponds to the radius of curvature through $\sin(\theta_0/2) = (12R_0^2/b_0^2 - 3)^{-1/2}$ with R_0 the spontaneous radius of curvature. The angle θ_{ij} is between the unit normal vectors $\hat{n}_i$ and $\hat{n}_j$ of the two adjacent subunits i and j ($\cos\theta_{ij} = \hat{n}_i \cdot \hat{n}_j$), respectively.

Two dimensionless parameters can then be readily identified: the spontaneous radius of curvature R_0/b_0 and the Foppl von Karman (FvK) number

$$\gamma = k_s b_0^2/k_b \ . \tag{148}$$

Panahandeh et al. performed a series of Monte Carlo simulations to obtain the lowest-energy configurations [238] for a triangulated spherical lattice with a random distribution of N_v vertices [236]. Their MC moves were designed such that the locations of disclinations were not fixed: pentamers and/or hexamers could move in order to obtain the minimum energy structures. The results of the simulations for all the structures ranging from $N_v = 12$ to 42 corresponding to the shells made of $n_s = 20$ to 80 number of subunits are illustrated in Fig. 31 in the form of a "shape" phase diagram of spontaneous radius of curvature R_0/b_0 and γ. Each colored region in the diagram corresponds to a single shell, which is shown with the same letter in Fig. 32. The phase diagram indicates that for small γ's where the bending energy is dominant compared to the stretching energy, the structure of shells is sensitive to the spontaneous radius of curvatures, *i.e.*, the size and symmetry of the shells change with the spontaneous radius of curvature. In contrast, for larger γ's, Fig. 31 shows that the structures with icosahedral symmetry are the dominant ones. This is consistent with the results of the continuum elasticity theory where structures with icosahedral symmetry constitute the minimum energy structures. We emphasize that at large γ, the stretching energy is dominant over the bending energy, a limit that has been discussed extensively further above.

It is important to note that Paquay et al. studied the equilibrium structures of interacting Morse particles placed on the surface of a sphere as a function of temperature and found that icosahedral shells are the most robust one against thermal fluctuations [239].

The structures illustrated in Fig. 32 reveal the sensitivity of the shell symmetries with respect to the position of pentamers. Despite this sensitivity, under many circumstances viral shells or other protein nanocages assemble spontaneously *in vitro* to form structures with icosahedral or other symmetries. This raises the following important questions: What properties of diverse coat proteins, common among all of them, lead to the assembly of nano-shells with a specific size and symmetry? And what are the minimum design principles necessary for the formation of the symmetric shells? These questions were addressed by Wagner and Zandi [240] who employed a very simple growth model to explain why shells with the same symmetries were observed in many disparate biological systems. In particular, the focus of their work was whether the path to the icosahedral structures needed to be reversible all the way through the shell completion.

Wagner and Zandi [240] studied the irreversible growth of small shells following the local minimum energy path, which was based on the following assumptions: A new triangle was added at the boundary of a growing shell such that

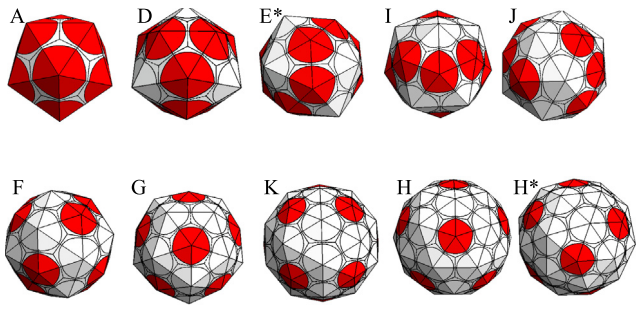

Fig. 32. The shells corresponding to the shaded regions in the phase diagram of Fig. 31. The structures from left to right and top to bottom correspond to $n_s = 20,\ 28,\ 36,\ 40,\ 44,\ 50,\ 60,\ 76,\ 80$ and 80 subunits with icosahedral ($T = 1$), tetrahedral, D_2(tennis ball), D_2, D_2, D_3, icosahedral ($T = 3$), tetrahedral, icosahedral ($T = 4$) and D_{5h}, respectively.
Source: Adapted from [236].

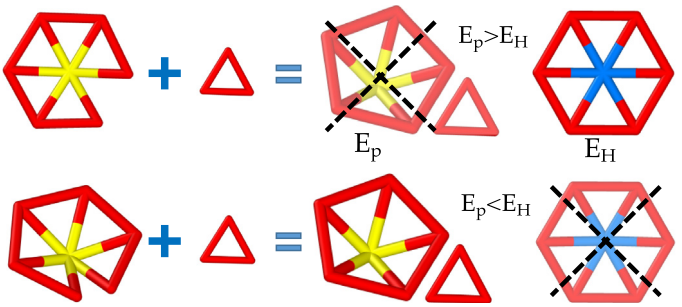

Fig. 33. The process of formation of a hexamer and a pentamer: The top figure corresponds to the case in which five trimers join at a vertex with an opening angle close to $\pi/3$ but the bottom to an angle much smaller than $\pi/3$. Depending on the energy per subunit a pentamer E_p or a hexamer E_H forms.
Source: Adapted from [160].

it would have the maximum number of bonds with the adjacent subunits. This mimics the condition under which the attractive interaction between subunits is weak and thus coat proteins can move around and explore the free energy landscape. Nevertheless once a pentamer or hexamer formed, the interactions become so strong that it can no longer dissociate and the process becomes irreversible.

The process of formation of a pentamer based on the minimization of local energy is illustrated in Fig. 33. During the simulations after the completion of each pentamer or hexamer, the triangular lattice relaxes to the minimum energy configuration [240]. The irreversible structures obtained based on this algorithm Ref. [240] are illustrated in the form of a phase diagram of the dimensionless ratio of bending to stretching modulus (γ) and the spontaneous radius of curvature in Fig. 34. Similar to the equilibrium phase diagram, each region in the irreversible diagram refers to a different symmetric structure noted with a capital letter and illustrated in Fig. 32. The shells appearing only in the irreversible phase diagram are shown in Fig. 35.

Unlike the equilibrium phase diagram, there is a white region in the irreversible diagram in which only irregular structures form. There are indeed some noticeable differences between the two phase diagrams, see Figs. 31b and 34. Two small regions (structures B and C) in the irreversible phase diagram (Fig. 34) corresponding to $n_s = 24$ and 26 do not constitute the minimum free energy structures. In the equilibrium phase diagram, they are both replaced by the structure D, a clathrin shell, which has $n_s = 28$ and is called mini-coat. The other clathrin shells, hexagonal barrel (structure E) obtained in the irreversible growth has $n_s = 36$ with D_{6h} dihedral symmetry. The equilibrium structure of the shell with the same $n_s = 36$ has the symmetry of a tennis ball, the structure E^* in Figs. 31b and 34. The E and E^* structures have the same number of subunits but different symmetries.

Nevertheless, there are striking similarities between equilibrium and irreversible phase diagrams. This is rather unexpected, considering the irreversibility of assembly and the fact that the principles of detailed balance is violated in this growth process. In fact, due to the irreversible steps, the grown structures could be completely far from equilibrium, but we still observe that the two phase diagrams are quite similar. We will explain the physics behind these similarities in the continuum model below.

The above equilibrium and irreversible structures were obtained under the condition when the spontaneous radius of curvature is small, corresponding to $T \leq 4$. In the next section, we review the assembly of larger shells.

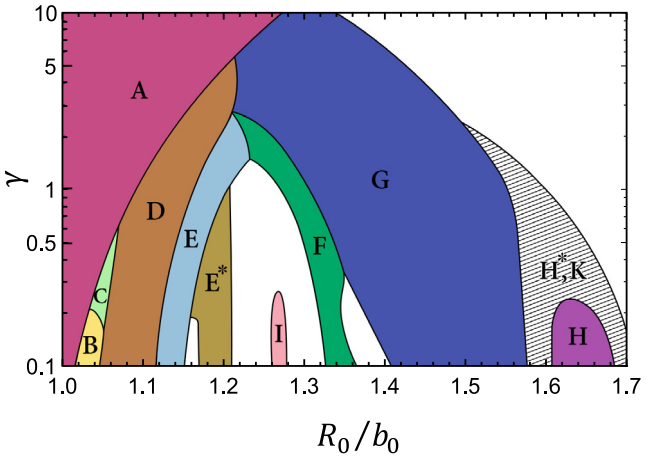

Fig. 34. Phase diagram of the irreversible growth: the shaded regions denoted by letters (A) through (H) correspond to only one type of symmetric shell. However, in the hashed region several irregular structures assemble in addition to (H^*) and (K) shells. The structure K forms at the phase boundary between H^* and the neighboring white region. Different types of structures without any specific symmetry form in the white regions. *Source:* Adapted from [240].

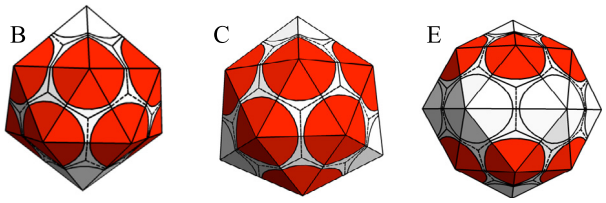

Fig. 35. The symmetric protein cages appearing only in irreversible assembly conditions. The structures from left to right have $n_s = 24,\ 26$ and 36 subunits with D_6, D_3 and D_{6h} symmetry respectively. They are denoted by $B,\ C$ and E. [236].

4.7. Equilibrium structures of large shells

Fig. 36 shows several large viral shells ($T > 4$) with icosahedral symmetry. Based on the results of continuum elasticity theory and the simulations obtained in Figs. 31b and 34, one expects that large icosahedral structures also could readily assemble if both γ and the spontaneous radius of curvature, R/b_0 are large. Quite unexpectedly, this is not the case: During the simulations, when the radius of spontaneous curvature R_0/b_0 was increased, no empty large icosahedral shell were formed [241]. In fact, Ning et al. [241] thoroughly studied the formation of shells for large R/b_0 and high γ's and only cylindrical or conical structures were obtained in their simulations, which are pertinent to the structure of retroviruses. Fig. 37 shows the step by step growth of a conical and cylindrical shell [242]. The spontaneous radius of curvature for the conical capsid is slightly smaller than the cylindrical one.

In the case of conical capsids, as the curved lattice grows, the inclusion of pentamers (disclinations) becomes unavoidable in order to relieve accumulated stress. However, as the spontaneous curvature decreases, the shell can grow without the inclusion of a disclination. As illustrated in the figure, the opposing edges of the growing shells eventually curl and reach each other, becoming connected by the presence of an attractive potential mimicking the hydrophobic interaction between the proteins [242]. Conical shapes therefore emerge through simple irreversible growth of elastic sheets. The cylindrical capsids form if the radius of spontaneous curvature is so large that no pentamer is energetically allowed to form [242].

These studies show that large viruses, such as the ones presented in Fig. 36, cannot just spontaneously grow from their building blocks, and a more complex mechanism is in place. In fact, structures illustrated in Fig. 36 and in general all viral shells with $T > 4$ need scaffolding to form structures with icosahedral symmetry, which we will discuss next.

4.8. Elasticity theory of the assembly of virus shells by scaffolding proteins (or inner core)

Many experiments show that all structures illustrated in Fig. 36 need scaffolding proteins to successfully assemble (note that all of them display icosahedral order). A minimal model for scaffolding was considered in Ref. [166], where it was represented as a large spherical core that interacted attractively with the triangular subunits, implemented through Lennard Jones potential. The dynamics of the shell growth was the same as the one explained for the small ones in the

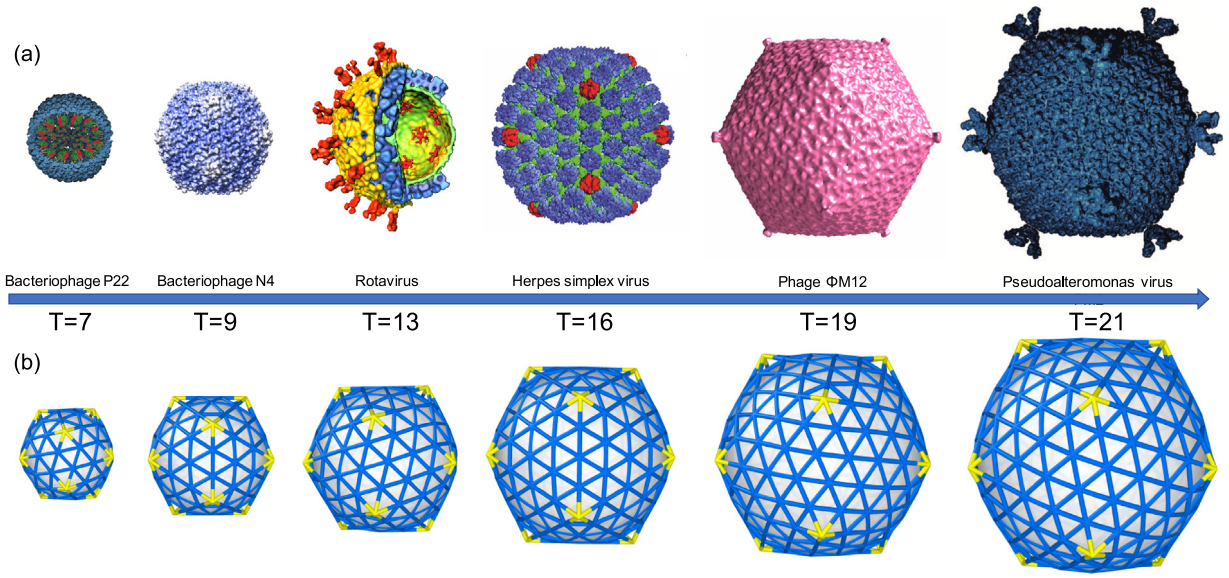

Fig. 36. (a) From left to right: Bacteriophage P22 [243], Bacteriophage N4 [244], Rotavirus [245], Herpes simplex virus [246], Phage ΦM12 [247] and Pseudoalteromonas virus [248]. The T number of each capsid is presented below it. The scaffolding proteins and hydrogenases inside the capsid of Bacteriophage P22 and the inner shell of Rotavirus are also shown in the figure. All viruses in the figure need scaffolding proteins as illustrated for Bacteriophage P22. Rotavirus is the one virus in the figures that needs a preformed scaffolding layer. Fig. 1b. From left to right: $T = 7$, $T = 9$, $T = 13$, $T = 16$, $T = 19$ and $T = 21$. They are all obtained in the simulations.
Source: Adapted from [160].

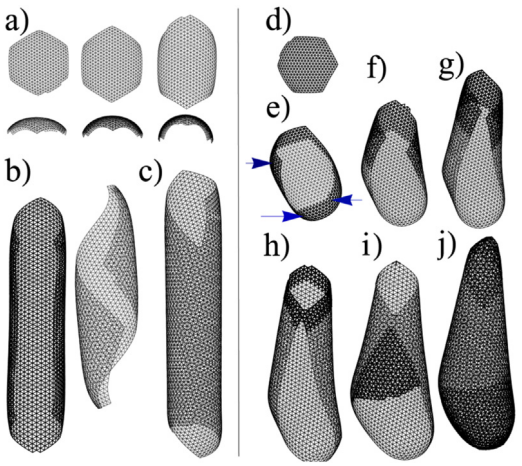

Fig. 37. (a–c) shows the snap shots of simulations of the growth of a cylindrical tube. (d–j) illustrates the snap shots of simulations for the formation of a conical shell. Three arrows in (e) indicated the position of three pentagons.
Source: Adapted from [242].

previous section and is illustrated in Fig. 33. Several snapshots of the growth for a $T = 13$ structure are illustrated in Fig. 38, with the size of the spherical core chosen to commensurate with $T = 13$ number.

Quite amazingly, in the presence of scaffolding layer, the irreversible dynamics defined in Fig. 33 resulted in structures with icosahedral symmetry. All structures between $T = 7$ and $T = 21$ were tested in Ref. [160] and in all cases the icosahedral symmetry was achieved without a single error. As explained previously, the symmetry of a shell is very sensitive to the location of its pentamers. Indeed, the formation of icosahedral structures through the irreversible growth model with a huge number of subunits involved, is quite unexpected.

To explain these results, Li et al. [160] resorted to the continuum elasticity theory as described in the previous section, see Eq. (66) for the Airy function, Eq. (67) for the stress and Eq. (68) for the free energy. They considered a spherical cap with an aperture angle θ_m and the geodesic radius $R_m = \theta_m R$, as illustrated in Fig. 38b.

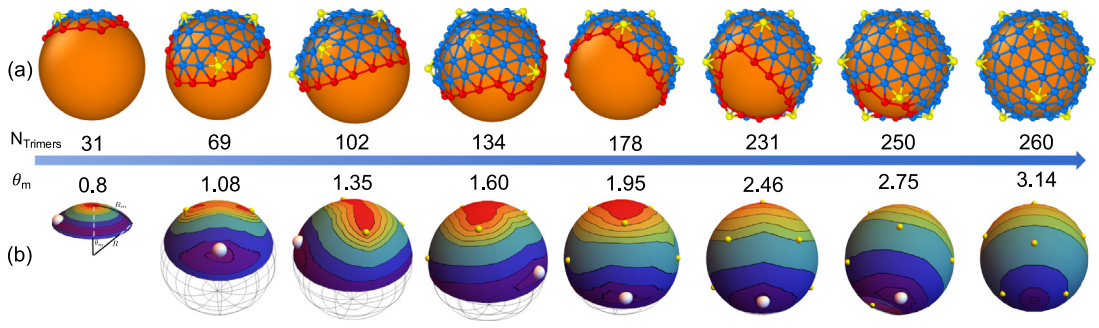

Fig. 38. The first row shows the snapshots of simulations and the second row the results of the continuum theory for the assembly of a $T = 13$ structure. The triangles in the caps represent the trimers. The yellow vertices correspond to pentamers, blue ones to hexamers and red ones to the cap edge. The preformed scaffolding layer or inner core is illustrated with the gold core. The caps in the second row show the energy contourplots with the most recent disclinations (the largest yellow ball) forming in the purple energy well. The geodesic shell size is denoted with $R_m = R\theta_m$. The red region has the highest energy and purple the lowest one.
Source: Adapted from [160].

For the spherical cap shown in Fig. 38b, the actual metric is $ds^2 = g_{\mu\nu}dx^\mu dx^\nu = dr^2 + R^2\sin^2(r/R)d\phi^2$, with the stress free boundary conditions, $\sigma^{rr} = \sigma^{\phi r} = 0$. With the above definitions, the topological constraint Eq. (201) is satisfied exactly for a sphere. The energy then becomes

$$F_c^l(\theta_m, \mathbf{x}_i) = E_0(\theta_m) + \sum_{i=1}^{N} E_{0d}(\mathbf{x}_i, \theta_m) + \sum_{i=1}^{N}\sum_{j=1}^{N} \hat{E}_{dd}(\mathbf{x}_i, \mathbf{x}_j, \theta_m) \tag{149}$$

with E_0 is the free energy of the hexamers, E_{0d} the interplay between Gaussian curvature and pentamers and $\hat{E}_{dd}$ describes disclination(pentamer) interactions. It is convenient to separate this last term as

$$F_c^{dd} = \sum_{i=1}^{N}\sum_{j=1}^{N} \hat{E}_{dd}(\mathbf{x}_i, \mathbf{x}_j, \theta_m) = \sum_{i=1}^{N} E_{self}(\mathbf{x}_i) + \sum_{i=1}^{N}\sum_{j>i}^{N} E_{dd}(\mathbf{x}_i, \mathbf{x}_j), \tag{150}$$

where $E_{self}(\mathbf{x}_i)$ is the disclination self-energy, which depends on the location of a pentamer relative to the boundary and E_{dd} is the disclination–disclination interaction.

Fig. 38b illustrates the growth of a spherical cap as a function of time whose size monotonically changes from $\theta_m = 0$ to $\theta_m = \pi$. For each cap with the size θ_m, the free energy given in Eq. (149) is calculated and compared to the one with an additional new defect (local condition) [160]. Once Li et al. found that the latter one is favorable, they added a new defect to the cap. Their calculations show that for small values of θ_m, the cap grows without any defects. However, to some extent quite counter intuitively, the first disclination appears off center, resulting from the competition between the disclination self-energy promoting the formation of disclination at the boundary and the Gaussian curvature–disclination interaction E_{0d} whose minimum energy occurs at the cap center. The calculation performed in Ref. [160] shows that as the size of the cap increases, the formation of a new disclination becomes energetically favorable in that an energy well appears attracting a new disclination. Fig. 38b illustrates the contour plots of total elastic energies for spherical caps with $\theta_m = 0.8$ through $\theta_m = \pi$. In each plot the bigger ball shows the position of the last energy valley, in which the next disclination will form. Amazingly, both in the continuum model and simulations, the disclinations (pentamers) always form at the locations that later in the growth process will become the vertices of an icosahedron.

To understand the role of stress in the formation of icosahedral symmetry, the stretching energy vs. N (number of subunits assembled) for a $T = 13$ shell is illustrated in Fig. 39 for six different values of FvK number $\gamma > 1$. If γ is small, the shell does not form icosahedral structures and the elastic energy of the cap grows more or less linearly with the number of subunits N, see the thick black line in Fig. 39 for $\gamma = 2$. However, for higher γ-values, the pentamers appear one by one exactly at the vertices of an icosahedron as the shell grows. As each pentamer forms, the elastic energy of the cap drops as shown with arrows in Fig. 39. The caps with different γ-values could follow different pathways right at the beginning of the assembly, and as such the number of hexamers might be different before the formation of the first few pentamers. However, as the cap grows and some hexamers are assembled, the location of the pentamers becomes more

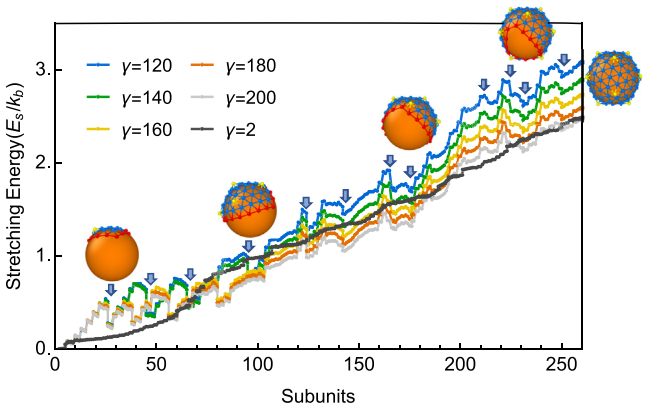

Fig. 39. The stretching energy of a $T = 13$ shell vs. number of trimers. For small FvK numbers ($\gamma = 2$, black line), the energy does not decrease when a pentamer forms. However, for large FvK numbers ($\gamma \gg 1$), the energy drops as a pentamer assembles.
Source: Adapted from [160].

precise with respect to the previously formed ones, independent of γ-values. It is interesting to note that the bending energy of the caps grows linearly with N, the number of subunits, for any γ-values.

The continuum elasticity theory described above reveals the presence of deep attracting potential wells for the formation of disclinations as a crystalline cap grows. One might wonder if such potential wells exist in the discrete systems where the formation of icosahedral structures is not feasible because of the number of subunits and the finite size of the system. Indeed the extensive similarities between equilibrium and irreversible phase diagrams in Figs. 31b and 34 indicate that for the symmetric shells other than icosahedral ones there are also deep potential wells for the formation of disclinations at specific locations during the growth process, leading to the assembly of different types of symmetric shells depending on the physical properties of protein subunits. More recently, Li et al. studied the ground states of crystalline caps consisting of positive disclination defects and found that the defects are distributed preserving icosahedral subgroup symmetries in spherical caps [249].

In passing, we note that the presence of genome can modify the preferred structure of protein subunits. Erdemci et al. compared the free energy of encapsulation of a genome by a cone and a cylinder [250]. Using the field theory techniques borrowed from polymer physics, they found that the free energy of a genome entrapped in a cylindrical shell is lower than that of a chain confined in a cone, if the genome interact attractively with the capsid wall. In the absence of attractive interaction, they showed that the genome "prefers" to be confined in a conical shell, consistent with the experimental studies of Ganser et al. [251]. This is also consistent with the simulations of growth of a shell when the scaffolding layer or an inner core does not interact with capsid subunits [241]. Ning et al. modeled the genome of HIV as a soft ball [241], which was based on the findings of several experiments indicating that HIV genome condenses right at the beginning of capsid assembly as illustrated in Fig. 41 as an orange ball. The figure shows that the elastic sheet grows into a conical shell in the presence of the genome. In these simulations, the capsid proteins are attached at one point to the genome (ball) but they do not interact attractively with it. Ning et al. showed that the presence of the ball promotes the formation of conical capsids over the cylindrical ones but, and yet no icosahedral structures were observed despite the large γ-values (stretching dominant regime) employed in the simulations. Thus the presence of a scaffolding layer that interact attractively with protein subunits is essential for the formation of icosahedral structures similar to the ones shown in Fig. 36.

All the simulations presented in this section were performed under the irreversible conditions in that once a pentamer or hexamer formed, it could no longer dissociate. More recent Monte Carlo simulations by Panahandeh et al. are completely reversible. They show even further that icosahedral order arises due to the high cost of elastic energy associated with the formation of pentamers in the "wrong" positions, which break the symmetry. The reversible simulations reveal the crucial role of elastic energy in the assembly of error-free symmetric protein shells. Fig. 40 illustrates that during the growth process if the pentamers form in the positions that break icosahedral order, they will dissociate and reassemble at the new locations where the symmetry can be preserved . This is quite unexpected: Many bonds have to be broken to disassemble a pentamer well inside the shell, far from the edge. However, apparently the elastic energy becomes so strong that if necessary, many bonds will break to adjust the location of pentamers.

Up to this point in this review, we have only focused on the symmetry of viral capsids and the factors contributing to it. However it is widely accepted that the electrostatic interaction between negative charges on RNA and positive charges on capsid proteins is the driving force for the spontaneous assembly of viral shells. Further, in the case of DNA viruses, the electrostatic interaction between negative charges on DNA and positive charges on capsid proteins decreases the internal pressure exerted by DNA on viral shells. In the next section we will present the research modeling capsid as a charged sphere followed by a section on the role of genome on the assembly of viral shells.

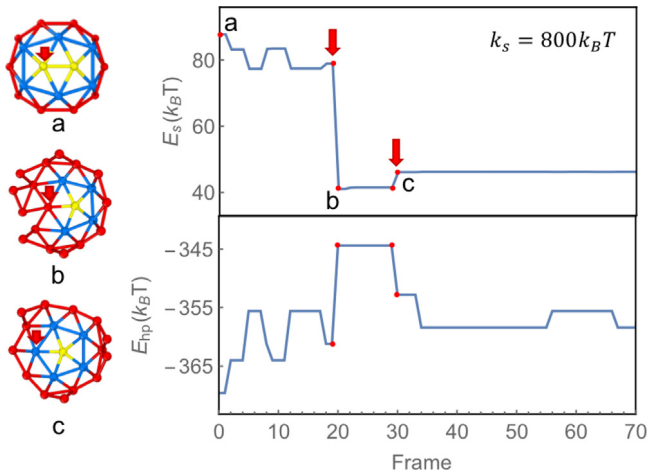

Fig. 40. The snapshots of Monte Carlo simulations for a growing capsid. The assembly is reversible and the subunits can associate and dissociate as the growth proceeds. The right column illustrates the elastic and hydrophobic energies as a function of number of MC moves or time. (a) Two pentamers are assembled in the "wrong" positions after 24 subunits are assembled. (b) The first red arrow indicates the position in which the elastic energy becomes so high that the bonds can easily be broken to decrease the energy (around 20 MC steps). At this point, the hydrophobic energy (point b in the energy plots) increases due to the bond breakage. (c) The hydrophobic energy decreases but the elastic energy slightly increases after a hexamer forms. The attractive hydrophobic interaction between proteins is $\epsilon_{hp} = -1.4k_BT$, the chemical potential of free subunits in solution $\mu = -14.6k_BT$, and the protein's stretching rigidity $k_s = 800k_BT$ and bending rigidity $k_b = 200k_BT$.
Source: Adapted from [252].

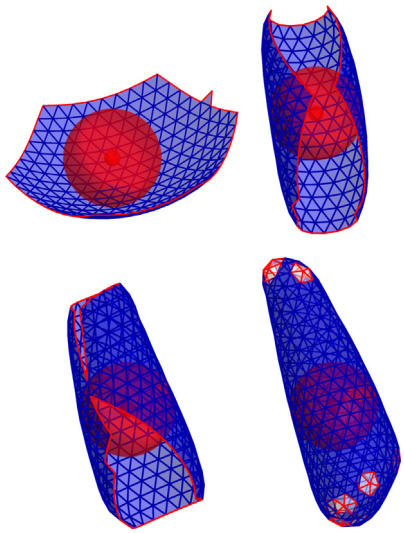

Fig. 41. The snap shots of the growth of a conical capsid around a genome. There is no attractive interaction between the genome and proteins. The spherical core represents the HIV RNA, which has been condensed due to the interaction with positively charged nucleocapsid proteins. There is only steric interaction between RNA and the capsid. The genome is connected to the capsid only at one point.
Source: Adapted from [241].

5. Fundamentals of genome packaging in viruses

Viruses are tenuous, yet robust, macromolecular structures stabilized by an interplay of interactions operating in the "living matter", *grosso modo* decomposable into direct electrostatic and van der Waals forces [253,254], as well as indirect solvent structure-mediated interactions [255]. The van der Waals interactions are generic, being a direct consequence of charge fluctuations, either dipolar in nature [256], or monopolar as in the Kirkwood–Schumaker forces between proteins with dissociable amino acid moieties [257]. While the indirect solvent-mediated interactions are still relatively poorly understood, they can be decomposed into the hydrophobic and/or the hydration counterparts [258,259]. Van der Waals interactions, a functional of the frequency dependent dielectric response of the macromolecules and the intervening medium [260,261], are – in contrast to the assembly of multi-lamellar lipid aggregates [262] – seldom invoked explicitly

in the context of virus assembly, while implicitly they contribute to the hydrophobic interactions that play an important role in the stabilization of protein aggregates [263,264]. On the contrary, the electrostatic interactions are ubiquitous in virus assembly and are quite specific, depending crucially on the identity of the interacting molecules and their charged states. Capsid proteins as well as nucleic acids in aqueous solution are charged, a result of dissociable amino acids and phosphate backbone in contact with the solution. Thus they are subject to electrostatic interactions mediated by mobile ions in the bathing solution, that make a very strong impact on the details of the virus assembly process as well as the packaging of the genome inside the capsid as will become clear in the subsequent sections.

5.1. Electrostatics of viral shells and genomes

Electrostatics is often invoked as one of the driving forces if not the most important one in capsid [265] as well as full virion assembly [266]. Electrostatic interactions were first considered in structural studies of TMV gels by Bernal and Fankuchen [267]. Interestingly, the Poisson–Boltzmann theory of electrostatic interactions was applied to the case of viruses [268] soon after its very formulation [269].

The number of charges carried by the genome and proteins of virions depend on the solution conditions and the structural distribution of dissociable groups on the solvent accessible surface. At neutral *pH* all the PO_4 groups along the phosphate backbone of the genome, having $pK \sim 2.2$ [270], are dissociated and thus impart a large *net negative charge* to DNA and/or RNA. In the *B* conformation, DNA has an elementary charge every 0.147 nm along its contour, or two per each base pair every 0.34 nm, while for RNA the phosphate–phosphate backbone bond has a length of 0.6 nm, basically determined by the structural properties of the phosphate and the ribose sugars [271], amounting to a much smaller linear charge density. Due to this large concentration of charge, any compactification of genomic molecules requires either an energy input or an efficient way to reduce the inherent charge.

Proteins, on the other hand, do not exhibit much universality in charge distribution and magnitude, and can carry a net charge of either sign [272], stemming from the local charge separation at ionizable amino acid residues, crucial for protein–protein as well as protein–genome electrostatic interactions [273–277]. This mechanism of charge separation, referred to as the *charge regulation of proteins*, differentiates between the undissociable charged groups buried inside the proteins on the one hand, and the solvent-exposed dissociable surface charges on the other. In principle, only *ab initio* computations can provide detailed values for the partial charges buried inside or exposed on the solvent accessible protein surface, but calculations of this type are usually hampered by the sheer size and number of atoms one needs to invoke in order to achieve a necessary amount of realism [278,279].

5.2. Experimentally inferred charge of viral shells and complete virions

Experimental determination of the charge of virus capsids is never microscopic, but relies on probing the collective effects of the charge, like the total electrophoretic mobility of the bare capsid or the complete virion [280], the total charge detected by the non-contact AFM tip [281], and/or as the indirect pH effects on the charge and the capsid shape and size [38,276,277,282]. In particular the non-contact AFM spectroscopy, a variant of the AFM imaging and nanoindentation experiments described in Section 3.3, combined with the predicted strength of the tip-capsid interactions based on detailed molecular modeling, can provide a direct insight into the charged state of the capsid as well as the encapsidated genomic cargo.

When immersed in an electrolyte solution with an imposed external electric field, a charged colloidal body will start moving under the influence of the field until it reaches a steady state velocity proportional to the external field with the proportionality coefficient identified as the *electrophoretic mobility*. The relation between the latter and the charge carried by the colloidal body is highly non-trivial and can be analyzed only for some very idealized models [283]. The investigation of the electrophoretic mobility of different viruses as well as its dependence on solution conditions has been analyzed for a number of different viruses such as CCMV, Cucumber Mosaic Virus, Reovirus Type 3, Bacteriophage MS2 (see Ref. [280] and references therein). Quantitative connection between the electrophoretic mobility and the solvent exposed surface charge cannot be assumed to have the same functional dependence on the system parameters as in the case of simpler colloids [284]. The effective charge can thus be either qualitatively different from the bare charge, or basically identical to the bare charge. In any case, the pH and the ionic strength of the solution have an overwhelming effect on the charge of either the empty capsid, complete virion or isolated capsid proteins. For instance, CCMV can exist as the wild-type virion, as empty capsids, or as the free capsid proteins, whose charges have been measured as functions of pH and ionic strength, Fig. 42. The solution conditions do not only change the amount of charge but maybe even more importantly, determine its overall sign that can change as a function of both solution parameters. A quantitative analysis of the electrophoretic experiments would require a detailed knowledge of the connection between the hydrodynamic mobility, the electrostatic charge, and the electrostatic potential, which renders the problem less practical for quantitative analysis than employing more direct methodologies such as the non-contact AFM [285].

There are several long and short-range colloidal forces affecting the interaction between an AFM tip and a virus particle [285], that are in general separable into the attractive van der Waals and the repulsive electrostatic double layer forces [258]. They allow for a quantitative interpretation of the measured force data and provide an interpretation of the range of the forces through the Debye screening length, as will be explained in detail in Section 5.5, and of the strength

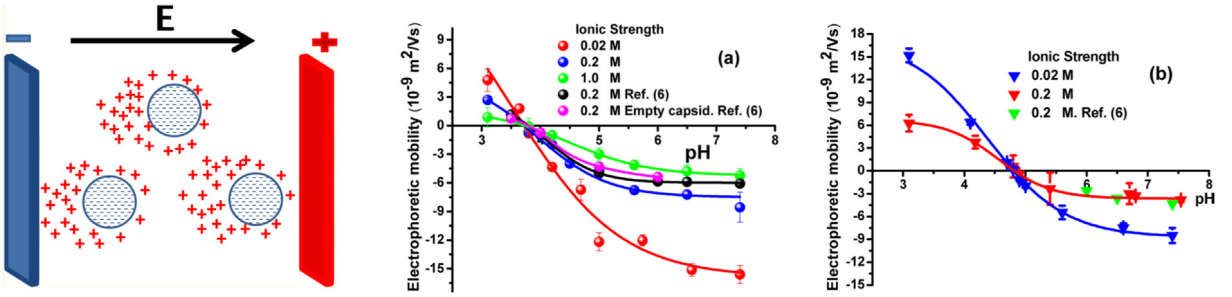

Fig. 42. Left: Schematic representation of the electrophoresis experiment. Middle: (a) Electrophoretic mobility for the wild-type CCMV virion at three different ionic strengths as a function of pH. Right: (b) Electrophoretic mobility of CCMV capsid protein for different values of ionic strength. The graph also contains data on empty virus capsids from Ref. [287].
Source: Adapted from Ref. [280].

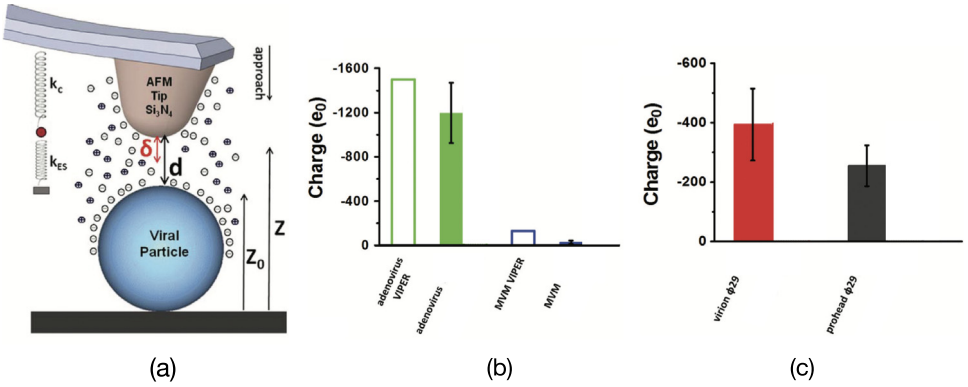

Fig. 43. (a) Schematical depiction of the AFM spectroscopy assay on a viral particle at low salt buffer conditions. Z is the piezo displacement, Z_0 is the point of contact, δ is the deflection of the cantilever and d is the effective AFM tip-virus gap, assuming that the viral deformation is negligible for small enough forces. (b) The column graphs show the comparison between the viral particle charge estimated from VIPERdb [288] (empty column) and extracted from experimental data in 2 mM NaCl with pH = 7.8 buffer conditions. Particles of adenovirus (green bar) and 11 particles of minute virus of mice (blue bar); (c) Charge of bacteriophage ϕ29: 12 virions (red bar) and 7 proheads (black bar) extracted from experimental data.
Source: Adapted from Ref. [285].

of the van der Waals interactions, which will not be addressed further [21]. Other solution parameters, such as the pH, are less straight-forward to incorporate into this framework or require much more detailed modeling [286]. Nevertheless, non-contact AFM force spectroscopy has been used successfully to characterize the electrostatic interactions between an AFM tip and different kinds of virus particles, allowing for a detailed estimation of the charge density of ϕ29 bacteriophage prohead and virion, adenovirus, and the capsid of minute virus of mice (MVM) at physiological conditions [280]. AFM force spectroscopy is sufficiently accurate to determine the electrostatic charge of different viral particles in buffer solutions by using single force-distance assays with statistically significant, measurable differences in the charge between different virus types as well as empty capsids and full virions. Since the electrostatic interaction between the AFM tip and the charged virus capsid depends crucially on the nature of the viral capsid and the presence of encapsidated genetic material, it appears possible to use electrostatic AFM spectroscopy also for non-invasive probing and identification of virus capsids and their molecular cargo (see Fig. 43).

5.3. Structural charge distribution of viral shells

Models of electrostatic interactions of viruses with any amount of verisimilitude have to be derived from detailed charge distributions on the inner (*epitopal*) and outer (*hypotopal*) solvent exposed surfaces of the capsid extracted directly from structural data [289,290]. The standard assumption is that the dissociation cost for charges buried in the protein interior is too high and so the buried amino acids remain undissociated [291], which is not always the case [292], or the local environment of a buried ionizable amino acid is changed and consequently its charge is modified [293,294]. In principle, only a complete *ab initio* quantum chemical calculation of the electronic and bonding properties of capsid proteins in contact with aqueous solvent and neighboring proteins could resolve the issue of the correct charging model for the amino acids [295].

The charge of the capsid proteins (CP) originates primarily from the deprotonated carboxylate $RCOOH \rightleftharpoons RCOO^- + H^+$ on the side chains of aspartic and glutamic acids, the deprotonated hydroxyl of the phenyl group of tyrosine

Table 3
Intrinsic pK_a values of dissociable amino acid (side-chain) functional groups in bulk dilute aqueous solutions, obtained from 541 measured bulk pK values for Asp, Glu, His, Cys, Tyr, and Lys side chains, and the C and N termini of 78 folded proteins, taken from Ref. [296]. The pK value specifically for arginine was taken from the recent equilibrium acid dissociation constant of the arginine guanidinium group, taken from Ref. [297].

	ASP	GLU	TYR	ARG	HIS	LYS	CYS	C-terminus	N-terminus
pK_a	3.5 ± 1.2	4.2 ± 0.9	10.3 ± 1.2	13.8 ± 0.1	6.6 ± 1.0	10.5 ± 1.1	6.8 ± 2.7	3.3 ± 0.8	7.7 ± 0.5

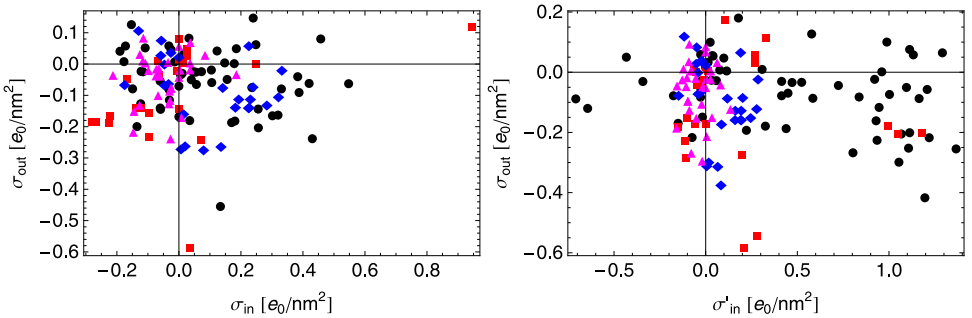

Fig. 44. Left panel: Surface charge densities on the hypotopal (horizontal axis) and epitopal (vertical axis) shell of the capsid without the CP N-terminals. The majority, about 3/4, of the viruses tend to have a slightly negatively charged epitope and a positively charged hypotope. Right panel: same as left but with included charges residing on the disordered N-terminals of the capsid proteins. Obviously there is a shift of the inner shell charge towards more positive values.
Source: Adapted from Ref. [299].

ROH $\rightleftharpoons$ $RO^- + H^+$ and from the protonated amine group of arginine and lysine $RNH_2^+ \rightleftharpoons RNH + H^+$ and $RNH_3^+ \rightleftharpoons RNH_2 + H^+$ as well as the secondary amine of histidine. Bare capsid charges can be calculated from the structural amino acids residing on the solvent accessible surface, obtainable from the primary structure and the bulk pK_as of the individual dissociable residues. The most recent values for the bare dissociation equilibrium constants for the chargeable amino acids as well as the N- and C-termini of the protein chain are given in Table 3. The bare charges as a function of the solution *pH* are then obtained from the Henderson–Hasselbalch equations [298] for the protonation–deprotonation equilibrium of the form

$$RH \rightleftharpoons R^- + H^+ \qquad \text{and} \qquad RH^+ \rightleftharpoons R + H^+$$

with the intrinsic equilibrium constants given by pK_a. The bare charge of the dissociable moiety, $q_i^{(0)}$, is then

$$q_i^{(0)} = \frac{\pm e_0}{1 + \exp\left(\pm \ln 10 (pH - pK_a^{(i)})\right)}, \tag{151}$$

where ± applies to protonation–deprotonation equilibrium.

Assuming that at physiological *p*H (7.4) aspartic acid (ASP) and glutamic acid (GLU) carry a net charge of $-1.0\ e_0$, lysine (LYS) and arginine (ARG) carry a net charge of $+1.0\ e_0$, and histidine (HIS) a fractional net charge of $+0.1\ e_0$ [300], it is then possible to deduce the charges of the complete capsid shell from structural data deposited in the Viperdb [301] and pdb [302]. These *canonical values* of the capsid surface charge densities then lie within the range from -0.4 to $+0.4\ e_0/\text{nm}^2$, which is a typical range for polypeptides, see Fig. 44. This is smaller than the effective charge of DNA, $\sim 1\ e_0/\text{nm}^2$, and comparable to the value for phospholipid membranes, $\sim 0.1 - 1\ e_0/\text{nm}^2$. A discernible feature of the charge distribution is that the epitopal surface charge density is close to zero or slightly negative, with no pronounced asymmetry. On the other hand, the hypotopal charge density exhibits more variation, especially if the charge of the protein N-terminals is added to the solvent exposed charge (see below), and is conspicuously skewed towards positive values, in particular for the case of viruses with a single-stranded genome, see Fig. 44. Combining these data with the structural data for the size of the virus capsids [299] then yields an estimate for a total canonical charge Q of the capsid, being the sum of the hypotopal and epitopal charge, obtained in the range of $|Q| \leq 4500 e_0$.

However, what is actually observable are not the bare, canonical charges but the effective charges as modified by the collective electrostatic interactions, demanding a consistent evaluation of the charges as well as the electrostatic potential due to ionic screening and pH (charge regulation) [303]. Instead of the Henderson–Hasselbalch equations one then needs to consider [262]

$$q_i = \frac{\pm e_0}{1 + \exp\left(\pm \ln 10\ (pH - pK_a^{(i)}) \pm \beta e_0 \phi(i)\right)}, \tag{152}$$

where $\phi(i)$ is the collective electrostatic potential at the site i, due to all the other chargeable sites in the system. Since the dissociation process and the local electrostatic field are thus coupled via the charge regulation mechanism [304],

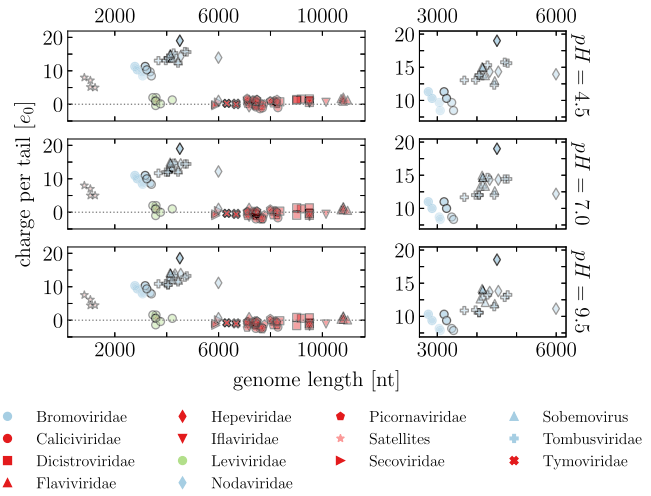

Fig. 45. Left: Average charge on the N-terminals of viruses compared to the characteristic lengths of their genomes, at three different values of *pH*, 4.5, 7.0 and 9.5. The tails are obtained using the STRIDE assignment of protein secondary structure [319]. Right: Smaller plots enlarge the part of the plot showing those viral families which utilize positively charged tails. For details refer to the original paper.
Source: Adapted from Ref. [320].

the degree of dissociation depends self-consistently on the local *pH* as $\ln 10\ (pH - pK_a^{(i)}) \longrightarrow \ln 10\ (pH - pK_a^{(i)}) \pm \beta e_0 \phi(i)$ [286,305]. In order to understand the salient features of the electrostatic interaction in the context of viruses, one needs to analyze the distribution of charge, its variation with the solution variables such as pH and ionic strength, and then deduce the ensuing electrostatic potential and electrostatic energies [276,277,306,307].

5.4. Structural charge of the disordered protein N-terminals

The protein charges considered above are however not the only charges residing on the capsid, since the available structural data do not include the usually disordered *arginine rich motifs* (ARMs) of capsid protein N-terminals, invisible to structural probes but carrying a significant amount of charge, implicated in the electrostatics driven assembly of virions [308]. Furthermore, the total positive charge on the capsid inner surface including the charge contributed by ARMs of the N-terminals, was observed to correlate with the length of the genomic RNA for a diverse group of ss-RNA viruses [309–314]. Nevertheless, the total charge of RNAs packaged into capsids of different ss-RNA viruses was also found to be consistently greater, by about a factor of two, than the positive charge of the ARMs lining the interiors of the capsids, thus making these viruses *negatively overcharged* [266,307,310]. This overcharging can be due to different causes, among which the RNA branching topology [315,316], the nonuniform icosahedral charge distribution [317] or the direct specific RNA-hypotope non-electrostatic interactions due to packaging signals [318] are possible candidates.

Since there are no structural data for the configuration of the N-terminals, their charges are assumed to be located on the hypotopal side of the capsid. While the intrinsically disordered ARMs are flexible in the isolated protein, they may become ordered in the capsid *via* interactions with other viral components. Taking this into account, two complementary definitions of the N-terminal need to be considered:

(i) the standard one, which identifies the part of the CP extending from the tip of its N-terminus to the first occurrence of a given structured part of the CP.
(ii) the first intrinsically disordered, contiguous region of the CP, starting again from its N-terminus, as obtained from a number of different disorder predictor algorithms [320].

The first definition takes into account the flexibility of the N-terminals and contrasting it with the structured part of the CP, while the second definition accentuates the role of disorder in the N-terminal regions of viral CPs. They were both used to determine the length and the charge state of the N-terminals of 80 distinct (and 116 in total) viruses in detail [320], thus extending the previous work of Hu et al. [321], based on a dataset of 27 viruses, where the N-terminal was defined as the flexible sequence of amino acids, starting from the protein N-terminus and ending at the first α-helix (H) or β-sheet (E).

Fig. 45 compares the average charge on the viral N-terminals and the characteristic lengths of their wild-type genomes. Notably the genome lengths of viruses which utilize positively charged N-terminals appear to reach only a limited value ($\sim$ 6k nt). Other viruses, which do not possess positively charged N-terminals, tend to have longer genomes, all the way up to 10k nt. The exceptions in the opposite sense are the phages belonging to the Leviviridae family, which do not possess any tails, and yet pack genomes of only 3–4k nt in length. Some of these phages, such as MS2, are known to utilize

RNA packaging signals to direct their capsid assembly [318]. Comparing the charge on the N-terminals of viruses and the lengths of the corresponding wild-type genome packaged in them, it seems that there is no "universal" genome-to-capsid charge ratio in viruses with positively charged tails, when the size of genome is beyond 6k nt. The analysis of Bozic and Podgornik [320] for the charge and tail length seems to indicate that actually many viruses apparently fail to show any correlation between the genome length and the charge on the N-terminals [320], a conclusion certainly at odds with previous assertions that there might exist a possible universal value of the genome-to-tail charge ratio in viruses with positively charged tails [311,312], but in line with another approach [314] where no universal genome-to-capsid charge ratio was found.

5.5. Poisson–Boltzmann theory of electrostatic interactions

In order to calculate the collective electrostatic potential that is needed to solve self-consistently for the CP charge, see Eq. (152), one needs to invoke the *Poisson–Boltzmann (PB) theory*, which connects the electrostatic potential with the CP charge. The two together, charge regulation boundary condition and the PB theory provide a closed system of equations connecting the state of the dissociable protein groups on the outer and inner surface of the capsid with the capsid geometry and the bathing solution conditions. The capsid is standardly assumed permeable to the ions, but impermeable to the genomic molecule (DNA or RNA) inside the capsid. The equilibrium profile of the electrostatic potential is obtained from a minimization of an appropriate free energy [303].

The free energy for this system is composed of the contributions stemming from the chemical equilibrium of the dissociable surface amino acid groups, the entropy of the mobile ionic species, and the electrostatic interaction energy of all the charged species. The volume part of the free energy for the case of uni-valent salt solution has the simple Poisson–Boltzmann form that can be written as [303,322–324]

$$F_V[n_+, n_-, \psi, \nabla\psi] = \int_V \mathrm{d}^3 r \left[-\frac{\varepsilon_0 \varepsilon}{2} (\nabla\psi)^2 + e(n_+ - n_-)\psi + \rho_e \psi \right.$$
$$\left. + k_B T \sum_{i=\pm} n_i \left[\ln(n_i a^3) - 1 \right] - (\mu_+ n_+ + \mu_- n_-) \right]. \tag{153}$$

The position dependent dielectric constant $\varepsilon = \varepsilon(\mathbf{r})$ has a value $\varepsilon = \varepsilon_w (\simeq 80)$ in the aqueous solution and $\varepsilon = \varepsilon_p (\simeq 4)$ in the interior of the proteinaceous shell. $n_\pm(\mathbf{r})$ are the number densities at position $\mathbf{r}$ of the salt $\pm$ ions, k_B is the Boltzmann constant, T the temperature, $\psi(\mathbf{r})$ is the local electrostatic potential, $\mu_\pm$ are the chemical potentials of the monovalent salt ions and $\rho_e(\mathbf{r})$ is the external charge density, *e.g.*, the charge density of the genome packed inside the capsid or the charges of the dissociable protein amino acids. Minimization of Eq. (153) then yields the full non-linear Poisson–Boltzmann equation,

$$\varepsilon_0 \varepsilon \nabla^2 \psi(\mathbf{r}) = 2 e n_b \sinh\left[\beta e \psi(\mathbf{r})\right] - \rho_e(\mathbf{r}), \tag{154}$$

or its linearized Debye–Hückel equivalent, valid for small enough ($\beta e \psi \leq 1$) electrostatic potentials, in the form

$$\nabla^2 \psi(\mathbf{r}) = \kappa_D^2 \psi(\mathbf{r}) - \rho_e(\mathbf{r})/(\varepsilon_0 \varepsilon). \tag{155}$$

Here n_b is the bulk salt concentration and κ_D is the inverse Debye screening length set by the ionic strength of the uni-valent ionic solution, i.e., $\kappa_D^2 = 2\beta e^2 n_b/(\varepsilon_0 \varepsilon)$. Typically for a uni-valent salt the Debye screening length is given by $\kappa_D^{-1} \approx 0.3\ \mathrm{nm}/[n_b]$, where the salt concentration n_b is measured in moles per liter, setting the spatial scale of electrostatic interactions.

If the charges on macromolecular surfaces are assumed to be fixed with surface charge density σ_0, we have in Eq. (153)

$$\int_V \mathrm{d}^3 r \rho_e \psi \longrightarrow \oint_S \mathrm{d}^2 r \sigma_0 \psi(S) \tag{156}$$

where the surface integral is taken at the solvent exposed macromolecular surfaces. Minimization of the free energy, then yields again the bulk PB equation, Eq. (154) but with $\rho_e = 0$, as well as a boundary condition

$$\left(-\varepsilon_0 \varepsilon_p (\nabla \psi_p(r) \cdot \mathbf{n}) + \varepsilon_0 \varepsilon_w (\nabla \psi_w(r) \cdot \mathbf{n}) \right)_{r=R} = \sigma_0, \tag{157}$$

where $r = R$ is the location of the solvent accessible surface bearing fixed charges. The above PB equation and the boundary condition represent the essence of the standard PB theory as applied to proteinaceous aggregates [286].

Despite its known deficiencies the PB theory, especially for monovalent salts and when complemented with numerical solutions including charge regulation of the chargeable capsid protein amino-acids [286,325], provides quite an accurate *quantitative description* of the charged state of the capsid as well as the encapsidated genome [307]. However, for polyvalent salts the PB ionic screening framework breaks down, leading to more complicated electrostatic interaction mechanisms [326,327].

5.5.1. PB theory: Fixed charge model of the proteinaceous shell

As for the contribution of the dissociated protein charge, one can consider different models with the most important distinction between an infinitely thin proteinaceous shell with a single resulting surface charge density, or a finite thickness shell, with the resulting hypotopal and epitopal surface charge densities σ_{in} and σ_{out} [306,328,329]. Since for the majority of virus capsids the thickness of the shell, w, is found to be between 2–4 nm [299], the latter model is more realistic. Assuming first that σ_{in} and σ_{out} are given, fixed and constant, and that the electrostatic potential itself is continuous across the two surfaces, the Debye-Hückel limit was solved explicitly by Shojaei et al. [330]. Assuming that $\mu = \varepsilon_p/\varepsilon_w < 1$ the total electrostatic free energy comes out as

$$\frac{1}{4\pi R^2}F(\sigma_{in},\sigma_{out},\kappa_D,w,R) = \frac{1}{2\kappa_D\varepsilon_0\varepsilon_w}\left(f_0(\sigma_{in},\sigma_{out},\kappa_D,w) + \frac{f_1(\sigma_{in},\sigma_{out},\kappa_D,w)}{\kappa_D R} + \frac{f_2(\sigma_{in},\sigma_{out},\kappa_D,w)}{(\kappa_D R)^2}\right), \tag{158}$$

where $R_{in} = R$ and $R_{out} = R + w$ are the inner and outer shell radii. It is clear that the f_0 term corresponds to the electrostatic renormalization of the surface energy, f_1 to the renormalization of the spontaneous curvature and f_2 to the renormalization of the bending rigidity. These different contributions to the electrostatic free energy can be obtained as

$$f_0(\sigma_{in},\sigma_{out},\kappa_D,w) = \frac{\mu(\sigma_{in}+\sigma_{out})^2 + (\kappa_D w)(\sigma_{in}^2+\sigma_{out}^2)}{2\mu + (\kappa_D w)}, \tag{159}$$

$$f_1(\sigma_{in},\sigma_{out},\kappa_D,w) = (\kappa_D w)\left(\frac{(3\mu + 2(\kappa_D w) - 1)\sigma_{out}^2 + 2\mu\sigma_{in}\sigma_{out} - (\mu-1)\sigma_{in}^2}{2\mu + (\kappa_D w)}\right), \tag{160}$$

and

$$f_2(\sigma_{in},\sigma_{out},\kappa_D,w) = \frac{\kappa_D w}{(2\mu + (\kappa_D w))^2}\Big((\mu-1)\left[(\kappa_D w)(\mu-1) - \mu\right]\sigma_{in}^2 - 2\mu((\kappa_D w)+1)(\mu-1)\sigma_{in}\sigma_{out} + \left[(\kappa_D w)^3 + (\kappa_D w)^2(4\mu-1) + (\kappa_D w)(5\mu^2 - 4\mu + 1) - \mu(\mu-1)\right]\sigma_{out}^2\Big) \tag{161}$$

In general the above free energy is obviously not symmetric in the two surface charge densities, but the asymmetry is overall small [330]. In the limit of vanishing shell thickness $w \to 0$ the above free energy reduces to known forms [331].

The functional dependence of the free energy, Eq. (158), on the radius of the shell, implies also a dependence of the surface tension, the spontaneous curvature and the curvature elastic modulus of the shell on the charge densities and the bathing solution properties [330]. From the numerical results it then follows that the electrostatic free energy cannot only change the value of spontaneous curvature, but even its sign, as a function of dimensionless shell thickness, $\kappa_D w$, but also as a function of the charge asymmetry at a fixed value of the shell thickness [330]. The position of the change of sign of the spontaneous curvature depends strongly on the values of the parameters characterizing the system, and is in general more pronounced the closer the charge ratio is to the value $r_{min} = \varepsilon_p/(\varepsilon_p - \varepsilon_w)$, that depends only on the static values of the dielectric permittivities.

5.5.2. PB theory: Charge regulation model of the proteinaceous shell

The charge state of dissociable amino acids depends on the *local pH* and *local salt* concentration right at the dissociation sites *via* the charge regulation process. In this case, the protein charges are not given by their structural values, but need to be determined self consistently by including the dependence of the protein charges, Eq. (152), on the local electrostatic potential [305,332]. Both surfaces of the virus shell are then treated as uniformly charged with charge composition corresponding to the actual distribution of dissociable amino acids for any type of the capsid considered. The outer and inner surface charge densities are then given as

$$\sigma_{in,out}(\psi) = \frac{e}{R_{in,out}^2}\sum_{k=\{\pm\}}\frac{\pm 1}{1 + e^{\pm \ln 10(pH - pK_\pm) \mp \beta e\psi}}, \tag{162}$$

where $\{-\} = Asp, Glu, Tyr, Cys$ and $\{+\} = Arg, Lys, His$, respectively on the hypotopal (in) and epitopal (out) surface. The PB equation, Eq. (154), together with the charge regulation then presents a consistent formulation of the electrostatic potential calculation for an empty viral shell as shown by Nap, Božič, Szleifer and Podgornik [286]. The numerical solution of this set of equations then yields the dependence of the effective charge density on the inner and outer capsid surface and on the bathing solution parameters, such as pH and salt concentration.

The approach delineated above has been applied explicitly to the bacteriophage PP7 capsid. It is usually assembled *in vitro* at a slightly basic pH of 8.0–8.5 [333,334] with an isoelectric point, corresponding to zero net charge of the capsid, in the range of 4.3–4.9 [335] for salt concentrations of NaCl (0, 40, 100 mM), that actually moves towards lower values as the salt concentration increases [336]. The first important characteristics of the calculated PP7 capsid charge density is that for low pH the inner as well as outer surface are positive, while for high pH the capsid charge turns negative, see Fig. 46. In addition, the hypotopal surface charge density shows an almost constant plateau for a range of pH values whose exact position depends on the salt concentration, suggesting a buffering behavior under physiological pH and ionic strength

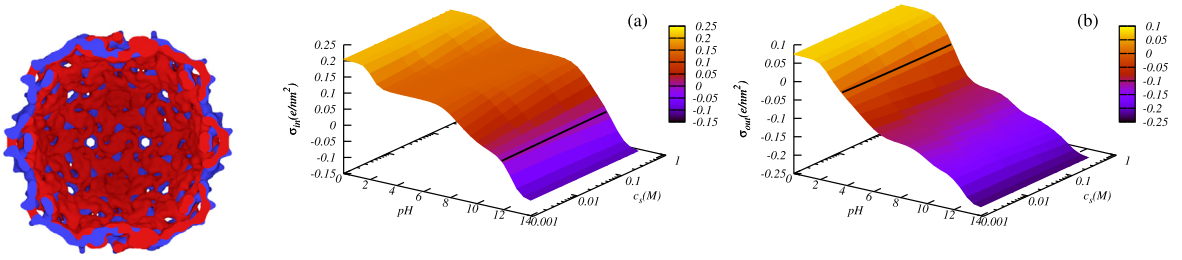

Fig. 46. Charge density distribution of the PP7 capsid and its variation with pH and salt. Left: Schematic distribution of charges on the capsid. Red represents positive and blue negative charges. Middle: Surface charge density of the hypotopal surface. Right: Surface charge density of the epitopal surface, as a function of solution pH and salt concentration in molar units. The black solid lines correspond to the isoelectric points (zero net charge). The isoelectric point of the outer shell is located around pH $\simeq$ 3.8, while that one of the inner shall is located at a different value of pH $\simeq$ 11.7. The inner radius is taken as $R_{in} = 11.8$ nm and the outer radius of $R_{out} = 13.8$ nm, consistent with the structural data.
Source: Adapted from Nap et al. Ref. [305].

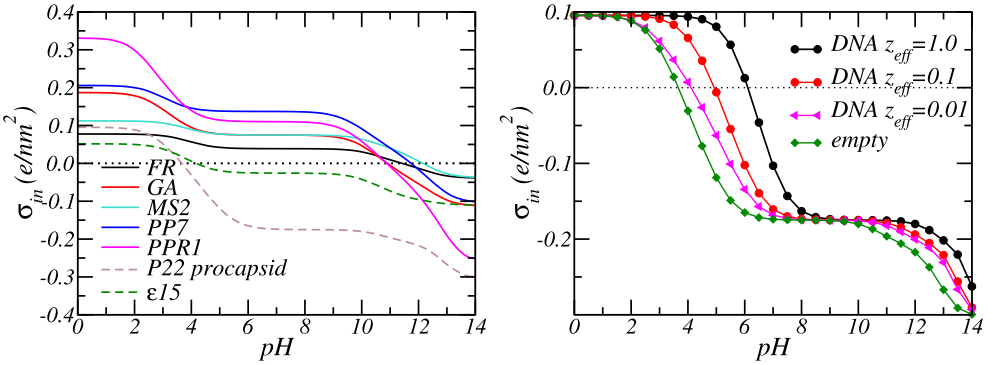

Fig. 47. Left: Hypotopal charge density for various bacteriophage capsids, as a function of solution pH for a salt concentration of $c_s = 100$ mM. The buffering plateau seems to be a universal feature for all the analyzed capsids, while the sign of the charge at the plateau differs depending on the identity of the capsid. Right: Hypotopal charge density as a function of pH for a salt concentration of $c_s = 100$ mM in the case of the PP7 capsid with different cargos. The 'dsDNA' cargo was modeled as a homogeneous volume charge distribution throughout the inside of the capsid, with the dsDNA of the PP7 procapsid having 44k base pairs. z_{eff} is the fraction of charge per base pair. $z_{eff} = 1$ corresponds to two canonical negative charges per base pair.
Source: Adapted from Ref. [286].

conditions. This plateau is fully developed only for the hypotopal surface that interacts with the genome and needs to electrostatically stabilize its encapsidation. Structurally, it can be seen that it is connected with the prevalence of arginine and lysine on th inner surface of the capsid.

Comparing the charge distribution of the PP7 hypotope with other phages, corroborates the presence of this buffering action, even if other bacteriophages exhibit substantially different amino acid distributions, see Fig. 47, and the exact amount of surface charge is specific for a given bacteriophage, so that different capsids show a pronounced variation of charge all the way to its sign at a set value of pH. epsilon 15 and p22 capsid at physiological pH are negatively charged on the inside, while the other phages are positively charged. This is possibly related to the fact that they are dsDNA phages which use molecular motors to load their dsDNA cargo, while the other ones all contain the ss-RNA genome and self-assemble spontaneously and concurrently with their ss-RNA genomic material. The sign of the hypotopal charge then directly reflects the nature of the virus.

The negative sign of the inner surface charge is correlated with the work required to load these capsids with their negatively charged genomic material. In fact, modeling the encapsidated genome cargo by a uniform negative charge smeared inside of the (P22) capsid, leads to a decrease and even reversal of the sign of the inner charge density due to the charge regulation in the presence of genome, see Fig. 47. At a fixed pH, *e.g.* pH = 6, the empty capsid would exhibit a negatively charged hypotope that would turn positive as the effective charge of the genome cargo is increased. This synergy between the genome charge and the hypotope charging state can substantially modify the work needed to load the capsid and could play a role in the observed "wetting" of the hypotope by a condensed toroidal DNA in the presence of some condensing agents [337].

The complicated features of electrostatic interactions, implying a pronounced pH as well as salt strength effects, introduce qualitative changes in the charge state of the capsid, which can switch from net positive to net negative depending on the characteristics of the solution. The charge of the capsid thus has no meaning, unless the solution conditions are specified unambiguously. In addition, one needs to be aware that the bulk bathing solution pH and salt

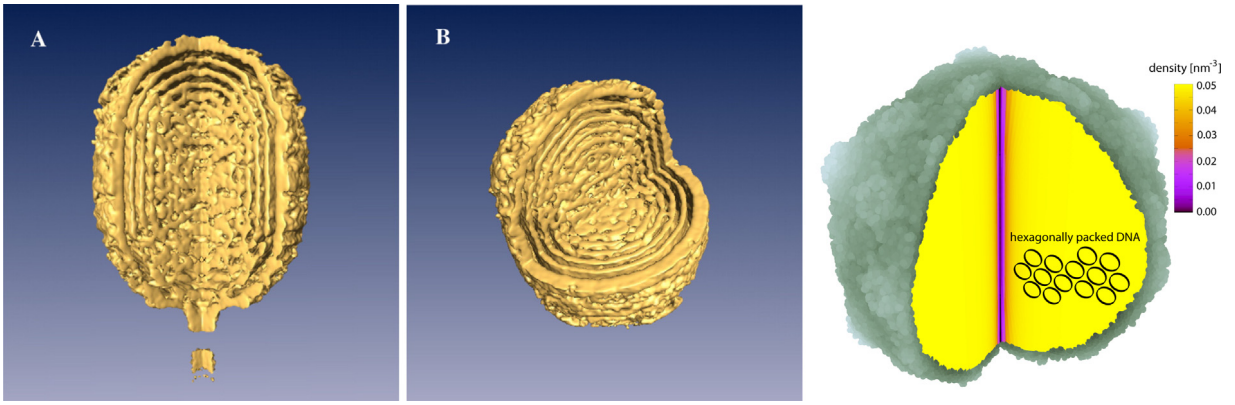

Fig. 48. (A) and (B): Surface rendered cryo-EM three-dimensional reconstruction of the full-length ϕ29 packaged genome. The degree of packing order increases from the center toward the capsid wall, with six concentric shells visible in longitudinal and transverse sections of the volume. Adapted from Ref. [377]. Right: A schematic representation of the inverse spool with a small axial depletion region near the axis of the spool. Adapted from Ref. [361].

concentrations are in general different from the local ones, determining the charged state of the CPs at the capsid surface, and one should thus consider molecular details such as the acid–base equilibrium of the amino acids and their exact distribution across the capsid wall in order to properly understand the charge state of the virus capsid.

5.6. DNA packaging in bacteriophages

For many bacteriophages, the delivery of DNA into the host cell proceeds by an ejection process [338,339], whereby the viral shells are left intact outside of the bacterial cell, while the genome is pushed through the punctuated bacterial wall [340]. Inside the bacteriophage capsids DNA packing can exhibit a whole range of structures with *axial inverse spool symmetries* [341–346], spherical concentric symmetries, as well as liquid crystalline polydomain phase mosaic structures characterized by a homogeneous DNA density [347,348]. In general these packaging structures are quite different from the packaging conformations observed in unconfined, condensed DNA [349]. The inverse spool model of DNA packing in bacteriophages was first cast into quantitative terms by Riemer and Bloomfield [350] and subsequently repeatedly elaborated on various levels of sophistication [51,351–365]. The inverse spool packing of the DNA confined to the capsid 8allows it to act like a *coiled osmotic spring* once it is allowed to expand [366], releasing its chemical and mechanical energy through the portal complex on docking onto a bacterial cell wall [367].

5.6.1. Experimental determination of genome packing and forces resisting its confinement

Early X-ray scattering studies on λ bacteriophage by Earnshaw and Harrison [368] indicated a three-dimensional genome packing geometry characterized by a concentric layered structure of the DNA within the capsid, shown for the case of ϕ29 bacteriophage cryo-TEM density reconstruction and its schematic representation in Fig. 48. For a given species, there appears also to be a strong correlation between the genome length (mutant vs. wild type) and the overall DNA density, fully confirmed by more detailed detailed X-ray studies [369] as well as cryo electron microscopy [342,370–372]. The corresponding DNA density for many ds-DNA viruses at full packing then approaches near crystalline densities, deep inside the ordered part of the DNA phase diagram [365]. Other studies, however, suggested different models for the genome packing: folded toroidal spool [341], a ball of yarn without any well-defined spooling axis [368], liquid crystalline drop with hairpins or folds [348,373] or an ordering mosaic of multiple homogeneously ordered domains [374], separated by defect walls and forming a structure akin to a confined *twist grain boundary* liquid crystal. In fact, analysis of DNA conformation inside partially filled capsids based on different cryo-TEM data as a function of the physico-chemical environment variables such as the nature of ions, the solution osmotic pressure and temperature, indicate that there can exist not a single well defined conformation, but a wide variety of different DNA conformations [375,376].

Two different venues have been pursued to quantify the properties of the coiled osmotic DNA spring inside the capsid [366]: *in singulo DNA packaging experiments*, pioneered by Bustamante and coworkers on ϕ29 phage [367], and *collective osmotic ejection inhibition experiments*, pioneered by Gelbart and coworkers on the λ phage [51].

In the *in singulo* packaging experimental setup a force-clamp and ramped stretching techniques in combination with a laser trap setup show that an "internal" packaging force resists DNA confinement in the capsid, originating in (i) DNA self-repulsion, (ii) the confinement energy associated with increased DNA bending, and (iii) entropy loss for lowest values of DNA encapsidation density [363,378]. The internal force can reach values of up to $\sim$ 100 pN at 100% packaging, depending on the length of the viral genome and ionic conditions of the bathing solution, with the identity of the salt ions and the ionic strength effects confirming that electrostatic repulsion makes a large contribution to the internal force [355,379].

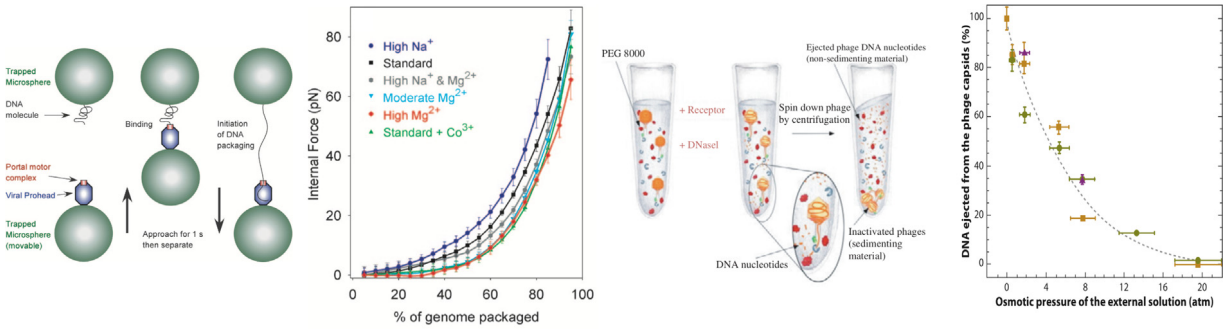

Fig. 49. Left: *Single molecule DNA packaging experiments*. Internal packaging force resisting the DNA confinement, measured as a tension on the DNA tether connecting the virus capsid and the optically trapped sphere with DNA attached to its surface [378], depends on the packaged genome length. Adapted from Ref. [378]. Right: *Collective osmotic ejection inhibition experiments*. The osmotic ejection of DNA is counteracted by the variable solution (PEG) osmotic pressure. The fraction of DNA ejected as a function of the osmotic pressure is then calculated from the absorbance of free nucleotides of the digested ejected DNA in the bathing solution. Adapted from Ref. [382] and Ref. [53].

The internal force can be quantitatively described by the inverse spool model [358,361,364,380], with small discrepancies between theory and experiment possibly due to inaccuracy in the capsid volume size, less-ordered non-inverse spool DNA packing geometries, and/or non-equilibrium or dissipative effects [379,381] (see Fig. 49).

In the collective osmotic ejection experiments, the osmotic pressure dependence of the degree of genome ejection is measured. When the host receptor, as is the case for λ and T5 phages, is added to a solution containing virus, it induces a conformational change that opens up the tail, releasing the wound up DNA osmotic coil, ejecting the DNA [53]. An opposing force can be provided by the water-soluble polymer poly(ethylene glycol) (PEG) in solution but excluded from the capsid, that acts as an osmoticant providing a counteracting osmotic force [369,383]. The osmotic ejection experiment then involves measuring the fraction of the DNA ejected as a function of the applied solution osmotic pressures [364]. Since the experiment measures the dependence of the encapsidated DNA density on the applied solution osmotic pressure, one could state that what is measured is the DNA equation of state, *i.e.*, the dependence of the osmotic pressure on the DNA density. Elucidating the connection between the *in viro* and *in vitro* equations of state then provides a proper description of the measured osmotic behavior of confined DNA [52,355–358,361,384].

5.6.2. DNA osmotic pressure in vitro

The osmotic pressure of encapsidated DNA depends on the nature of its ordering and the corresponding form of the osmotic pressure as a function of DNA density [385–387]. In the regime of densities relevant for DNA packing in the viral capsids, DNA is either in a cholesteric phase or hexagonal/hexatic liquid crystalline phase [365], the two phases differing in the nature and range of the positional and orientational ordering [388]. The dependence of the osmotic pressure on the DNA density is composed of two contributions stemming from the solvent structure effects and screened electrostatics [388]. The electrostatic part can be rationalized on the basis of the Poisson–Boltzmann theory as applied to an array of ordered DNA molecules [389], while the solvent structure effects are usually rationalized in terms of the phenomenological theory of hydration interaction [390,391].

The linearized Poisson–Boltzmann equation, Eq. (154), can be solved in a cylindrical cell model [389,392], a variant of the Wigner–Seitz model in solid state physics, mimicking the effect of nearest neighbors in an ordered, locally nematic array [365]. The inner boundary of the cell is the surface of the charged DNA cylinder, $r = a$, and the outer cell radius is halfway between nearest neighbors, $r = D$. If the density of the DNA phosphates is ρ, then $\rho^{-1} = \pi(D^2 - a^2)L_{bp} = \left(\sqrt{3}/2\, D_{hex}^2 - \pi a^2\right) L_{bp}$, where L_{bp} is the length per base pair, and D_{hex} is the interaxial spacing between DNA helices, assumed to be locally packed with hexagonal symmetry. At the inner cell boundary the electrostatic field is given by the surface charge density of the DNA cylinder, σ obtained from the axial separation between the charges along DNA, *i.e.*, one charge per 1.7 Å., while at the outer boundary the field has to be zero by symmetry [389,392]. The electrostatic component of the osmotic pressure in the DNA array is then obtained to the lowest order in the interaxial spacing as [365]

$$p_0(\rho) = A_e \left(\frac{K_0(\kappa_D D)}{K_1(\kappa_D a)}\right)^2 \sim \frac{\sigma^2}{\epsilon\epsilon_0 K_1^2(\kappa_D a)}\, \frac{\pi}{2}\, \frac{e^{-2\kappa_D D}}{\kappa_D D} \tag{163}$$

where $A_e = \sigma^2/\epsilon\epsilon_0$ and $K_{0,1}(x)$ are the modified Bessel functions. In the case of monovalent salts, such as NaCl, the Debye screening length is calculated as $\lambda_D = \kappa_D^{-1} = 3.08\ \text{Å}/\sqrt{I(M)}$, where $I(M)$ is the molar ionic concentration. $A_e \simeq 155$ atm, nearly independent of NaCl concentrations [388,393,394].

While the electrostatic contribution to the interactions between DNA molecules is based solidly on either Poisson–Boltzmann theory or some variant of it [303], the solvent structural contribution is much more difficult to handle and only phenomenological theories can be cast into explicit calculational forms that can provide some conceptual insight and

scaling laws for the solvent mediated interactions [391]. To predict the range of magnitudes of the hydration repulsion on a quantitative level, detailed simulations are required [395,396], that take into account subtle differences in the interaction enthalpy and entropy of hydrated molecular groups including all relevant degrees of freedom.

The first rationalization of the solvent mediated interaction based on water structuring has been proposed in a phenomenological order parameter-based theory [390,391], which is formulated as a Landau free energy of the symmetry based order parameter with a volume and surface component. The order parameter can be based on different types of water ordering: projected dipolar vector order, projected nematic bivector order, projected quadrupolar order parameter component perpendicular to the surface, and water tetrahedrality order parameter [391]. To the lowest order the Landau free energy expanded in terms of order parameter and its derivatives is formally similar to the linearized Poisson–Boltzmann free energy as a function of the mean electrostatic potential, the main difference being in the spatial symmetry (symmetric vs. antisymmetric) vs. the orientation of the macromolecular surface, stemming from the boundary interaction terms [396]. A robust prediction of the phenomenological theories of the hydration interactions between chemically identical surfaces, such as two vicinal, parallel DNA molecules, leads to the total interaction osmotic pressure, *i.e.*, sum of water structural and electrostatic components of the form

$$p_0(\rho) = A_h\left(\frac{K_0(\kappa_h D)}{K_1(\kappa_h a)}\right)^2 + A_e\left(\frac{K_0(\kappa_D D)}{K_1(\kappa_D a)}\right)^2, \tag{164}$$

where λ_h is now the hydration decay length, $\lambda_h \approx 2.2$ Å, while fits to measured osmotic pressure give $A_h \simeq 1019$ atm [388]. The term osmotic here refers to the fact that all the components of the DNA solution are exchangeable through the capsid wall, except the DNA which is confined.

What is actually measured in the bulk is the contribution of bare interactions and conformational fluctuations of the chain [386]. The total bulk equation of state thus contains not only the interaction part but also the conformational entropy [363]. At concentrations, or equivalently interaxial spacings, close to full packing in the capsid, the equation of state is dominated by the hydration repulsion and screened electrostatic repulsion, whereas the entropy contribution is usually negligible. It can become important at smaller DNA packing fractions or for larger radii of the virus capsid where the full bulk equation of state, with the conformational fluctuations included, is preferable.

5.6.3. Quantifying the DNA osmotic pressure in viro

In an inverse spool configuration [51,339,356,358,361,363,397,398] the total osmotic pressure p of encapsidated DNA is shared between the *bulk equation of state* p_0 and the *deformation stress*, f_D, depending on density and curvature deformation, leading to an inhomogeneous DNA packing density, $\rho = \rho(\mathbf{r})$. Formally the relationship between the two can be obtained from the osmotic equilibrium equation [361,365], stipulating that the total osmotic pressure as a function of encapsidated DNA density, $p(\rho)$, equals its bulk osmotic pressure at the same density, $p_0(\rho)$, plus the curvature contribution, $f_D(\rho, R)$ such that

$$p_0(\rho) + f_D(\rho, R) = p_0(\rho) + \tfrac{1}{2}(k_B T)\rho\ \frac{\mathcal{L}_p L_{bp}}{r_\perp^2} = p, \tag{165}$$

where the axial distance from the inverse spool axis is $r_\perp = r\sin\theta$.

The total osmotic pressure inside the capsid, where the measured interaxial spacings between DNA molecules are in the range $\sim$ 2–3 nm, corresponding to DNA densities of $\sim 600 - 400$ mg/ml, extracted from the bulk equation of state is in the interval of $\sim$ 10–100 atm. Experimentally, the λ phage DNA osmotic pressures can be estimated at 38 and 11 atm for the full length and b221 strains, with the corresponding ejection inhibition pressures at 32 and 12 atm, respectively [384]. Converted into the energy scale this amounts to 38 000 k_BT (full length 48.5 kbp), or equivalently 0.8 k_BT per base pair, which is an order of magnitude larger than the bending energy per base pair associated with the average radius of curvature, see Fig. 50. The exact number depends on the length of DNA as well as the solution conditions but it can also change sign, *e.g.*, in the case of mM Co^{3+} or spermine^{4+}, because of the strong electrostatic correlation effects [369,399,400].

The DNA single molecule and collective ejection inhibition experiments clearly implicate the identity and concentration of the solution ions as important regulators of the DNA packaging [53,369,378,401]. The strength of DNA–DNA interactions, or any other charged macromolecule [402], can be diminished by increasing the monovalent ion, *e.g.* Na^+ concentration, purely by enhancing its screening effect [403]. Note that the chemical identity of the uni-valent ions can influence specific interactions between the ions, *e.g.* Na^+ vs. Li^+, K^+, Cs^+, or Tri-methyl-ammonium cations, and the DNA surface [404]. The effect of multivalent ions is more complicated, connected to the electrostatic correlation effect that cannot be rationalized in the framework of the Poisson–Boltzmann theory [326,399,405]. It either leads to diminished repulsive interactions as in the case of $[Mg^{2+}] \leq 10$ mM [406], or to a reversal of sign of electrostatic interactions, as is the case of the tetravalent amine [*spermine*] ≥ 1 mM, and other higher valency multivalent cations, that can lead to "like-charge attraction" between DNA molecules, inducing DNA condensation [271,407]. Similar effects can be discerned also in encapsidated DNA at various solution conditions, confirming the importance of electrostatic interactions in viral packing [378,408].

Electrostatic effects *in vitro* have been investigated directly by Qiu et al. in the case of λ-bacteriophage by probing the density of the encapsidated DNA with small angle X-ray scattering (SAXS) and deconvoluting the DNA–DNA interaction energies within the intact phage by combining the measured interaxial spacings in the capsid with measurements of

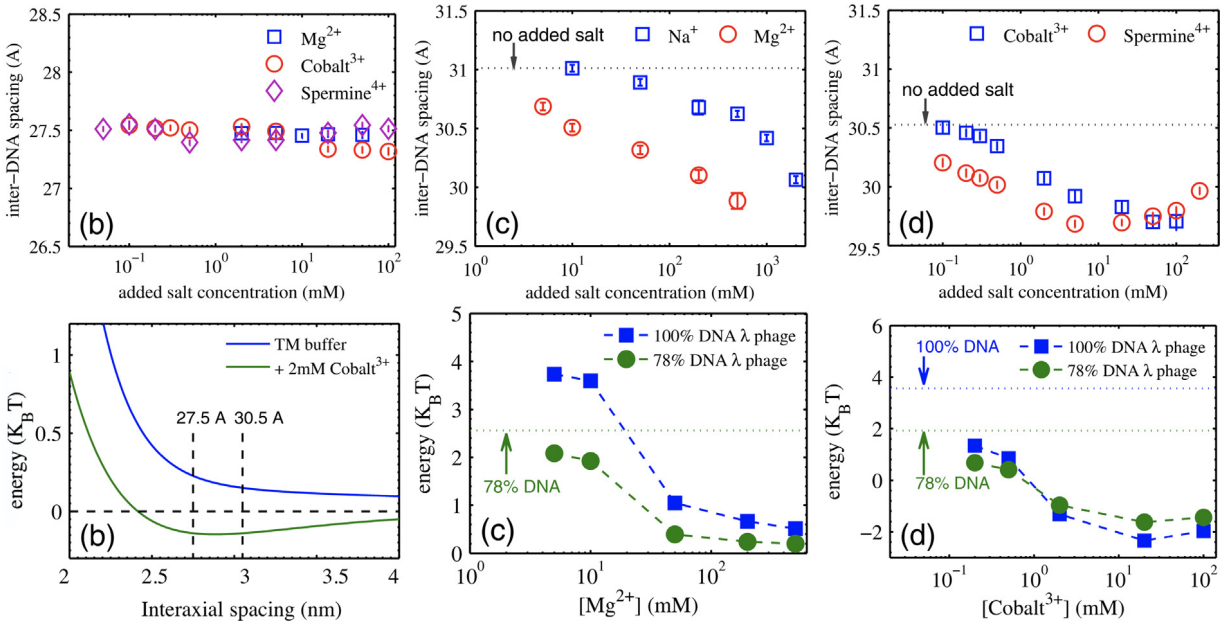

Fig. 50. Effects of electrostatics on the DNA packing density in λ-bacteriophage. Top: Measurements of (b) DNA–DNA interaxial spacing (in Angstroms) as a function of added multivalent cation concentration in standard buffer. (c) DNA–DNA interaxial spacing as a function of added mono- and divalent cation concentration. The dotted line indicates the interaxial spacing with no added salt (i.e., pure 50 mM Tris buffer). (d) DNA–DNA interaxial spacing as a function of added tri- and tetravalent cation concentration in TM buffer. The dotted line indicates the interaxial spacing with no added salt (i.e., TM buffer only). Bottom: (b) Interaction energy per 0.1 nm, vs. interaxial spacing. (c) and (d) Total interaction energies in units of 10^4 of DNA inside phage capsids, for two different DNA lengths in 50 mM Tris buffer for (c), and TM buffer for (d). The energies for zero Mg^{2+} and for zero Co^{3+}, are indicated by dotted horizontal lines.
Source: Adapted from Ref. [369].

the DNA osmotic pressure in bulk DNA assemblies under the same bathing salt conditions [369]. Experimentally one observes, see Fig. 50, that the electrostatic effects depend crucially on the length of encapsidated DNA. In the case of the full length native λ phage DNA (48.5 kbp), the addition of di-, tri-, and tetra-valent counterions has almost no effect on the DNA–DNA separation, remaining essentially constant at 2.75 nm interaxial spacing. This minimal effect of adding salts is consistent with the fact that at such small interaxial spacings the DNA–DNA repulsion is dominated by the hydration interaction that does not depend on the salt concentration. On the other hand, for the shortest (37.8 kbp b221 λ phage strain) DNA available, the measured spacing in the TM buffer is larger, amounting to 3.05 nm, and corresponding to a significantly weaker DNA–DNA repulsion. Additions of Na^+, Mg^{2+}, Co^{3+}-hexammine and spermine^{4+} cations all result in a significant decreases of DNA–DNA separation. In the case of Na^+, Mg^{2+} the DNA–DNA interaction is repulsive and favors maximal DNA spacing, so that the observed decrease in interaxial spacings from 1.1 to 0.97 nm can be attributed to the differences in the DNA bending elasticity. The addition of multivalent cations Co^{3+}-hexammine and spermine^{4+} to the b221 strain, at an order of magnitude smaller concentrations than the monovalent and/or divalent cation, also induces progressively smaller interaxial spacings, consistent with the electrostatic correlation effect of multivalent ions. Interestingly enough, at [spermine^{4+}] $\geq$ 20 mM and [Co^{3+}] $\geq$ 100 mM the DNA interaxial spacing exhibits a non-monotonic behavior consistent with the reentrant behavior of DNA condensation [409,410], known to be a salient feature of strongly charged systems [411].

Optical tweezer measurements indicate that the forces measured with the bacteriophage $\phi 29$ [379] are several-fold higher than ejection forces (estimated from osmotic pressure times DNA cross section area) measured with λ-bacteriophage [369]. They also implicate ionic screening as having a strong effect on the packing forces when the counterion is Na^+, lowering the packaging force as well as preventing the full length genome to be encapsidated. The effects of Mg^{2+} and Co^{3+} are also consistent with the charge correlation effects resulting in a significant decrease of the packaging force.

5.6.4. Non-spool-like DNA configurations

Contrary to dense DNA solutions in the bulk [395,396], no atomistic simulations of DNA packaging in viral capsids are available. Coarse-grained simulations of confined semiflexible polymers mimicking DNA in viral shells have been performed at various levels of detail, starting from the seminal work of Gelbart and Ben-Shaul [355–358] and reviewed extensively [415–421], are usually based on interaction potentials of either Lennard-Jones modified by screened electrostatics type [413,414,418,422,423] with a strong enough attractive minimum to mimick the charge correlation effect

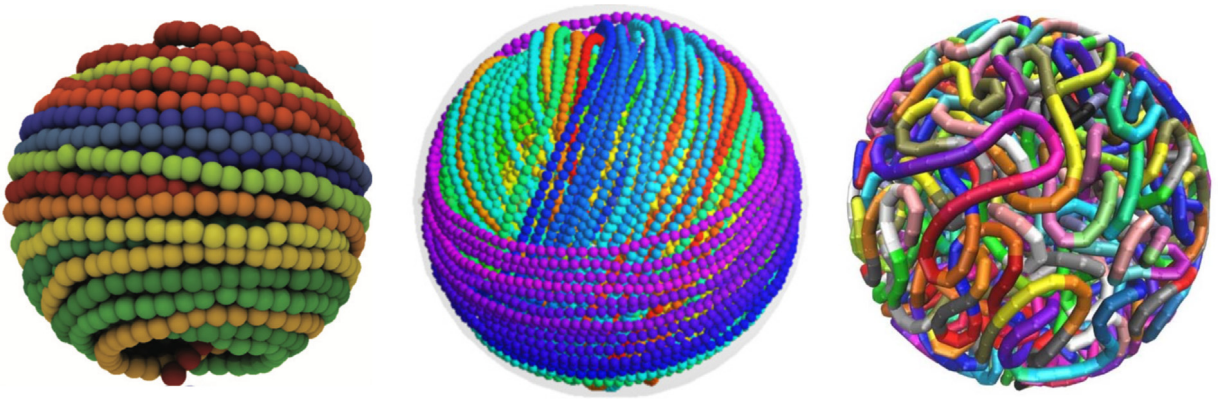

Fig. 51. Comparison of three different configurations of DNA packing in a virus capsid as deduced from coarse grained simulations. Left: an ordered, inverse spool configuration with a single rotational axis [412], based on simulations of a semiflexible chain of beads, with Lennard-Jones and screened electrostatic interactions together with chiral nematic interaction terms. Middle: a nested sequence of multiple inverse spools, showing no collective rotational axis from simulations based on a semiflexible chain of beads with limited extensibility and an excluded-volume soft-sphere interaction potential [413]. Right: a fully disordered packaging of a confined coarse-grained chain with screened repulsive electrostatic interactions and angle-dependent bending and stretching terms. The model includes the ability of random kink generation that results in significantly more disordered configurations [414].
Source: Adapted from Refs. [412–414].

with polyvalent cations [358]. Alternatively they are based on a purely phenomenological form such as the nematic interaction [424], possibly including also the contribution of DNA chirality [412] and twist [425]. In order to compare the simulation results with experiments, specific electrostatic DNA interactions and entropic contributions need to be considered to explain the energetics of confinement [339] and the conformation of the confined DNA [380] that both eventually depend on the details of the interaction potential.

While there is no *a priori* assumption of the symmetry of DNA packing inside the capsid, nevertheless most of the configurations obtained in simulations display inverse-spool-like states, see Fig. 51. However, packing into icosahedral capsids was shown to have a discernible stochastic component [416], and strong non-equilibrium trapping into one of energetically vicinal entrapment states is often observed. Apart from the inverse-spool like states, non-spool-like symmetry has also been reported, including multidomain spool packing [413,417], with elastic kinks [414], and knots [412,426] providing yet other mechanisms affecting the local liquid-crystalline order of compacted DNA. The configurations observed in all these nonequilibrium simulations crucially depend on the applied protocol, *e.g.*, on the details of the external forcing provided by the packaging-motor driven DNA encapsidation in bacteriophages [339], resulting in a wide variety of behaviors even for models that are otherwise quite similar. In this conformational *embarras de richesses* the ground-state packing configurations could provide a well-defined baseline scenario with which nonequilibrium configurations can be compared and assessed.

The ground states of confined elastic chains have received much less attention then the simulations with forced encapsidation of DNA [374,427–429]. Using the full Landau–de Gennes form of the nematic free energy density [427,429] or rigorous field-theory framework [424], one can derive more general encapsidated configurations that are possibly devoid of any spool-like axial symmetry or indeed exhibiting complicated topology of Hopf fibrations, being of the general type sometimes observed also in non-equilibrium simulations [380,416]. In this case the configuration of the director and density fields can be quite complicated with domain walls that can partition the interior of the capsid into multiple phase regions of the type observed recently by Leforestier et al. in cryomicroscopy of T5 bacteriophage [347,348]. In addition analytical calculations and computer simulations of a long elastic filament confined to a spherical container one observes an ordering mosaic of multiple homogeneously ordered domains, composed of concentric spools, but also other morphologies which resemble topological links [374].

5.7. RNA packaging in plant, animal and human viruses

The process of spontaneous co-assembly of single-stranded RNA and capsid proteins is in marked contrast with the genome encapsidation in double-stranded DNA viruses such as the bacteriophages, which involves a motor protein inserting the genome into a pre-formed empty capsid. This fundamental difference between RNA and DNA viruses is connected to the fact that RNA exhibits pronounced flexibility and is characterized by a very complicated secondary and tertiary structure that depends sensitively on nucleotide sequence, while DNA is a relatively stiff linear negatively charged polymer with a 50 nm persistence length, comparable to the scale of the viral capsid. Consequently, the statistical conformation of DNA is completely different from that of RNA [430]. This is basically the reason why motor proteins

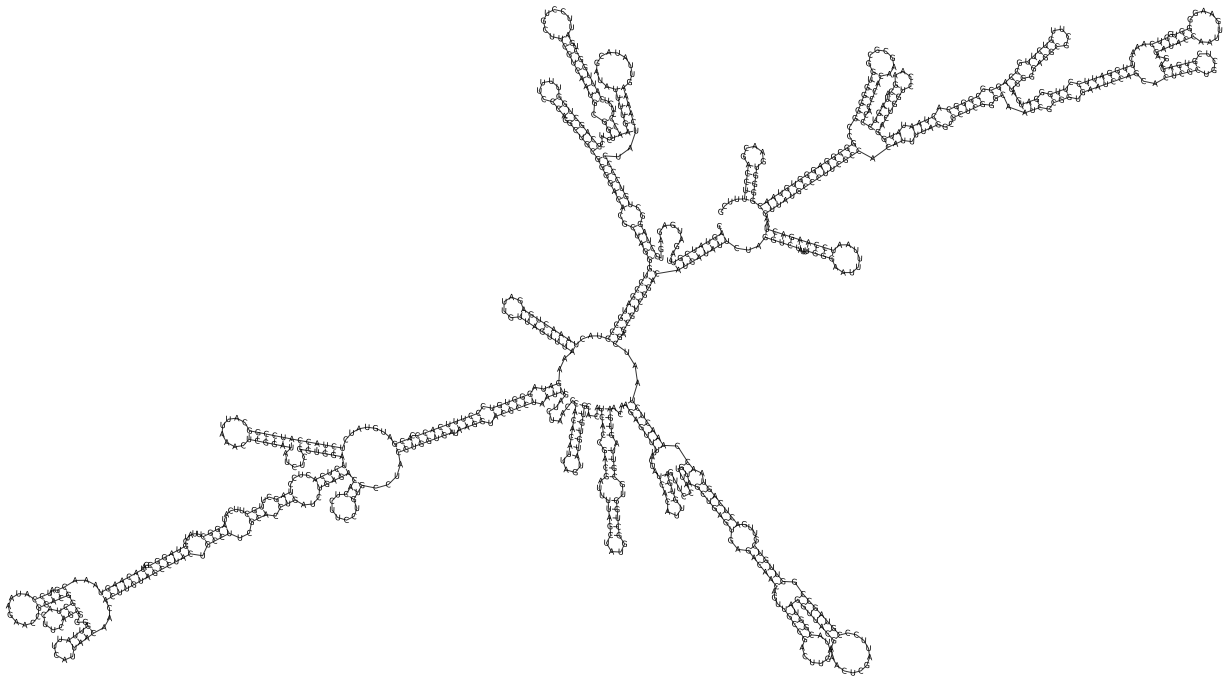

Fig. 52. The "minimum free energy" structure of a random RNA with 1000 nucleotide obtained through the RNAfold program from the Vienna RNA package [433]. The figure clearly reveals the highly branched structure of a random ss-RNA as a result of base-pairing.

must perform a great deal of work against the forces arising from DNA confinement while RNA viruses can assemble spontaneously *in vitro* under appropriate conditions.

In fact, reconstitution experiments performed over 60 years ago showed that when the purified capsid proteins of TMVs and its RNA genome were combined in aqueous solution under the right conditions of pH and ionic strength, fully infectious TMV particles were formed [431]. TMV was, in fact, the first virus that was reconstituted in vitro. A dozen years later the first "spherical" virus was reconstituted in vitro: CCMV. Once again, infectious viral particles were formed spontaneously from the self-assembly of the purified RNA genome and capsid proteins [287].

The spontaneous incorporation of genome in the capsid is the distinguishable feature of self-assembly of RNA viruses, which gives rise to a number of important questions. What are the fundamental building blocks or the assembly units of different viral shells? [65]. What is the maximum length of genome that can be encapsidated in a viral shell? Does the length of genome determine the size of viral shell? Equivalently, what is the relation between the radius of gyration of the encapsidated genome and the capsid radius? Is the genome pressurized by confinement in the capsid? Since little information is available about the three-dimensional nature "size and shape" of long RNA molecules containing thousands of nucleotides, several self-assembly experiments replaced RNA with linear negatively charged polymers like polyvinyl sulfonate (PVS) or polystyrene sulfonate (PSS) [432].

Also because of unknown RNA tertiary structure effects–resulting from self-complementary base pairing in the viral RNA sequence–it is a highly non-trivial issue how to model the RNA component in viral self-assembly. To this end, most theoretical and numerical work to date has been focused on linear polymers, with some effort being spent on branched polymers to study the role of RNA in conferring stability to viral shells. Fig. 52 shows a ss-RNA with 1000 nucleotides assuming a branched structure in solution due to base-pairing between the nucleotide bases. The branched structure in the figure is obtained employing the RNAfold program from the Vienna RNA package [433].

In what follows we first present the experimental efforts for deciphering the role of RNA in virus assembly including topology, size and charges and then we focus on the theoretical approaches.

5.7.1. Experiments with linear polymers

Several years ago, to elucidate the impact of length of genome on the size of capsid, Hu et al. studied the *in vitro* self-assembly of virus-like-particles (VLPs) formed by the capsid protein of CCMV and the negatively charged PSS, a highly flexible polyelectrolyte chain, for molecular weights ranging from 400 kDa to 3.4 MDa (1900 to 16 500 monomers) [432]. As illustrated in Fig. 53, they found that the size of CCMV capsid increases from pseudo $T = 2$ to $T = 3$ structures with increasing the length of PSS chain. More specifically, a jump in the capsid size was observed when the monomer number increased from 4900 monomers (1 MDa) to 9800 monomers (2 MDa). While these experiments shed light on the impact

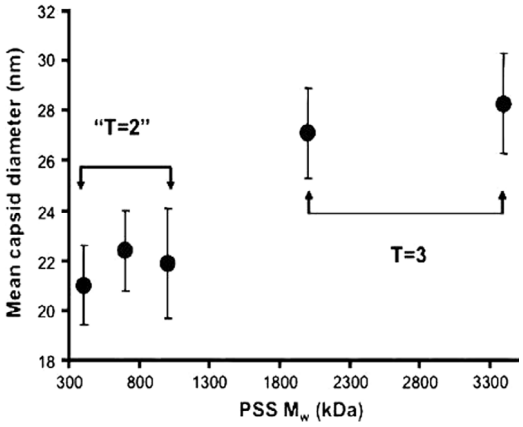

Fig. 53. The mean capsid diameter as a function of the molecular mass of encapsidated PSS. The figure reveals a jump in the capsid T number when the molecular mass increases from 1 to 2 MDa.
Source: Adapted from Ref. [432].

of the genome length on the size of a capsid, they do not determine the optimal number of encapsidated monomers for a given capsid size.

To obtain the optimal length of the encapsidated polymer for a CCMV capsid, Gelbart, Knobler and collaborators repeated the above experiments with much shorter PSS chains (38 kDa, 180 monomers), each with 180 negative charges. As shown in Fig. 54a, they found a bimodal distribution of particle diameters corresponding to $T = 1$ and pseudo $T = 2$ structures [434]. According to their experiments there were on average two polymers in each $T = 1$ capsid and three in each $T = 2$. Since the natural size of CCMV capsid is $T = 3$, the results were unexpected. To obtain a $T = 3$ structure, the ratio of PSS:CP molar ratio was increased from 34 : 1 to 4.2 : 1. Assuming that with increasing number of polymers compared to capsid proteins in solution, more polymers can be packaged in one single capsid and the chances of obtaining larger capsid would consequently increase. Quite interestingly, it was found that the fraction of $T = 2$ capsids increased by a factor of 3 and still no $T = 3$ structures were formed.

It is important to note that there are 600 and 1200 positive charges on the inner wall of $T = 1$ and $T = 2$ capsids of CCMV, respectively. Thus in the experiments with 180 monomers noted above, the ratio of negative to positive charges is 0.6 for the $T = 1$ and 0.45 for $T = 2$ capsids. This result is quite unexpected, as the ratio of negative charges to the positive ones in many ss-RNA viruses has been measured to be approximately about 1.6. The overcharging of ss-RNA viruses is intriguing and has been the subject of many papers [312,313,315–317,432,435,436], which will be addressed in the theory part of this section. The results of undercharging or under-compensation of the protein positive charge in the experiments with linear short polymers might appear puzzling but the theoretical calculations have also shown undercharging of VLPs with linear polymer [313,315] and overcharging of virus particles and VLP's with RNA enclosed.

The above experiments also reveal the importance of stoichiometry ratio: The relative numbers of $T = 1$ to $T = 2$ structures depend on the molar ratio of capsid protein (CP) to PSS. The impact of stoichiometry ratio on the encapsidation of low molecular weight PSS by CCMV coat protein has also previously been studied by Sikkema et al. [437]. Following up on the early experiments of Bancroft [438], they investigated a change in capsid size as they increased the ratio of the PSS to coat protein concentrations. Remarkably, at constant coat protein concentration, small stoichiometric ratios produced both $T = 1$ and $T = 3$ particles whereas at higher ratios only $T = 1$ particles formed in solution. The impact of stoichiometry ratio has already been subject of several theoretical studies Refs. [439–442] and reviewed in Ref. [443].

5.7.2. Experiments with RNAs of different lengths

To explore the basis of overcharging in virions that encapsulate RNA and undercharging with linear polymers, Gelbart, Knobler and collaborators repeated the experiments presented in the previous section but using truncated BMV RNA of different lengths: 1.0, 2 and 2.5, 3.6 and 4 kilo base (kb) [444]. Several puzzling results were observed in these experiments. The size distribution of VLPs with a 1.0, 1.5, 2.0 and 2.5-kb RNA indicated a mixed population of $T = 2$ and $T = 3$ capsids. No $T = 1$ structure was formed. Also they observed that molecules shorter than 2.0 kb were packaged completely but only in multiple copies, *e.g.*, two 1.0-kb RNAs in a $T = 2$ or two 1.5-kb RNAs in a $T = 3$ capsid. Interestingly in all these cases the RNA-capsid complexes were overcharged, *i.e.*, more negative charges are on RNA than on capsid proteins.

Since for all these experiments, the proteins of CCMV capsids were mixed with RNA of BMV, an obvious question arises: how does CCMV RNA compete with BMV RNA if they both have the same length? Also how does RNA compete with a linear polymer in a head-to-head competition? How different lengths of RNA compete with each other in the assembly experiments?

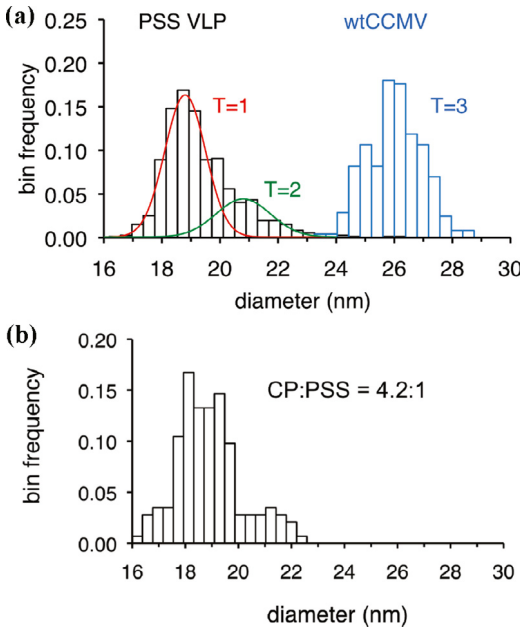

Fig. 54. (a) Distribution histogram of diameter of PSS VLPs (in black) formed employing a molar ratio of 34 CP to 1 PSS based on images of 900 capsids. The Gaussian curves are fitted with the centers at 18.8 and 20.8 nm to measure the number of $T = 1$ (72%) and $T = 2$ (28%) particles. The wild type measurements for CCMV are plotted in blue for reference. (b) Size distribution histograms for encapsulated PSS with CCMV CP with a mole ratio of 4.2 to 1.
Source: Adapted from [434].

5.7.3. Head-to-head competition experiments

To study the competitiveness of RNA with certain size, a set of experiments in Ref. [444] was designed such that two different RNAs compete "head-to-head" for a limited amount of CP. More specifically, a competition experiment consisted of mixing equal masses of the competitor RNA and full length BMV RNA with CCMV capsid proteins at a capsid protein/total RNA mass ratio 3:1 that is ideal for packaging of only half of the RNA in solution. For the purpose of experiments, the CCMV capsid proteins were mixed with BMV RNA to eliminate the chance of any specific interactions that might exist between CCMV capsid proteins and its native RNA. Therefore in these experiments only the effect of length of RNA was investigated.

It is important to note that at $pH > 6.5$, protein-protein interactions in CCMV are weak and as such the shell formed by virus coat proteins around one RNA can dissociate and assemble around another one. Thus, it seems that at neutral pH, different RNA/CP complexes are in thermal equilibrium, which include different lengths of RNA attached to CPs, loosely assembled capsids, or a combination of both. The competition experiments always start at pH 7 and then pH is lowered to 4.5 in which the capsids are completely closed and the protein-protein interaction is so strong such that the capsid can no longer disassemble in order to reassemble around another RNA.

Fig. 55 illustrates the result of the competitive experiments, relative packaging efficiency of ss-RNAs as a function of length of RNA [444]. According to these experiments, CP often leaves the shorter RNA and go to the longer BMV RNA. The case of 2.5-kb is particularly interesting: when 2.5-kb RNA alone was packaged, roughly equal numbers of $T = 2$ and $T = 3$ capsids were formed; in contrast, the diameter distribution for the capsids forming from the competition between wt BMV RNA and 2.5-kb RNA showed only a single size assembled, corresponding to $T = 3$. For the case of 4.0-kb RNA, they found asymmetric ellipsoidal capsids, with an axial ratio of 1.5. These experiments indicate the difficulty of singling out the effect of RNA size but nevertheless it appears that the native BMV RNA whose length is almost the same as CCMV wild type RNA get packaged more efficiently than the truncated BMV RNAs.

More recently [445], another set of head-to-head experiments were done between a ss-RNA with no secondary or higher order structure (polyU) and native CCMV RNA. While viral RNAs are highly branched because of long distance base-pairing between nucleotides and thus more compact to be encapsidated by viral proteins, the experiments reveal that in a head-to-head competition between polyU and CCMV RNA, the capsid proteins of CCMV preferentially "choose" the linear polymer!

These experiments will be discussed in the theory/simulation sections below. However, before we start the theory section, we will present another experiment in which we find that in addition to RNA length, the number of charges on capsid proteins play an important in the assembly and stability of virus particles.

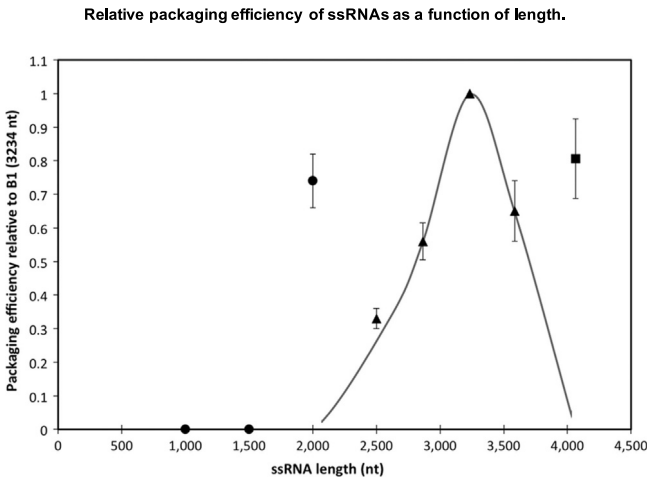

Fig. 55. Relative packaging efficiency of RNAs by CCMV capsid efficiency vs. length. The standard deviations are illustrated by the vertical bars. All quantities are given with respect to BMV RNA1 with 3224 nt. The triangles denote competitions in which the competitor RNAs assemble into $T = 3$ structures only. The circles show the situations where both $T = 2$ and $T = 3$ capsids assemble, and the squares correspond to the formation of both $T = 3$ and $T = 4$. The relative packaging efficiency has a maximum at 3.2 kb corresponding to the case in which the RNAs can only assemble into $T = 3$ structures.
Source: Adapted from Ref. [444].

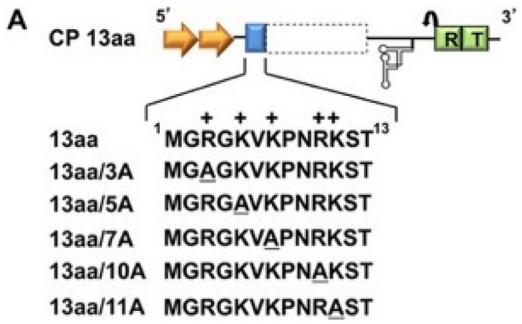

Fig. 56. Mutations are engineered into the N-terminal 13 amino acid motif of capsid proteins. Positively charged amino acid residues Arginine (R, at positions 3 and 10) or lysine (K at positions 5, 7 and 11) are denoted by a + sign and are substituted one at a time. Alanine or lysine substitutions at the corresponding locations are underlined.
Source: Adapted from Ref. [309].

5.7.4. The number of charges on capsid proteins and optimal length of RNA

An important feature of several plant RNA viruses is the presence of cationic arginine-rich polypeptide chains that form the N-terminals or N-termini of the capsid protein [436,446,447], see Section 5.4.

In the case of STMV, *e.g.*, it has been demonstrated that neutralization of N-proximal positive charges decreased the efficiency of RNA packaging [309]. The first N-terminal 13 amino acids (aa) region in STMV capsid protein is positively charged because of the presence of 2 arginine and 3 lysine residues (see Fig. 56). In a set of *in vivo* experiments, a series of mutations on the N-terminal 13 aa motif of virus coat proteins were engineered to modify the location and number of charges on the N-terminal and their impacts on genome packaging were evaluated [309].

Sivanandam et al. substituted the lysine residue located at position 3, 5, 7 and 11 with alanine, one at the time as illustrated in Fig. 56 [309]. These mutants replicated and assembled into virions. However, the analysis of packaged RNA revealed that a truncated STMV (i.e. STMVΔ150) preferentially packaged over genomic RNA see Fig. 57. The results of this study accentuates the significance of the positively charged residues in the replication and genome packaging of STMV. Interestingly, a positively charged aa at position 3 was shown to be obligatory for packaging of STMV progeny, indicating the interactions beyond electrostatics, like steric or specific RNA-protein (packaging signals) interactions play an important role in the assembly.

All above experiments show the urgency of developing theoretical and numerical groundwork for modeling RNA to explain several observed unexpected results. We would like to emphasize that there have been several thorough reviews covering the role of genome on the virus assembly using particle-based simulations [443,448]. In this paper, we focus on the analytical, numerical and most recent simulations.

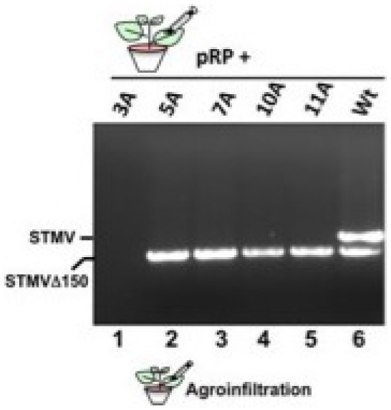

Fig. 57. Analysis of viral RNA recovered from N. benthamiana plants co-infiltrated with pRP. The shorter variant of STMV RNA is shown in lanes 1 through 5 and wt STMV RNA in lane 6.

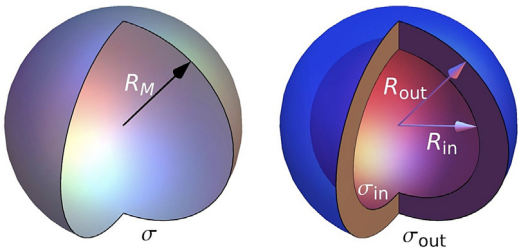

Fig. 58. Models of viral capsids. Left: an infinitely thin shell model described by a single net surface charge density. Right: a finite thickness shell model, with different epitopal and hypotopal charge densities as well as a separate dielectric core of the shell. The continuum ss-RNA encapsidation models are usually framed within the inifinitely thin shell model.

5.8. Theoretical description of ss-RNA packaging

On the most basic level ss-RNA is a charged, flexible polymer or a *polyelectrolyte*. There are many levels on which one can describe the system of this type but from the point of view of calculations, the continuum model is the most convenient and easiest to formalize. Of course it is understood that when one compares the results of this model with either simulations, usually based on discrete models of polymer chains, or actual experiments with many other implicit decorations of the basic model, one needs to make sensible comparisons.

An important simplification is also related to the description level of the viral shell. The capsid can be considered either as infinitely thin with a single net surface charge density, or indeed as a finite thickness shell, with an inner and outer walls both charged separately, see the discussion in Section 5.3. The positive charges are often concentrated on the capsid interior surface, while, typically negative charges are concentrated on the capsid exterior surface. In the case of finite thickness models, one needs to take into account not only the capsid surface charge densities, but also its explicit dielectric properties, see Fig. 58. The continuum ss-RNA encapsidation models are usually used with the infinitely thin shell model.

5.8.1. ss-RNA as a linear polymer

Among the many formulations of the adsorption of polymer chains to a surface, the simplest is the self-consistent field theory introduced by Edwards and reviewed by de Gennes [449]. In the *ground state dominance approximation* (GSDA)where only the dominating contribution to the polymer partition function is considered, the total free energy of a confined linear chain is,

$$\beta F = \beta F_V + \beta F_S \tag{166}$$

where $\mathcal{F}_V$ is the volume term and the surface term βF_S describes the interaction between the monomers and the confining surface [450]. The volume free energy of a confined chain can be written as the sum of an entropic term associated with the confinement of the chain and an excluded volume term [313,451],

$$\beta \mathcal{F}_V = \int \mathrm{d}^3\mathbf{r} \left\{ \frac{a^2}{6} |\nabla \Phi(\mathbf{r})|^2 + \frac{1}{2} \upsilon_0 \Phi^4(\mathbf{r}) - \lambda \left(\Phi^2(\mathbf{r}) - \frac{N}{V} \right) \right\}, \tag{167}$$

with $\Phi^2(\mathbf{r})$ the monomer density at position r, β the inverse temperature in units of energy, v_0 the effective excluded volume per monomer and a the statistical Kuhn length of the chain averaged over the entire sequence along the genome. The Lagrange multiplier λ ensures that the number of monomers inside the capsid is fixed at

$$N = \int d^3\mathbf{r}\ \Phi^2(\mathbf{r}). \tag{168}$$

The surface term can be written in the form of

$$\beta\mathcal{F}_S = -\gamma\beta a^3 \int \mathrm{d}^2\mathbf{r}\ \Phi^2(R), \tag{169}$$

representing the attractive contact energy of the RNA chain with the capsid surface, where R is the capsid radius and γ denote the adsorption energy per unit area. The electrostatic attraction between RNA and the capsid shell is assumed to be short-ranged due to the presence of salt screening and as such can be approximated by either a contact potential, as in Eq. (169), or by an interaction potential with a finite range.

Eq. (167) obtained through GSDA has been employed extensively to study the assembly of viral shells. Recently, Li et al. [452] have used the self-consistent field theory (SCFT) to investigate the validity of GSDA in studying virus assembly. They find that there are two regimes in which GSDA results are accurate. First, when the genomic RNA length is long enough compared to the capsid radius, and second, when the interaction between the genome and capsid is so strong that the genome is basically localized next to the wall. In particular, they find that for the case in which RNA is more or less distributed uniformly in the shell, regardless of the length of RNA, GSDA is not a good approximation. As the polymer–shell interaction becomes stronger, the energy gap between the ground state and first excited state increases, and then GSDA becomes a better approximation. Thus in most virus assembly conditions, GSDA is useful to extract important information.

Minimization of the total free energy with respect to $\Phi(\mathbf{r})$ then yields two Euler–Lagrange equations, one for the volume part and one for the surface part. The former is obtained in the form of an Edwards equation for the monomer density field

$$\frac{a^2}{6}\nabla^2\Phi(\mathbf{r}) = -\lambda\Phi(\mathbf{r}) + \upsilon_0\Phi^3(\mathbf{r}), \tag{170}$$

while the latter is obtained in the form of a boundary condition

$$\mathbf{n}\cdot\nabla\Phi(|\mathbf{r}| = R) = \kappa_D\Phi(|\mathbf{r}| = R) \tag{171}$$

where $\mathbf{n}$ is the normal to the capsid surface and $\kappa_D = 6\beta a\gamma$ an inverse length representing the interaction strength between the RNA and the wall. These two equations can be solved numerically to obtain the genome monomer density profile $\Phi^2(r)$ inside the capsid.

Hu et al. [312] solved Eq. (170) subject to the boundary condition given in Eq. (171) with the constraint presented in Eq. (168) to explain the jump in the capsid radius as a function of genome length, see the experiment illustrated in Fig. 53. They found that as the size of the linear chain increases, the optimal diameter of the capsid increases, too. However, since icosahedral shells have a lower elastic energy compared to the other type of spherical shells, they showed that the capsid diameter remains constant for over a range of genome lengths and then if the length increases beyond a certain size, the capsid structure changes from one T number to the next larger one, consistent with the experiments presented in Fig. 53. Using also Eq. (167) but ignoring the impact of curvature on the genome adsorption to the capsid wall, van der Schoot and Bruinsma calculated the encapsidation free energy and found that it goes through a minimum as a function of number of monomers [441]. They showed that there is an optimal length for a given capsid radius.

In the above papers the electrostatic interactions were considered purely as short ranged, implicitly described by an excluded volume term. This approximation has some validity only for the case of large electrolyte screening but in general, electrostatic interactions between the monomer as well as between the monomers and the virus inner wall should be included explicitly. With this in mind, Siber and Podgornik included explicitly the genome–capsid electrostatic interactions [313] and used a generalized free energy *Ansatz*, composed of three terms

$$\beta F = \beta F_V + \beta F_S + \beta F_{ES}, \tag{172}$$

where the last one pertains explicitly to the electrostatic interactions, while the other two are the same as introduced above. The electrostatic free energy of a system composed of a simple monovalent salt (see Section 5.5) and a linear polyelectrolyte chain can be written in complete analogy to Eq. (154) as a sum of a bulk and a surface part

$$\beta F_{ES} = -\beta\int_V \mathrm{d}^3r\left[\frac{\varepsilon_0\varepsilon}{2}\left(\nabla\psi(\mathbf{r})\right)^2 + 2k_BTn_b\cosh\beta e\psi(\mathbf{r})\right] - \beta\int_S \mathrm{d}^2r\ \sigma\ \psi(\mathbf{r}) + \beta\int_V \mathrm{d}^3r\ \tau\ \psi(\mathbf{r})\Phi^2(\mathbf{r}). \tag{173}$$

The first two terms are the PB free energy of the monovalent salt and the capsid with constant surface charge density σ, while the last term describes the electrostatic interaction of a polymer chain with linear charge density τ with the mean electrostatic potential $\psi(\mathbf{r})$ [313]. The concentration of the monovalent salt ions in the bulk is n_b.

The minimization of the above free energy then again yields two volume Euler–Lagrange equations and two surface Euler–Lagrange equations. One should consider the minimization with respect to two fields, *i.e.*, the polymer monomer

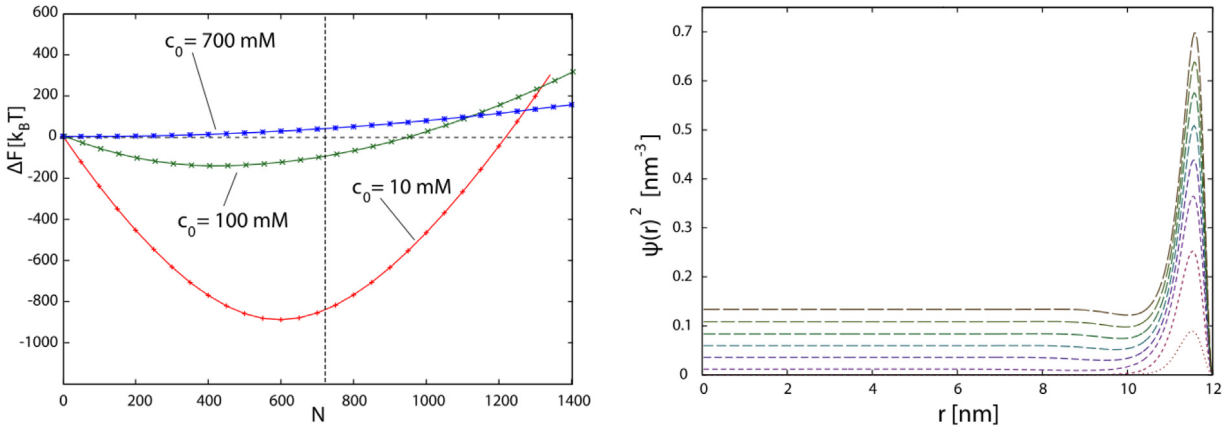

Fig. 59. Left: The free energy differences, $\Delta F(N) = F(N) - F(0)$, describing the complexation of the capsid with the polyelectrolyte molecule, composed of N monomers. The parameters used are $\tau = e_0$, $a = 0.5$ nm, $\upsilon_0 = 0.05$ nm^3, $T = 300$ K, $\sigma = 0.4$ e/nm^2, and $R = 12$ nm for different bulk concentrations of the salt ions ($n_b = 10$,100, and 700 mM). The vertical dashed line denotes the number of monomers for which the polyelectrolyte charge equals in magnitude the capsid charge ($N \approx 724$). Right: The radial polyelectrolyte monomer density distribution, $\Phi^2(r)$, for $n_b = 100$ mM, with $N = 100$, 300, 500, 700, 900, 1100, 1300, and 1500 (from lower to upper curves).
Source: Adapted from Ref. [313].

density field Φ and the mean electrostatic potential ψ. The former gives the modified Edwards equation, Eq. (170), in the form

$$\frac{a^2}{6}\nabla^2\Phi(\mathbf{r}) = -\lambda\Phi(\mathbf{r}) + \upsilon_0\Phi^3(\mathbf{r}) + \beta\tau\Phi(\mathbf{r})\psi(\mathbf{r}), \tag{174}$$

with the same boundary condition as given in Eq. (171). The solution $\Phi(\mathbf{r})$ exists only inside the capsid, $|\mathbf{r}| \leq R$, because the capsid is impermeable to RNA that is confined inside it. On the other hand, the minimization with respect to the mean electrostatic potential yields a modified standard PB equation (compared to Eq. (154)) for inside the capsid as follows,

$$\frac{\beta e^2}{4\pi\lambda_B}\nabla^2\psi_{in}(\mathbf{r}) = +2n_b e \sinh\beta e\psi_{in}(\mathbf{r}) - \tau\Phi^2(\mathbf{r}) \tag{175}$$

and for the outside as,

$$\frac{\beta e^2}{4\pi\lambda_B}\nabla^2\psi_{out}(\mathbf{r}) = +2n_b e \sinh\beta e\psi_{out}(\mathbf{r}). \tag{176}$$

Here $\lambda_B = e^2\beta/4\pi\epsilon\epsilon_0$, is the Bjerrum length, a measure of the dielectric constant (ϵ) of the solvent and is about 0.7 nm for water at room temperature. The boundary condition is then derived from the surface electrostatic energy and has the same form as Eq. (157)

$$\varepsilon_0\varepsilon\Big(-\mathbf{n}\cdot\nabla\psi_{in}(|\mathbf{r}| = R) + \mathbf{n}\cdot\nabla\psi_{out}(|\mathbf{r}| = R)\Big) = \sigma, \tag{177}$$

where $\mathbf{n}$ is again the capsid surface normal and the index *in*/*out* refers to the mean electrostatic potential inside and outside of the capsid, as the electrostatic field exists on both sides of the capsid. The above boundary condition assumes an infinitely thin capsid model, see Fig. 58.

Numerical solutions of the above set of the linear polyelectrolte Poisson–Boltzmann equations yield the complete free energy of the system and depends on three parameters that describe the free energy of the capsid–polyelectrolyte complexation: the polyelectrolyte length (i.e. the number of monomers, N), the bulk concentration of mono-valent salt, n_b, and the capsid surface charge density, σ. The free energy, see Fig. 59, exhibits a minimum, pointing to an optimal number of monomers, N_c, which can be packed within a capsid and depends strongly on the bulk salt concentration. The figure shows that increased salt concentration would hinder the formation of functional viruses for polyelectrolyte beyond certain length. In addition, the calculated optimal number of monomers corresponds to RNA charge that is *less than the protein charge*, explaining to some extent the phenomena of undercharging observed in the experiments with linear polymers [434], illustrated in Fig. 54 and reviewed in Section 5.7.1. The calculated monomer density of the ss-RNA is always concentrated in a shell close to the capsid, see Fig. 59.

In the studies described above, ss-RNA has been modeled as a linear polymer. However, base pairing between complementary nucleotides gives rise to branched or more complex structures like pseudoknots. Erdemci et al. developed a simple model and studied the impact of base-pairing including pseudoknots on the statistical conformations of ss-RNA entrapped inside an adsorbing spherical shell [453]. Quite interestingly, they found that the profile of RNA inside a viral shell undergoes a sharp transition from collapsed to an extended state depending on the length of RNA, consistent with the experimental observations [453].

Since in general pseudoknots are rare in nature and RNA adopts a highly branched structure in solution, we focus here on the studies focused on modeling RNA as branched polymers [454]. In the next section we present theoretical models and simulations investigating the impact of RNA branching on the stability of viral shells.

5.8.2. ss-RNA as a branched polymer

The phenomena of undercharging with linear polymers reveals the urgency for the extension of polyelectrolyte Edwards–De Gennes equations to include the affinity of RNA for base-pairing in order to assess whether the RNA secondary structure plays an important role in virus overcharging. Randomly branched polymers have been used extensively as the simplest starting model for studying the conformational entropy of self-associating RNA. Dealing with branched polymers is a rather difficult task but Lubensky and Issacson (LI) have developed a model for flexible annealed branched polymers in which the polymer can fluctuate freely over all possible branching configurations [455,456].

To calculate the configurational entropy of the chain, following the LI model, Erdemci-Tandogan et al. [315,316] assumed a single polymer with no closed loops, enclosed in the capsid, and added two terms to Eq. (167), describing the contribution of branching to the free energy such that the modified volume free energy of the branched polymer configuration is now given by

$$\beta\mathcal{F}_V = \int \mathrm{d}^3\mathbf{r}\left\{\frac{a^2}{6}|\nabla\Phi(\mathbf{r})|^2 + \frac{1}{2}\upsilon_0\Phi^4(\mathbf{r}) - \lambda\left(\Phi^2(\mathbf{r}) - \frac{N}{V}\right) - \frac{1}{\sqrt{a^3}}\left(f_e\Phi + \frac{a^3}{6}f_b\Phi^3\right)\right\} \tag{178}$$

with f_b and f_e the fugacity of the *branch-points* and stem-loops or hair-pins which are considered as *end-points*, respectively. The numbers of end- and branch-points N_e and N_b of the polymer are related to the fugacities f_e and f_b as follows

$$N_e = -f_e\frac{\partial\beta F_V}{\partial f_e} \qquad \text{and} \qquad N_b = -f_b\frac{\partial\beta F_V}{\partial f_b}. \tag{179}$$

In the absence of closed loops and for a single polymer chain the number of end points depends on the number of branched points as follows

$$N_e = N_b + 2. \tag{180}$$

The total free energy is again composed of three parts, just as in the case of the linear chain, Eq. (172). The volume part given in Eq. (178) describes the polymer entropy loss due to having a non-uniform polymer density, non-electrostatic self-repulsion of the monomers and the free energy change stipulated by the annealed branching of the polymer. The second part, βF_S, involves the non-electrostatic interactions between the polymer and the capsid wall and the third one, βF_{ES}, describes the contribution of electrostatic interactions between the polymer, the shell and the salt ions at the level of Poisson–Boltzmann theory [313,315].

By varying the free energy functional with respect to fields $\psi(r)$ and $\Phi(r)$, one derives a new set of coupled non-linear Euler–Lagrange differential equations, describing the monomer density, and the mean electrostatic potential inside and outside of the capsid shell. The Euler–Lagrange equation for the monomer density field can be cast into the form

$$\frac{a^2}{6}\nabla^2\Phi = -\mathcal{E}\Phi(\mathbf{r}) + \beta\tau\psi(\mathbf{r})\Phi(\mathbf{r}) + \upsilon\Phi^3 - \frac{f_e}{2\sqrt{a^3}} - \frac{\sqrt{a^3}}{4}f_b\Phi^2 \tag{181}$$

with the boundary condition at the surface of the shell given by Eq. (171), investigated in the case of two limiting forms, corresponding to either vanishing surface interaction energy (the Neumann boundary condition $\mathbf{n}\cdot\nabla\Phi(|\mathbf{r}| = R) = 0$) or infinitely large surface interaction energy (Dirichlet boundary condition $\Phi(|\mathbf{r}| = R) = 0$). Furthermore, from Eq. (179) the connection between the *fugacities* of the branch points and end-points, and the *number* of end- and branch-points, N_e and N_b, can be derived as

$$N_e = \frac{f_e}{\sqrt{a^3}}\int_V d^3\mathbf{r}\ \Phi(\mathbf{r}) \qquad \text{and} \qquad N_b = \frac{f_e\sqrt{a^3}}{6}\int_V d^3\mathbf{r}\ \Phi^3(\mathbf{r}). \tag{182}$$

The polyelectrolyte PB equation for the branched chain does not differ from the one for the linear chain, Eq. (175), inside the shell, and , Eq. (176), outside the shell. The boundary condition connecting the electrostatic potential inside and outside of the shell again has the same form as Eq. (177).

Since many ss-RNA viruses self-assemble spontaneously *in vitro*, it is expected that the osmotic pressure due to the confinement of RNA inside the capsid to be zero or negative [307]. By contrast, as described in Section 5.6, most ds-DNA viruses are under a large positive osmotic pressure $\simeq 10 - 100$ atm, exerting a force from the inside out on the capsid, implying that active mechanisms, such as molecular motors that use up ATP molecules, are required to pack their genome, see also Section 5.6.3. The excess osmotic pressure due to the presence of genome can be derived in the standard way from the total free energy of the capsid with the enclosed polyelectrolyte as

$$P(N) = -\left(\left.\frac{\partial F}{\partial V}\right|_{Q_c,N} - \left.\frac{\partial F}{\partial V}\right|_{Q_c,N=0}\right), \tag{183}$$

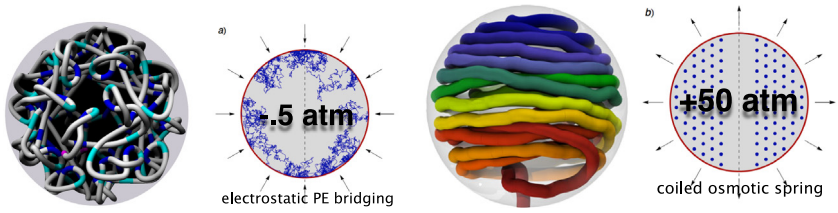

Fig. 60. Sketch of the pressure and structure of an ss-RNA [Panel (a)] vs ds-DNA virus [Panel (b)]. The genome is shown in blue, capsid in red, arrows indicate the direction of pressure. Cross section through the capsid in the case of ss-RNA genome, showing a distinct boundary layer close to the inner surface of the virus with a depleted region in the middle. In the ds-DNA case the genome density within the capsid is (almost) uniform, showing pronounced orientational and positional ordering.
Source: Adapted from Marenduzzo et al. [421], Fokine et al. [457] and Siber et al. [307].

where V is the volume and Q_c the total charge of the capsid. Interestingly enough, for a confined flexible polyelectrolyte this osmotic pressure is often found to be small and negative, i.e. the electrostatic force is directed inward to decrease the radius of the capsid. The typical magnitudes of the pressures are on the order of atm at physiological salt conditions, or smaller for capsids of larger radii. This is in clear contrast with osmotic pressure in the case of ds-DNA bacteriophages, where positive osmotic pressures acting outward are two orders of magnitude larger. This fundamental difference in osmotic pressure is schematically depicted in Fig. 60.

The negative values of osmotic pressure are in fact often found in the interaction of charged planar surfaces with an oppositely charged polyelectrolyte chain in between, see the discussion in Refs. [307,316], due to the electrostatic *polyelectrolyte bridging configurations* of the chain, inducing attractive interactions between apposed surfaces that result in a negative value of the osmotic pressures. The very same mechanism is operating in the case of the linear or branched polyelectrolyte chain confined to a spherical charged shell.

Numerical solutions of the free energy of a branched polyelectrolyte enclosed inside a capsid and the osmotic pressure acting on the shell have been investigated in detail [315,316]. The plots of the free energy, F and osmotic pressure P vs. the monomer number N are given in Fig. 61(a) and (b), respectively. The solid and dotted lines correspond to linear polymers with $f_b = 0$ and dashed and dotted-dashed lines to branched polymers with $f_b = 3.0$. The salt concentrations are 10 mM (solid and dashed lines) and 100 mM (dotted and dotted-dashed lines). The figure clearly demonstrates that the free energy minimum becomes deeper and moves towards longer chains as the degree of branching increases. In fact, Fig. 61(c) shows that the optimal length of genome associated with the minimum of free energy depends on f_b such that more monomers are packaged as the degree of branching increases.

Fig. 62(a) shows that the free energy becomes deeper as the polymer becomes more branched, *i.e.* as f_b increases. This elucidates why a branched polymer is packaged more efficiently than the linear one at equal salt concentrations. It further explains why some RNAs could be encapsulated more efficiently than others, or indeed the linear polyelectrolytes. It is worth mentioning that the impact of branching is more pronounced at high salt. At low salt concentrations, the branching effect is less important because electrostatics then becomes the dominant force. Nevertheless, the optimal length of encapsidated genome is still longer for branched polymers compared to linear ones at low salt concentrations. Fig. 62(b) displays a plot of the ratio of number of branched points to the optimal number of monomers vs. the branching fugacity, which increases for higher f_b values.

The phenomena of overcharging in viruses can be explained at least in part by the effect of RNA branching. The total number of charges in a virus is $Q = Q_p + Q_c = \tau N + 4\pi R^2\sigma$ with $Q_p = \tau N$ the genome charges and $Q_c = 4\pi R^2\sigma$ the charges on the capsid. Fig. 62(c) shows the charge ratio of the genome to the capsid vs. the fugacity of branched points for two different salt concentrations at the minimia of the free energy. Obviously, the virion becomes overcharged for the values of $f_b > 2$ at 10 mM and $f_b > 1$ at 100 mM, where the two values corresponding to the genome and the capsid charges cross. Interestingly, the osmotic pressure becomes more negative as the degree of branching increases as illustrated in Fig. 62(d). This indicates that the virus becomes more stable as a result of branching.

Several softwares including RNAsubopt and RNAfold [433] and mfold [458] can predict the secondary structures of RNA based on the free energy changes due to base-pairing and the loop closure of the ss-RNA. RNAfold and mfold calculate the possible sets of base-pairing of G-C and U-A according to the estimate of the corresponding minimum free energies. To date, most softwares are more accurate for small pieces of RNA; nevertheless, RNAsubopt can produce Boltzmann weighted secondary structures, appropriate for the calculation of ensemble average of any quantity.

RNAsubopt has been used to calculate the thermally averaged number of branch points for RNA1 of BMV and CCMV to elucidate the competition experiments between RNA1 of CCMV and BMV [444]. The ensemble of secondary structures can be generated by using the RNA1 sequences of both BMV and CCMV [459], and subsequently their thermally averaged number of branched points can be calculated. RNA1 of BMV has 65 branched points vs. 60.5 branched points of RNA1 of CCMV. These numbers confirm the experimental results of Comas-Garcia et al. [444], which showed that RNA1 of BMV would be preferentially packaged over RNA1 of CCMV. While RNAsubopt is more appropriate for short RNAs, it has been used for longer viral genomes ($2500 - 1000$ nucleotides), leading to important results and new insights [460,461].

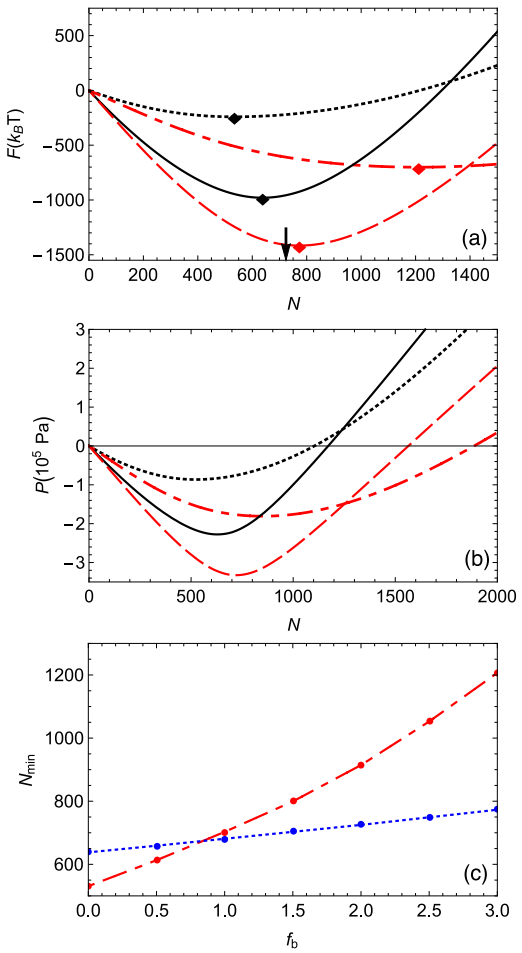

Fig. 61. Confined linear vs. branched polyelectrolyte chain. (a) Free energy as a function of monomer numbers for a linear polymer with $f_b = 0$ (solid and dotted lines) and a branched polymer with $f_b = 3.0$ (dashed and dotted–dashed lines) at two different values of salt concentrations, 10 mM (solid and dashed lines) and 100 mM (dotted and dotted–dashed lines). The arrow indicates the monomer number at which the full virus particle (capsid + polyelectrolyte) becomes neutral. (b) Osmotic pressure as a function of monomer number for a linear polymer with $f_b = 0$ (solid and dotted lines) and a branched polymer with $f_b = 3$ (dashed and dotted-dashed lines). Solid and dashed lines correspond to the salt concentration, 10 mM and dotted and dotted-dashed lines represent the salt concentration, 100 mM. (c) Minima of the free energy as a function of fugacity of branch points (f_b) at 10 mM (dotted lines) and 100 mM (dotted-dashed lines) salt concentrations. Other parameters used are $v_0 = 0.5$ nm^3, $\tau = -1$ e, $\sigma = 0.4$ e/nm^2, $b = 12$ nm, $a = 1$ nm and $T = 300$ K.
Source: Adapted from Erdemci-Tandogan et al. [315].

It is interesting to note that all the aforementioned experiments and calculations appear to be in contrast with the *in vitro* self-assembly experiments [445] of CCMV capsid proteins and polyU, a ss-RNA with no secondary or higher order structure. Beren et al. show that in the head-to-head competition experiments between the native CCMV viral RNA and polyU, the capsid proteins preferentially encapsulate polyU. Li et al. [160] calculated the free energy of the complex of RNA and capsid proteins to obtain the impact on the RNA encapsidation of genome stiffness due to RNA base-pairing. While viral RNAs are compact and highly branched, they could at the same time be more stiff because of base-pairing between the nucleotides. This effect can explain why under certain circumstances linear polymers is encapsidated more efficiently than viral RNA [445,462]. The free energy of RNA packaging by capsid proteins can increase if the effective Kuhn length of RNA increases as a result of base-pairing [160].

In addition to the mean-field calculations, scaling theories [439,442,463–465] have also been used to address the phenomena of overcharging. In particular Grosberg, Bruinsma and collaborators [463] also studied the work of encapsidation of viral RNA molecules vs randomized isomers and found that because of its branching, viral RNA has a distinct advantage to be encapsidated by viral capsid proteins.

All above calculations indicate that the secondary structure of RNA can give rise to the phenomena of overcharging. Quite interestingly, while several simulations on encapsulation of polymers with a fixed number of branching (quenched) as a model for RNA have also shown that the level of overcharging is a sensitive function of the secondary and tertiary structures of the RNA [436,466], the molecular dynamics simulations of Perlmutter et al. show that even linear polyanion

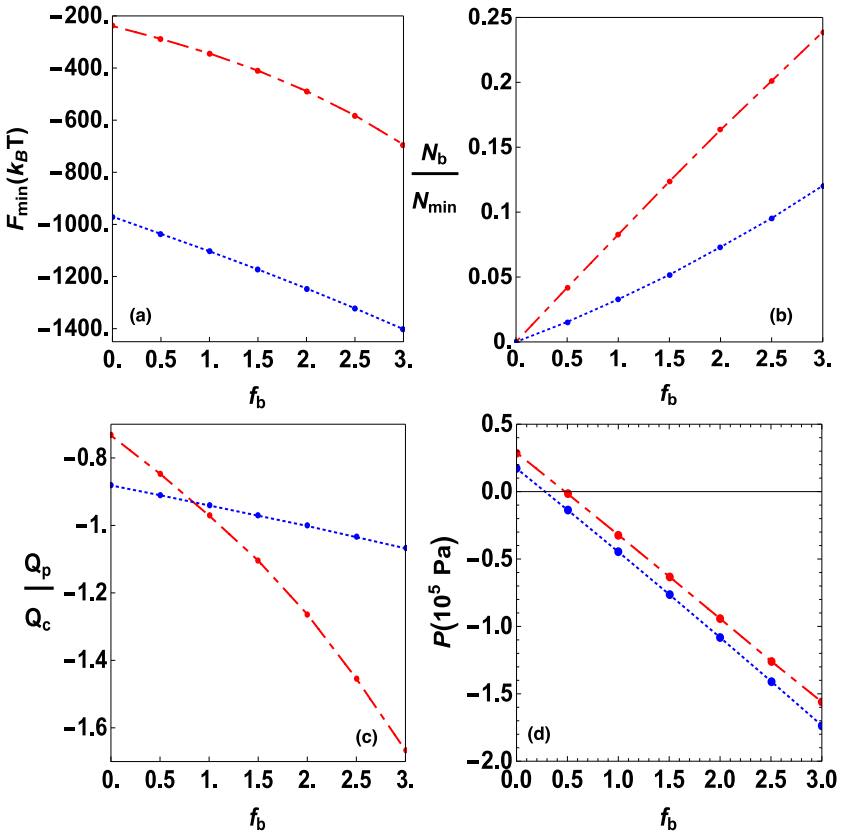

Fig. 62. Effects of branchiness. (a) Optimum free energy (b) Ratio of number of branched points to the number of monomers at the minima (c) Ratio of number of polymer charges to the capsid charges. When the two dependecies cross, the virion becomes overcharged. (d) Osmotic pressure for $N = 1200$ as a function of fugacity of branch points (f_b) at 10 mM (dotted lines) and 100 mM (dotted-dashed lines) salt concentrations. Other parameters used are $v_0 = 0.5$ nm^3, $\tau = -1$ e, $\sigma = 0.4$ e/nm^2, $R = 12$ nm, $a = 1$ nm and $T = 300$ K.

encapsulation can lead to overcharging [436]. This is in contrast with the mean-field calculations employing linear charged polymers and a uniformly charged sphere for which the optimal size of a genome is undercharged. In the next section we will look at the impact of N-terminal domain structure on the optimal genome length and how the presence of N-terminal tails can result in the overcharging of linear polymer–capsid complexes too.

5.8.3. The impact of N-terminal domain in overcharging

The experiments of Sivanandam et al. presented in Section 5.7.4 show that the length of encapsidated genome decreases as the number of charges on the N-terminal domain decreases. Moreover, their meanfield calculations have shown that for STMV, the optimal genome length becomes shorter when there are less positive charges on the capsid due to mutations, see Fig. 56. To improve the calculations performed in Section 5.8.2 and explain why the complex of linear polymer-capsid can also be overcharged, more recently Li et al. modeled N-terminal tails using Icosahedral spherical harmonics (see Section 2.2) for $T = 1$ and $T = 3$ structures with 60 and 180 positively charged regions, respectively. The charge distributions for structures with $T = 1$ and $T = 3$ icosahedral symmetry are shown in Fig. 63(a) and (b).

Li et al. considered both the "thin capsid model" where the charges are smeared on the inner wall of the spherical shell in 60 or 180 positions as shown in Fig. 63(a), and the "thick capsid model" with the charges protruded inside the capsid as shown in Fig. 63(b). For the thick capsid model, it is assumed that there are 60 ($T = 1$) or 180 ($T = 3$) protrusions presenting peptide tails (Fig. 63(b)) with charges uniformly distributed in the protruded domains. The main question is whether the presence of N-terminals, or in other words, the non-uniform charge density gives rise to the overcharging phenomena.

To include the N-terminal charge distribution, Li et al. added the term $\rho(\mathbf{r})dV$ to the free energy given in Eq. (167), with $\rho(\mathbf{r})$ the volume charge density corresponding to the charges on the N-terminal extended to the interior of the capsid. Minimizing the corresponding free energy with respect to the monomer density and electrostatic fields and considering the charge distribution based on Fig. 63, they obtained the polymer density profiles Φ^2 as a function of r, the distance from the center of the shell, as shown in Fig. 64(a) and (b) in three and one dimensions respectively. Since all the charges are sitting at the N-terminal tails with no charges on the wall between the domains, the polymer density is high at the

Fig. 63. Charge distribution of the capsid for (a) $T = 1$ thin capsid. The black spots show the regions with a uniform surface charge density. The charges are smeared on the surface representing the thin capsid model. (b) A $T = 3$ thick capsid. The charges are extended into the interior of the capsid.

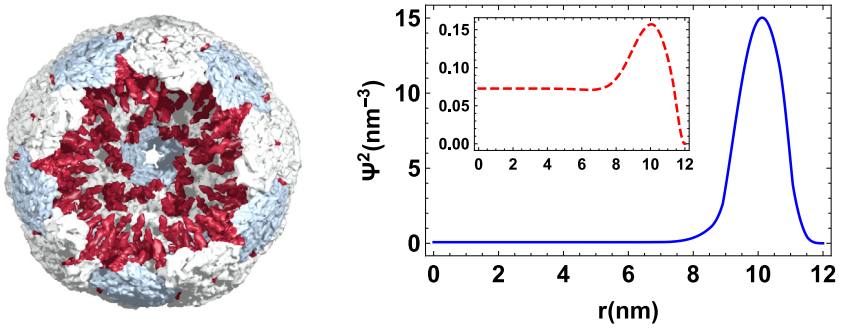

Fig. 64. Genome density profile of a $T = 3$ capsid in (a) 3D view. The protruded regions represent RNA (red). The density of RNA between N-terminals is very small and not shown in the figure. (b) 1D view as the function of capsid radius with non-uniform charge distribution. The figure shows the profiles along two different directions. The solid line corresponds to the direction in which the N-terminal tail is located and the dashed line to the direction without N-terminal tail (inset graph). In the absence of surface charge density and N-terminal tail (dashed curve), the density is still maximum close to the wall. The polymer is branched with $f_b = 3$, total monomer number $= 2411$, salt concentration $\mu = 100$ mM, $R = 12$ nm and $Qc = 1800$.
Source: Adapted from Ref. [160].

N-terminal regions and lower in the domains between N-terminal tails. The polymer density is lowest at the center of the capsid.

The results of Ref. [452] show that the optimal genome length increases for a non-uniform capsid charge distribution compared to a uniformly charged capsid and that the free energy becomes deeper for non-uniform capsid density indicating the higher efficiency of genome encapsidation. Another result of the study was that as the charges on the capsid are distributed *less* uniformly, the optimal length of encapsidated genome becomes longer.

To examine the impact of non-uniform charge distribution on the phenomena of overcharging, Li et al. calculated the encapsulation free energy as a function of genome length for a $T = 3$ structure as illustrated in Fig. 65. The dashed lines in the figure are related to a shell with a uniform charge density and the dotted lines correspond to the one with a non-uniform charge density. The results are obtained for both linear and branched polymers. For the non-uniform charge distribution, the optimal length of the encapsidated genome becomes longer as it is clearly illustrated in the figure. It is important to note that the phenomena of overcharging was observed only for the thick capsid model with the charges extended inside. No overcharging was observed when the charges were smeared non-uniformly over the surface of the capsid. The effect of RNA secondary structures on the optimal length of encapsidated genome is also illustrated in Fig. 65, showing that as the degree of branching increases, the optimal length of encapsidatd genome increases more for a capsid with the non-uniform charge distribution compared to the uniform one, with a transition from undercharging to overcharging depending on the degree of RNA branching and the distribution of charges on the capsid.

5.8.4. Packaging signal hypothesis

In principle, primary CP-RNA interactions are a combination of fundamental long-ranged electrostatic, hydrophilic–hydrophobic interactions, and short-ranged specific contacts between certain amino acids of the CPs and certain nucleotide sequence motifs of the RNA [467]. Strong electrostatic charge matching attraction between the CPs and the ss-RNA

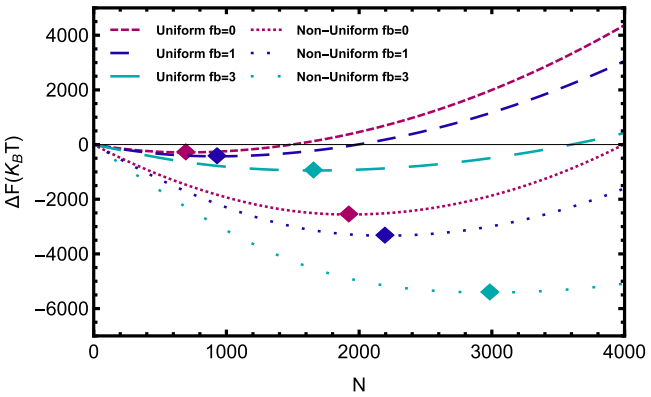

Fig. 65. Encapsulation free energy for a linear and branched polyelectrolyte as a function of monomer number for a capsid with uniform (dashed lines) and non-uniform (dotted lines) charge density. For a linear chain the branching fugacity $f_b = 0$ and increases to $f_b = 1.0$ and $f_b = 3.0$ as the chain becomes more branched. The diamonds indicate the minimum of free energy. Other parameters used correspond to a $T = 3$ virus: total capsid charges on capsid $Q_c = 1800$, $a = 1.0$ nm, $v = 0.01$ nm^3, $\mu = 100$ mM, $R = 12$ nm, tail length $= 4$ nm.

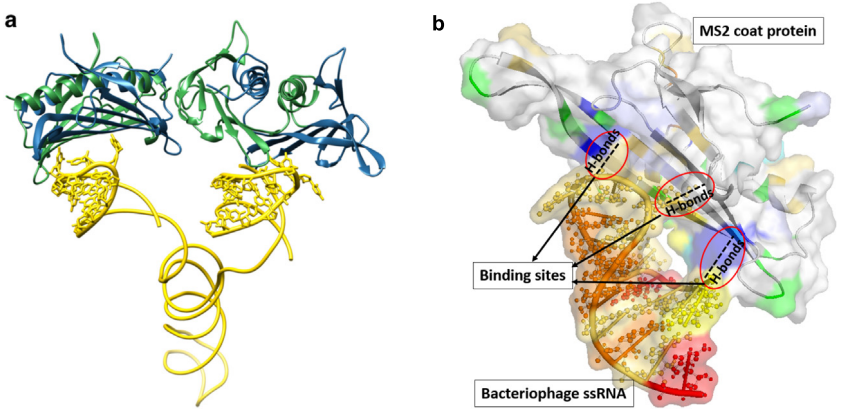

Fig. 66. Location of the binding sites in the MS2 bacteriophage. a: Two neighboring, consecutive stem loop PS sites of the MS2 genome (yellow) (PDB ID: 5TC1) in the linear genomic sequence are mapped on adjacent binding sites on the hypotope capsid protein (shown as ribbons) based on the icosahedrally averaged X-ray structure (PDB ID: 1ZDH12). Adapted from Ref. [318]. b: The MS2 coat protein and the RNA stem loop with explicit identification of the binding sites. The binding sites are associated with the strongest *ab initio* calculated hydrogen bonds in the nucleoprotein complex. Adapted from Ref. [472].

viral genome have been shown to initiate and drive the assembly of a number of viruses, as in the well-studied examples of CCMV [266] or BMV [447,468]. Although electrostatic interactions are without any doubt among the fundamental constituents of the virus self-assembly process [307,469], universal charge matching cannot explain all of the molecular details and specificities of the self-assembly process that are still not fully understood [470], despite great advances in high-resolution structure determination of virus particles [471] (see Fig. 66).

The point of departure of the *packaging signal hypothesis* is the indication of different *in vitro* and *in vivo* studies that the capsid self-assembly proceeds not by unspecific generic electrostatic associations, but through highly specific interactions between particular sections of RNA containing the so-called *packaging signals* (PSs, also defined as the origin of assembly sites, OASs) [470]. These PSs provide specific binding sites between the CPs and certain sequence recognition motifs of viral RNA [473,474], that are distributed along the genome, acting collectively to control the capsid self-assembly *in vitro* [474]. These primary specific CPRNA interactions within the virus capsid then appear as the key elements controlling its self-assembly [470,475], enabling the virus to differentiate between cognate genomes and cellular RNAs, and to complete the assembly process speedily and efficiently in an environment characterized by capsid protein concentrations that are much lower than in most *in vitro* studies. Although these CP-RNA interactions are then *grosso modo* sequence specific, the details of the molecular nature of this specificity and its relation to fundamental molecular interactions between the genome and the capsid proteins are not clear at all [472].

The packaging signal hypothesis with multiple copies of PSs at well defined symmetry allowed positions along the genome, results into an enhanced assembly efficiency [470]. Specific contacts between stem-loop motifs and CP subunits of the PS type have been postulated in the case of MS2 bacteriophage [476] (see Fig. 68) and the STNV [477] genome

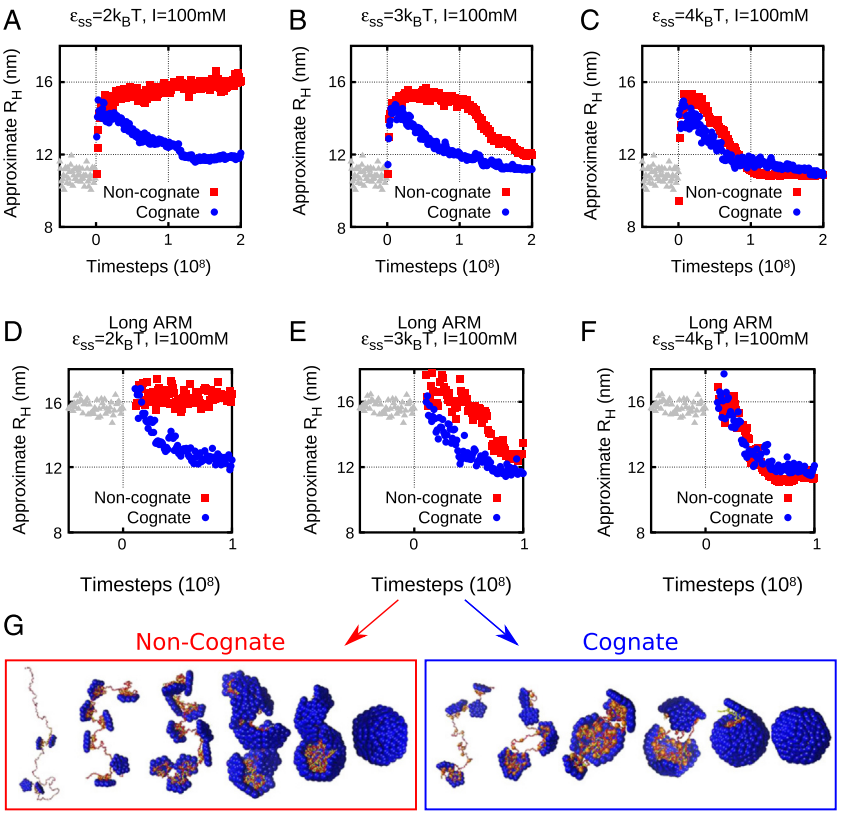

Fig. 67. (a) (A–F) Radius of hydration RH vs simulation time steps for different assembly path, for both non-cognate (red squares) and cognate RNAs(blue dots). The RH values before the addition of subunits to the solution are illustrated as (triangles). The subunit–subunit interaction energy ϵ_{ss} goes up from left to right. In the top row (A–C), the number of charges on ARM is +5, and the length of genome is 575 segments. In the second row (D-F), the number of charges on ARM increases to + 10, and the RNA length to 910 segments. (G) Snapshots of simulations related to (E), for both non-cognate RNA (left) and cognate RNA (right).
Source: Adapted from [479].

sequences, but with very different modes of action. In the MS2 PSs case the stem-loops share the core loop recognition motif $-XXYA-$ (X denoting any nucleotide and Y a pyrimidine) [478], while in the STNV case the minimal stem-loop motif consists of the sequence $-AXXA-$, where X is again any nucleotide [474]. The identification of these PSs was based on experimental protocols analyzed by bioinformatics and geometric approaches based on the Hamiltonian path (see below) distribution. Large-scale *ab initio* quantum chemical computations unraveling the critical details of the consensus CP-RNA molecular interactions have been set up only in the case of the MS2 bacteriophage [472]. The analysis of bonding and partial charge distribution on wild-type and mutated nucleoprotein complexes (PDB IDs: 1ZDH and 5MSF) indicate that the exact binding sites with the strongest hydrogen bonding interaction are located at LYS43-A4, ARG49-C13, TYR85-C5, and LYS61-C5. This fundamental level of understanding of the nature of the specific interactions implicated in the PS hypothesis at present thus exists only for a single bacteriophage.

The original motivation for the packaging signal hypothesis was the efficient capsid formation and thus it is likely that it could be widespread in nature, including also a number of viral families infecting humans. There are indications that even some DNA viruses, such as Hepatitis Bs, incorporate packaging signals in its pregenomic RNA [318]. It is likely that multiple dispersed RNA sequence/structure motifs varying around a central recognition motif with identifiable binding sites [472] that interact in a specific way with the capsid protein in the assembly process will be possibly identified also in other viral systems.

To study the effect of short packaging signal sites on the virus assembly, Permutter and Hagan performed a series of Brownian Dynamics (BD) simulations. Their goal was to explore whether packaging signal segments promote a more efficient assembly due to specific interactions with CPs [479]. They developed a coarse-grained particle-based computational model for CPs and RNA considering both nonspecific electrostatics and specific PS interactions.

To compare their results with the experiments, they calculated the hydrodynamic radii (RH) of the complexes of genome-CPs intermediates through a number of Brownian Dynamics simulations. More specifically, they used the HYDROPRO program that has been shown to produce reliable predictions for RH in similar systems [480]. They compared their findings with the RHs obtained using the single-molecule fluorescence correlation spectroscopy experiments

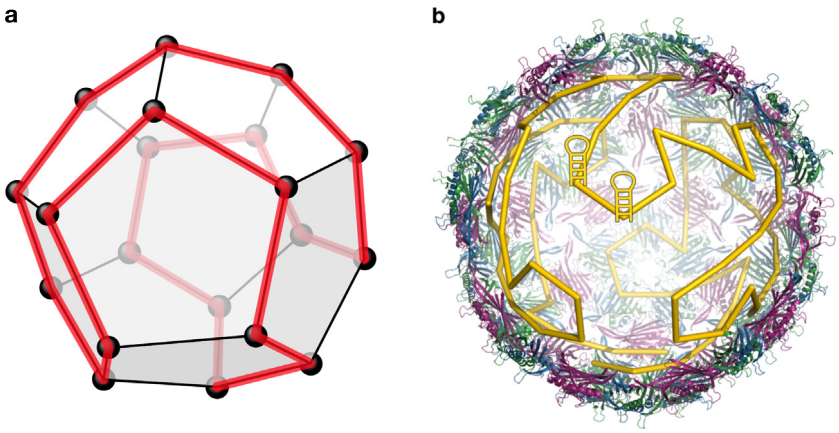

Fig. 68. Hamiltonian path representation of the MS2 genome organization.a: An example of a schematic Hamiltonian path of RNA connecting binding sites on the hypotope. The 3D configuration of RNA and the length of RNA between the PS is not represented. Adapted from Ref. [484]. b: A Hamiltonian path or a cycle where beginning and end coincide. Through every vertex of a dodecahedron, a dual of icosahedron, corresponding to an idealized RNA Hamiltonian path across the edges of capsid pentamers.

monitoring the assembly of proteins around both cognate and non-cognate RNAs [474,481]. The *in vitro* experiments show that under certain conditions the assembly of CPs around cognate RNAs is rapid but around noncognate RNAs is slower. The experiments also reveal that during the assembly of CPs around non-cognate RNA, RH first increases before decreasing to the native size of the capsid. In contrast, around non-cognate RNA, the RH of the protein-genome complex either stays constant or suddenly collapses and then gradually increases to the size of a native capsid.

Fig. 67 illustrates the simulation results for the salt concentration $C_{salt} = 100$ mM and different values of subunit–subunit interaction ϵ_{ss}. According to the simulations, weak subunit–subunit interactions with no PSs lead to disordered aggregates while RH monotonically increases with time, (Fig. 67A) [479]. However in the presence of PSs, the RH first increases due to the attachment of subunits and then decreases as the capsid forms. If the subunit–subunit interaction is strong ($\epsilon_{ss} = 3k_BT$, Fig. 67B), the assembly is successful with or without PSs. Nevertheless the RH increases more and for longer periods of time in the absence of PS, indicating that the PSs improve the assembly rate. For very strong subunit–subunit interactions ($\epsilon_{ss} = 4k_BT$), PSs have little impact and the rate of assembly is the same for cognate and non-cognate RNAs (Fig. 67C) .

In the above simulations the authors used relatively short (575) segments of RNA at $C_{salt} = 100$ mM because based on their previous work this was the optimal length for RNA to be encapsidated by CPs with the number of charges on ARM equal to +5 [436]. In their simulations then the RH of RNA before assembly was less than the size of the full formed capsid. However, the measured RH went up significantly following adsorption of subunits, and then it later went down when the entire capsid was formed. They repeated the above simulations for RNA with 910 segments with an RH similar to or larger than the capsid size. They increased the charges on ARMS from +5 to +10(Fig. 67DF). With longer RNA and more charges on ARMs, RH does not increase significantly upon subunit absorption, consistent with experiments [479].

Computer simulations in Ref. [479] elucidate how the virus assembly depends on (a) the number of PSs , (b) the PS binding affinity, and (c) the distribution of PS binding affinities along the genome. Based on the results of [479], the assembly efficiency is the highest in the presence of one high affinity PS in combination of multiple low affinity PSs, consistent with previous studies [475]. Further, their studies in Ref. [479] show that the assembly pathways in the presence of PSs involve more compact intermediates as compared to non-cognate RNAs.

5.8.5. The hamiltonian path model

The structural data on virus packing enabled by the EM reconstruction of bacteriophage MS2 at medium/high resolution have revealed not only the structures of the protein shell but also of the genomic RNA distribution [482,483]. Analysis of these data suggests that if the co-assembly of the capsid protein and the ss-RNA genome is sequential, the packaging signal:capsid protein (PS:CP) contacts should also be made in sequential order. This sequence would then yield a connected string that provides a detailed geometric representation of the assembly pathway [318]. While the configuration of this connecting RNA string is not unique, each of its possible realizations traces out a polyhedral shape with vertices at the hypotopal PS binding sites, and edges connecting contact lines between neighboring capsomers. A geometric perspective based on the configuration(s) of this connecting RNA string that is consistent with structural data is the *Hamiltonian path analysis* (HPA), as set forth by Twarock et al. [484], describing sequence-specific contacts between the MS2 genome and its protein shell in *geometric terms*.

A Hamiltonian path is a graph-theoretical concept that can be defined as a path between two vertices of a graph that visits each vertex exactly once. The Hamiltonian path on a polyhedron then analogously describes a specific path along its edges characterized by a *connected path*, visiting every polyhedral vertex once and only once.

In the context of virus protein:genome co-assembly the Hamiltonian path traces out the linear sequential order in which capsomers are assembled into the growing shell as well as the structural connectivity of this path along the hypotope, see Fig. 68. The Hamiltonian path, as shown in this figure, does not take into account the exact or even average location of the viral genome apart from the segments in proximity of the PS, while the rest of the RNA chain can make excursions into the capsid interior. It is not clear at this point how the close association between the RNA PS and the binding sites of the capsid, together with the entropy of the chain that is not interacting closely with the shell, determine the statistical weights of various possible Hamiltonian paths. The self-avoiding Hamiltonian path on the polyhedron is thus only 'topologically equivalent' to the *much more complicated* and tortuous 3D path of an actual RNA molecule confined to the capsid.

Another facet of the RNA packing problem is the self-association of RNA, concurrent to its co-assembly with the capsid proteins. Rudnick and Bruinsma [485] analyzed in detail the icosahedral packing of the RNA viral genome, and conjectured that the icosahedral organization of ss-RNA viral genome could be based on the exploitation of the partial double stranded secondary structure of the viral RNA. A Hamiltonian path along the capsid hypotope could then consist of a subset of edges of a polyhedron with double stranded RNA section and side-branches covering the remaining edges.

The Rudnick–Bruinsma conjecture also opens up a more general question as to the restrictions that the icosahedral symmetry imposes on the specific interactions between the genome and the coat proteins. A regular spatial organization of the genome should be reflected also in quasi-regular segmentation of viral genomic sequences. In fact, quasi-regular segmentation of genomic sequences related to the virion assembly and the genome packaging within icosahedral capsid was indeed found in the case of STMV and different strains of STNV as well as several other viruses, by combining discrete direct and double Fourier transforms of their nucleotide sequences [486].

Most of the experiments reviewed up to now were focused on the equilibrium properties of viruses. In the final section of this review, we present the most recent experiments dealing with the kinetics assembly of viruses with many questions remaining open.

6. Virus growth. Experimental approaches

The strikingly accurate architecture of icosahedral virus shells promoted detailed studies of their structure by ensemble averaging methods such as X-ray crystallography and cryo-electron microscopy with single particle reconstruction. The long held view from these experiments is that, unlike micelles, microcrystals, and finite two-dimensional arrays of molecules on surfaces, which all self-assemble, virus particles must be, at least in certain cases, remarkably identical at every scale. These self-control and self-termination of the virus assembly process make virus growth a unique paradigm in molecular assembly [487]. It is now also a coveted goal in synthetic, biomimetic nanomaterials [488].

It was not, however, until the advent of native mass spectrometry that the true measure of stoichiometric control and therefore variability in an ensemble of icosahedral viruses could be quantified. Recent native mass spectrometry studies [489–491] of icosahedral viruses with triangulation numbers between 3 and 7 have shown sharp mass peaks indicative of defect-free, remarkably monodisperse samples, Fig. 69. For instance, Snijder et al. have measured by electrospray ionization mass spectrometry the in vitro assembled $T = 7$ capsids of HK97, a bacteriophage, at $17\,942 \pm 4$ kDa, with the monomer subunit being 42.15 kDa [492]. Uetrecht *et al.* have studied the $T = 3$ and $T = 4$ capsids of hepatitis B virus (HBV) and found their respective masses at 3012 ± 3 kDa and 4014 ± 5 kDa [489]. (The HBV assembly subunit is a protein dimer of ~ 40 kDa). Keifer et al. examined the P22 phage by charge-detection mass spectrometry (CDMS) and found an extremely sharp mass distribution centered at 52 MDa [491]. This is the largest mass for a virus particle measured to date. Note that CDMS is a single particle measurement. In all these cases the spread of the mass distribution peak is significantly less than the mass of a subunit. Therefore, these viruses and virus shells are practically stoichiometrically accurate to within one subunit and the mass spectrometry results confirm the early view that, for a few viruses large and small that share the icosahedral construction principles, the pathways of virus self-assembly must be regulated by very effective quality-control mechanisms [487]. It has been well-established that no two snowflakes are alike [493], but when it comes to certain viruses, the opposite does seem true.

Icosahedral viruses make for nearly ideal examples of spherical crystallography [159], and, correspondingly, a detailed presentation is given in Section 4. However, studies of protein crystals growth suggest that there should be a price to pay for structural accuracy: Because proteins are orientationally asymmetrical, strong growth conditions that would otherwise speed up the formation of crystals from simpler molecules, are often detrimental for protein crystal growth [252,494]. This is because proteins need a comparably extended time with respect to simple molecules in order to orientationally explore a possible binding site. Moreover, it is a well-known fact to biomolecular crystallographers that proteins and nucleoprotein complexes tend to only crystallize within a small range of solution thermodynamic parameters (the "crystallization slot") [495]. Therefore, to assemble proteins in a lattice, slow kinetics and "just right" thermodynamic conditions are favored. Do viruses abide by the same thermodynamic rules or have they acquired ways to bypass such limitations?

6.1. Levinthal's paradox

Nearly 50 years ago C. Levinthal noted in a seminal paper that, while the time required for proteins to fold is typically less than a second, to fold a polypeptide chain into a native structure by a random search sequence would take an

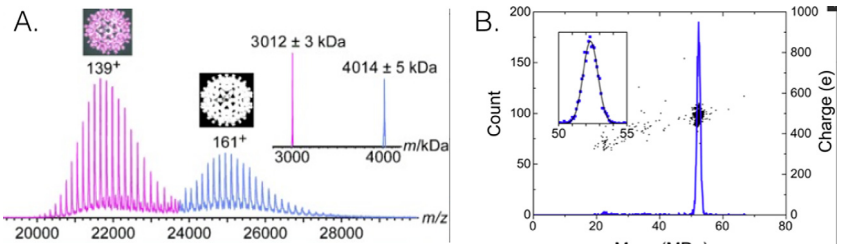

Fig. 69. The accurate stoichiometry of in vitro assembled icosahedral virus capsids and wild-type virus particles suggests exquisite control of the assembly process for certain viruses. In recent years, mass spectrometry methods have provided a detailed quantitative statistical analysis of mass distributions in populations of viruses and virus like particles. A. HBV mass spectrum with resolved charge states (from Ref. [489]). B. Charge-detection mass spectrum of the P22 phage head. Each dot represents a pair of charge and mass detected separately from an ion. The blue peak is the corresponding mass histogram (from Ref. [491]).

astronomical time [496]. The generally-accepted viewpoint that solves this puzzle postulates the existence of a single stepwise pathway, formed by the progressive organization of an ensemble of partially folded structures (sequence of intermediates). The folding complex slides spontaneously towards the native structure on a free energy surface that resembles a rough funnel [497].

Larson & McPherson suggested an assembly model for the single-stranded positive sense RNA STMV in which the RNA assumes a double role, first coding for the amino acid sequence of viral proteins, and second as a scaffold of binding sites placed in suitable locations that dictate the order and rate of virion growth [498]. Similarly, in a study of the MS2 phage assembly, Dykeman et al. suggested that the assembly of certain viruses is so fast, and the multiplicity of possible pathways is so great that the virus assembly process is reminiscent of Levinthal's paradox for protein folding [473]. Like for protein folding, a single stepwise pathway was proposed which relies on the existence of multiple RNA-packaging signals distributed along the genome [473,474], see also Section 5.8.4.

On the other hand, early studies of the physical principles aimed at explaining polyhedral virus structure proposed that virus assembly is a process akin to crystallization [24]. Indeed, kinetic models derived from the nucleation–elongation model worked out by Oosawa for the polymerization of actin filaments [499], have been successful in reproducing experimental trends observed by time-course static light scattering and size-exclusion chromatography for the in vitro assembly of empty capsids of viruses and bacteriophages [500–504]. The assembly of empty capsids is considered relevant to virus growth because: (1) empty capsid structures are often virtually structurally indistinguishable from the native virion shell and native protein–protein interactions can be studied this way decoupled from cargo–protein interactions, and (2) for some icosahedral DNA bacteriophages such as P22, the capsid is first assembled as an empty cage and then the DNA is encapsulated. Thus, in certain cases the empty capsid represents a true intermediate step in virus formation.

Note that for isometric capsids, capsid growth is geometrically frustrated: local symmetry cannot propagate uniformly throughout when growing on a surface topologically equivalent to a sphere, a point that we have described in great detail, see section on elasticity in curved space. This is why there must be defects in the ground state, (such as pentameric disclinations, scar dislocations, or vacancies) a situation that is not encountered in space-filling, three dimensional protein crystals. An interesting question which has elicited attention lately is how might these stresses associated with frustrated growth, influence the assembly pathway [146,160,252,505].

6.2. *Capsids* vs. *protein nanocrystals*

It is useful at this point to compare empty capsid growth with the growth rates expected from a regular protein crystal. The median assembly time of empty capsids, i.e. the time at which the reaction is 50% complete, depends strongly on subunit concentration, typically ranging from hundreds of seconds to tens of hours for protein concentrations from 0.1 mM to 0.01 mM, respectively, Fig. 70 [443].

The dominant crystal growth mechanism of protein crystals is via surface step addition, with the linear step velocity, v_{step}, being proportional with solution supersaturation [506]. v_{step} is constant when the protein concentration in solution and solution temperature are constant.

Considering the case of an isometric virus of radius R, a complete virus shell of area $A = 4\pi R^2$ would contain $N(R)$ proteins:

$$N(R) = \frac{4\pi R^2}{a}$$

where a stands for the area of an oligomer. If the linear step velocity, v_s is known, the mean time it takes to add an oligomer to the growing shell is:

$$t_a \approx \frac{\sqrt{a}}{v_s}$$

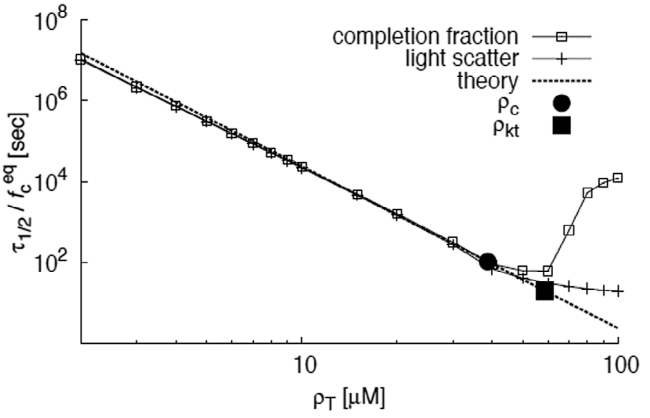

Fig. 70. Median assembly time $\tau_{1/2}$ normalized to the equilibrium fraction of subunits in complete capsids f_c^{eq} as a function of coat protein (CP) concentration. Theoretical estimates were obtained by solving a system of rate equations that describe the time evolution of concentrations of empty capsid intermediates.
Source: From Ref. [443].

The estimated total time t_{vs} to grow a virus shell by crystallization is then:

$$t_v = N(R) \cdot t_a = \frac{4\pi R^2}{a} \cdot \frac{\sqrt{a}}{v_s} = \frac{4\pi R^2}{\sqrt{a} v_s} \tag{184}$$

In terms of numbers, the radius of a typical $T = 3$ virus such as the CCMV is $R = 14$ nm. The virus shell contains $N = 90$ dimer subunits, each occupying a surface area of approximately 27 nm^2.

De Yoreo and Velikhov give v_s values for canavalin [506], a $\sim$ 100 kDa protein, of $\sim$ 100 nm/s at 10 mg/ml (100 μM). Virus coat oligomers are similarly sized ($\approx$ 50 kDa). The concentration in most capsid assembly experiments ranges between 10 to 100 μM. Therefore, the expected values for the linear step velocity fall in the range: $v_s = 10$–100 nm/s.

With these numbers, the time t_v for the completion of a virus shell at protein crystal growth rates ranges between a few seconds to a few minutes, depending on concentration. The time scale for protein crystal growth is faster by 1–3 orders of magnitude than that estimated based on experimental data for empty virus shells, Fig. 70, which exemplifies the median assembly time obtained from light scattering as a function of concentration. From the estimate provided by Eq. (184) and the data in Fig. 70, we infer that empty capsids may take longer to grow than similarly sized, regular protein crystals.

By contrast, the ensemble-averaged kinetics of virus growth in the presence of RNA is at least 3 orders of magnitude faster than that of empty capsid assembly. For instance, time resolved small-angle X-ray scattering experiments have shown that small ($T = 1, 3$) icosahedral capsids will assemble around RNA in tens of ms at μM concentrations [462,507]. Moreover, since the assembly process is composed of a nucleation and an elongation step, each having its own characteristic time, bulk measurement methods will average between these two times. In *in vitro* virus assembly, often elongation is much faster than nucleation [443,508]. Because of that, single particle elongation rates are likely to exceed the measured ensemble-averaged ones, which will appear slower due to mixing of the slower nucleation and the faster elongation steps in overall kinetics. The main difference here between ensemble and individual kinetics of assembly stems from the two step nucleation–elongation model, which involves a time-lag between the initial mixing and the growth take-off. The time-lag is a random variable related to the occurrence of nucleation, *i.e.* the instance when the growth takes off, and fluctuates among the particles of an ensemble [310,451,509]. Such fluctuations around the mean lead to an apparent (ensemble-averaged) rate that can be significantly longer than the actual single-particle growth rate, Fig. 71. This observation highlights the importance of single-particle time-resolved experiments.

To conclude this section, the assembly process of empty capsids seems indeed akin to protein crystallization not only structurally, but also in terms of kinetics, although subtle and interesting differences due to the necessary presence of defects are expected. It appears that the coat protein (CP) blueprint does not contain by itself the key to the Levinthal's paradox for viruses. This highlights the central role of the nucleic acid in the assembly process, since assembly in presence of genomic molecules occurs at rates that are generally far higher than those for protein crystallization and for empty capsid growth. Attempts at protein crystallization driven at similar rates would most likely fail by defect pile-up. By what means then, do RNA viruses preserve assembly accuracy at fast assembly speed?

It is worth noting here that H. Crane suggested as early as 1950 that both accuracy and speed would be greatly facilitated by the principle of subassembly, i.e. by simultaneously creating subassemblies, which then assemble in larger structures [510]. Indeed all viruses mentioned in this review have building blocks or subunits that have an oligomeric nature and form immediately at replication (e.g. the SV40 subunit is a pentamer, the ring-like TMV subunit is a 34-mer). The paradox of accuracy at fast assembly speed is a topic very actively pursued. We review in the following recent insights

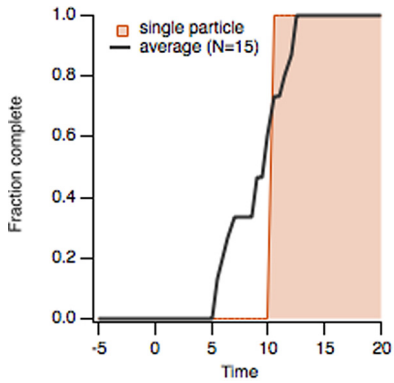

Fig. 71. Simulated normally distributed individual time lags around a mean ($\langle\tau\rangle = 10$, $\sigma_\tau = 2$) result in a comparatively broad, gradual takeoff of the ensemble-averaged assembly kinetics (black line). In this example, the time associated with an individual particle growth (orange) was ∼20 times shorter than the apparent time observed for the ensemble.

into the mechanisms and time scales of virus assembly in presence of RNA by ensemble and single particle time-resolved studies.

Viruses can replicate inside the host cell in a relatively broad range of conditions of temperature, stage of the cell life-cycle, stage of infection, cellular nutrient availability, etc. Since *in vitro* protein–protein and protein–RNA interactions resulting in oligomerization tend to be sensitive to changes in pH, salinity, temperature, and because assembly is extremely sensitive to concentration, a first question that arises is whether this versatility might be achieved by a multiplicity of pathways, each apt to lead to productive virus formation at a different set of conditions. Indeed, different mechanisms have been proposed and examined experimentally and theoretically. These mechanisms are not meant to be presented as mutually exclusive. Instead, as we shall see, one may become dominant depending on conditions.

6.3. Kinetic experiments and assembly mechanisms

6.3.1. Nucleation-elongation

The nucleation–elongation model [499] has been first discussed in relation with empty icosahedral capsid formation from CP subunits [501]. This mechanism is believed to also operate in presence of RNA, provided CP subunit–subunit attractive interactions are strong comparatively to RNA–protein interactions. One may ask how can RNA speed up the assembly by at least 3 orders of magnitude with respect to empty capsids, if the RNA-CP initial binding interactions are weaker than CP-CP interactions? Recently, Panahandeh et al. have shown that the Cp–genome interaction lowers the energy barrier of capsid formation, which can significantly speed up the assembly because of the associated Boltzmann factor [252].

Another explanation is that the RNA acts as an electrostatic antenna [511,512]. RNA is negatively charged, the lumenal side of CPs is usually strongly positively charged, and the Debye layer at common assembly conditions is ∼ 2 nm. CPs in solution stick and slide through one dimensional diffusion toward the nucleus site. Hu and Shklovskii have calculated that the effect of enhanced CP capture and guided diffusion, could speed up the assembly process by a factor of 10 [511]. In addition, an increase in virus stability, and thus assembly irreversibility, could be obtained by switching the conformation of subunits in solution to a new, assembly-competent state, after the initial CP-RNA weak-binding.

Induced fit subsequent to electrostatic binding was first observed in the assembly of tobacco mosaic virus (TMV) – a virus formed of a helical array of protein molecules, or subunits, in which a single molecule of RNA is embedded [513]. TMV is not icosahedral, but it is a ss-RNA virus, and it follows the nucleation–elongation pathway. TMV assembles its helix from pre-assembled oligomeric rings which are stable in solution. Initial interaction with RNA converts the closed ring into a lock-washer form [514]. Thus, the ring becomes a helical nucleus for CP helical array formation.

As an example of time-resolved study of icosahedral capsid assembly following the nucleation–elongation mechanism, Kler *et al.* studied the encapsidation of ss-RNA (500 nt) in a dodecameric cage formed of pentameric VP1 protein subunits of the simian virus SV40 [507].

SV40 has a circular double-stranded DNA genome (5243 bases), which it encapsulates in a capsid composed of 72 pentamers of the structural protein VP1. Thus, the native SV40 triangulation number is $T = 7$. Purified VP1 pentamers will assemble on circular dsDNA to form virus-like particles [515], and on short RNAs in which case it forms smaller, T=1 particles [507]. The assembly reaction progression was followed by a stopped flow approach with time-resolved small-angle X-ray scattering (TR-SAXS).

Rapid mixing of VP1 pentamers with RNA in assembly buffer led to the following main results: TR-SAXS scattering spectra at successive times suggest very low intermediate concentration along the reaction pathway. The existence of an

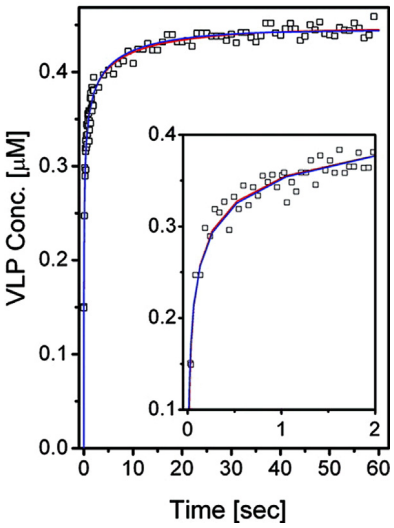

Fig. 72. Concentration of $T = 1$ VP1 virus-like particles as a function of time from TR-SAXS experiments. Inset: the first 2 s on an expanded scale. Line: predicted assembly kinetics from solving the master equation for the nucleation–elongation model. The reaction kinetics were modeled assuming the RNA initially nucleated either with a VP1 pentamer (blue curve), a dimer of pentamers (red curve), or a trimer of pentamers (black solid curve; not seen due to overlap with the red curve) [507].

isosbestic point pointed to a reaction dominated by two states (complete particles and free subunits). At 15 μM VP1, the reaction is already approximately half-way after 30 ms, Fig. 72.

The progression of the scattering spectra $I(q,t)$ where q is the scattering vector, and t is the time, could be fitted assuming a two-state reaction model having a single free parameter, $\alpha(t)$ corresponding to the time-dependent concentration of VLPs (Fig. 72):

$$I(q,t) = \alpha(t) I_{VLP}(q) + [\beta_0 - 12\alpha(t)] I_{penta}(q) + [\gamma_0 - \alpha(t)] I_{RNA}(q) \tag{185}$$

In Eq. (185), $I_{VLP}(q)$, $I_{penta}(q)$, and $I_{RNA}(q)$ are normalized basis spectra for capsid, pentamers, and RNA, respectively.

Fitting the data in Fig. 72 allowed estimates of the association energy between RNA and the VP1 pentamer (−6 kcal/mol) and of the elongation energy (−2.7 kcal/mol per contact). These numbers are somewhat surprising because both association energies appear to be very weak. Moreover, elongation is much faster than nucleation, but elongation energies appear to be smaller than RNA-VP1 energies. However, one should keep in mind that VP1 oligomers are pentavalent. Multivalency explains the larger thermodynamic force driving elongation. Furthermore, the relatively low association energy of VP1 to RNA was proposed to be due to an occlusion of the binding site by the C-termini, which occurs in free pentamers in solution. Upon RNA binding, the VP1 C termini are released, the pentamer slides along the RNA until it meets the nucleus for VLP growth, and the C-termini connect with neighboring pentamers stabilizing the complex. It is not known at this point whether there is any sequence specificity. It appears that a simple two-state nucleation–elongation model relying upon very weak interactions and cooperativity is sufficient to reproduce the very fast assembly of preassembled oligomers into cages encapsulating nucleic acid [507].

6.3.2. En masse

Many of the icosahedral virus capsids have coat proteins that follow the canonical motif [516] of a bulky beta-barrel structural domain responsible for the structural organization of the capsid, to which a flexible positively-charged arm is attached, Fig. 73. The flexible cationic arm points towards the interior and associates with the nucleic acid, which often adopts a condensed state smeared at the lumenal interface of the capsid. The brome mosaic virus (BMV) is a typical example [517].

BMV is a member of the alphavirus superfamily. Sharing multiple features with the widely-spread group of small ss-RNA icosahedral viruses [518], BMV has been very well studied, and is relatively well understood. It has a multipartite genome formed of 4 segments: RNA1, RNA2, RNA3 and RNA4, of 3.2 kb, 2.8 kb, 2.1 kb and 0.8 kb, respectively. The RNA1 and RNA2 molecules are individually packaged, while RNA3 and 4 are packaged together. The three types of particles have indistinguishable capsid structure, but distinct physical properties which depend on the type of RNA they contain [117]. Genome partition in multiple identical capsids suggests that the RNA-CP interactions are largely non-specific, with the capsid being able to adapt to different cargoes. Due to its potential for bionanotechnology applications [519], this feature elicited strong interest, and a variety of polyanions [434,438] including charged nanodroplets [520], DNA micelles [521], and nanoparticles [522] have been shown to be possible to encapsulate efficiently, by in-vitro self-assembly of virus-like particles at solution conditions similar to those required for reconstitution of infectious viruses from viral RNA and CP.

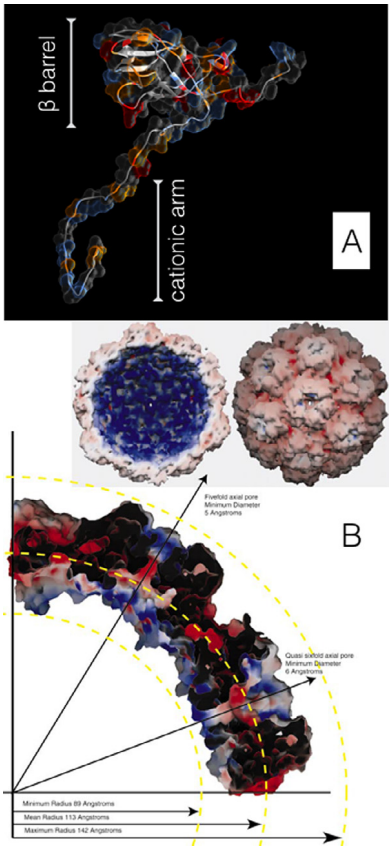

Fig. 73. A. BMV coat protein structure showing a basic flexible arm extended towards the interior of the capsid where it interacts with the nucleic acid, and the beta barrel domain at the capsid surface. B. Cross-section of the BMV capsid model. Positively charged residues are in blue, negatively charged in red. The RNA tends to spread at the lumenal interface of the capsid and condense radially in an amorphous nucleo-protein layer.
Source: Adapted from Ref. [517].

Not only RNA-CP interactions are such that one virus' genome could be packaged in other virus' coat, but also the CPs of different ss-RNA icosahedral viruses (for which BMV is the archetype) were shown to be sufficiently permissive or marginally specific to co-assemble efficiently [523,524].

Since the assembly interfaces in BMV-like viruses are principally hydrophobic in character [516], and because they appear to be marginally specific, while a strong electrostatic, nonspecific interaction between RNA and CP is also part of the process, McPherson suggested an alternative model [525] (frequently called the "en masse" model) to the sequential nucleation-growth model. According the "en masse" mechanism, the nucleic acid attracts CP subunits in solution to its surface through long-range electrostatic interactions with the amino terminal tails. The positively charged tails associate with the negatively charged RNA in fluid form, and the protein subunits are drawn and preoriented into a roughly spherical shell about the core. Hydrophobic interfaces start to associate, which leads to a molecular complex resembling a reverse micelle [525]. Thus, the nucleation–elongation and the "en masse" pathways correspond to situations in which intermediates are either predominantly ordered or disordered, respectively.

Computer simulations by Perlmutter et al. suggested that controlling the relative differences in the magnitudes of protein-protein and protein-genome binding affinities may be sufficient to predict which pathway occurs [526]. The "en masse" pathway was predicted to be the dominant one when the RNA-CP interactions are comparatively strong. Since the strength of CP-CP attractive interactions is controlled by the solution pH and the strength of attraction between CP and ss-RNA can be controlled by ionic strength, Garmann et al. have investigated switching between different pathways in the in vitro assembly of CCMV virus like particles by velocity sedimentation and electron microscopy [266]. Thus, in an assembly mixture at neutral pH, CP binds reversibly to the RNA in a nucleoprotein complex. Regardless whether exogenous or cognate, RNA exchange occurs between nucleoprotein complexes and solution [527]. At acidic pH, excess protein unbinds from RNA/CP complexes and virus-like particles form irreversibly.

Recently, Chevreuil et al. carried out TR-SAXS experiments by rapidly mixing purified CCMV CP subunits and viral RNA and measuring their aggregation state as a function of time. Consistent with previous experiments and simulations [266,526], their measurements provided direct evidence for a switch between the en masse and sequential pathways by

tuning the magnitude and range of constitutive interactions through changes in the pH and ionic strength. Specifically, at low final ionic strength and neutral pH the electrostatic RNA-CP interactions are strong comparatively with CP-CP interactions, and CP subunits (dimers) bound on the genome very rapidly ($\sim$ 28 ms). Their mean number per complex remained stable for longer than $\sim$ 10 min at about 77 subunits. A subsequent relaxation occurred over a time three orders of magnitude longer than the binding time [462]. Interestingly, the RNA-CP binding energy with native genome, was found to be moderate ($\sim 7k_BT$) despite its electrostatic nature.

We have seen that virus CP assembly on nucleic acid substrates can have high efficiencies, despite much accelerated growth rates with respect to simple protein crystallization, and empty capsid assembly. This is true even when exogenous RNA substrates are used, provided the right buffer conditions. We have also seen that one protein can adopt different pathways with the optimal pathway being a function of the relative interaction strengths operating among the constitutive elements of a virus. However, at this point, it is unclear what exactly drives the virus assembly inside a cell. It is possible that, for viruses like BMV it is driven by pH since there is a progressive acidification of the endomembrane system involved in the secretory pathways of plant cells [528]. Furthermore, RNA replication by positive-strand RNA viruses such as BMV or CCMV is closely associated with cellular membranes, and RNA packaging by CPs is replication-coupled [529,530]. Induction of membrane alterations similar to vesicle packets in BMV infected plant cells [530] is a wide-spread phenomenon encountered in many other positive strand RNA virus-infected cells, where m the replication complex is associated with membrane invaginations [531]. However, in the absence of other viral genes, BMV CP alone is sufficient to induce large numbers of vesicles similar to those in which RNA replication complexes form, observed in viral infections [530]. This suggests that organelle membranes might play a role in bromovirus assembly inside cells, but what that role might be is still unclear.

Another difficulty and possible difference between in vitro and in vivo experiments is raised by the actual concentration of viral components, which is poorly characterized inside cells, at the moment. Sub-nanomolar concentrations are expected when averaging over the entire cell volume and over the infection cycle, although the intracellular CP and viral RNA local concentrations in the highly compartmentalized environment of the cell are unknown. It is likely that these concentrations are much lower than the 1–10 μM required by the ensemble averaging measurement methods traditionally used in time-resolved and equilibrium in vitro assembly studies. At low concentrations, subtle differences in interaction selectivity may become important. This may explain how viruses are able to preferentially package cognate RNA instead of exogenous, cellular RNAs and other polyanions. Single particle approaches have the ability to probe assembly in real time, at low concentrations [481]. Such experiments have brought to light yet another paradigm in virus assembly, one that will take advantage of the presence of specific RNA-CP binding motifs to render assembly efficient at concentrations orders of magnitude below the pseudo-critical CP concentration for capsid assembly.

6.4. In singulo *kinetics*

In singulo assembly kinetic approaches offer two main advantages: (i) access to processes occurring at low CP concentrations, and, (ii) direct access to pathway intermediates and assembly time-scales (provided sufficient temporal resolution is available).

In singulo real-time experimental approaches to virus assembly include: fluorescence correlation spectroscopy (FCS) [481], atomic force microscopy (AFM) [532], resistive-pulse sensing with nanofluidic channel integrated pores [533], stop-flow charge detection mass spectrometry [534], single-particle fluorescence microscopy [535], and interferometric scattering microscopy [536].

6.4.1. *A new assembly paradigm*

In singulo approaches backed by computations have led to a shift in emphasis in the search for potential principles directing virus assembly [537]. The shift puts front and center genomic RNA elements with specific, high-affinity binding to the cognate CP, called packaging signals (PS). The first observation of PS involvement in assembly was made on the turnip crinkle virus [538]. However, a large body of research on the MS2 bacteriophage, especially the multi-pronged approaches employed by Stockley and colleagues including biochemical [539], biophysical [481], mathematical modeling [475,540], and molecular simulation [473,541] have made MS2 the archetypal system for the development of assembly models that include sequence selectivity in RNA encapsidation.

MS2 contains one positive-sense single-stranded RNA, 3569 nucleotides encapsulated in a $T = 3$ capsid of $\sim$27 nm in diameter [542]. The packaged MS2 RNA is organized mostly in double-stranded form, folded in hair-pin loops. The latter are classic signature motifs for potential PSs [543].

Single molecule FCS is an optical method that measures the hydrodynamic diameter of single particles from fluctuations in fluorescence intensity as they cross the focus of a probe laser beam [544]. Borodavka et al. have applied FCS to the measurement of MS2 assembly kinetics in the limit of low CP concentration. In their approach viral coat proteins, assembly intermediates, genomic RNAs, and capsids diffuse progressively more slowly producing considerably longer correlations in the fluorescent signal. This provides a way to determine the hydrodynamic radius for selectively labeled moieties in the presence of unlabeled species. The hydrodynamic radius is computed from the autocorrelation function obtained from intensity fluctuations.

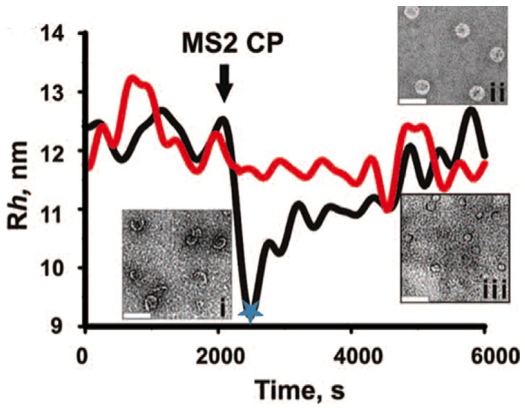

Fig. 74. The change in hydrodynamic radius of fluorescently-labeled MS2 RNA (black) as MS2 CP is added to solution (at a time represented by the black arrow). A ∼25% drop in the hydrodynamic radius is apparent, soon after MS2 CP addition to the RNA solution for MS2 RNA, but not for noncognate RNA from satellite tobacco necrosis virus (STNV). Electron micrographs of negatively stained assembly reactions at several points in the pathway are shown.
Source: From Ref. [481].

Fig. 74 shows the time-resolved changes in the apparent hydrodynamic radius of MS2 genomic RNA with genomic RNA from another virus (non-cognate to MS2 CP) as a control. Sufficient protein was added to the RNA solution to allow each RNA to form a complete capsid.

Subsequent to hydrodynamic radius collapse, the MS2 nucleoprotein complex grows over the span of approximately one hour, presumably by addition of CP to the size of a virus particle, the end result of the process. Transmission electron microscopy corroborates this interpretation (Fig. 74 inset). The noncognate, STNV RNA exhibits much slower dynamics when MS2 CP is added.

As expected, the comparatively very low concentration conditions significantly slowed down kinetics with respect to TR-SAXS studies of BMV and SV40 (Sections 6.3.1 and 6.3.2). Thus, the initial collapse appears to occur over a period less than a few minutes, while the subsequent CP addition step takes much longer. It is interesting that the nucleation step is faster than the subsequent growth step, when high affinity PS sequences are present. For this to make biological sense, the CP and viral RNA concentrations should be regulated in a way that avoids depletion of free CP by forming too many nuclei at a time.

The data in Fig. 74 makes a compelling case for the role of PS in the coassembly at low concentrations of cognate MS2 protein and RNA. However, we note that the temporal range for FCS over which fluctuations originate from single molecule emission is of the order of 10^{-3} s, the usual diffusion time. Therefore, the results in Fig. 74 which reconstruct behavior along the reaction time, do so from averaging contributions of many molecules that go in and out the focus volume. To have access to truly individual behavior, a different method is needed. Fluorescence from single molecules is a low-background technique, but has the drawback of photobleaching, which limits the total number of photons per molecule and thus the dynamic range of the measurement. Moreover, labeling RNA and/or protein could adversely affect their interaction. It is therefore of interest to develop label-free methods that are able to follow encapsidation of a single genome, preferably with ms time resolution. Such an approach is interferometric scattering microscopy [545,546].

6.4.2. Interferometric scattering microscopy

Interferometric scattering microscopy exploits the enhancement in optical contrast due to constructive interference between the background reflection from an interface between two transparent media of different indices of refraction and the scattered field from a scatterer situated in the immediate vicinity of the interface, Fig. 75 [536,545]. As in a heterodyne detection scheme, the signal is amplified by a reference beam, which in this case is coming from reflection by the substrate interface. The magnitude of the interference cross-term between reference (reflected) and signal (scattered) light is proportional to the volume of the scatterer, instead of the volume squared as when measuring the scattered light intensity by methods such as dark-field microscopy. As a consequence, interferometric scattering microscopy is advantageous when detecting small particles. In addition to single particle detectivity down to a few nm, the method possesses impressive sub-ms time resolution, and wide-field imaging capabilities, i.e. several particles can be analyzed simultaneously.

Garmann et al. have employed interferometric scattering microscopy to measure the assembly kinetics of single MS2 virus particles on MS2 RNA strands tethered to the surface of a coverslip [547]. Comparisons of individual assembly trajectories acquired simultaneously indicated that most trajectories exhibit a sigmoidal time-dependence with plateau scattering intensity values similar to those acquired from complete particles. Each trajectory is characterized by a lag time after which the trajectory takes off, Fig. 76. Lag times fluctuate widely. The lag time distribution roughly spanned an

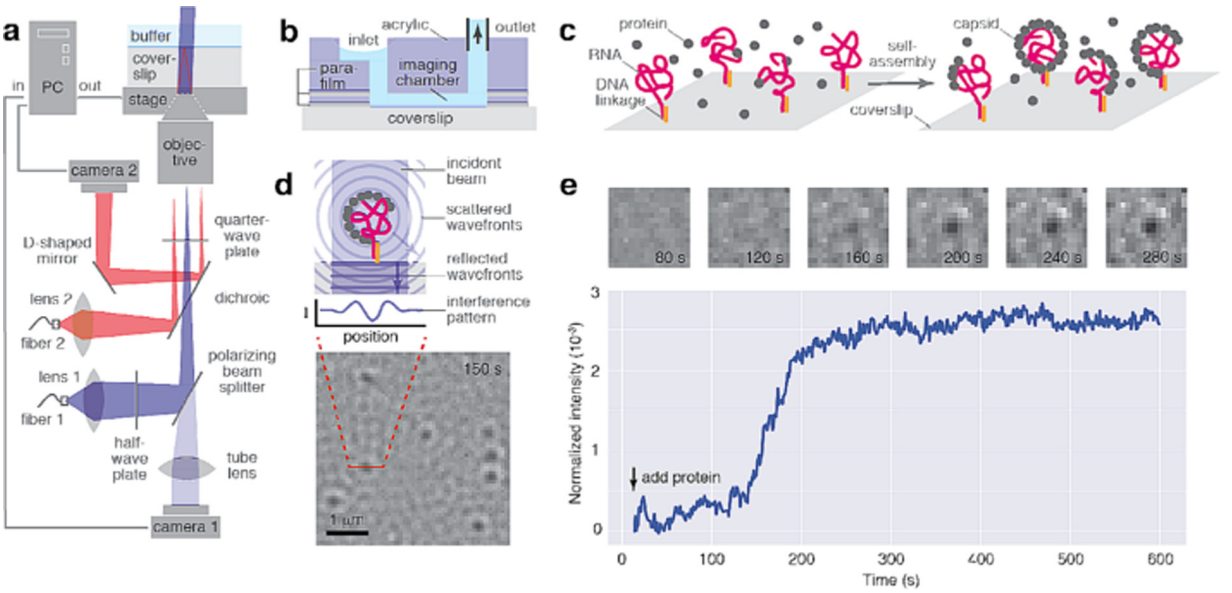

Fig. 75. (a) Diagram of the interferometric scattering microscope employed by Garmann et al. to measure MS2 assembly kinetics. (b) Schematic of the flow cell used to introduce the MS2 coat protein dimers. (c) Association of proteins with viral RNA molecules that are tethered to a coverslip by DNA linkages leads to increased scattering by the complex, which interferes with the phase-shifted reflected wavefront resulting in optical intensity contrast. (d) As the assemblies grow, they scatter more light; several assemblies (dark spots) are investigated at once. (e) Time-series corresponding to a single assembly, and a plot of the normalized intensity collected from the assembling particle, as a function of time. At μM CP concentrations, most of an individual assembly appears to take less than a minute.
Source: From Ref. [536].

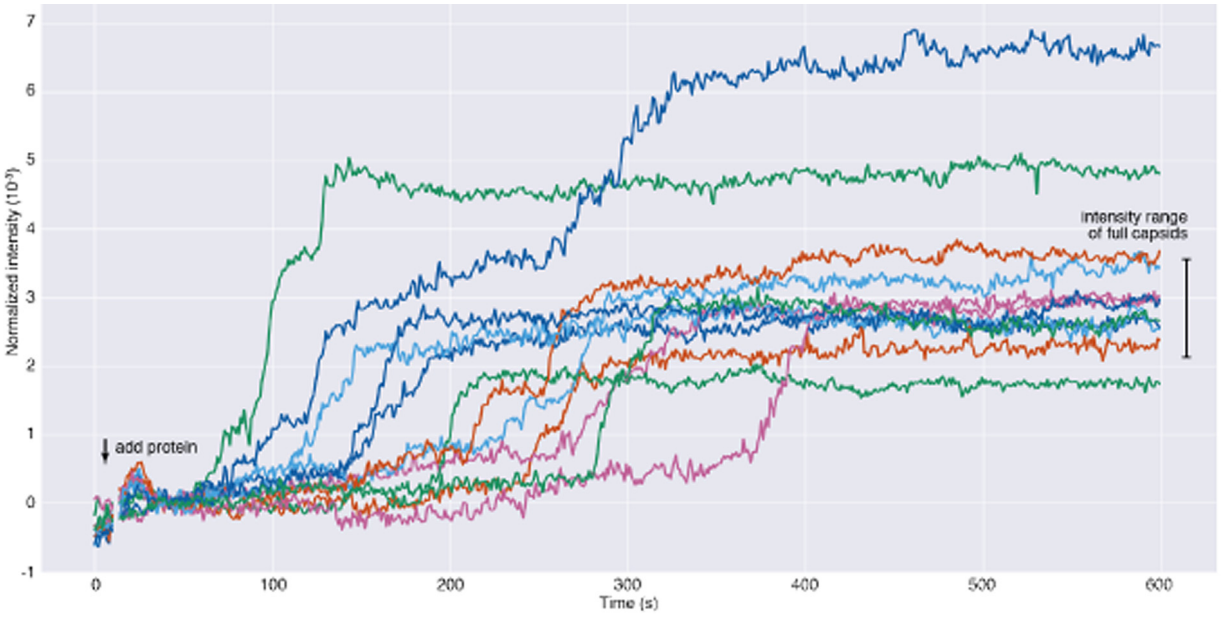

Fig. 76. Scattered intensity of 12 randomly chosen spots as a function of time. The vertical bar shows the expected intensity of a full capsid. The extracted intensities are measured at 1000 Hz and shown with a 1000-frame average.
Source: From Ref. [536].

interval between 0 and 350 s. This lag time is not to be confused with the delay time due to diffusion of the coat protein inside the microchannel. The latter was estimated to be $\sim$ 40 s, after mixing.

Since, at μM concentrations the collision rate is of the order of 10^3 s^{-1}, and the root-mean-square displacement of a single protein is of the order of 10 μm in 1 s, fluctuations of waiting times are unlikely to originate in concentration

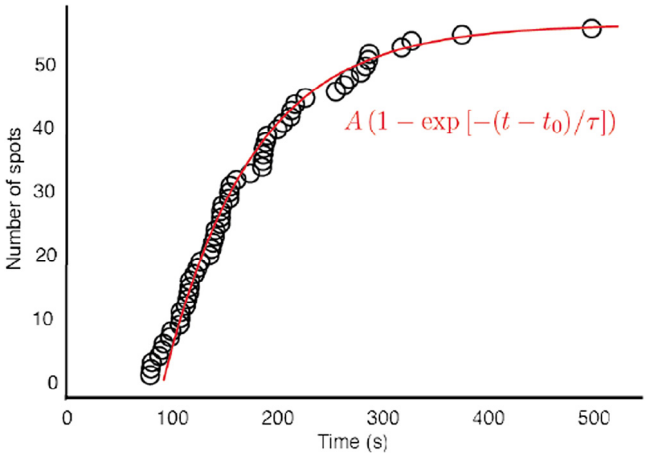

Fig. 77. Cumulative distribution of wait times.
Source: From Ref. [536].

fluctuations, and assembly reactions are not diffusion limited. The likely explanation for the observed waiting time is the existence of a free-energy barrier associated with nucleation [548]. This aspect and the subsequent rapid growth once assembly is initiated, are reminiscent of the nucleation/elongation process.

The cumulative distribution of wait times that precede the rapid increase in scattering was determined by counting the number of spots in the full field of view as a function of time, Fig. 77. This distribution is representative for the ensemble average of the scattering intensity, if one neglects contributions from smaller intermediates. Comparing Fig. 77 with any of the traces in Fig. 76, we see how the averaging effect described in Fig. 71 can obscure actual assembly kinetic features which are important for establishing the mechanism of assembly (Fig. 76). Thus, the fast rise after the waiting time suggests a cooperative elongation step, while the ensemble-averaged behavior could be fitted by a Langmuir uncorrelated association model similar to Langmuir adsorption.

It is interesting to compare the FCS experimental results for MS2 from Ref. [481] (Fig. 74) with the interferometric scattering results (Fig. 76). Before the comparison, it should be noted that there are four potentially important differences between the two works:

- There is a $\sim$ 1000-fold difference in CP concentration (with the FCS experiments at the lowest concentration).
- While using the same viral RNA, thermal denaturation and annealing was part of the interferometric scattering sample preparation protocol, i.e. misfolded regions could have been present [536].
- The time resolution of the FCS experiment is limited by the time required to construct the correlation function (60 s) [481]. However, judged from the bandwidth-limit of random fluctuations in Fig. 74, it appears the actual time resolution was closer to $\sim$ 300 s. In any case, FCS was 2–3 orders of magnitude slower than interferometric scattering microscopy.
- FCS measures the hydrodynamic radius, while the interferometric scattering contrast is proportional with mass.

The FCS experiments indicated a two step process with an initial collapse or folding of the RNA, followed by a slow buildup to the hydrodynamic radius associated with a complete particle. An RNA condensation step would be difficult to observe by interferometric scattering, since scattering would not be sensitive to hydrodynamic radius changes at that scale. On the other hand, the direct observation of a lag time would be difficult to achieve by FCS with its averaging among RNAs at different stages of encapsulation and its limited time resolution. Does the initial RNA collapse in Fig. 74 represent the formation of the nucleus for elongation? Is reaching the plateau in Fig. 76 simultaneous with reaching the final structure or is there still a slower process of annealing going on as the results in Fig. 74 seem to suggest? Are we seeing two distinct mechanisms, which switch as the concentrations change? These are still open questions which are borne from the advent of improved, *in singulo* methods of experimentation. They also highlight the challenges and the importance of a multi-pronged approach when attempting to decipher the pathways of virus assembly.

6.5. Outlook

While significant advances have been made in modeling and understanding physical mechanisms responsible for viral structure and self-assembly, there are many details that remain poorly understood, as to how they relate to the fundamental microscopic physical interactions driving and defining their mesoscopic growth and form.

Many experiments reviewed in the previous sections show that viruses can assemble within a relatively broad parameter space. At low CP concentrations, efficient assembly critically relies on poorly understood details of specific

interactions between RNA and CP, with RNA getting packaged upon association with CP in a stepwise process reminiscent of protein folding. However, depending on the stage of infection, high concentrations of virus CP may accumulate in cells: for instance, the pentons of Adenovirus serotype 5 are at such high concentrations that they form intranuclear crystalline inclusions [549], and the phiX174 icosahedral bacteriophage forms crystalline condensates in most cells, a few hours post infection [550]. At those high concentrations, productive assembly pathways are likely driven by cooperative, multiple, weak interactions – a process akin to crystallization, which, because of the identity of participating subunits, does not require solving a Levinthal paradox. In sum, there might be multiple pathways possible for one virus, leading to the same end result: a highly symmetric protein container, with a near-equilibrium structure, encapsulating the genome. How can virus assembly be at the same time precise and rapid is still unclear, but the studies we reviewed here seem to indicate that the free-energy landscape leading to the end result is relatively smooth. Is this smoothness a built-in coat protein feature? These and related questions remain very much open.

The high yield of non-defective capsids that assemble *in vivo* and *in vitro* is remarkable, considering that hundreds or in many cases thousands of protein subunits must arrange to form a shell with icosahedral order. How the interaction of genome with capsid proteins determines the assembly mechanisms and products is a basic question of physical virology. How it is possible to have multiple nucleation points on the genome and still obtain an error-free shell is another mystery. In this review, we attempted to provide what is known in the field but many questions remain unanswered.

While the *in vitro* experiments have significantly contributed to our understanding of virus assembly, the mechanism of formation of capsids *in vivo* could be quite different. For example, all the en masse assembly experiments start at pH 7–7.5 where amorphous genome-CP complexes form. The self-assembly experiments reviewed in the previous section show that upon decreasing pH to 5, the amorphous structures undergo a disorder–order transition and symmetric closed shells with $T = 3$ structures form. How viruses assemble at pH 7 inside the cells remains a mystery. Only very recent *in vitro* experiments [252] reveal that at high protein concentration, the closed capsids can assemble at pH 7 or 7.5 but the symmetry of the shells is still under question.

To add to the emerging kaleidoscopic picture of the virus assembly mechanisms, a few observations concerning the generality of our discussion (or rather the lack thereof) are worth making. Thus, in contrast with BMV, in some nonenveloped icosahedral viruses, the RNA is partially ordered, with a structure reflecting capsid symmetry (e.g. bean pod mottle virus, satellite tobacco mosaic virus, pariacoto virus, and the flock house virus) [308] and pathways of assembly seem to be different from the ones discussed here. Such a distinct mechanism involving partial ordering of RNA is believed to occur in the case of tymoviruses. In this case, unlike other ss-RNA icosahedral viruses, natural preparations of tymoviruses contain a significant fraction of empty capsids. It has been shown that nearly complete capsids will form entirely through protein-protein interactions [551]. Therefore, the tymovirus assembly seems to be driven by CP-CP rather than RNA-CP interactions. This proposed assembly mechanism has the capsids assemble first, with the RNA being drawn into the capsid through multivalent interactions with the capsid intermediate, at a late stage during growth [517]. This scenario is similar to the one proposed for genome packaging in polyovirus (PV), according to which empty procapsids may dock to the replication complex via protein/protein interaction, the emerging genomic RNA being stuffed in them with the help of a viral ATPase [552].

Intrinsic defects arising from geometric frustration and interacting via a field of mechanical stresses that propagate over large distances, hold an important role in the establishment of the relationship between structure and stability. Elasticity theory provided productive pathways in predicting global properties born out of such interactions. However, in *in vitro* studies of virus mechanics under external stress, elastic behavior was found to become quickly intertwined with plasticity, an aspect that has been much less studied. Finally, concepts which better include the large fluctuations likely to occur in mechanical variables over the interactions times relevant to biology will need to be developed.

A better understanding of the physical mechanisms and the role of physical interactions behind virus growth, form, mechanical and thermodynamic properties, will require a combination of theoretical methods, and new experimental approaches. In particular, the combined dynamic range covered by the experimental observations discussed here, taken together, spans 5 orders of magnitude. It is therefore necessary to pursue approaches with sufficient temporal resolution and dynamic range, with low detection limits. Moreover, there is an especially strong need for real-time methods capable of following assembly processes both *in vitro*, and inside cells, which would allow benchmarking more sophisticated theoretical models.

Acknowledgments

A.T would like to acknowledge discussions with M. Bowick, A. Cacciuto, G. Grason, Siyu Li, D. Mehta, D. Nelson, D. Vella, D. Wales. The work of AT is supported by National Science Foundation, DMR-CMMT 1606336.

R.P. would like to acknowledge discussions with V. Lorman, S. Rochal, A. Leforestier, D. Marenduzzo, C. Micheletti, A. Lošdorfer Božič, A. Šiber, I. Szleifer, J.D. Farrell and the support of the 1000-Talents Program of the Chinese Foreign Experts Bureau.

B.D. would like to acknowledge the support from the U.S. Army Research Office, award number W911NF-17-1-0329; from the U.S. Department of Energy, Office of Science, the Basic Energy Sciences Division, under award number DESC0010507; and from the National Science Foundation, the CBET program, under award number EAGER-1740432.

R.Z. would like to acknowledge discussions with Paul van der Schoot, Jef Wagner, Gonca Erdemci, Siyu Li, Sanaz Pananhandeh, Yinan Dong and Alireza Ramezani. The work of RZ was supported by the National Science Foundation through Grant No. DMR-1719550.

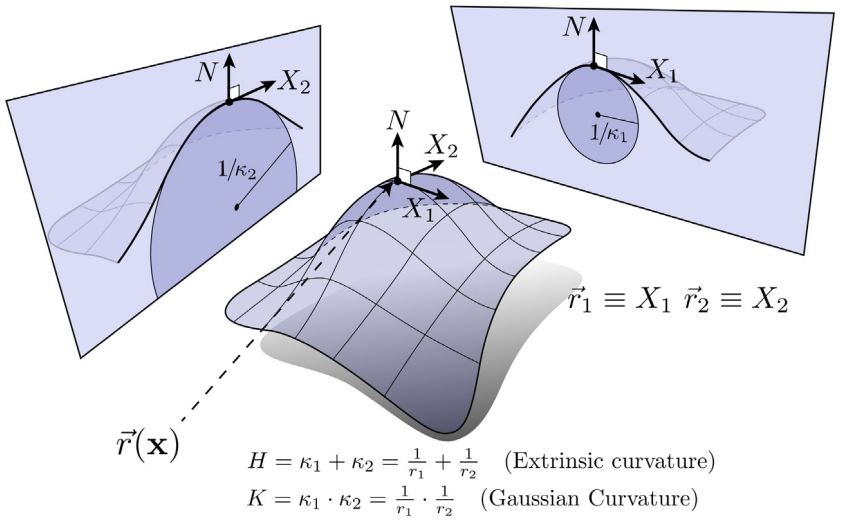

Fig. 78. Illustration of the different concepts of differential geometry used in the text. The figure is a modification from http://www.cs.cmu.edu/kmcrane/Projects/DDG/ and has been used under a Creative Commons Attribution-NonCommercial-NoDerivs 3.0 Unported License.

Appendix. Mathematical background

A.1. Survey of differential geometry

In this section we provide a minimal background necessary to make the review self-contained. For derivations and further materials we refer to Refs. [157,553]. If $\vec{r}(\mathbf{x})$ (see Eq. (12) and Fig. 78) defines a surface in D-dimensional space, then

$$\vec{r}_\alpha \equiv \frac{\partial}{\partial x_\alpha}\vec{r}\ , \tag{186}$$

where $\alpha = 1, 2$, define two vectors that are linearly independent and define the tangent plane to the surface, as shown in Fig. 78. In 3D there is one vector perpendicular to the tangent plane, and is given by

$$\vec{N} = \vec{r}_1 \times \vec{r}_2/|\vec{r}_1 \times \vec{r}_2|\ . \tag{187}$$

the three vectors $\left\{\vec{r}_\alpha, \vec{N}\right\}$ define a base for the 3D vector space at each point where the surface is defined, see Fig. 78.

The metric tensor is given by

$$g_{\alpha\beta} = \vec{r}_\alpha \cdot \vec{r}_\beta = \partial_\alpha \vec{r} \cdot \partial_\beta \vec{r}\ , \tag{188}$$

and $g^{\alpha\beta}$ is defined according to $g_{\alpha\beta}g^{\beta\gamma} = \delta^\gamma_\alpha$, where δ is the Kronecker delta. The metric determinant g

$$g = \det(g_{\alpha\beta}) \tag{189}$$

and Christoffel Symbols(CS)

$$\Gamma^\delta_{\alpha\beta} = \frac{1}{2}g^{\delta\gamma}\left(\partial_\alpha g_{\beta\gamma} + \partial_\beta g_{\alpha\gamma} - \partial_\gamma g_{\alpha\beta}\right)\ , \tag{190}$$

are also defined. The importance of the CS is that they enable to define a derivative ∇_α for any vector field defined on the surface, according to

$$\nabla_\alpha V^\beta = \partial_\alpha V^\beta + \Gamma^\beta_{\alpha\delta}V^\delta\ . \tag{191}$$

It is possible, see Ref. [553], to show that

$$\frac{\partial^2\vec{r}}{\partial x_\alpha \partial x_\beta} = \partial_\alpha \vec{r}_\beta = \Gamma^\delta_{\alpha\beta}\vec{r}_\delta + K_{\alpha\beta}\vec{N}\ , \tag{192}$$

which defines the tensor $K_{\alpha\beta}$, also known as the second fundamental form (the metric $g_{\alpha\beta}$ is the first fundamental form). The advantage of these more advanced methods is that they enable a more explicit calculation of the Extrinsic H and

Gaussian curvature K than following the process outlined in Fig. 78 that requires calculating the two surface curvatures r_1, r_2 explicitly. The extrinsic curvature is the appropriate trace of the second fundamental form

$$H = g^{\alpha\beta} K_{\alpha\beta}. \tag{193}$$

A very important result, known as "Gauss theorema egregium" states that

$$K_{\alpha\beta}K^{\alpha\beta} - (g^{\alpha\beta}K_{\alpha\beta})^2 = g^{\alpha\gamma}g^{\beta\delta}K_{\alpha\beta}K_{\gamma\delta} - (g^{\alpha\beta}K_{\alpha\beta})^2 = -2K \ . \tag{194}$$

An alternative form of the "Gauss theorema egregium" is obtained by using Eq. (193), leading to

$$K_{\alpha\beta}K^{\alpha\beta} = -2K + H^2 \ . \tag{195}$$

The derivatives of the normal satisfy

$$\partial_\alpha \vec{N} = K_{\alpha\beta} g^{\beta\gamma} \vec{r}_\gamma \ , \tag{196}$$

which allows to derive the identity

$$g^{\alpha\beta}\partial_\alpha \vec{N} \cdot \partial_\beta \vec{N} = K_{\alpha\beta}K^{\alpha\beta} = H^2 - 2K, \tag{197}$$

which will be used to provide a discretization for Eq. (36). We refer to the recent paper [166] for further relevant results that relate the metric and the covariant derivatives.

A.2. Survey of topology

A property of a surface is called topological if it remains true upon continuous changes of the its shape. A typical example is the Euler theorem, which states that for any triangulation of a sphere (or any of its deformations, such a polyhedra, ellipse, etc.)

$$\chi_E \equiv N_v - N_e + N_F = 2 \ , \tag{198}$$

where χ_E defines the Euler characteristic and N_v, N_E and N_F are the number of vertices, edges and faces respectively. This relation is clearly satisfied by the three polyhedra considered in Fig. 23, as it is clear from Table 1. This relation appears in many conspicuous ways. One way is the Gauss–Bonet theorem [553], which states that for any closed surface

$$\int d^2\mathbf{x}\sqrt{g}K(\mathbf{x}) = 2\pi\,\chi_E \ . \tag{199}$$

Thus, for any surface that can be continuously deformed to a sphere, the integral is equal to $2\pi \times 2 = 4\pi$. It can be easily verified from Table 1 that this relation is, indeed, satisfied. The Gauss–Bonet theorem applies also to the disclination density, so that

$$\iint d^2\mathbf{x}\sqrt{g}s(\mathbf{x}) = 2\pi\,\chi_E \ , \tag{200}$$

where again, for those surfaces that are topological equivalent to a sphere the integral is equal to 4π. In terms of the disclination charges, see Eq. (39), the above relation is

$$\begin{aligned} 2\pi\,\chi_E \ &= \ \frac{\pi}{3}\sum_{i=1}^{N_G} q_i \\ 12 \ &= \ \sum_{i=1}^{N_G} q_i \quad \text{(Spherical topology)} \ , \end{aligned} \tag{201}$$

which maybe satisfied by twelve $q = +1$, six $q = 2$ or 4 $q = 3$, see Fig. 23. Also, it may be satisfied by $(12 + n)$ $q = +1$ and (n) $q = -1$ disclinations, where $n \geq 0$ is an arbitrary integer.

If the surfaces are not closed, but have a boundary, the formulation of the Gauss–Bonet theorem becomes more involved. We refer to the specialized references for a discussion [157].

References

[1] D'Arcy Wentworth Thompson, On Growth and Form, Courier Dover Publications, 1942.
[2] David Paez-Espino, Emiley A. Eloe-Fadrosh, Georgios A. Pavlopoulos, Alex D. Thomas, Marcel Huntemann, Natalia Mikhailova, Edward Rubin, Natalia N. Ivanova, Nikos C. Kyrpides, Uncovering Earth's virome, Nature 536 (7617) (2016) 425–430.
[3] Welkin Johnson, Elio Schaechter, Virus in the Room, Microbe 8 (3) (2013) 150.
[4] S.J. Flint, L.W. Enquist, V.R. Racaniello, A.M. Skalka, Principles of Virology, Vol. 1, John Wiley & Sons, 2009.
[5] S.J. Flint, L.W. Enquist, V.R. Racaniello, A.M. Skalka, Principles of Virology, Vol. 1-2, ASM Press, 2004.
[6] Elena Serrano, Guillermo Rus, Javier García-Martínez, Nanotechnology for sustainable energy, Renew. Sustain. Energy Rev. 13 (9) (2009) 2373–2384.

[7] Yun Jung Lee, Hyunjung Yi, Woo-Jae Kim, Kisuk Kang, Dong Soo Yun, Michael S. Strano, Gerbrand Ceder, Angela M. Belcher, Fabricating genetically engineered high-power lithium-ion batteries using multiple virus genes, Science 324 (5930) (2009) 1051–1055.
[8] Dahyun Oh, Jifa Qi, Binghong Han, Geran Zhang, Thomas J. Carney, Jacqueline Ohmura, Yong Zhang, Yang Shao-Horn, Angela M. Belcher, M13 virus-directed synthesis of nanostructured metal oxides for lithium-oxygen batteries, Nano Lett. 14 (8) (2014) 4837–4845.
[9] George M. Church, Yuan Gao, Sriram Kosuri, Next-generation digital information storage in DNA, Science 337 (6102) (2012) 1628.
[10] Tom Geller, The forever disc, Commun. ACM 57 (5) (2014) 24–26.
[11] Ibrahim Yildiz, Sourabh Shukla, Nicole F. Steinmetz, Applications of viral nanoparticles in medicine, Curr. Opin. Biotechnol. 22 (6) (2011) 901–908.
[12] Benjamin Schwarz, Trevor Douglas, Development of virus-like particles for diagnostic and prophylactic biomedical applications, Wiley Interdiscip. Rev. Nanomed. Nanobiotechnol. 7 (5) (2015) 722–735.
[13] Justin Judd, Michelle L. Ho, Abhinav Tiwari, Eric J. Gomez, Christopher Dempsey, Kim Van Vliet, Oleg A. Igoshin, Jonathan J. Silberg, Mavis Agbandje-McKenna, Junghae Suh, Tunable protease-activatable virus nanonodes, ACS Nano 8 (5) (2014) 4740–4746.
[14] Xinlei Huang, Barry D. Stein, Hu Cheng, Andrey Malyutin, Irina B. Tsvetkova, David V. Baxter, Nicholas B. Remmes, Jeanmarie Verchot, Cheng Kao, Lyudmila M. Bronstein, Bogdan Dragnea, Magnetic virus-like nanoparticles in N. benthamiana plants: A new paradigm for environmental and agronomic biotechnological research, ACS Nano 5 (5) (2011) 4037–4045.
[15] Robert J. Usselman, Shefah Qazi, Priyanka Aggarwal, Sandra S. Eaton, Gareth R. Eaton, Stephen Russek, Trevor Douglas, Gadolinium-loaded viral capsids as magnetic resonance imaging contrast agents, Appl. Magn. Reson. 46 (3) (2015) 349–355.
[16] Bongsu Jung, Ayala L.N. Rao, Bahman Anvari, Optical nano-constructs composed of genome-depleted brome mosaic virus doped with a near infrared chromophore for potential biomedical applications, ACS Nano 5 (2) (2011) 1243–1252.
[17] Ying-Zhong Ma, Rebekah A. Miller, Graham R. Fleming, Matthew B. Francis, Energy transfer dynamics in light-harvesting assemblies templated by the tobacco mosaic virus coat protein, J. Phys. Chem. B 112 (22) (2008) 6887–6892.
[18] Amy M. Wen, Rudolf Podgornik, Giuseppe Strangi, Nicole F. Steinmetz, Photonics and plasmonics go viral: self-assembly of hierarchical metamaterials, Rend. Lincei - Sci. Fis. Nat. 26 (2015) 129–141.
[19] Sebyung Kang, Masaki Uchida, Alison O'Neil, Rui Li, Peter E. Prevelige, Trevor Douglas, Implementation of p22 viral capsids as nanoplatforms, Biomacromolecules 11 (10) (2010) 2804–2809.
[20] John P. Casey, Roberto J. Barbero, Nimrod Heldman, Angela M. Belcher, Versatile de novo enzyme activity in capsid proteins from an engineered M13 bacteriophage library, J. Am. Chem. Soc. 136 (47) (2014) 16508–16514.
[21] Roger H. French, V. Adrian Parsegian, Rudolf Podgornik, Rick F. Rajter, Anand Jagota, Jian Luo, Dilip Asthagiri, Manoj K. Chaudhury, Yet-ming Chiang, Steve Granick, et al., Long range interactions in nanoscale science, Rev. Modern Phys. 82 (2) (2010) 1887–1944.
[22] R. Phillips, S.R. Quake, The biological frontier of physics, Phys. Today 59 (5) (2006) 38–43.
[23] Francis H.C. Crick, James D. Watson, Structure of small viruses, Nature 177 (4506) (1956) 473–475.
[24] D.L.D. Caspar, Aaron Klug, Physical principles in construction of regular viruses, Cold Spring Harb. Symp. Quant. Biol. 27 (1962) 1.
[25] Reza Khayat, Nicholas Brunn, Jeffrey A. Speir, John M. Hardham, Robert G. Ankenbauer, Anette Schneemann, John E. Johnson, The 2.3-angstrom structure of porcine circovirus 2, J. Virol. 85 (15) (2011) 7856–7862.
[26] Xiaodong Yan, Paul R. Chipman, Tonje Castberg, Gunnar Bratbak, Timothy S. Baker, The marine algal virus Ppv01 has an icosahedral capsid with T=219 quasisymmetry, J. Virol. 79 (14) (2005) 9236–9243.
[27] D.L. Caspar, A. Klug, Physical principles in the construction of regular viruses, Cold Spring Harb. Symp. Quant. Biol. 27 (1962) 1–24.
[28] In analogy to the famous *Aufbau Prinzip* for the construction of multielectron atoms that states a set of rules for the buildup of complex atoms.
[29] Luigi E. Perotti, Ankush Aggarwal, Joseph Rudnick, Robijn Bruinsma, William S. Klug, Elasticity theory of the maturation of viral capsids, J. Mech. Phys. Solids 77 (2015) 86–108.
[30] Padmaja Natarajan, Gabriel C. Lander, Craig M. Shepherd, Vijay S. Reddy, Charles L. Brooks III, John E. Johnson, Exploring icosahedral virus structures with viper, Nat. Rev. Microbiol. 3 (2005) 809–817.
[31] T.T. Nguyen, Robijn F. Bruinsma, William M. Gelbart, Elasticity theory and shape transitions of viral shells, Phys. Rev. E 72 (2005) 051923.
[32] V.L. Lorman, S.B. Rochal, Density-wave theory of the capsid structure of small icosahedral viruses, Phys. Rev. Lett. 98 (18) (2007) 185502–1–185502–4.
[33] V.L. Lorman, S.B. Rochal, Landau theory of crystallization and the capsid structures of small icosahedral viruses, Phys. Rev. B 77 (2008) 224109–224112.
[34] S.B. Rochal, O.V. Konevtsova, A.E. Myasnikova, V.L. Lorman, Hidden symmetry of small spherical viruses and organization principles in ?anomalous? and double-shelled capsid nanoassemblies, Nanoscale 8 (2016) 16976–16988.
[35] G.J. Morgan, Historical review: Viruses, crystals and geodesic domes, Trends Biochem. Sci. 28 (2003) 86.
[36] Reidun Twarock, Antoni Luque, Structural puzzles in virology solved with an overarching icosahedral design principle, Nat. Comm. (2019).
[37] L.D. Landau, E.M. Lifshitz, Statistical Physics, Vol. 5, Butterworth-Heinemann, 1980.
[38] William R. Wikoff, James F. Conway, Jinghua Tang, Kelly K. Lee, Lu Gan, Naiqian Cheng, Robert L. Duda, Roger W. Hendrix, Alasdair C. Steven, John E. Johnson, Time-resolved molecular dynamics of bacteriophage HK97 capsid maturation interpreted by electron cryo-microscopy and X-ray crystallography, J. Struct. Biol. 153 (2006) 300–306.
[39] $P_l^m(x) = (-1)^m(1-x^2)^{m/2}\frac{d^m}{dx^m}P_l(x)$, where $P_l(x)$ is the Legendre polynomial of degree m.
[40] Roya Zandi, David Reguera, Robijn F. Bruinsma, William M. Gelbart, Joseph Rudnick, Origin of icosahedral symmetry in viruses, Proc. Natl. Acad. Sci. USA 101 (2004) 15556–15560.
[41] Ting Chen, Zhenli Zhang, Sharon C. Glotzer, A precise packing sequence for self-assembled convex structures, Proc. Natl. Acad. Sci. 104 (2007) 717.
[42] N. Cohan, The spherical harmonics with the symmetry of the icosahedral group, Proc. Camb. Phil. Soc. 54 (1958) 28–38.
[43] Ruben D. Cadena-Nava, Mauricio Comas-Garcia, Rees F. Garmann, A.L.N. Rao, Charles M. Knobler, William M. Gelbart, Self-assembly of viral capsid protein and rna molecules of different sizes: Requirement for a specific high protein/rna mass ratio, J. Virol. 86 (2012) 3318.
[44] Guillaume Tresset, Jingzhi Chen, Maelenn Chevreuil, Nama Nhiri, Eric Jacquet, Yves Lansac, Two-dimensional phase transition of viral capsid gives insights into subunit interactions, Phys. Rev. Appl. 7 (2017) 014005.
[45] Oren M. Elrad, Michael F. Hagan, Encapsulation of a polymer by an icosahedral virus, Phys. Biol. 7 (2010) 1–17.
[46] B. Schmidt, P. Zdanska, Solution of the time-dependent schrodinger equation for highly symmetric potentials, Comput. Phys. Comm. 127 (2000) 290–308.
[47] Sanjay Dharmavaram, Fangming Xie, William Klug, Joseph Rudnick, Robijn Bruinsma, Orientational phase transitions and the assembly of viral capsids, Phys. Rev. E 95 (2017) 062402.
[48] Sanjay Dharmavaram, Fangming Xie, William Klug, Joseph Rudnick, Robijn Bruinsma, Landau theory and the emergence of chirality in viral capsids, Europhys. Lett. 116 (2016) 26002.
[49] G. Fredrickson, The Equilibrium Theory of Inhomogeneous Polymers, Oxford University Press, 2006.

[50] D.E. Smith, S.J. Tans, S.B. Smith, S. Grimes, D.L. Anderson, C. Bustamante, The bacteriophage straight phi29 portal motor can package dna against a large internal force, Nature 413 (6857) (2001) 748–752.
[51] A. Evilevitch, L. Lavelle, C.M. Knobler, E. Raspaud, W.M. Gelbart, Osmotic pressure inhibition of dna ejection from phage, Proc. Natl. Acad. Sci. 100 (16) (2003) 9292–9295.
[52] W.M. Gelbart, C.M. Knobler, Virology: Pressurized viruses, Science 323 (5922) (2009) 1682–1683.
[53] Charles M. Knobler, William M. Gelbart, Physical chemistry of dna viruses, Annu. Rev. Phys. Chem. 60 (2009) 367–383.
[54] Roya Zandi, Joseph Rudnick, Ramin Golestanian, Probing polyelectrolyte elasticity using radial distribution function, Phys. Rev. E 67 (2003) 021803.
[55] Roya Zandi, Joseph Rudnick, Ramin Golestanian, Anomalous bending of a polyelectrolyte, Phys. Rev. E 67 (2003) 061805.
[56] Roya Zandi, Ramin Golestanian, Joseph Rudnick, Electromechanical stiffening of rods and tubes, Appl. Phys. Lett. 84 (26) (2004) 5467–5469.
[57] R. Zandi, J. Rudnick, R. Golestanian, Radial distribution function of rod-like polyelectrolytes, Eur. Phys. J. E 9 (1) (2002) 41–46.
[58] A.D. Hershey, M. Chase, Independent functions of viral protein and nucleic acid in growth of bacteriophage, J. Gen. Physiol. 36 (1) (1952) 39–56.
[59] M. Marsh, A. Helenius, Virus entry: Open sesame, Cell 124 (4) (2006) 729–740.
[60] R. Tuma, P.E. Prevelige, G.J. Thomas, Mechanism of capsid maturation in a double-stranded DNA virus, Proc. Natl. Acad. Sci. USA 95 (17) (1998) 9885–9890.
[61] Anastasia A. Aksyuk, Michael G. Rossmann, Bacteriophage assembly, Viruses 3 (3) (2011) 172–203.
[62] David Veesler, John E. Johnson, Virus maturation, Annu. Rev. Biophys. 41 (2012) 473–496.
[63] Marian Baclayon, Glen K. Shoemaker, Charlotte Uetrecht, Sue E. Crawford, Mary K. Estes, B.V. Venkataram Prasad, Albert J.R. Heck, Gijs J.L. Wuite, Wouter H. Roos, Prestress strengthens the shell of norwalk virus nanoparticles, Nano Lett. 11 (11) (2011) 4865–4869.
[64] W.S. Klug, W.H. Roos, G.J.L. Wuite, Unlocking internal prestress from protein nanoshells, Phys. Rev. Lett. 109 (16) (2012) 168104.
[65] G. Polles, G. Indelicato, R. Potestio, P. Cermelli, R. Twarock, C. Micheletti, Mechanical and assembly units of viral capsids identified via quasi-rigid domain decomposition, PLoS Comput. Biol. 9 (11) (2013) e1003331.
[66] L. Ponzoni, G. Polles, V. Carnevale, C Micheletti, Spectrus: a dimensionality reduction approach for identifying dynamical domains in protein complexes from limited structural datasets, Structure 23 (2015) 1516–1525.
[67] Wesley I. Sundquist, Hans-Georg Kräusslich, Hiv-1 assembly, budding, and maturation, Cold Spring Harb. Perspect. Med. 2 (7) (2012) a006924.
[68] Nitzan Kol, Yu Shi, Marianna Tsvitov, David Barlam, Roni Z. Shneck, Michael S. Kay, Itay Rousso, A stiffness switch in human immunodeficiency virus, Biophys. J. 92 (5) (2007) 1777–1783.
[69] Hong-Bo Pang, Liron Hevroni, Nitzan Kol, Debra M. Eckert, Marianna Tsvitov, Michael S. Kay, Itay Rousso, Virion stiffness regulates immature hiv-1 entry, Retrovirology 10 (2013) 4.
[70] Mariska G.M. van Rosmalen, Glen R. Nemerow, Gijs J.L. Wuite, Wouter H. Roos, A single point mutation in precursor protein vi doubles the mechanical strength of human adenovirus, J. Biol. Phys. 44 (2) (2018) 119–132.
[71] Xing Zhang, Lei Jin, Qin Fang, Wong H. Hui, Z. Hong Zhou, 3.3 å cryo-em structure of a nonenveloped virus reveals a priming mechanism for cell entry, Cell 141 (3) (2010) 472–482.
[72] Eric Barrow, Anthony V. Nicola, Jin Liu, M.O. Robbins, H. Gao, R. Radhakrishnan, R. Radhakrishnan, T. Gregory, D.J. Capon, G.H. Cohen, Multiscale perspectives of virus entry via endocytosis, Virol. J. 10 (1) (2013) 177.
[73] David Boal, Mechanics of the Cell, Cambridge University Press, Cambridge UK;; New York, 2002.
[74] Tomas Kirchhausen, Clathrin, Annu. Rev. Biochem. 69 (2000) 699–727.
[75] G. Bao, X.R.R. Bao, Shedding light on the dynamics of endocytosis and viral budding, Proc. Natl. Acad. Sci. USA 102 (29) (2005) 9997–9998.
[76] H. Ewers, A. Helenius, Lipid-mediated endocytosis, Cold Spring Harb. Perspect. Biol. 3 (8) (2011) a004721.
[77] H.J. Gao, W.D. Shi, L.B. Freund, Mechanics of receptor-mediated endocytosis, Proc. Natl. Acad. Sci. USA 102 (27) (2005) 9469–9474.
[78] Roya Zandi, David Reguera, Joseph Rudnick, William M. Gelbart, What drives the translocation of stiff chains?, Proc. the Natl. Acad. Sci. USA 100 (2003) 8649.
[79] Ilona Rissanen, Robert Stass, Antra Zeltina, Sai Li, Jussi Hepojoki, Karl Harlos, Robert J.C. Gilbert, Juha T. Huiskonen, Thomas A. Bowden, Structural transitions of the conserved and metastable hantaviral glycoprotein envelope, J. Virol. 91 (21) (2017).
[80] Sheng Cao, Wei Zhang, Characterization of an early-stage fusion intermediate of Sindbis virus using cryoelectron microscopy, Proc. Natl. Acad. Sci. USA 110 (33) (2013) 13362–13367.
[81] Long Li, Joyce Jose, Ye Xiang, Richard J. Kuhn, Michael G. Rossmann, Structural changes of envelope proteins during alphavirus fusion, Nature 468 (7324) (2010) 705–708.
[82] E.W. Kitajima, J.A. Lauritis, Plant virions in plasmodesmata, Virology 37 (4) (1969) 681–685.
[83] Thomas C. Mettenleiter, Breaching the barrier—the nuclear envelope in virus infection, J. Mol. Biol. 428 (10) (2016) 1949–1961.
[84] Xin Yi, Huajian Gao, Kinetics of receptor-mediated endocytosis of elastic nanoparticles, Nanoscale 9 (1) (2017) 454–463.
[85] J.P. Michel, I.L. Ivanovska, M.M. Gibbons, W.S. Klug, C.M. Knobler, G.J.L. Wuite, C.F. Schmidt, Nanoindentation studies of full and empty viral capsids and the effects of capsid protein mutations on elasticity and strength, Proc. Natl. Acad. Sci. USA 103 (16) (2006) 6184–6189.
[86] Sarah Katen, Adam Zlotnick, The thermodynamics of virus capsid assembly, Methods Enzymol. 455 (2009) 395–417.
[87] L.D. Landau, E.M. Lifshitz, Theory of Elasticity, Vol. 7, Butterworth-Heinemann, 1986.
[88] David de Sancho, Anshul Sirur, Robert B. Best, Molecular origins of internal friction effects on protein folding rates, Nature Commun. 5 (2014) 4307.
[89] Julian F.V. Vincent, Structural Biomaterials, nceton University Press, 2012.
[90] Mercedes Hernando-Pérez, Cheng Zeng, M. Carmen Miguel, Bogdan Dragnea, Intermittency of deformation and the elastic limit of an icosahedral virus under compression, ACS Nano 13 (7) (2019) 7842–7849.
[91] W.H. Roos, R. Bruinsma, G.J.L. Wuite, Physical virology, Nat. Phys. 6 (10) (2010) 733–743.
[92] Wouter H. Roos, How to perform a nanoindentation experiment on a virus, Methods Mol. Biol. 783 (2011) 251–264.
[93] Pedro J. de Pablo, Mauricio G. Mateu, Mechanical properties of viruses, Subcell. Biochem. 68 (2013) 519–551.
[94] Pedro J. de Pablo, Atomic force microscopy of virus shells, Semin. Cell Dev. Biol. 73 (2018) 199–208.
[95] Florence Tama, Charles L. Brooks, Diversity and identity of mechanical properties of icosahedral viral capsids studied with elastic network normal mode analysis, J. Mol. Biol. 345 (2) (2005) 299–314.
[96] Gerard Adriaan Vliegenthart, Gerhard Gompper, Mechanical deformation of spherical viruses with icosahedral symmetry, Biophys. J. 91 (3) (2006) 834–841.
[97] Tatiana Kuriabova, Alex J. Levine, Nanorheology of viscoelastic shells: Applications to viral capsids, Phys. Rev. E 77 (3) (2008) 031921.
[98] Anton Arkhipov, Wouter H. Roos, Gijs J.L. Wuite, Klaus Schulten, Elucidating the mechanism behind irreversible deformation of viral capsids, Biophys. J. 97 (7) (2009) 2061–2069.
[99] Eric R. May, Charles L. Brooks, Determination of viral capsid elastic properties from equilibrium thermal fluctuations, Phys. Rev. Lett. 106 (18) (2011) 188101.

[100] Ankush Aggarwal, Eric R. May, Charles L. Brooks, William S. Klug, Nonuniform elastic properties of macromolecules and effect of prestrain on their continuum nature, Phys. Rev. E 93 (1) (2016) 012417.
[101] Maria Aznar, Antoni Luque, David Reguera, Viral nanomechanics with a virtual atomic force microscope, J. Phys. Condens. Matter 30 (2018) 264001.
[102] Elvira Tarasova, Dmitry Nerukh, All-atom molecular dynamics simulations of whole viruses, J. Phys. Chem. Lett. 9 (19) (2018) 5805–5809.
[103] Arturo M. Baró, Ronald G. Reifenberger, Atomic Force Microscopy in Liquid : Biological Applications, Wiley-VCH, 2012.
[104] Y.G. Kuznetsov, A. McPherson, Atomic force microscopy in imaging of viruses and virus-infected cells, Microbiol. Mol. Biol. Rev. 75 (2) (2011) 268–285.
[105] Pedro J. de Pablo, Mariano Carrión-Vázquez, Imaging biological samples with atomic force microscopy, Cold Spring Harb. Protoc. 2014 (2) (2014) 167–177.
[106] Sanjay Kumar, Valerie M. Weaver, Mechanics, malignancy, and metastasis: The force journey of a tumor cell, Cancer Metastasis Rev. 28 (1–2) (2009) 113–127.
[107] A. Ortega-Esteban, A.J. Perez-Berna, R. Menendez-Conejero, S.J. Flint, C. San Martin, P.J. de Pablo, Monitoring dynamics of human adenovirus disassembly induced by mechanical fatigue, Sci. Rep. 3 (2013).
[108] Yuri G. Kuznetsov, Chuan Xiao, Siyang Sun, Didier Raoult, Michael Rossmann, Alexander McPherson, Atomic force microscopy investigation of the giant mimivirus, Virology 404 (1) (2010) 127–137.
[109] Pedro J. de Pablo, Mercedes Hernando-Pérez, Carolina Carrasco, José L. Carrascosa, Direct visualization of single virus restoration after damage in real time, J. Biol. Phys. 44 (2) (2018) 225–235.
[110] I.L. Ivanovska, P.J. de Pablo, B. Ibarra, G. Sgalari, F.C. MacKintosh, J.L. Carrascosa, C.F. Schmidt, G.J.L. Wuite, Bacteriophage capsids: tough nanoshells with complex elastic properties, Proc. Natl. Acad. Sci. USA 101 (20) (2004) 7600–7605.
[111] V. Krishnamani, C. Globisch, C. Peter, M. Deserno, Breaking a virus: Identifying molecular level failure modes of a viral capsid by multiscale modeling, Eur. Phys. J. Spec. Top. (2016) 1–18.
[112] Melissa M. Gibbons, William S. Klug, Influence of nonuniform geometry on nanoindentation of viral capsids, Biophys. J. 95 (8) (2008) 3640–3649.
[113] V. Tvergaard, A. Needleman, Indentation of pressurized viscoplastic polymer spherical shells, J. Mech. Phys. Solids 93 (2016) 16–33.
[114] J.P. Michel, I.L. Ivanovska, M.M. Gibbons, W.S. Klug, C.M. Knobler, G.J.L. Wuite, C.F. Schmidt, Nanoindentation studies of full and empty viral capsids and the effects of capsid protein mutations on elasticity and strength, Proc. Natl. Acad. Sci. USA 103 (16) (2006) 6184–6189.
[115] Milagros Castellanos, Rebeca Pérez, Carolina Carrasco, Mercedes Hernando-Pérez, Julio Gómez-Herrero, Pedro J. de Pablo, Mauricio G. Mateu, Mechanical elasticity as a physical signature of conformational dynamics in a virus particle, Proc. Natl. Acad. Sci. USA 109 (30) (2012) 12028–12033.
[116] J. Snijder, C. Uetrecht, R.J. Rose, R. Sanchez-Eugenia, G.A. Marti, J. Agirre, D.M.A. Guérin, G.J.L. Wuite, A.J.R. Heck, W.H. Roos, Probing the biophysical interplay between a viral genome and its capsid, Nature Chem. 5 (6) (2013) 502–509.
[117] Robert Vaughan, Brady Tragesser, Peng Ni, Xiang Ma, Bogdan Dragnea, C. Cheng Kao, The tripartite virions of the brome mosaic virus have distinct physical properties that affect the timing of the infection process, J. Virol. 88 (11) (2014) 6483–6491.
[118] Bodo D. Wilts, Iwan A.T. Schaap, Christoph F. Schmidt, Swelling and softening of the cowpea chlorotic mottle virus in response to ph shifts, Biophys. J. 108 (10) (2015) 2541–2549.
[119] J. Snijder, V.S. Reddy, E.R. May, W.H. Roos, G.R. Nemerow, G.J.L. Wuite, Integrin and defensin modulate the mechanical properties of adenovirus, J. Virol. 87 (5) (2013) 2756–2766.
[120] Wouter H. Roos, Ilya Gertsman, Eric R. May, Charles L. Brooks, John E. Johnson, Gijs J.L. Wuite, Mechanics of bacteriophage maturation, Proc. Natl. Acad. Sci. USA 109 (7) (2012) 2342–2347.
[121] George J. Papakonstantopoulos, Robert A. Riggleman, Jean-Louis Barrat, Juan J. de Pablo, Molecular plasticity of polymeric glasses in the elastic regime, Phys. Rev. E 77 (4) (2008) 041502.
[122] M. Hernando-Pérez, S. Lambert, E. Nakatani-Webster, C.E. Catalano, P.J. de Pablo, Cementing proteins provide extra mechanical stabilization to viral cages, Nature Commun. 5 (2014).
[123] Alejandro Valbuena, Mauricio G. Mateu, Kinetics of surface-driven self-assembly and fatigue-induced disassembly of a virus-based nanocoating, Biophys. J. 112 (4) (2017) 663–673.
[124] J. Snijder, I.L. Ivanovska, M. Baclayon, W.H. Roos, G.J.L. Wuite, Probing the impact of loading rate on the mechanical properties of viral nanoparticles, Micron 43 (12) (2012) 1343–1350.
[125] Dennis M. Dimiduk, Chris Woodward, Richard Lesar, Michael D. Uchic, Scale-free intermittent flow in crystal plasticity, Science 312 (5777) (2006) 1188–1190.
[126] Carlotta Negri, Alessandro L. Sellerio, Stefano Zapperi, M. Carmen Miguel, Deformation and failure of curved colloidal crystal shells, Proc. Natl. Acad. Sci. USA 112 (47) (2015) 14545.
[127] Mikko J. Alava, Lasse Laurson, Stefano Zapperi, Crackling noise in plasticity, Eur. Phys. J. Spec. Top. 223 (48) (2014) 2353–2367.
[128] B. Stephanidis, S. Adichtchev, P. Gouet, A. McPherson, A. Mermet, Elastic properties of viruses, Biophys. J. 93 (4) (2007) 1354–1359.
[129] Chi-Kuang Sun, Yi-Chun Tsai, Yi-Jan E. Chen, Tzu-Ming Liu, Hui-Yuan Chen, Han-Ching Wang, Chu-Fang Lo, Resonant dipolar coupling of microwaves with confined acoustic vibrations in a rod-shaped virus, Sci. Rep. 7 (1) (2017) 4611.
[130] Cheng Zeng, Mercedes Hernando-Pérez, Bogdan Dragnea, Xiang Ma, Paul van der Schoot, Roya Zandi, Contact mechanics of a small icosahedral virus, Phys. Rev. Lett. 119 (3) (2017) 038102.
[131] Mathias Buenemann, Peter Lenz, Mechanical limits of viral capsids, Proc. Natl. Acad. Sci. USA 104 (24) (2007) 9925–9930.
[132] Roya Zandi, David Reguera, Mechanical properties of viral capsids, Phys. Rev. E 72 (2) (2005) 021917.
[133] Daniel Moreno-Cerrada, Chloe Rodríguez, Francisco Moreno-Madrid, Ekaterina Selivanovitch, Trevor Douglas, Pedro J. de Pablo, Miguel Manso Silván, Loading the dice: The orientation of virus-like particles adsorbed on titanate assisted organosilanized surfaces, Biointerphases 14 (1) (2019) 011001.
[134] U. Seifert, R. Lipowsky, Adhesion of vesicles, Phys. Rev. A 42 (8) (1990) 4768–4771.
[135] W. Helfrich, Elastic properties of lipid bilayers: theory and possible experiments, Z. Naturforsch. C. 28 (11) (1973) 693–703.
[136] David Veesler, Thiam-Seng Ng, Anoop K. Sendamarai, Brian J. Eilers, C. Martin Lawrence, Shee-Mei Lok, Mark J. Young, John E. Johnson, Chi-yu Fu, Atomic structure of the 75 mda extremophile sulfolobus turreted icosahedral virus determined by cryoem and x-ray crystallography, Proc. Natl. Acad. Sci. USA 110 (14) (2013) 5504.
[137] D.S. Goodsell, Adenovirus, 2010.
[138] Shane D. Trask, Sarah M. McDonald, John T. Patton, Structural insights into the coupling of virion assembly and rotavirus replication, Nat. Rev. Microbiol. 10 (3) (2012) 165–177.
[139] Eugene Wu, Glen R. Nemerow, Virus yoga: the role of flexibility in virus host cell recognition, Trends Microbiol. 12 (4) (2004) 162–169.
[140] Carolyn M. Teschke, Amy McGough, Pamela A. Thuman-Commike, Penton release from p22 heat-expanded capsids suggests importance of stabilizing penton-hexon interactions during capsid maturation, Biophys. J. 84 (4) (2003) 2585–2592.
[141] Jörg Votteler, Wesley I. Sundquist, Virus budding and the escrt pathway, Cell Host Microbe 14 (3) (2013) 232–241.

[142] Elizabeth R. Wright, Jordan B. Schooler, H. Jane Ding, Electron cryotomography of immature hiv-1 virions reveals the structure of the ca and sp1 gag shells, EMBO J. 26 (8) (2007) 2218–2226.
[143] The molecular architecture of hiv, J. Mol. Biol. 410 (4) (2011) 491–500.
[144] Lars-Anders Carlson, John A.G. Briggs, Bärbel Glass, James D. Riches, Martha N. Simon, Marc C. Johnson, Barbara Müller, Kay Grünewald, Hans-Georg Kräusslich, Three-dimensional analysis of budding sites and released virus suggests a revised model for hiv-1 morphogenesis, Cell Host Microbe 4 (6) (2008) 592–599.
[145] Guillermo R. Lázaro, Suchetana Mukhopadhyay, Michael F. Hagan, Why enveloped viruses need cores—the contribution of a nucleocapsid core to viral budding, Biophys. J. 114 (3) (2018) 619–630.
[146] Guangnan Meng, Jayson Paulose, David R. Nelson, Vinothan N. Manoharan, Elastic instability of a crystal growing on a curved surface, Science 343 (6171) (2014) 634–637.
[147] Rodrigo E. Guerra, Colm P. Kelleher, Andrew D. Hollingsworth, Paul M. Chaikin, Freezing on a sphere, Nature 554 (7692) (2018) 346–350.
[148] C. Rankl, F. Kienberger, L. Wildling, J. Wruss, H.J. Gruber, D. Blaas, P. Hinterdorfer, Multiple receptors involved in human rhinovirus attachment to live cells, Proc. Natl. Acad. Sci. 105 (46) (2008) 17778–17783.
[149] Christian Sieben, Christian Kappel, Rong Zhu, Anna Wozniak, Christian Rankl, Peter Hinterdorfer, Helmut Grubmüller, Andreas Herrmann, Influenza virus binds its host cell using multiple dynamic interactions, Proc. Natl. Acad. Sci. USA 109 (34) (2012) 13626–13631.
[150] David Alsteens, Richard Newton, Rajib Schubert, David Martinez-Martin, Martin Delguste, Botond Roska, Daniel J. Mueller, Nanomechanical mapping of first binding steps of a virus to animal cells, Nature Nanotechnol. 12 (2) (2017) 177–183.
[151] Richard Newton, Martin Delguste, Melanie Koehler, Andra C. Dumitru, Pawel R. Laskowski, Daniel J. Mueller, David Alsteens, Combining confocal and atomic force microscopy to quantify single-virus binding to mammalian cell surfaces, Nat. Protoc. 12 (11) (2017) 2275–2292.
[152] Henry Eyring, Viscosity, plasticity, and diffusion as examples of absolute reaction rates, J. Chem. Phys. 4 (4) (1936) 283–291.
[153] E. Evans, K. Ritchie, Dynamic strength of molecular adhesion bonds, Biophys. J. 72 (4) (1997) 1541–1555.
[154] Raymond W. Friddle, Aleksandr Noy, James J. De Yoreo, Interpreting the widespread nonlinear force spectra of intermolecular bonds, Proc. Natl. Acad. Sci. USA 109 (34) (2012) 13573–13578.
[155] D.R. Nelson, Defects and Geometry in Condensed Matter Physics, Cambridge Press, 2002.
[156] Paul M. Chaikin, T.C. Lubensky, Principles of Condensed Matter Physics, Cambridge University Press, 1995.
[157] M. Nakahara, Geometry, Topology and Physics, Adam Hilger, 1990.
[158] J.F. Sadoc, R. Mosseri, Geometrical Frustration, Cambridge University Press, 1999.
[159] M. Bowick, A. Cacciuto, D.R. Nelson, A. Travesset, Crystalline order on a sphere and the generalized Thomson problem, Phys. Rev. Lett. 89 (18) (2002) 185502.
[160] Siyu Li, Polly Roy, Alex Travesset, Roya Zandi, Why large icosahedral viruses need scaffolding proteins, Proc. Natl. Acad. Sci. (2018) 201807706.
[161] Mauricio G. Mateu, Mechanical properties of viruses analyzed by atomic force microscopy: A virological perspective, Virus Res. 168 (1–2) (2012) 1–22.
[162] M. Kleman, J. Friedel, Disclinations, dislocations, and continuous defects: A reappraisal, RMP 80 (1) (2008) 61–115.
[163] N.D. Mermin, The topological theory of defects in ordered media, Rev. Modern Phys. 51 (1979) 591–648.
[164] H.S. Seung, David R. Nelson, Defects in fiexible membranes with crystalline order, Phys. Rev. A 38 (1988) 1005–1018.
[165] Alex Travesset, Universality in the screening cloud of dislocations surrounding a disclination, Phys. Rev. B 68 (11) (2003) 115421–15.
[166] Siyu Li, Roya Zandi, Alex Travesset, Elasticity in curved topographies: Exact theories and linear approximations, Phys. Rev. E 99 (2019) 063005.
[167] Mark J. Bowick, Angelo Cacciuto, David R. Nelson, Alex Travesset, Crystalline particle packings on a sphere with long-range power-law potentials, Phys. Rev. B 73 (2) (2006) 024115–024116.
[168] R. Osserman, A Survey of Minimal Surfaces, Dover Publications, Mineola, 1986.
[169] Sten Andersson, S.T. Hyde, Kare Larsson, Sven Lidin, Minimal surfaces and structures: from inorganic and metal crystals to cell membranes and biopolymers, Chem. Rev. 88 (1) (1988) 221–242.
[170] William T.M. Irvine, Vincenzo Vitelli, Paul M. Chaikin, Pleats in crystals on curved surfaces, Nature 468 (7326) (2010) 947–951.
[171] Amir Azadi, Gregory M. Grason, Emergent structure of multidislocation ground states in curved crystals, Phys. Rev. Lett. 112 (2014) 225502.
[172] Amir Azadi, Gregory M. Grason, Neutral versus charged defect patterns in curved crystals, Phys. Rev. E 94 (2016) 013003.
[173] Alex Travesset, Structure of curved crystals in the thermodynamic limit and the perfect screening condition, Phys. Rev. E 94 (2016) 063001.
[174] E. Efrati, E. Sharon, R. Kupferman, Elastic theory of unconstrained non-euclidean plates, J. Mech. Phys. Solids 57 (4) (2009) 762–775.
[175] Michael Moshe, Eran Sharon, Raz Kupferman, Elastic interactions between two-dimensional geometric defects, Phys. Rev. E 92 (2015) 062403.
[176] W.T. Koiter, On the nonlinear theory of thin elastic shells, Proc. K. Ned. Acad. Wet. B 69 (1966) 1–54.
[177] A. Travesset, Ground state of a large number of particles on a frozen topography, Phys. Rev. E 72 (3) (2005) 036110–036118.
[178] Mark J. Bowick, David R. Nelson, Alex Travesset, Interacting topological defects on frozen topographies, Phys. Rev. B 62 (13) (2000) 8738–8751, Copyright (C) 2007 The American Physical Society Please report any problems to prola@aps.org PRB..
[179] A. Pérez-Garrido, M.J.W. Dodgson, M.A. Moore, Influence of dislocations in thomson's problem, Phys. Rev. B 56 (1997) 3640–3643.
[180] M. Bowick, A. Cacciuto, D.R. Nelson, A. Travesset, Crystalline order on a sphere and the generalized thomson problem, Phys. Rev. Lett. 89 (18) (2002) 185502–185505, Copyright (C) 2007 The American Physical Society Please report any problems to prola@aps.org PRL..
[181] Vincenzo Vitelli, J.B. Lucks, D.R. Nelson, Crystallography on curved surfaces, Proc. Natl. Acad. Sci. 103 (33) (2006) 12323–12328.
[182] Mark Bowick, Homin Shin, Alex Travesset, Dynamics and instabilities of defects in two-dimensional crystals on curved backgrounds, Phys. Rev. E 75 (2) (2007) 021404.
[183] Mark J. Bowick, Luca Giomi, Two-dimensional matter: order, curvature and defects, Adv. Phys. 58 (5) (2009) 449–563.
[184] Siyu Li, Roya Zandi, Alex Travesset, Gregory Grason, Ground states of crystalline caps: Generalized jellium on curved space, Phys. Rev. Lett. 123 (2019) 145501.
[185] T. Regge, General relativity without coordinates, Il Nuovo Cimento (1955-1965) 19 (3) (1961) 558–571.
[186] A.R. Bausch, M.J. Bowick, A. Cacciuto, A.D. Dinsmore, M.F. Hsu, D.R. Nelson, M.G. Nikolaides, A. Travesset, D.A. Weitz, Grain boundary scars and spherical crystallography, Science 299 (5613) (2003) 1716–1718.
[187] Graziano Vernizzi, Rastko Sknepnek, Monica Olvera de la Cruz, Faceting ionic shells into icosahedra via electrostatics, Proc. Natl. Acad. Sci. 104 (47) (2007) 18382–18386.
[188] Graziano Vernizzi, Rastko Sknepnek, Monica Olvera de la Cruz, Platonic and archimedean geometries in multicomponent elastic membranes, Proc. Natl. Acad. Sci. 108 (11) (2011) 4292–4296.
[189] Gregory M. Grason, Colloquium: Geometry and optimal packing of twisted columns and filaments, RMP 87 (2) (2015) 401–419.
[190] J.J. Thomson, On the structure of the atom: an investigation of the stability and periods of oscillation of a number of corpuscles arranged at equal intervals around the circumference of a circle; with application of the results to the theory of atomic structure, Phys. Rev. B 55 (1904) 3816.
[191] L.L. Whyte, Unique arrangements of points on a sphere, Amer. Math. Monthly 59 (9) (1952) 606–611.
[192] L.T. Wille, Searching potential energy surfaces by simulated annealing, Nature 324 (1986) 46.
[193] T. Erber, G.M. Hockney, Equilibrium configurations of n equal charges on a sphere, J. Phys. A: Math. Gen. 24 (23) (1991) L1369.

[194] L. Glasser, A.G. Every, Energies and spacings of point charges on a sphere, J. Phys. A: Math. Gen. 25 (9) (1992) 2473.
[195] Eric Lewin Altschuler, Timothy J. Williams, Edward R. Ratner, Farid Dowla, Frederick Wooten, Method of constrained global optimization, PRL 72 (17) (1994) 2671–2674.
[196] J.R. Morris, D.M. Deaven, K.M. Ho, Genetic-algorithm energy minimization for point charges on a sphere, Phys. Rev. B 53 (1996) R1740–R1743.
[197] A. Pérez-Garrido, M. Ortuño, E. Cuevas, J. Ruiz, Many-particle jumps algorithm and thomson's problem, J. Phys. A: Math. Gen. 29 (9) (1996) 1973.
[198] A. Pérez-Garrido, M.A. Moore, Symmetric patterns of dislocations in thomson's problem, PRB 60 (23) (1999) 15628–15631.
[199] Eric Lewin Altschuler, Antonio Pérez-Garrido, Global minimum for thomson's problem of charges on a sphere, PRE 71 (4) (2005) 047703.
[200] David J. Wales, Sidika Ulker, Structure and dynamics of spherical crystals characterized for the thomson problem, PRB 74 (21) (2006) 212101.
[201] David J. Wales, Hayley McKay, Eric L. Altschuler, Defect motifs for spherical topologies, PRB 79 (22) (2009) 224115.
[202] Oren M. Becker, Martin Karplus, The topology of multidimensional potential energy surfaces: Theory and application to peptide structure and kinetics, J. Chem. Phys. 106 (4) (1997) 1495–1517.
[203] David J. Wales, Mark A. Miller, Tiffany R. Walsh, Archetypal energy landscapes, Nature 394 (1998) 758.
[204] D* Wales, Energy Landscapes, Cambridge University Press, 2003.
[205] Dhagash Mehta, Jianxu Chen, Danny Z. Chen, Halim Kusumaatmaja, David J. Wales, Kinetic transition networks for the thomson problem and smale's seventh problem, PRL 117 (2) (2016) 028301.
[206] E.B. Saff, A.B.J. Kuijlaars, Distributing many points on a sphere, Math. Intelligencer 19 (1) (1997) 5–11.
[207] Henry Cohn, Yang Jiao, Abhinav Kumar, Salvatore Torquato, Rigidity of spherical codes, Geom. Topol. 15 (4) (2011) 2235–2273.
[208] E. Bendito, A. Carmona, A.M. Encinas, J.M. Gesto, Estimation of fekete points, J. Comput. Phys. 225 (2) (2007) 2354–2376.
[209] David J. Wales, Chemistry, geometry, and defects in two dimensions, ACS Nano 8 (2) (2014) 1081–1085.
[210] D.S. Roshal, O.V. Konevtsova, A.E. Myasnikova, S.B. Rochal, Assembly of the most topologically regular two-dimensional micro and nanocrystals with spherical, conical, and tubular shapes, PRE 94 (5) (2016) 052605.
[211] Andrew M. Mascioli, Christopher J. Burke, Mathew Q. Giso, Timothy J. Atherton, Defect structure and percolation in the packing of bidispersed particles on a sphere, Soft Matter 13 (39) (2017) 7090–7097.
[212] A. Slosar, R. Podgornik, On the connected-charges thomson problem, Europhys. Lett. 75 (4) (2006) 631–637.
[213] S. Schneider, G. Gompper, Shapes of crystalline domains on spherical fluid vesicles, Europhys. Lett. 70 (2005) 136.
[214] Alexander Yu Morozov, Robijn F. Bruinsma, Assembly of viral capsids, buckling, and the asaro-grinfeld-tiller instability, Phys. Rev. E 81 (2010) 041925.
[215] Gregory M. Grason, Defects in crystalline packings of twisted filament bundles. i. continuum theory of disclinations, Phys. Rev. E 85 (3) (2012) 031603.
[216] Mark Bowick, Alex Travesset, The statistical mechanics of membranes, Phys. Rep. 344 (4–6) (2001) 255–308.
[217] Benny Davidovitch, Yiwei Sun, Gregory M. Grason, Geometrically incompatible confinement of solids, Proc. Natl. Acad. Sci. 116 (5) (2018) 1483–1488.
[218] Alexander E. Lobkovsky, Boundary layer analysis of the ridge singularity in a thin plate, PRE 53 (4) (1996) 3750–3759.
[219] T.A. Witten, Hao Li, Asymptotic shape of a fullerene ball, Europhys. Lett. 23 (1) (1993) 51.
[220] Alexander E. Lobkovsky, T.A. Witten, Properties of ridges in elastic membranes, PRE 55 (2) (1997) 1577–1589.
[221] Jack Lidmar, Leonid Mirny, David R. Nelson, Virus shapes and buckling transitions in spherical shells, Phys. Rev. E 68 (2003) 051910–1–051910–10.
[222] Michael Gomez, Derek E. Moulton, Dominic Vella, The shallow shell approach to pogorelov problem and the breakdown of 'mirror buckling', Proc. R. Soc. A 472 (2187) (2016).
[223] T.A. Witten, Stress focusing in elastic sheets, RMP 79 (2) (2007) 643–675.
[224] Carlo Carraro, David R. Nelson, Grain-boundary buckling and spin-glass models of disorder in membranes, PRE 48 (4) (1993) 3082–3090.
[225] T.T. Nguyen, Robijn F. Bruinsma, William M. Gelbart, Continuum theory of retroviral capsids, Phys. Rev. Lett. 96 (2006) 078102.
[226] Antonio Šiber, Buckling transition in icosahedral shells subjected to volume conservation constraint and pressure: Relations to virus maturation, Phys. Rev. E 73 (6) (2006) 061915–1–061915–10.
[227] Chloe M. Funkhouser, Rastko Sknepnek, Monica Olvera de la Cruz, Topological defects in the buckling of elastic membranes, Soft Matter 9 (1) (2013) 60–68.
[228] Rastko Sknepnek, Graziano Vernizzi, Monica Olvera de la Cruz, Buckling of multicomponent elastic shells with line tension, Soft Matter 8 (3) (2012) 636–644.
[229] Antonio Šiber, Rudolf Podgornik, Stability of elastic icosadeltahedral shells under uniform external pressure: Application to viruses under osmotic pressure, Phys. Rev. E 79 (2009) 011919.
[230] Dominic Vella, Amin Ajdari, Ashkan Vaziri, Arezki Boudaoud, Indentation of ellipsoidal and cylindrical elastic shells, PRL 109 (14) (2012) 144302.
[231] Dominic Vella, Amin Ajdari, Ashkan Vaziri, Arezki Boudaoud, The indentation of pressurized elastic shells: from polymeric capsules to yeast cells, J. R. Soc. Interface 9 (68) (2012) 448.
[232] Eric Reissner, Stresses and small displacements of shallow spherical shells. ii, J. Math. Phys. 25 (1–4) (1946) 279–300.
[233] James R. Fitch, The buckling and post-buckling behavior of spherical caps under concentrated load, Int. J. Solids Struct. 4 (4) (1968) 421–446.
[234] Ashkan Vaziri, L. Mahadevan, Localized and extended deformations of elastic shells, Proc. Natl. Acad. Sci. USA 105 (23) (2008) 7913.
[235] William S. Klug, Robijn F. Bruinsma, Jean-Philippe Michel, Charles M. Knobler, Irena L. Ivanovska, Christoph F. Schmidt, Gijs J.L. Wuite, Failure of viral shells, PRL 97 (22) (2006) 228101.
[236] Sanaz Panahandeh, Siyu Li, Roya Zandi, The equilibrium structure of self-assembled protein nano-cages, Nanoscale 10 (2018) 22802–22809.
[237] D.M. Salunke, D.L. Caspar, R.L. Garcea, Polymorphism in the assembly of polyomavirus capsid protein vp 1, Biophys. J. 56 (1989) 887–900.
[238] Z. Li, H.A. Scheraga, Monte carlo-minimization approach to the multiple-minima problem in protein folding, Proc. Natl. Acad. Sci. 84 (19) (1987) 6611–6615.
[239] Stefan Paquay, Halim Kusumaatmaja, David J. Wales, Roya Zandi, Schoot van der Schoot, Energetically favoured defects in dense packings of particles on spherical surfaces, Soft Matter 12 (2016) 5708–5717.
[240] Jef Wagner, Roya Zandi, The robust assembly of small symmetric nanoshells, Biophys. J. 109 (5) (2015) 956–965.
[241] Jiying Ning, Gonca Erdemci-Tandogan, Ernest L. Yufenyuy, Jef Wagner, Benjamin A. Himes, Gongpu Zhao, Christopher Aiken, Roya Zandi, Peijun Zhang, In vitro protease cleavage and computer simulations reveal the hiv-1 capsid maturation pathway, Nature Commun. 7 (2016) 13689.
[242] Artem Levandovsky, Roya Zandi, Nonequilibirum assembly, retroviruses, and conical structures, Phys. Rev. Lett. 102 (2009) 198102–1–198102–4.
[243] Paul C. Jordan, Dustin P. Patterson, Kendall N. Saboda, Ethan J. Edwards, Heini M. Miettinen, Gautam Basu, Megan C. Thielges, Trevor Douglas, Self-assembling biomolecular catalysts for hydrogen production, Nature Chem. 8 (2) (2016) 179.
[244] Kyung H. Choi, Jennifer McPartland, Irene Kaganman, Valorie D. Bowman, Lucia B. Rothman-Denes, Michael G. Rossmann, Insight into dna and protein transport in double-stranded dna viruses: the structure of bacteriophage n4, J. Mol. Biol. 378 (3) (2008) 726–736.

[245] Joseph B. Pesavento, Mary K. Estes, B.V. Venkataram Prasad, Ii, 1. structural organization of the genome in rotavirus, in: Viral Gastroenteritis, in: Perspectives in Medical Virology, vol. 9, Elsevier, 2003, pp. 115–127.
[246] Z. Hong Zhou, Matthew Dougherty, Joanita Jakana, Jing He, Frazer J. Rixon, Wah Chiu, Seeing the herpesvirus capsid at 8.5 å, Science 288 (5467) (2000) 877–880.
[247] M. Elizabeth Stroupe, Tess E. Brewer, Duncan R. Sousa, Kathryn M. Jones, The structure of sinorhizobium meliloti phage ϕm12, which has a novel t= 19l triangulation number and is the founder of a new group of t4-superfamily phages, Virology 450 (2014) 205–212.
[248] Hanna M. Oksanen, et al., Ictv virus taxonomy profile: Corticoviridae, J. Gen. Virol. 98 (5) (2017) 888–889.
[249] Siyu Li, Roya Zandi, Alex Travesset, Gregory M. Grason, Ground states of crystalline caps: Generalized jellium on curved space, Phys. Rev. Lett. 123 (2019) 145501.
[250] Gonca Erdemci-Tandogan, Jef Wagner, Paul van der Schoot, Roya Zandi, Role of genome in the formation of conical retroviral shells, J. Phys. Chem. B 120 (2016) 6298.
[251] Barbie K. Ganser, Su Li, Victor Y. Klishko, John T. Finch, Wesley I. Sundquist, Assembly and analysis of conical models for the hiv-1 core, Science 2 (1999) 80–83.
[252] Sanaz Panahandeh, Siyu Li, Laurent Marichal, Rafael Leite Rubim, Guillaume Tresset, Roya Zandi, How a virus circumvents energy barriers to form symmetric shells, 2019, submitted.
[253] Deborah Leckband, Jacob Israelachvili, Intermolecular forces in biology, Q. Rev. Biophys. 34 (2) (2001) 105–267.
[254] Rudolf Podgornik, D. Harries, J. DeRouchey, H.H. Strey, V.A. Parsegian, Interactions in macromolecular complexes used as nonviral vectors for gene delivery, in: Gene Therapy: Therapeutic Mechanisms and Strategies, third ed., N. Smyth Templeton, Marcel Dekker, New York, 2008, pp. 443–484.
[255] Carel van Oss, The Properties of Water and their Role in Colloidal and Biological Systems, Academic Press, Reading Massachusetts, 2008.
[256] V.A. Parsegian, Van Der Waals Forces: A Handbook for Biologists, Chemists, Engineers, and Physicists, Cambridge University Press, 2005.
[257] N. Adzic, R. Podgornik, Charge regulation in ionic solutions: Thermal fluctuations and kirkwood-schumaker interactions, Phys. Rev. E 91 (2015) 022715.
[258] Jacob Israelachvili, Intermolecular & Surface Forces, second ed., Academic Press, Amsterdam, 1991.
[259] Alexei V. Finkelstein, Oleg B. Ptitsyn, Protein Physics, first ed., Academic Press, London, 2002.
[260] T. Simonson, Electrostatics and dynamics of proteins, Rep. Progr. Phys. 66 (2003) 737–787.
[261] L.M. Woods, D.A.R. Dalvit, A. Tkatchenko, P. Rodriguez-Lopez, A.W. Rodriguez, R. Podgornik, A materials perspective on casimir and van der waals interactions, Rev. Modern Phys. 88 (2016) 045003.
[262] B.W. Parsegian, V.A. Ninham, Application of the lifshitz theory to the calculation of van der waals forces across thin lipid films, Nature 224 (1969) 1197–1198.
[263] C.M. Roth, A.M. Lenhoff, Improved parametric representation of water dielectric data for lifshitz theory calculations, J. Colloid Interface Sci. 179 (1996) 637–639.
[264] Xueyu Song, Xuefeng Zhao, The van der waals interaction between protein molecules in an electrolyte solution, J. Chem. Phys. 120 (2004) 2005–2009.
[265] Yuejiao Xian, Chitra B. Karki, Sebastian Miki Silva, Lin Li, Chuan Xiao, The roles of electrostatic interactions in capsid assembly mechanisms of giant viruses, Int. J. Mol. Sci. 20 (8) (2019).
[266] Rees F. Garmann, Mauricio Comas-Garcia, Ajaykumar Gopal, Charles M. Knobler, William M. Gelbart, The assembly pathway of an icosahedral single-stranded RNA virus depends on the strength of inter-subunit attractions, J. Mol. Biol. 426 (5) (2014) 1050–1060.
[267] J. Bernal, I. Fankuchen, X-ray and crystallographic studies of plant virus preparations, J. Gen. Physiol. 25 (1941) 111–165.
[268] G. Oster, Two-phase formation in solutions of tobacco mosaic virus and the problem of long-range forces, J. Gen. Physiol. 33 (1950) 445–473.
[269] E.J.W. Verwey, J.Th.G. Overbeek, Theory of the Stability of Lyophobic Colloids, first ed., Elsevier, Amsterdam, 1948.
[270] F. Ruggeri, F. Zosel, N. Mutter, M. Rozycka, M. Wojtas, A. Ozyhar, B. Schuler, M. Krishnan, Single-molecule electrometry, Nature Nanotechnol. 12 (2017) 488–495.
[271] Victor A. Bloomfield, Donald M. Crothers, Ignacio Tinoco, John E. Hearst, David E. Wemmer, Peter A. Killman, Douglas H. Turner, Nucleic Acids: Structures, Properties, and Functions, first ed., University Science Books, Herndon, 2000.
[272] A. Finkelstein, O. Ptitsyn, Protein Physics: A Course of Lectures, second ed., Academic Press, 2016.
[273] Mikael Lund, Bo Jonsson, On the charge regulation of proteins, Biochemistry 44 (2005) 5722–5727.
[274] Fernando Luis Barroso da Silva, Mikael Lund, Bo Jonsson, Torbjorn Akesson, On the complexation of proteins and polyelectrolytes, J. Phys. Chem. B 110 (2006) 4459–4464.
[275] Fernando Luis Barroso da Silva, Bo Jonsson, Polyelectrolyte-protein complexation driven by charge regulation, Soft Matter 5 (2009) 2862–2868.
[276] H.-K. Lin, P. van der Schoot, R. Zandi, Impact of charge variation on the encapsulation of nanoparticles by virus coat proteins, Phys. Biol. 9 (2012) 066004.
[277] R. Kusters, H.-K. Lin, R. Zandi, I. Tsvetkova, B. Dragnea, P. van der Schoot, Role of charge regulation and size polydispersity in nanoparticle encapsulation by viral coat proteins, J. Phys. Chem. B 119 (2015) 1869–1880.
[278] P. Adhikari, A.M. Wen, R.F. French, V.A. Parsegian, N. Steinmetz, R. Podgornik, Wai-Yim Ching, Electronic structure, dielectric response, and surface charge distribution of RGD (1FUV) peptide, Sci. Rep. 4 (2014) 5605.
[279] R. Eifler, R. Podgornik, N. Steinmetz, R.F. French, V.A. Parsegian, Wai-Yim Ching, Charge distribution and hydrogen bonding of a collagen α2-chain in dry, hydrated and protonated/deprotonated structural models, Int. J. Quantum Chem. 116 (2016) 681–691.
[280] J.R. Vega-Acosta, R.D. Cadena-Nava, W.M. Gelbart, C.M. Knobler, J. Ruiz-Garcia, Electrophoretic mobilities of a viral capsid, its capsid protein, and their relation to viral assembly, J. Phys. Chem. B 118 (8) (2014) 1984–1989.
[281] Pedro J. de Pablo, The application of atomic force microscopy for viruses and protein shells: Imaging and spectroscopy, Adv. Virus Res. 105 (2019) 161–187.
[282] O.V. Konevtsova, D.S. Rochal, A. Losdorfer, R. Podgornik, S.B. Rochal, Hidden symmetry of the anomalous bluetongue virus capsid and its role in the infection process, Soft Matter 15 (2019) 7663.
[283] Hiroyuki Ohshima, Hiroyuki Ohshima Theory of Colloid and Interfacial Electric Phenomena, Vol. 12, Elsevier, 2006.
[284] Richard W. O'Brien, Lee R. White, Electrophoretic mobility of a spherical colloidal particle, J. Chem. Soc. Faraday Trans. 2 74 (1978) 1607–1626.
[285] M. Hernando-Pérez, A.X. Cartagena-Rivera, A. Lodorfer Boi, P.J.P. Carrillo, C. San Martn, M.G. Mateu, A. Raman, R. Podgornik, P.J. de Pablo, Quantitative nanoscale electrostatics of viruses, Nanoscale 7 (2015) 17289–17298.
[286] Rykkert J. Nap, Anže Lošdorfer Božič, Igal Szleifer, Rudolf Podgornik, The role of solution conditions in the bacteriophage PP7 capsid charge regulation, Biophys. J. 107 (2014) 1970–1979.
[287] M.W. Johnson, G.W. Wagner, J.B. Bancroft, A titrimetric and electrophoretic study of cowpea chlorotic mottle virus and its protein, J. Gen. Virol. 19 (1973) 263.
[288] Mauricio Carrillo-Tripp, Craig M. Shepherd, Ian A. Borelli, Sangita Venkataraman, Gabriel Lander, Padmaja Natarajan, John E. Johnson, Charles L. Brooks III, Vijay S. Reddy, Viperdb2: an enhanced and web api enabled relational database for structural virology, Nucleic Acids Res. 37 (1) (2008).

[289] Samuel Karlin, Volker Brendel, Charge configurations in viral proteins, Proc. Natl. Acad. Sci. USA 85 (1988) 9396–9400.
[290] B. Michen, T. Graule, Isoeletric points in viruses, J. Appl. Microbiol. 109 (2010) 388–397.
[291] Alexei V. Finkelstein, Oleg B. Ptitsyn, Protein Physics: A Course of Lectures, Academic Press, 2002.
[292] M.R. Gunner, Junjun Mao, Yifan Song, Jinrang Kim, Factors influencing the energetics of electron and proton transfers in proteins, Biochim. Biophys. Acta 1757 (2006) 942–968.
[293] Daniel G. Isom, Brian R. Cannon, Carlos A. Castañeda, Aaron Robinson, Garcia-Moreno E. Bertrand, High tolerance for ionizable residues in the hydrophobic interior of proteins, Proc. Natl. Acad. Sci. USA 105 (2008) 17784–17788.
[294] Daniel G. Isom, Carlos A. Castañeda, Brian R. Cannon, Priya D. Velu, Garcia-Moreno E. Bertrand, Charges in the hydrophobic interior of proteins, Proc. Natl. Acad. Sci. USA 107 (2010) 16096–16100.
[295] F. Pichierri, Quantum proteomics, 2011, arXiv:1107.5853v1 [q-bio.BM].
[296] Gerald R. Grimsley, J. Martin Scholtz, C. Nick Pace, A summary of the measured pk values of the ionizable groups in folded proteins, Prot. Sci. 18 (2009) 247–251.
[297] Carolyn A. Fitch, Gerald Platzer, Mark Okon, Bertrand Garcia-Moreno, Lawrence P. McIntosh, Arginine: Its pka value revisited, Protein Sci. 24 (2015) 752–761.
[298] R. Phillips, J. Kondev, J. Theriot, H. Garcia, Physical Biology of the Cell, Taylor & Francis Group, 2013.
[299] Anže Lošdorfer Božič, Antonio Šiber, Rudolf Podgornik, How simple can a model of an empty viral capsid be? charge distributions in viral capsids, J. Biol. Phys. 38 (2012) 657–671.
[300] M.J. Betts, R.B. Russell, Amino acid properties and consequences of substitutions, in: M.R. Barnes, I.C. Gray (Eds.), Bioinformatics for Geneticists, Wiley, 2003.
[301] M. Carrillo-Tripp, C.M. Shepherd, I.A. Borelli, S. Venkataraman, G. Lander, P. Natarajan, J.E. Johnson, C.L. 3rd Brooks III, V.S. Reddy, Viperdb2: an enhanced and web api enabled relational database for structural virology, Nucleic Acids Res. 37 (2009) D436–442.
[302] H.M. Berman, J. Westbrook, Z. Feng, G. Gilliland, T.N. Bhat, H. Weissig, I.N. Shindyalov, P.E. Bourne, The protein data bank, Nucleic Acids Res. 28 (2000) 235–242.
[303] T. Markovich, D. Andelman, R. Podgornik, Charged membranes: Poisson-boltzmann theory, dlvo paradigm and beyond, chapter 9 in: Handbook of lipid membranes, in: C. Safinya, J. Raedler (Eds.), Handbook of Lipid Membranes, Chapter Chapter 9, Taylor and Francis, 2019, p. xxx..
[304] B.W. Ninham, V.A. Parsegian, Electrostatic potential between surfaces bearing ionizable groups in ionic equilibruim with physiologic saline solution, J. Theoret. Biol. 31 (1971) 405–0428.
[305] Anze Losdorfer Bozic, Rudolf Podgornik, Symmetry effects in electrostatic interactions between two arbitrarily charged spherical shells in the debye-hückel approximation, J. Chem. Phys. 139 (2013) 074902.
[306] Antonio Šiber, Rudolf Podgornik, Role of electrostatic interactions in the assembly of empty spherical viral capsids, Phys. Rev. E 76 (2007) 061906.
[307] Antonio Siber, Anze Losdorfer Bozic, Rudolf Podgornik, Energies and pressures in viruses: contribution of nonspecific electrostatic interactions, Phys. Chem. Chem. Phys. 14 (2012) 3746–3765.
[308] Anette Schneemann, The structural and functional role of RNA in icosahedral virus assembly, Annu. Rev. Microbiol. 60 (1) (2006) 51–67.
[309] Hitesh Sivanandam, Deborah Mathews, Rees Garmann, Gonca Erdemci-Tandogan, Roya Zandi, A.L.N. Rao, Functional analysis of the N-terminal basic motif of a eukaryotic satellite RNA virus capsid protein in replication and packaging, Sci. Rep. 6 (2016) 26328.
[310] Jason D. Perlmutter, Michael F. Hagan, Mechanisms of virus assembly, Annu. Rev. Phys. Chem. 66 (2015) 217–239.
[311] Vladimir A. Belyi, M. Muthukumar, Electrostatic origin of genome packing in viruses, Proc. Natl. Acad. Sci. USA 103 (2006) 17174–17178.
[312] Yufang Hu, Roya Zandi, Adriana Anavitarte, Charles M. Knobler, William M. Gelbart, Packaging of a polymer by a viral capsid: The interplay between polymer length and capsid size, Biophys. J. 94 (4) (2008) 1428–1436.
[313] Antonio Šiber, Rudolf Podgornik, Nonspecific interactions in spontaneous assembly of empty versus functional single-stranded RNA viruses, Phys. Rev. E 78 (2008) 051915.
[314] C.L. Ting, J. Wu, Z.G. Wang, Thermodynamic basis for the genome to capsid charge relationship in electrostatically-driven viral encapsidation, Proc. Natl. Acad. Sci. USA 108 (2011) 16986–16991.
[315] Gonca Erdemci-Tandogan, Jef Wagner, Paul van der Schoot, Rudolf Podgornik, Roya Zandi, Rna topology remolds electrostatic stabilization of viruses, Phys. Rev. E 89 (6) (2014) 022401.
[316] Gonca Erdemci-Tandogan, Jef Wagner, Paul van der Schoot, Rudolf Podgornik, Roya Zandi, Effects of rna branching on the electrostatic stabilization of viruses, Phys. Rev. E 94 (6) (2016) 022408.
[317] Siyu Li, Gonca Erdemci-Tandogan, Jef Wagner, Paul van der Schoot, Roya Zandi, Impact of a nonuniform charge distribution on virus assembly, Phys. Rev. E 96 (6) (2017) 022401.
[318] Reidun Twarock, Richard J. Bingham, Eric C. Dykeman, Peter G. Stockley, A modelling paradigm for rna virus assembly, Curr. Opin. Virol. 30 (6) (2018) 1–8.
[319] Dmitrij Frishman, Patrick Argos, Knowledge-based protein secondary structure assignment, Proteins: Struct. Funct. Bioinform. 23 (1995) 566–579.
[320] Anze Losdorfer Bozic, Rudolf Podgornik, Varieties of charge distributions in coat proteins of ssrna+ viruses, J. Phys.: Condens. Matter 30 (1) (2018) 024001.
[321] Tao Hu, Rui Zhang, B.I. Shklovskii, Electrostatic theory of viral self-assembly, Physica A 387 (2008) 3059–3064.
[322] Rikkert Nap, Peng Gong, Igal Szleifer, Weak polyelectrolytes tethered to surfaces: effect of geometry, acid–base equilibrium and electrical permittivity, J. Polym. Sci. B 44 (18) (2006) 2638–2662.
[323] Rikkert J. Nap, Igal Szleifer, How to optimize binding of coated nanoparticles: Coupling of physical interactions, molecular organization and chemical state, Biomater. Sci. 1 (2013) 814–823.
[324] Yael Avni, David Andelman, Rudolf Podgornik, Charge regulating macro-ions in salt solutions: screening properties and electrostatic interactions, Soft Matter 14 (2018) 6058.
[325] G. Trefalt, T. Palberg, M. Borkovec, Forces between colloidal particles in aqueous solutions containing monovalent and multivalent ions, Curr. Opin. Colloid Interface Sci. 27 (2017) 9–17.
[326] A.Yu. Grosberg, T.T. Nguyen, B.I. Shklovskii, The physics of charge inversion in chemical and biological systems, Rev. Modern Phys. 74 (2) (2002) 329–345.
[327] Leili Javidpour, Anž Lošdorfer Božič, Ali Naji, Rudolf Podgornik, Multivalent ion effects on electrostatic stability of virus-like nano-shells, J. Chem. Phys. 139 (2013) 154709.
[328] Willem K. Kegel, Paul van der Schoot, Competing hydrophobic and screened-coulomb interactions in hepatitis b virus capsid assembly, Biophys. J. 86 (2004) 3905–3913.
[329] Peter Prinsen, Paul van der Schoot, William M. Gelbart, Charles M. Knobler, Multishell structures of virus coat proteins, J. Phys. Chem. B 114 (2010) 5522–5533.
[330] H.R. Shojaei, A. Losdorfer Bozic, M. Muthukumar, R. Podgornik, Effects of long-range interactions on curvature energies of viral shells, Phys. Rev. E 93 (2016) 052415.

[331] B. Duplantier, Exact curvature energies of charged membranes of arbitrary shapes, Physica A 168 (1990) 179–197.
[332] Anze Losdorfer Bozic, Rudolf Podgornik, Anomalous multipole expansion: Charge regulation of patchy inhomogeneously charged spherical particles, J. Chem. Phys. 149 (2018) 163307.
[333] Kaspars Tars, Kerstin Fridborg, Maija Bundule, Lars Liljas, Structure determination of bacteriophage pp7 from pseudomonas aeruginosa: from poor data to a good map, Acta Crystallogr. D 56 (4) (2000) 398–405.
[334] Jerri C. Caldeira, David S. Peabody, Stability and assembly in vitro of bacteriophage PP7 virus-like particles, J. Nanobiotechnol. 5 (2007) 10.
[335] B. Michen, T. Graule, Isoelectric points of viruses, J. Appl. Microbiol. 109 (2) (2010) 388–397.
[336] Kurt Brorson, Hong Shen, Scott Lute, Jessica Soto Pérez, Douglas D. Frey, Characterization and purification of bacteriophages using chromatofocusing, J. Chromatogr. A 1207 (1–2) (2008) 110–121.
[337] Amelie Leforestier, Antonio Šiber, Francoise Livolant, Rudolf Podgornik, Protein-dna interactions determine the shapes of dna toroids condensed in virus capsids, Biophys. J. 100 (9) (2011) 2209–2216.
[338] Ian J. Molineux, Debabrata Panja, Popping the cork: mechanisms of phage genome ejection, Nat. Rev. Microbiol. 11 (2013) 194–204.
[339] Yi-Ju Chen, David Wu, William Gelbart, Charles M. Knobler, Rob Phillips, Willem K. Kegel, Two-stage dynamics of in vivo bacteriophage genome ejection, Phys. Rev. X 8 (2018) 021029.
[340] A. Fokine, M.G. Rossmann, Molecular architecture of tailed double-stranded dna phages, Bacteriophage 4 (2014) 6e28281.
[341] W.C. Earnshaw, J. King, S.C. Harrison, F.A. Eiserling, The structural organization of dna packaged within the heads of t4 wild-type, isometric and giant bacteriophages, Cell 14 (3) (1978) 559–568.
[342] Mario E. Cerritelli, Naiqian Cheng, Alan H. Rosenberg, Catherine E. McPherson, Frank P. Booy, Alasdair C. Steven, Encapsidated conformation of bacteriophage t7 dna, Cell 91 (2) (1997) 271–280.
[343] A. Fokine, P.R. Chipman, P.G. Leiman, V.V. Mesyanzhinov, V.B. Rao, M.G. Rossmann, Molecular architecture of the prolate head of bacteriophage t4, Proc. Natl. Acad. Sci. 101 (16) (2004) 6003–6008.
[344] Ye Xiang, Marc C. Morais, Anthony J. Battisti, Shelley Grimes, Paul J. Jardine, Dwight L. Anderson, Michael G. Rossmann, Rossmann structural changes of bacteriophage f29 upon dna packaging and release, EMBO J. 25 (21) (2006) 5229–5239.
[345] Juan Chang, Peter Weigele, Jonathan King, Wah Chiu, Wen Jiang, Cryo-em asymmetric reconstruction of bacteriophage p22 reveals organization of its dna packaging and infecting machinery, Structure 14 (6) (2006) 1073–1082.
[346] Wen Jiang, Juan Chang, Joanita Jakana, Peter Weigele, Jonathan King, Wah Chiu, Structure of epsilon15 bacteriophage reveals genome organization and dna packaging/injection apparatus, Nature 439 (7076) (2006) 612–616.
[347] A. Leforestier, S. Brasilšs, M. de Frutos, E. Raspaud, L. Letellier, P. Tavares, F. Livolant, Bacteriophage t5 dna ejection under pressure, J. Mol. Biol. 384 (3) (2008) 730–739.
[348] Amelie Leforestier, Francoise Livolant, The bacteriophage genome undergoes a succession of intracapsid phase transitions upon dna ejection, J. Mol. Biol. 396 (2) (2010) 384–395.
[349] Trinh X. Hoang, Hoa Lan Trinh, Achille Giacometti, Rudolf Podgornik, Jayanth R. Banavar, Amos Maritan, Phase diagram of the ground states of dna condensates, Phys. Rev. E 92 (2015) 060701(R).
[350] S.C. Riemer, V.A. Bloomfield, Packaging of dna in bacteriophage heads: Some considerations on energetics, Biopolymers 17 (1978) 785–794.
[351] I.S. Gabashvili, A.Yu. Grosberg, D.V. Kuznetsov, G.M. Mrevlishvili, Theoretical-model of dna packaging in the phage head, Biofizika 36 (5) (1991) 780–787.
[352] A. Yu. Grosberg, A.V. Zhestkov, On the theory of packing of double-helical dna: globular state of uniform elastic macromolecule in the small volume cavity, Biofizika 29 (2) (1984) 202–206.
[353] Theo Odijk, Hexagonally packed dna within bacteriophage t7 stabilized by curvature stress, Biophys. J. 75 (3) (1998) 1223–1227.
[354] T. Odijk, Statics and dynamics of condensed dna within phages and globules, Phil. Trans. R. Soc. A 362 (1820) (2004) 1497–1517.
[355] J. Kindt, S. Tzlil, A. Ben-Shaul, W.M. Gelbart, Dna packaging and ejection forces in bacteriophage, Proc. Natl. Acad. Sci. 98 (2001) 13671–13674.
[356] P.K. Purohit, J. Kondev, R. Phillips, Mechanics of dna packaging in viruses, Proc. Natl. Acad. Sci. 100 (6) (2003) 3173–3178.
[357] Prashant K. Purohit, Mandar M. Inamdar, Paul D. Grayson, Todd M. Squires, Jane Kondev, Rob Phillips, Forces during bacteriophage dna packaging and ejection, Biophys. J. 88 (2) (2005) 851–866.
[358] Shelly Tzlil, James T. Kindt, William M. Gelbart, Avinoam Ben-Shaul, Forces and pressures in dna packaging and release from viral capsids, Biophys. J. 84 (3) (2003) 1616–1627.
[359] W.S. Klug, M.T. Feldmann, M. Ortiz, Three-dimensional director-field predictions of viral dna packing arrangements, Comput. Mech. 35 (2) (2004) 146–152.
[360] W.S. Klug, M. Ortiz, A director-field model of dna packaging in viral capsids, J. Mech. Phys. Solids 51 (10) (2003) 1815–1847.
[361] A. Siber, M. Dragar, V.A. Parsegian, R. Podgornik, Packing nanomechanics of viral genomes, Eur. Phys. J. E 26 (3) (2008) 317–325.
[362] N.N. Oskolkov, P. Linse, I.I. Potemkin, A.R. Khokhlov, Nematic ordering of polymers in confined geometry applied to dna packaging in viral capsids, J. Phys. Chem. B 115 (2011) 422–432.
[363] Avinoam Ben-Shaul, Reply to the comment by s. harvey on entropy energy and bending of dna in viral capsids, Biophys. J. 106 (2) (2014) 493–496.
[364] Prashant K. Purohit, Mandar M. Inamdar, Paul D. Grayson, Todd M. Squires, Jane Kondev, Rob Phillips, Forces during bacteriophage dna packaging and ejection, Biophys. J. 88 (2) (2005) 851–866.
[365] R. Podgornik, A. Aksoyoglu, S. Yasar, D. Svensek, V.A. Parsegian, Dna equation of state: In vitro vs. in viro, J. Phys. Chem. B 120 (2016) 36051–36060.
[366] William M. Gelbart, Charles M. Knobler, The physics of phages, Phys. Today 61 (1) (2008) 42–47.
[367] Douglas E. Smith, Sander J. Tans, Steven B. Smith, Shelley Grimes, Dwight L. Anderson, Carlos Bustamante, The bacteriophage straight phi29 portal motor can package dna against a large internal force, Nature 413 (6857) (2001) 748–752.
[368] W.C. Earnshaw, S.C. Harrison, Dna arrangement in isometric phage heads, Nature 268 (3) (1978) 598–602.
[369] X. Qiu, D.C. Rau, V.A. Parsegian, L.T. Fang, C.M. Knobler, W.M. Gelbart, Salt-dependent dna-dna spacings in intact bacteriophage reflect relative importance of dna self-repulsion and bending energies, Phys. Rev. Lett. 106 (2) (2011) 028102–1–028102–4.
[370] Wen Jiang, Juan Chang, Joanita Jakana, Peter Weigele, Jonathan King, Wah Chiu, Structure of epsilon15 bacteriophage reveals genome organization and dna packaging/injection apparatus, Nature 439 (2006) 612–616.
[371] L.R. Comolli, A.J. Spakowitz, C.E. Siegerist, P.J. Jardine, S. Grimes, D.L. Anderson, B. Bustamante, K.H. Downing, Three-dimensional architecture of the bacteriophage phi 29 packaged genome and elucidation of its packaging process, Virology 371 (2) (2008) 267–277.
[372] Amelie Leforestier, Francoise Livolant, Structure of toroidal dna collapsed inside the phage capsid, J. Mol. Biol. 106, 384–395, 91579162.
[373] J. Lepault, J. Dubochet, W. Baschong, E. Kellenberger, Organization of double-stranded dna in bacteriophages: a study by cryo-electron microscopy of vitrified samples, EMBO J. 6 (5) (1987) 1507–1512.
[374] T. Curk, J.D. Farrell, J. Dobnikar, R. Podgornik, Spontaneous domain formation in spherically confined elastic filaments, Phys. Rev. Lett. 123 (2019) 047801.
[375] Amelie Leforestier, Polymorphism of dna conformation inside the bacteriophage capsid, J. Biol. Phys. 39 (2) (2013) 201–213.

[376] T. Liu, U. Sae-Ueng, D. Li, G.C. Lander, X. Zuo, B. Jonsson, D. Rau, I. Shefer, A. Evilevitch, Solid-to-fluid-like dna transition in viruses facilitates infection, Proc. Natl. Acad. Sci. 111 (41) (2014) 14675–14680.
[377] Luis R. Comolli, Andrew J. Spakowitz, Cristina E. Siegerist, Paul J. Jardine, Shelley Grimes, Dwight L. Anderson, Carlos Bustamante, Kenneth H. Downing, Three-dimensional architecture of the bacteriophage f29 packaged genome and elucidation of its packaging process, Virology 371 (2) (2008) 267–277.
[378] D.E. Smith, Single-molecule studies of viral dna packaging, Curr. Opin. Virol. 1 (2011) 134–141.
[379] Derek N. Fuller, John Peter Rickgauer, Paul J. Jardine, Shelley Grimes, Dwight L. Anderson, Douglas E. Smith, Ionic effects on viral dna packaging and portal motor function in bacteriophage ϕ29, Proc. Natl. Acad. Sci. USA 104 (27) (2007) 11245–11250.
[380] Anton S. Petrov, Stephen C. Harvey, Packaging double-helical dna into viral capsids: Structures, forces, and energetics, Biophys. J. 95 (2) (2008) 497–502.
[381] Nicholas Keller, Damian delToro, Shelley Grimes, Paul J. Jardine, Douglas E. Smith, Repulsive dna-dna interactions accelerate viral dna packaging in phage phi29, Phys. Rev. Lett. 112 (24) (2014).
[382] Elmar Nurmemmedov, Martin Castelnovo, CarlosEnrique Catalano, Alex Evilevitch, Biophysics of viral infectivity: matching genome length with capsid size, Q. Rev. Biophys. 40 (04) (2007).
[383] V.A. Parsegian, R.P. Rand, N.L. Fuller, D.C. Rau, Osmotic stress for the direct measurement of intermolecular forces, Methods Enzym. 127 (1986) 400–416.
[384] Paul Grayson, Alex Evilevitch, Mandar M. Inamdar, Prashant K. Purohit, William M. Gelbart, Charles M. Knobler, Rob Phillips, The effect of genome length on ejection forces in bacteriophage lambda, Virology 348 (2006) 430–436.
[385] R. Podgornik, H.H. Strey, K. Gawrisch, D.C. Rau, A. Rupprecht, V.A. Parsegian, Bond orientational order, molecular motion, and free energy of high-density dna mesophases, Proc. Natl. Acad. Sci. 93 (9) (1996) 4261–4266.
[386] H.H. Strey, V.A. Parsegian, R. Podgornik, Equation of state for polymer liquid crystals: Theory and experiment, Phys. Rev. E 59 (1) (1999) 999–1008.
[387] D. Durand, J. Doucet, F. Livolant, A study of the structure of highly concentrated phases of dna by x-ray diffraction, J. Phys. II France 2 (9) (1992) 1769–1783.
[388] Selcuk Yasar, Rudolf Podgornik, Jessica Valle-Orero, Mark R. Johnson, V. Adrian Parsegian, Continuity of states between the cholesteric line hexatic transition and the condensation transition in dna solutions, Sci. Rep. 4 (2014) 6877.
[389] W.M. Gelbart, R.F. Bruinsma, P.A. Pincus, V.A. Parsegian, Dna-inspired electrostatics, Phys. Today 53 (9) (2000) 38–44.
[390] S. Marcelja, N. Radic, Repulsion of interfaces due to boundary water, Chem. Phys. Lett. 42 (1976) 129–130.
[391] Matej Kanduc, Alexander Schlaich, Emanuel Schneck, Roland R. Netz, Hydration repulsion between membranes and polar surfaces: Simulation approaches versus continuum theories, Adv. Colloid Interface Sci. 208 (2014) 142–152.
[392] R. Fuoss, A. Katchalsky, S. Lifson, The potential of an infinite rod-like molecule and the distribution of the counter ions, Proc. Natl. Acad. Sci. USA 37 (1951) 579.
[393] H.H. Strey, J. Wang, R. Podgornik, A. Rupprecht, L. Yu, V.A. Parsegian, E.B. Sirota, Refusing to twist: Demonstration of a line hexatic phase in dna liquid crystals, Phys. Rev. Lett. 84 (14) (2000) 3105–3108.
[394] Helmut H. Strey, Rudi Podgornik, Donald C. Rau, V. Adrian Parsegian, Dna-dna interactions, Curr. Opin. Struct. Biol. 8 (3) (1998) 309–313.
[395] J. Yoo, A. Aksimentiev, The structure and intermolecular forces of dna condensates, Nucl. Acids Res. 44 (2016) 2036–2046.
[396] R. Podgornik J. Zavadlav, M. Praprotnik, Order and interactions in dna arrays: Multiscale molecular dynamics simulation, Sci. Rep. 7 (2017) 4775.
[397] Long Li, Jizeng Wang, On size-dependent stability and infectivity of λ bacterial phages, J. Appl. Phys. 117 (2015) 064702.
[398] Cheng-Yin Zhang, Neng-Hui Zhang, Influence of microscopic interactions on the flexible mechanical properties of viral dna, Biophys. J. 115 (2018) 317–325.
[399] A. Naji, M. Kanduc, J. Forsman, R. Podgornik, Perspective: Coulomb fluids – weak coupling, strong coupling, in between and beyond, J. Chem. Phys. 139 (2013) 150901.
[400] A. Evilevitch, L. Fang, A. Yoffe, M. Castelnovo, D.C. Rau, V.A. Parsegian, W.M. Gelbart, C.M. Knobler, Effects of salt concentrations and bending energy on the extent of ejection of phage genomes, Biophys. J. 94 (2008) 1110–1120.
[401] Jingqiang Li, Sithara S. Wijeratne, Xiangyun Qiu, Ching-Hwa Kiang, Dna under force: Mechanics, electrostatics, and hydration, Nanomaterials 5 (2015) 246–267.
[402] Gerard C.L. Wong, Lois Pollack, Electrostatics of strongly charged biological polymers: Ion-mediated interactions and self-organization in nucleic acids and proteins, Annu. Rev. Phys. Chem. 61 (2010) 171–189.
[403] Rudi Podgornik, Donald C. Rau, V. Adrian Parsegian, The action of interhelical forces on the organization of dna double helixes: fluctuation-enhanced decay of electrostatic double-layer and hydration forces, Macromolecules 22 (4) (1989) 1780–1786.
[404] R. Podgornik, D.C. Rau, V.A. Parsegian, Parametrization of direct and soft-undulatory forces between dna double helical polyelectrolytes in solutions of several different anions and cations, Biophys. J. 66 (1994) 962–971.
[405] Ramin Golestanian, Mehran Kardar, Tanniemola B. Liverpool, Collapse of stiff polyelectrolytes due to counterion fluctuations, Phys. Rev. Lett. 82 (1999) 4456–4459.
[406] D.C. Rau, V.A. Parsegian, Direct measurement of the inter-molecular forces between counterion-condensed dna double helices. evidence for long range attractive hydration forces, Biophys. J. 61 (1992) 246–259.
[407] I. Rouzina, V.A. Bloomfield, Competitive electrostatic binding of charged ligands to polyelectrolytes: planar and cylindrical geometries, J. Phys. Chem. 100 (1996) 9977.
[408] Charles M. Knobler, William M. Gelbart, Physical chemistry of dna viruses, Ann. Rev. Phys. Chem. 60 (1) (2009) 367–383.
[409] E. Raspaud, D. Durand, F. Livolant, Interhelical spacing in liquid crystalline spermine and spermidine-dna precipitates, Biophys. J. 88 (2005) 392–403.
[410] Jie Rau, Donald C. Yang, Incomplete ion dissociation underlies the weakened attraction between dna helices at high spermidine concentrations, Biophys. J. 89 (2005) 1932–1940.
[411] T.T. Nguyen, I. Rouzina, B.I. Shklovskii, Reentrant condensation of dna induced by multivalent counterions, J. Chem. Phys. 112 (2000) 2562–2568.
[412] Davide Marenduzzo, Enzo Orlandini, Andrzej Stasiak, De Witt Sumners, Luca Tubiana, Cristian Micheletti, Dna-dna interactions in bacteriophage capsids are responsible for the observed dna knotting, Proc. Natl. Acad. Sci. USA 106 (52) (2009) 22269–22274.
[413] D.C. Rapaport, Packaging stiff polymers in small containers: A molecular dynamics study, Phys. Rev. E 94 (2016) 030401(R).
[414] Christopher G. Myers, B. Montgomery Pettitt, Phage-like packing structures with mean field sequence dependence, J. Comput. Chem. 38 (2017) 1191–1197.
[415] Jaclyn C. LaMarque, Thuc vy L. Le, Stephen C. Harvey, Packaging double-helical dna into viral capsids, Biopolymers 73 (3) (2004) 348–355.
[416] Christopher Forrey, M. Muthukumar, Langevin dynamics simulations of genome packing in bacteriophage, Biophys. J. 91 (1) (2006) 25–41.
[417] C. Rebecca Locker, Stephen D. Fuller, Stephen C. Harvey, Dna organization and thermodynamics during viral packing, Biophys. J. 93 (2007) 2861–2869.

[418] D. Marenduzzo, Computer simulations of dna packing inside bacteriophages: elasticity, electrostatics and entropy, Comput. Math. Methods Med. 9 (3–4) (2008) 317–325.
[419] Stephen C. Harvey, Anton S. Petrov, Batsal Devkota, Mustafa Burak Boz, Viral assembly: a molecular modeling perspective, Phys. Chem. Chem. Phys. 11 (2009) 10553–10564.
[420] Anton S. Petrov, Stephen C. Harvey, Role of dna–dna interactions on the structure and thermodynamics of bacteriophages lambda and p4, J. Struct. Biol. 174 (2011) 137–146.
[421] D. Marenduzzo, C. Micheletti, E. Orlandini, Biopolymer organization upon confinement, J. Phys.: Condens. Matter 22 (2010) 283102.
[422] A.S. Petrov, S.C. Harvey, Packaging double-helical dna into viral capsids: structures, forces, and energetics, Biophys. J. 95 (2008) 497–502.
[423] I. Ali, D. Marenduzzo, J.M. Yeomans, Polymer packaging and ejection in viral capsids: Shape matters, Phys. Rev. Lett. 96 (2006) 208102–1–208102–4.
[424] Qin Liang, Ying Jiang, Jeff Z.Y. Chen, Orientationally ordered states of a wormlike chain in spherical confinement, Phys. Rev. 100 (2019) 032502.
[425] Andrew James Spakowitz, Zhen-Gang Wang, Dna packaging in bacteriophage: Is twist important? Biophys. J. 88 (2005) 3912–3923.
[426] C. Micheletti, D. Marenduzzo, E. Orlandini, Polymers with spatial or topological constraints: Theoretical and computational results, Phys. Rep. 504 (2011) 1–73.
[427] Daniel Svensek, Rudolf Podgornik, Confined chiral polymer nematics: Ordering and spontaneous condensation, Europhys. Lett. 100 (6) (2012) 66005.
[428] Daniel Svensek, Gregory M. Grason, Rudolf Podgornik, Tensorial conservation law for nematic polymers, Phys. Rev. E 88 (5) (2013).
[429] H. Shin, G.M. Grason, Filling the void in confined polymer nematics: Phase transitions in a minimal model of dsdna packing, Europhys. Lett. 96 (3) (2011) 36007.
[430] Roya Zandi, Joseph Rudnick, Constraints, histones, and the 30-nm spiral, Phys. Rev. E 64 (2001) 051918.
[431] H. Fraenkel-Conrat, R.C. Williams, Reconstitution of active tobacco mosaic virus from its inactive protein and nucleic acid components, Proc. Natl. Acad. Sci. USA 41 (10) (1955) 690–698.
[432] Yufang Hu, Roya Zandi, Adriana Anavitarte, Charles M. Knobler, William M. Gelbart, Packaging of a polymer by a viral capsid: The interplay between polymer length and capsid size, Biophys. J. 94 (4) (2008) 1428–1436.
[433] I.L. Hofacker, W. Fontana, P.F. Stadler, L.S. Bonhoeffer, M. Tacker, P. Schuster, Fast folding and comparison of RNA secondary structures, Monatsh. Chem. 125 (1994) 167.
[434] Ruben D. Cadena-Nava, Yufang Hu, Rees F. Garmann, Benny Ng, Alexander N. Zelikin, Charles M. Knobler, William M. Gelbart, Exploiting fluorescent polymers to probe the self-assembly of virus-like particles, J. Phys. Chem. B 115 (10) (2011) 2386–2391.
[435] Vladimir A. Belyi, M. Muthukumar, Electrostatic origin of the genome packing in viruses, Proc. Natl. Acad. Sci. USA 103 (46) (2006) 17174–17178.
[436] Jason D. Perlmutter, Cong Qiao, Michael F. Hagan, Viral genome structures are optimal for capsid assembly, Elife 2 (2013).
[437] F.D. Sikkema, M. Comellas-Aragones, R.G. Fokkink, B.J.M. Verduin, J.J.L.M. Cornelissen, R.J.M. Nolte, Monodisperse polymer-virus hybrid nanoparticles, Org. Biomol. Chem. 5 (2007) 54.
[438] J.B. Bancroft, E. Hiebert, C.E. Bracker, The effects of various polyanions on shell formation of some spherical viruses, Virology 39 (4) (1969) 924–930.
[439] Paul van der Schoot, Roya Zandi, Impact of the topology of viral rnas on their encapsulation by virus coat proteins, J. Biol. Phys. 39 (2) (2013) 289–299.
[440] H.K. Lin, P. van der Schoot, R. Zandi, Impact of charge variation on the encapsulation of nanoparticles by virus coat proteins, Phys. Biol. 9 (2012) 066004.
[441] P. van der Schoot, R. Bruinsma, Electrostatics and the assembly of an RNA virus, Phys. Rev. E 71 (2005) 061928.
[442] Bart van der Holst, Willem K. Kegel, Roya Zandi, Paul van der Schoot, The different faces of mass action in virus assembly, J. Biol. Phys. 44 (2) (2018) 163–179.
[443] Michael F. Hagan, Modeling viral capsid assembly, Adv. Chem. Phys. 155 (2013) 1–67.
[444] Mauricio Comas-Garcia, Ruben D. Cadena-Nava, A.L.N. Rao, Charles M. Knobler, William M. Gelbart, In vitro quantification of the relative packaging efficiencies of single-stranded rna molecules by viral capsid protein, J. Virol. 86 (22) (2012) 12271–12282.
[445] Christian Beren, Lisa L. Dreesens, Katherine N. Liu, Charles M. Knobler, William M. Gelbart, The effect of RNA secondary structure ontheself-assembly of viral capsids, Biophys. J. 113 (2) (2017) 339–347.
[446] A. Siber, R. Zandi, R. Podgornik, Thermodynamics of nanospheres encapsulated in virus capsids, Phys. Rev. E 81 (2010) 051919.
[447] Peng Ni, Zhao Wang, Xiang Ma, Nayaran Chandra Das, Paul Sokol, Wah Chiu, Bogdan Dragnea, Michael Hagan, C. Cheng Kao, An examination of the electrostatic interactions between the N-terminal tail of the brome mosaic virus coat protein and encapsidated RNAs, J. Mol. Biol. (2012).
[448] M.F. Hagan, R. Zandi, Recent advances in coarse-grained modeling of virus assembly, Curr. Opin. Virol. 18 (2016) 36–43.
[449] P.G. de Gennes, Some conformation problems for long macromolecules, Rep. Progr. Phys. 32 (1) (1969) 187–205.
[450] Roland R. Netz, David Andelman, Neutral and charged polymers at interfaces, Phys. Rep. 380 (1) (2003) 1–95.
[451] P. van der Schoot, R. Zandi, Kinetic theory of virus capsid assembly, Phys. Biol. 4 (2007) 296.
[452] Siyu Li, Henri Orland, Roya Zandi, Self consistent field theory of virus assembly, J. Phys.: Condens. Matter 30 (14) (2018) 144002.
[453] Gonca Erdemci-Tandogan, Henri Orland, Roya Zandi, Rna base pairing determines the conformations of rna inside spherical viruses, Phys. Rev. Lett. 119 (2017) 188102.
[454] Jef Wagner, Gonca Erdemci, Roya Zandi, Adsorption of annealed branched polymers on curved surfaces, J. Phys.: Condens. Matter 27 (2015) 495101.
[455] T.C. Lubensky, J. Isaacson, Field theory for the statistics of branched polymers, gelation, and vulcanization, Phys. Rev. Lett. 41 (1978) 829–832.
[456] T.C. Lubensky, J. Isaacson, Statistics of lattice animals and dilute branched polymers, Phys. Rev. A 20 (1979) 2130–2146.
[457] A. Fokine, P.R. Chipman, P.G. Leiman, V.V. Mesyanzhinov, V.B. Rao, M.G. Rossmann, Molecular architecture of the prolate head of bacteriophage t4, Proc. Natl. Acad. Sci. USA 101 (16) (2004) 6003–6008.
[458] M. Zuker, Mfold web server for nucleic acid folding and hybridization prediction, Nucleic Acids Res. 31 (2003) 3406.
[459] www.ncbi.nlm.nih.gov.
[460] A.M. Yoffe, P. Prinsen, A. Gopal, C.M. Knobler, W.M. Gelbart, A. Ben-Shaul, Predicting the sizes of large rna molecules, Proc. Natl. Acad. Sci. USA 105 (2008) 16153.
[461] L. Tubiana, A.L. Bozic, C. Micheletti, R. Podgornik, Synonymous mutations reduce genome compactness in icosahedral ssRNA viruses, Biophys. J. 108 (2015) 194.
[462] Maelenn Chevreuil, Didier Law-Hine, Jingzh Chen, Stéphane Bressanelli, Sophie Combet, Doru Constantin, Jéril Degrouard, Johannes Möller, Mehdi Zeghal, Guillaume Tresset, Nonequilibrium self-assembly dynamics of icosahedral viral capsids packaging genome or polyelectrolyte, Nature Commun. 9 (1) (2018) 3071.
[463] Joshua Kelly, Alexander Y. Grosberg, Robijn Bruinsma, Sequence dependence of viral rna encapsidation, J. Phys. Chem. B 120 (26) (2016) 6038–6050, PMID: 27116641.

[464] Roya Zandi, Paul van der Schoot, Size regulation of ss-rna viruses, Biophys. J. 96 (2009) 9–20.
[465] R.F. Bruinsma, M. Comas-Garcia, R.F. Garmann, A.Y. Grosberg, Equilibrium self-assembly of small rna viruses, Phys. Rev. E 93 (2016) 032405.
[466] Surendra W. Singaram, Rees F. Garmann, Charles M. Knobler, William M. Gelbart, Avinoam Ben-Shaul, Role of rna branchedness in the competition for viral capsid proteins, Acc. Chem. Res. 119 (2015) 13991.
[467] R.F. Garmann, M. Comas-Garcia, C.M. Knobler, W.M. Gelbart, Physical principles in the self-assembly of a simple spherical virus, Acc. Chem. Res. 49 (2016) 48.
[468] Vladimir A. Belyi, M. Muthukumar, Electrostatic origin of the genome packing in viruses, Proc. Natl. Acad. Sci. USA 103 (46) (2006) 17174–17178.
[469] Michael F. Hagan, A theory for viral capsid assembly around electrostatic cores, J. Chem. Phys. 130 (2009) 114902–114917.
[470] P.G. Stockley, R. Twarock, S.E. Bakker, A.M. Barker, A. Borodavka, E. Dykeman, R.J. Ford, A.R. Pearson, S.E. Phillips, N.A. Ranson, Packaging signals in single-stranded RNA viruses: nature's alternative to a purely electrostatic assembly mechanism, J. Biol. Phys. 39 (2013) 277.
[471] A. Routh, T. Domitrovic, J.E. Johnson, Host RNAs, including transposons are encapsidated by a eukaryotic single-stranded RNA virus, Proc. Natl. Acad. Sci. USA 109 (2012) 1907–1912.
[472] Lokendra Poudel, Reidun Twarock, Nicole F. Steinmetz, Rudolf Podgornik, Wai-Yim Ching, Impact of hydrogen bonding in the binding site between Capsid protein and MS2 Bacteriophage ssRNA, J. Phys. Chem. B 121 (2017) 6321–6330.
[473] Eric C. Dykeman, Peter G. Stockley, Reidun Twarock, Solving a Levinthal's paradox for virus assembly identifies a unique antiviral strategy, Proc. Natl. Acad. Sci. USA 111 (14) (2014) 5361.
[474] Nikesh Patel, Eric C. Dykeman, Robert H.A. Coutts, George P. Lomonossoff, David J. Rowlands, Simon E.V. Phillips, Neil Ranson, Reidun Twarock, Roman Tuma, Peter G. Stockley, Revealing the density of encoded functions in a viral RNA, Proc. Natl. Acad. Sci. USA 112 (7) (2015) 2227–2232.
[475] Peter G. Stockley, Neil A. Ranson, Reidun Twarock, A new paradigm for the roles of the genome in ssRNA viruses, Future Virol. 8 (6) (2013) 531–543.
[476] E.C. Dykeman, P.G. Stockley, R. Twarock, Dynamic allostery controls coat protein conformer switch- ing during MS2 phage assembly, J. Mol. Biol. 395 (2010) 916–923.
[477] Robert J. Ford, Amy M. Barker, Saskia E. Bakker, Robert H. Coutts, Neil A. Ranson, Simon E.V. Phillips, Arwen R. Pearson, Peter G. Stockley, Sequence-specific RNA-protein interactions overcome electrostatic barriers preventing assembly of satellite tobacco necrosis virus coat protein, J. Mol. Biol. 425 (2013) 1050–1064.
[478] P.G. Stockley, O. Rolfsson, G.S. Thompson, G. Basnak, S. Francese, N.J. Stonehouse, S.W. Homans, Ashcroft A.E., A simple RNA- mediated allosteric switch controls the pathway to formation of a T = 3 viral capsid, J. Mol. Biol. 369 (2007) 541–552.
[479] Jason D. Perlmutter, Michael F. Hagan, The role of packaging sites in efficient and specific virus assembly, J. Mol. Biol. 427 (15) (2015) 2451–2467.
[480] A. Ortega, D. Amorós, J. García de la Torre, Prediction of hydrodynamic and other solution properties of rigid proteins from atomic- and residue-level models, Biophys. J. 101 (4) (2011) 892–898.
[481] Alexander Borodavka, Roman Tuma, Peter G. Stockley, A two-stage mechanism of viral RNA compaction revealed by single molecule fluorescence, RNA Biol 10 (April) (2013) 481–489.
[482] Roman I. Koning, Josue Gomez-Blanco, Inara Akopjana, Javier Vargas, Andris Kazaks, Kaspars Tars, JoséMaría Carazo, Abraham J. Koster, Asymmetric cryo-em reconstruction of phage ms2 reveals genome structure in situ, Nat. Commun. 7 (12524) (2016) 12524.
[483] X. Dai, et al., In situ structures of the genome and genome-delivery apparatus in a single-stranded RNA virus, Nature 541 (7) (2017) 112–116.
[484] Reidun Twarock, German Leonov, Peter G. Stockley, Hamiltonian path analysis of viral genomes, Nat. Commun. 9 (9) (2018) 2021.
[485] Joseph Rudnick, Robijn Bruinsma, Icosahedral packing of RNA viral genomes, Phys. Rev. Lett. 94 (94) (2005) 038101.
[486] V.R. Chechetkin, V.V. Lobzin, Genome packaging within icosahedral capsids and large-scale segmentation in viral genomic sequences, J. Biomol. Struct. Dyn. (2018).
[487] D.L.D. Caspar, Self-control of self-assembly, Curr. Biol. 1 (1991) 30–32.
[488] Neil P. King, Willia Sheffler, Michael R. Sawaya, Breanna S. Vollmar, John P. Sumida, Ingemar André, Tamir Gonen, Todd O. Yeates, David Baker, Computational design of self-assembling protein nanomaterials with atomic level accuracy, Science 336 (6085) (2012) 1171–1174.
[489] Charlotte Uetrecht, Cees Versluis, Norman?R. Watts, Paul?T. Wingfield, Alasdair?C. Steven, Albert?J.?R. Heck, Stability and shape of Hepatitis?b virus Capsids in?vacuo, Angew. Chem. Int. Ed. 47 (33) (2008) 6247–6251.
[490] Charlotte Uetrecht, Cees Versluis, Norman R. Watts, Wouter H. Roos, Gijs J.L. Wuite, Paul T. Wingfield, Alasdair C. Steven, Albert J.R. Heck, High-resolution mass spectrometry of viral assemblies: molecular composition and stability of dimorphic hepatitis B virus capsids, Proc. Natl. Acad. Sci. USA 105 (27) (2008) 9216–9220.
[491] David Z. Keifer, Tina Motwani, Carolyn M. Teschke, Martin F. Jarrold, Measurement of the accurate mass of a 50 MDa infectious virus, Rapid Commun. Mass Spectrom. 30 (17) (2016) 1957–1962.
[492] Joost Snijder, Rebecca J. Rose, David Veesler, John E. Johnson, Albert J.R. Heck, Studying 18 mega dalton virus assemblies with native mass spectrometry ** NIH public access, Angew. Chem. Int. Ed. Engl. 52 (14) (2013) 4020–4023.
[493] Kenneth Libbrecht, Field Guide to Snowflakes : Identifying Crystal Types, the Science behind Snowflakes, Observation Tools and Tips, a Close-Up Look at Nature's Art, Voyageur Press, 2016.
[494] Jeremy D. Schmit, Ken Dill, Growth rates of protein crystals, J. Am. Chem. Soc. 134 (9) (2012) 3934–3937.
[495] A. George, W.W. Wilson, Predicting protein crystallization from a dilute solution property, Acta Crystallogr. Sect. D Biol. Crystallogr. 50 (4) (1994) 361–365.
[496] C. Levinthal, Are there pathways for protein folding?, J. Chim. Phys. 65 (1968) 44–45.
[497] C.L. Brooks, J.N. Onuchic, D.J. Wales, Statistical thermodynamics. Taking a walk on a landscape, Science 293 (5530) (2001) 612–613.
[498] Steven B. Larson, Alexander McPherson, Satellite tobacco mosaic virus RNA: structure and implications for assembly, Curr. Opin. Struct. Biol. 11 (1) (2001) 59–65.
[499] Fumio Oosawa, Sho Asakura, Thermodynamics of the Polymerization of Protein, Academic Press, 1975.
[500] M. Cuillel, C. Berthet-Colominas, B. Krop, A. Tardieu, P. Vachette, B. Jacrot, Self-assembly of brome mosaic virus capsids. Kinetic study using neutron and x-ray solution scattering, J. Mol. Biol. 164 (4) (1983) 645–650.
[501] P.E. Prevelige, D. Thomas, J. king, Nucleation and growth phases in the polymerization of coat and scaffolding subunits into icosahedral procapsid shells, Biophys. J. 64 (3) (1993) 824–835.
[502] A. Zlotnick, J.M. Johnson, P.W. Wingfield, S.J. Stahl, D. Endres, A theoretical model successfully identifies features of hepatitis B virus capsid assembly, Biochemistry 38 (44) (1999) 14644–14652.
[503] Greg L. Casini, David Graham, David Heine, Robert L. Garcea, David T. Wu, In vitro papillomavirus capsid assembly analyzed by light scattering, Virology 325 (2) (2004) 320–327.
[504] Chao Chen, C. Cheng Kao, Bogdan Dragnea, Self-assembly of brome mosaic virus capsids: Insights from shorter time-scale experiments, J. Phys. Chem. A 112 (39) (2008) 9405–9412.
[505] Martin Castelnovo, Viral self-assembly pathway and mechanical stress relaxation, Phys. Rev. E 95 (5) (2017) 052405.
[506] James J. De Yoreo, Peter G. Velikov, Biomineralization, Rev. Mineral. Geochem. 54 (2003) 57–94.

[507] Stanislav Kler, Roi Asor, Chenglei Li, Avi Ginsburg, Daniel Harries, Ariella Oppenheim, Adam Zlotnick, Uri Raviv, RNA encapsidation by SV40-derived nanoparticles follows a rapid two-state mechanism, J. Am. Chem. Soc. 134 (21) (2012) 8823–8830.
[508] Adam Zlotnick, Stephen J. Stray, How does your virus grow? understanding and interfering with virus assembly, Trends Biotechnol. 21 (12) (2003) 536–542.
[509] Roya Zandi, Paul van der Schoot, David Reguera, Willem Kegel, Howard Reiss, Classical nucleation theory of virus capsids, Biophys. J. 90 (6) (2006) 1939–1948.
[510] H.R. Crane, Principles and problems of biological growth, Sci. Mon. 70 (6) (1950) 376–389.
[511] Tao Hu, B.I. Shklovskii, Kinetics of viral self-assembly: Role of the single-stranded RNA antenna, Phys. Rev. E 75 (5) (2007) 051901.
[512] Adam Zlotnick, J. Zachary Porterfield, Joseph Che-Yen Wang, To build a virus on a nucleic acid substrate, Biophys. J. 104 (7) (2013) 1595–1604.
[513] Aaron Klug, From virus structure to chromatin: X-ray diffraction to three-dimensional electron microscopy, Annu. Rev. Biochem. 79 (2010) 1–35.
[514] P.J.G. Butler, A. Klug, Assembly of the particle of tobacco mosaic virus from RNA and disks of protein, Nat. New Biol. 229 (2) (1971) 47–50.
[515] Santanu Mukherjee, Mahmoud Abd-El-Latif, Michal Bronstein, Orly Ben-nun Shaul, Stanislav Kler, Ariella Oppenheim, High cooperativity of the SV40 major capsid protein VP1 in virus assembly, PLoS One 2 (8) (2007) e765.
[516] Sherwood Casjens, Virus Structure and Assembly, Jones & Bartlett Pub., 1985.
[517] Robert W. Lucas, Steven B. Larson, Alexander McPherson, The crystallographic structure of brome mosaic virus, J. Mol. Biol. 317 (1) (2002) 95–108.
[518] C. Cheng Kao, K. Sivakumaran, Brome mosaic virus, good for an RNA virologist's basic needs, Mol. Plant Pathol. 1 (2) (2000) 91–97.
[519] Amy M. Wen, Nicole F. Steinmetz, Design of virus-based nanomaterials for medicine, biotechnology, and energy, Chem. Soc. Rev. 45 (15) (2016) 4074–4126.
[520] Connie B. Chang, Charles M. Knobler, William M. Gelbart, Thomas G. Mason, Curvature dependence of viral protein structures on encapsidated nanoemulsion droplets, ACS Nano 2 (2) (2008) 281–286.
[521] Minseok Kwak, Inge J. Minten, Diana-Milena Anaya, Andrew J. Musser, Melanie Brasch, Roeland J.M. Nolte, Klaus Müllen, Jeroen J.L.M. Cornelissen, Andreas Herrmann, Virus-like particles templated by DNA micelles: a general method for loading virus nanocarriers, J. Am. Chem. Soc. 132 (23) (2010) 7834–7835.
[522] Irina B. Tsvetkova, Bogdan Dragnea, Encapsulation of nanoparticles in virus protein shells, in: Brendan Orner (Ed.), Methods Mol. Biol, Springer, 2015, (chapter 1).
[523] B. Chen, J.W. Randles, R.I.B. Francki, Mixed-subunit capsids can be assembled in vitro with coat protein subunits from two cucumoviruses, J. Gen. Virol. 76 (1995) 971–973.
[524] G.W. Wagner, J.B. Bancroft, The self-assembly of spherical viruses with mixed coat proteins, Virology 34 (4) (1968) 748–756.
[525] A. McPherson, Micelle formation and crystallization as paradigms for virus assembly, Bioessays 27 (4) (2005) 447–458.
[526] Jason D. Perlmutter, Matthew R. Perkett, Michael F. Hagan, Pathways for virus assembly around nucleic acids, J. Mol. Biol. 426 (18) (2014) 3148–3165.
[527] Mauricio Comas-Garcia, Ruben D. Cadena-Nava, A.L.N. Rao, Charles M. Knobler, William M. Gelbart, In vitro quantification of the relative packaging efficiencies of single-stranded RNA molecules by viral capsid protein, J. Virol. 86 (22) (2012) 12271–12282.
[528] Alexandre Martinière, Elias Bassil, Elodie Jublanc, Carine Alcon, Maria Reguera, Hervé Sentenac, Eduardo Blumwald, Nadine Paris, In vivo intracellular ph measurements in tobacco and arabidopsis reveal an unexpected ph gradient in the endomembrane system w, Plant Cell 25 (2013) 4028–4043.
[529] J. Chen, P. Ahlquist, Brome mosaic virus polymerase-like protein 2a is directed to the endoplasmic reticulum by helicase-like viral protein 1a, J. Virol. 74 (9) (2000) 4310–4318.
[530] Devinka Bamunusinghe, Jang-Kyun Seo, A.L.N. Rao, Subcellular localization and rearrangement of endoplasmic reticulum by Brome mosaic virus capsid protein, J. Virol. 85 (6) (2011) 2953–2963.
[531] Benjamin G. Kopek, Guy Perkins, David J. Miller, Mark H. Ellisman, Paul Ahlquist, Three-dimensional analysis of a viral rna replication complex reveals a virus-induced mini-organelle, PLoS Biol. 5 (9) (2007) e220.
[532] María Medrano, Miguel Ángel Fuertes, Alejandro Valbuena, Pablo J.P. Carrillo, Alicia Rodríguez-Huete, Mauricio G. Mateu, Imaging and quantitation of a succession of transient intermediates reveal the reversible self-assembly pathway of a simple icosahedral virus Capsid, J. Am. Chem. Soc. 138 (47) (2016) 15385–15396.
[533] Panagiotis Kondylis, Jinsheng Zhou, Zachary D. Harms, Andrew R. Kneller, Lye Siang Lee, Adam Zlotnick, Stephen C. Jacobson, Nanofluidic devices with 8 pores in series for real-time, resistive-pulse analysis of hepatitis b virus Capsid assembly, Anal. Chem. 89 (9) (2017) 4855–4862.
[534] Corinne A. Lutomski, Nicholas A. Lyktey, Elizabeth E. Pierson, Zhongchao Zhao, Adam Zlotnick, Martin F. Jarrold, Multiple pathways in Capsid assembly, J. Am. Chem. Soc. 140 (17) (2018) 5784–5790.
[535] Nolwenn Jouvenet, Sanford M. Simon, Paul D. Bieniasz, Visualizing HIV-1 assembly, J. Mol. Biol. 410 (4) (2011) 501–511.
[536] Rees F. Garmann, Aaron M. Goldfain, Vinothan N. Manoharan, Measurements of the self-assembly kinetics of individual viral capsids around their RNA genome, 2018, p. 265330, bioRxiv.
[537] Peter E. Prevelige, Follow the yellow brick road: A paradigm shift in virus assembly, J. Mol. Biol. 428 (2 Pt B) (2015) 416–418.
[538] F. Qu, T.J. Morris, Encapsidation of turnip crinkle virus is defined by a specific packaging signal and RNA size, J. Virol. 71 (2) (1997) 1428–1435.
[539] Óttar Rolfsson, Stefani Middleton, Iain W. Manfield, Simon J. White, Baochang Fan, Robert Vaughan, Neil A. Ranson, Eric Dykeman, Reidun Twarock, James Ford, C. Cheng Kao, Peter G. Stockley, Direct evidence for packaging signal-mediated assembly of bacteriophage MS2, J. Mol. Biol. 428 (2 Pt B) (2016) 431–448.
[540] Reidun Twarock, Mathematical virology: a novel approach to the structure and assembly of viruses, Philos. Trans. R. Soc. A-Math. Phys. Eng. Sci. 364 (1849) (2006) 3357–3373.
[541] Victoria L. Morton, Eric C. Dykeman, Nicola J. Stonehouse, Alison E. Ashcroft, Reidun Twarock, Peter G. Stockley, The impact of viral RNA on assembly pathway selection, J. Mol. Biol. 401 (2) (2010) 298–308.
[542] Karin Valegård, Lars Liljas, Kerstin Fridborg, Torsten Unge, The three-dimensional structure of the bacterial virus MS2, Nature 345 (6270) (1990) 36–41.
[543] Gary W. Witherell, Jonatha M. Gott, Olke C. Uhlenbeck, Specific interaction between RNA phage coat proteins and RNA, Prog. Nucleic Acid Res. Mol. Biol. 40 (1991) 185–220.
[544] R. Rigler, E.S. Elson, Fluorescence Correlation Spectroscopy. Theory and Applications, Springer, 2001.
[545] Volker Jacobsen, Patrick Stoller, Christian Brunner, Viola Vogel, Vahid Sandoghdar, Interferometric optical detection and tracking of very small gold nanoparticles at a water-glass interface, Opt. Express 14 (1) (2006) 405.
[546] Philipp Kukura, Helge Ewers, Christian Müller, Alois Renn, Ari Helenius, Vahid Sandoghdar, High-speed nanoscopic tracking of the position and orientation of a single virus, Nature Methods 6 (12) (2009) 923–927.
[547] Rees F. Garmann, Aaron M. Goldfain, Vinothan N. Manoharan, Measurements of the self-assembly kinetics of individual viral capsids around their rna genome, Proc. Natl. Acad. Sci. USA 116 (45) (2019) 22485–22490.

[548] Roya Zandi, David Reguera, Howard Reiss, Nucleation rates in a new phenomenological model, J. Phys. Chem. B 110 (44) (2006) 22251–22260, PMID: 17078666.
[549] Laure Franqueville, Petra Henning, Maria Magnusson, Emmanuelle Vigne, Guy Schoehn, Maria E. Blair-Zajdel, Nagy Habib, Leif Lindholm, G. Eric Blair, Saw See Hong, Pierre Boulanger, Protein crystals in adenovirus type 5-infected cells: Requirements for intranuclear crystallogenesis, structural and functional analysis, PLoS One 3 (8) (2008) e2894.
[550] Helen M.E. Duyvesteyn, Helen M. Ginn, Maija K. Pietilä, Armin Wagner, Johan Hattne, Jonathan M. Grimes, Elina Hirvonen, Gwyndaf Evans, Marie-Laure Parsy, Nicholas K. Sauter, Aaron S. Brewster, Juha T. Huiskonen, David I. Stuart, Geoff Sutton, Dennis H. Bamford, Towards in cellulo virus crystallography, Sci. Rep. 8 (1) (2018) 3771.
[551] S. Sri Krishna, C.N. Hiremath, S.K. Munshi, D. Prahadeeswaran, M. Sastri, H.S. Savithri, M.R.N. Murthy, Three-dimensional structure of physalis mottle virus: Implications for the viral assembly, J. Mol. Biol. 289 (4) (1999) 919–934.
[552] Yutong Song, Oleksandr Gorbatsevych, Yin Liu, Joann Mugavero, Sam H. Shen, Charles B. Ward, Emmanuel Asare, Ping Jiang, Aniko V. Paul, Steffen Mueller, Eckard Wimmer, Limits of variation specific infectivity and genome packaging of massively recoded poliovirus genomes, Proc. Natl. Acad. Sci. 114 (2017) E8731–E8740.
[553] M. Do Carmo, Differential Geometry of Curves and Surfaces, Prentice-Hall, 1976.